Electron Spectroscopy: Theory, Techniques and Applications

Volume 2

Edited by

C. R. Brundle

IBM Research
5600 Cottle Road
San Jose
California 95193, U.S.A.

and

A. D. Baker

Queens College
The City University of New York
Kissena Boulevard
Flushing, New York 11367, U.S.A.

Contents

ix

1

Basic Concepts of X-ray Photoelectron Spectroscopy

C. S. FADLEY*

Department of Chemistry, University of Hawaii, Honolulu, Hawaii 96822

1

I. INTRODUCTION

X-ray photoelectron spectroscopy has by now become a widely-used technique for studying the properties of atoms, molecules, solids, and surfaces. The extent of development between the first experiments of this type by Robinson and Rawlinson in 1914[1] and the present state of the art is indeed great, with most of this growth occurring within the last 10–20 years under the stimulation of pioneering studies begun in the early 1950s,[2, 3] particularly those carried out at Uppsala University.[3] From the first observations that core photoelectron peak intensities could be used for quantitative analysis by Steinhardt and co-workers[2] and that core electron binding energies exhibited chemically-induced shifts by Siegbahn and co-workers,[3] the number of distinct physical and chemical effects noted has expanded considerably. Thus, together with numerous developments in interpretive theory, this expansion has provided a rich panoply of information that can be derived by analysing different aspects of an x-ray photoelectron spectrum. To be sure, a greater understanding of the theoretical models underlying these phenomena has not always led to results as directly interpretable in simple chemical or physical terms as was initially imagined, but the overall scope of information derivable is nonetheless large enough to be useful in a broad range of disciplines.

The number of publications involving x-ray photoelectron spectroscopy (which is commonly referred to by one of the two acronyms *XPS* or *ESCA* ≡ electron spectroscopy for chemical analysis) is thus by now quite large, and includes several prior reviews[3, 4–10] and conference proceedings,[11, 12] as well as other chapters in this series on specific problems or areas of application.[13, 14] Thus, no comprehensive review of the literature will be attempted here, but rather only a concise discussion of various basic experimental and theoretical concepts, together with selected examples exhibiting different effects. In certain more newly developed areas, or for subjects in which confusion seems to exist in the literature, a somewhat more detailed treatment will be made. The instrumentation and experimental data discussed will be primarily restricted to that involving exciting radiation produced in a standard type of x-ray tube, thus providing an operational definition of XPS. Thus, photon energies of $\gtrsim 100$ eV will be considered, with principal emphasis on the most common 1·2–1·5 keV range. The more recently initiated photoemission studies utilizing synchrotron radiation[15] will thus not be included. The theoretical models discussed may, on the other hand, often apply directly to photoelectron emission experiments performed at lower photon energies as, for example, in conventional ultraviolet photoelectron spectroscopy (UPS) for which $h\nu$ is typically in the 5–40 eV range or in synchrotron studies. Alternatively, the models utilized in XPS may represent some particular

limit that cannot be used at lower energies. Thus, at several points, comparisons between low-energy- and high-energy-photoemission experiments will be made.

The fundamental experiment in photoelectron spectroscopy involves exposing the specimen to be studied to a flux of nearly monoenergetic radiation with mean energy $h\nu$, and then observing the resultant emission of photoelectrons, whose kinetic energies will be described most simply by the photoelectric equation:

$$h\nu = E_b^V(k) + E_{kin} \tag{1}$$

in which $E_b^V(k)$ is the binding energy or ionization potential of the kth level as referred to the vacuum level and E_{kin} is the photoelectron kinetic energy. (A more exact definition of binding energy, including a discussion of reference levels, is presented in Section II.B.3.) In general, both Auger electrons and secondary electrons (usually resulting from inelastic scattering processes) will also be emitted from the specimen, but it is generally possible to distinguish these electrons from true photoelectrons by methods to be discussed later in this section. There are three fundamental properties characterizing each emitted photoelectron: its kinetic energy, its directions of emission with respect to the specimen and the exciting radiation, and, for certain rather specialized experimental situations, the orientation of its spin. These three properties thus give rise to three basic types of measurements that are possible on the emitted electron flux.

(1) *The number distribution of photoelectrons with kinetic energy.* This measurement produces an electron spectrum or energy distribution curve (EDC) and, of course, requires some sort of electron energy analyser or spectrometer, of which several types are currently being utilized. In the dispersive spectrometers most commonly used in XPS, electron spectra are usually measured at fixed angles of electron emission (or over a small range of emission angles) relative to both the photon source and the specimen.

(2) *The distribution of photoelectron intensity with angle of emission.* Such angular-resolved measurements can be made relative to the photon propagation direction or to axes fixed with respect to the specimen. Generally, these measurements require kinetic energy distribution determinations at each of several angles of emission.

(3) *The spin polarization or spin distribution of the photoelectron intensity.* These measurements require a specimen that has somehow been magnetically polarized, usually by an external field, so that more photoelectrons may be emitted with one of the two possible spin orientations than with the other. Then the relative numbers of spin-up and spin-down photoelectrons are measured.[16] Such spin polarization measurements have so far only been

made with ultraviolet radiation for excitation, and they will not be discussed further here.

The additional time and experimental complexity required for angular distribution or spin polarization measurements have resulted in the fact that most XPS studies up to the present time have involved only kinetic energy distributions with a fixed geometry of the photon source, specimen, and spectrometer. However, measurements of both types (2) and (3) seem fruitful from several points of view, and angular-resolved XPS studies in particular have grown in importance in recent years.[17]

As an illustration of certain typical features observed in fixed-angle XPS spectra, Fig. 1 shows data obtained from an aluminum specimen exposed to monochromatized x-rays of 1487 eV energy. In Fig. 1(a), a broad-scan spectrum of 1000 eV width is displayed, and various prominent photoelectron peaks are labelled according to their level of origin from O1s to valence. The oxygen KLL Auger structure is also partially visible at the low-kinetic-energy end of the spectrum. The oxygen peaks arise from oxygen atoms present in a surface oxide layer; the C1s peak is due to an outermost surface layer of contaminants containing carbon. As is usually the case, the photo-electron peaks are considerably narrower and simpler in structure than the Auger peaks. Each electron peak exhibits to one degree or another an approximately constant background on its low-kinetic-energy side that is due to inelastic scattering; that is, electrons arising via the primary photoemission or Auger process that produces the sharp "no-loss" peak have been inelastically scattered in escaping from the specimen so as to appear in an "inelastic tail" or energy-loss spectrum.[18] Depending upon the types of excitation possible within the specimen, the inelastic tails may exhibit pronounced structure also, as is evident in the multiple peaks formed below the Al2s and Al2p no-loss features (which are due to the excitation of collective valence electron oscillations or plasmons[19] in aluminium metal), as well as the single broad peak in the O1s inelastic tail (which is due to one-electron excitations from the occupied to the unoccupied valence levels of aluminum oxide). The inelastic tail below C1s is considerably weaker due to the relatively thin layer of carbon-containing species present (approximately two atomic layers); thus, for this sample, C1s photoelectrons could escape with a relatively low probability of being inelastically scattered.

In Fig. 1(b), an expansion of the low-kinetic-energy region of the same aluminum spectrum is shown, and several other features are more clearly discernible. The plasmon loss structure is well resolved, and peaks associated with the excitation of up to four plasmons are seen. A magnified view of the rather low-intensity valence photoelectron region also shows complex spectral structure associated primarily with the overlapping metal- and oxide-valence levels. In general, XPS valence photoelectron intensities are approximately
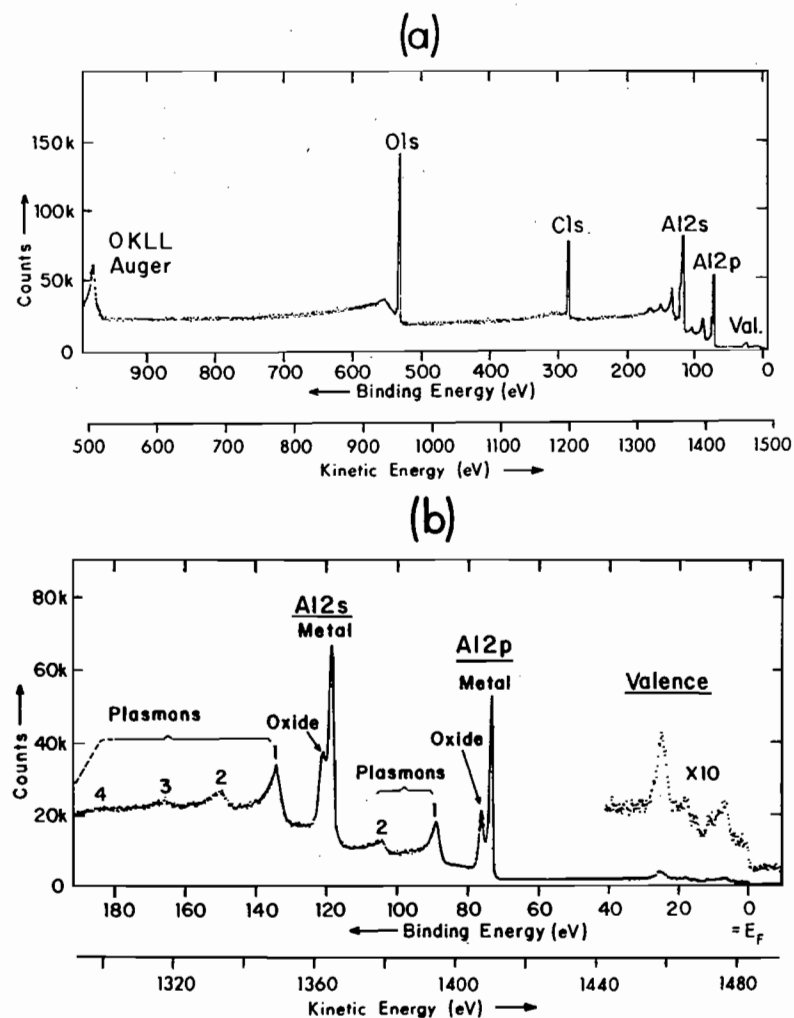
Fig. 1. Typical XPS spectra obtained from an oxidized aluminium specimen with a carbonaceous contaminant overlayer. Monochromatized AlKα radiation was used for excitation. (a) Overall spectrum with all major no-loss features labelled. (b) Expanded-scale spectrum of the Al2s, Al2p, and valence regions. Chemically-shifted oxide- and metal-core peaks are indicated, as well as inelastic loss peaks due to bulk plasmon creation.

an order of magnitude lower than those of the most intense core levels in a given specimen, but they are nonetheless high enough to be accurately measured and studied by using longer data acquisition times to improve statistics. An additional and chemically very significant feature in Fig. 1(b) is the splitting of the Al2s and Al2p photoelectron peaks into two components,

one associated with oxide and one associated with metal. This splitting or chemical shift is caused by the change in the aluminum chemical environment between oxide and metal.

In analysing XPS spectra, it is important to be able to distinguish as well as possible intensity resulting from Auger processes and inelastic scattering events. An Auger peak can be identified by: (1) comparing the observed peak energy with other experimental or theoretical Auger energies expected to be associated with the atom or atoms present, and (2) changing the photon energy by some amount $\Delta(h\nu)$ and then noting whether the peak shifts in kinetic energy by $\Delta(h\nu)$ according to Eq. (1) (and thus is a photoelectron peak) or remains fixed in kinetic energy (and thus has an Auger origin). Inelastic loss structure is often not as easily discernible in complex photoelectron spectra as for the examples shown in Fig. 1, but can be identified by: (1) looking for nearly identical features at kinetic energies below different no-loss peaks, as all high-energy electrons will be capable of the same excitations in inelastic scattering (although perhaps with probabilities that show a weak dependency on kinetic energy), and (2) comparing observed structure with independently-determined energy-loss spectra for the specimen material.[18]

A further very important point in connection with XPS studies of solid specimens is that the probability of inelastic scattering during escape from the sample is high enough that the mean depth of emission of no-loss electrons may be as small as a few atomic layers, and is never much larger than approximately 10 atomic layers.[20, 21] Thus, any analysis based on these no-loss peaks is inherently providing information about a very thin layer near the specimen surface, and this is, for example, the reason why O1s and C1s peaks due to thin surface overlayers are readily apparent in Fig. 1. This surface sensitivity of XPS (or any form of electron spectroscopy) can be exploited for studying various aspects of surface physics and chemistry,[22] but, on the other hand, must also be viewed as a potential source of error in trying to derive the true bulk properties of a given specimen.

In the following sections, various aspects of x-ray photoelectron spectroscopy are treated in more detail. In Section II, the instrumentation and experimental procedures required are reviewed. In Section III, the theoretical description of the photoemission process is discussed in detail so as to provide an accurate background for the consideration of various specific effects or areas of application; the use of XPS for the study of valence levels in molecules and solids is also considered. Section IV discusses chemical shifts of core-electron binding energies and various models used for interpreting them. Several effects primarily related to complexities in the final state of photoemission (namely relaxation phenomena, multiplet splittings, various many-electron interactions, and vibrational broadenings) are considered in Section V. In Section VI, various aspects of angular distribution measurements on

solids are considered. Finally, Section VII summarizes the present state of the technique and points out certain likely areas for future development.

II. EXPERIMENTAL CONSIDERATIONS

The basic components necessary for performing an XPS experiment consist of a radiation source for excitation, the specimen to be studied, an electron energy analyser, and some form of detection and control system. Each of these four distinct aspects of the experimental system is considered below. There are by now several commercial sources for complete XPS spectrometer systems[23–30] which represent various design approaches to each of these components.

A. Radiation Sources

The standard x-ray tube consists of a heated-filament cathode from which electrons are accelerated toward a suitable solid anode (usually water-cooled) over a potential of the order of 5–20 kV. Holes formed in the inner levels of the anode atoms by electron bombardment are then radiatively filled by transitions from higher-lying levels, with the resultant emission of x-rays. A thin, x-ray-transmitting window separates the excitation region from the specimen in most tubes. In general, more than one relatively sharp x-ray line will be emitted by any anode material, and the energy widths associated with various lines can also vary considerably from line to line or from element to element.[31] An additional source of radiation from such a tube is a continuous background of bremsstrahlung.[31] The choice of an anode material and operating conditions is thus made so as to achieve the closest possible approximation to a single, intense, monochromatic x-ray line. Various design geometries for such x-ray tubes are discussed in the literature,[3, 4, 31–36] with one obvious choice being whether to hold the anode or cathode at ground potential.

The anode materials most commonly utilized in XPS studies are Mg and Al, and, to a much lesser degree, Na and Si. Each of the members of this sequential series of second-row atoms gives rise to an x-ray spectrum that is dominated by a very intense, unresolved, $K\alpha_1$–$K\alpha_2$ doublet resulting from transitions of the type $2p_{\frac{3}{2}} \rightarrow 1s$ and $2p_{\frac{1}{2}} \rightarrow 1s$, respectively. The first demonstrations that such low-Z anodes could be utilized in XPS studies were by Henke.[32] These were followed approximately five years later by higher resolution applications by Siegbahn and co-workers.[3] The mean energies of the x-rays produced in such sources are: $NaK\alpha_{1, 2}$—$1041\cdot0$ eV,[35] $MgK\alpha_{1, 2}$—$1253\cdot6$ eV,[37] $AlK\alpha_{1, 2}$—$1486\cdot6$ eV[38] and $SiK\alpha_{1, 2}$—$1739\cdot5$ eV.[39] At these x-ray energies, aluminium or beryllium windows of 10–30 μm thickness are sufficiently transmitting for use in separating the tube and specimen region. Additional x-ray lines are also produced in such tubes, as indicated in Fig. 2

for a magnesium anode[37] (note the logarithmic scale). These consist of satellites arising from $2p \rightarrow 1s$ transitions in atoms that are doubly-ionized (KL in Fig. 2), triply-ionized (KL²), etc., and are denoted variously as Kα', Kα_3, Kα_4, ..., Kα_{14}. Kα_3 and Kα_4 are by far the most intense, and, in Mg and Al, they occur at about 10 eV above the K$\alpha_{1,2}$ peak and with intensities of approximately 8% and 4% of K$\alpha_{1,2}$, respectively. Photoelectron spectra obtained with non-monochromatized sources of this type thus always exhibit a characteristic double peak at kinetic energies ~ 10 eV above the strong
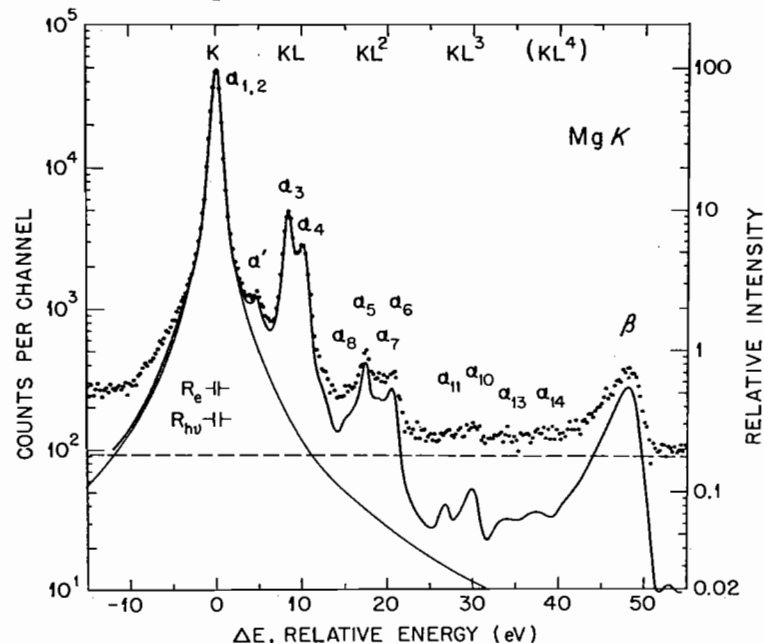

Fig. 2. The K x-ray emission spectrum of Mg metal as emitted by a non-monochromatized x-ray source. The peaks indicated $\alpha_{1,2}, ..., \beta$ correspond to various transitions into the K=$1s$ subshell. The dashed line is an average background and the solid line is the net spectrum. Note the logarithmic intensity scale. The notation K corresponds to a single initial $1s$ hole, KL to initial holes in both $1s$ and $2s$ or $2p$, KL² to a single initial hole in $1s$ and two initial holes in $2s$, $2p$, etc. (From Krause and Ferreira, ref. 37.)

K$\alpha_{1,2}$ peaks. The Kα', Kα_5, ..., Kα_{14} satellites are $\lesssim 1\%$ of K$\alpha_{1,2}$ in magnitude, and so, for most applications, can be neglected. An additional band of Kβ x-rays arises at energies approximately 45–50 eV above K$\alpha_{1,2}$ and is the result of valence$\rightarrow 1s$ transitions; the Kβ intensity is approximately 1% of K$\alpha_{1,2}$ for Mg and Al.[37] Thus, to a first approximation, the x-ray spectrum consists only of the very intense K$\alpha_{1,2}$ x-ray and most work has been based solely on an analysis of K$\alpha_{1,2}$-produced photoelectron peaks. However, in any study involving weak photoelectron peaks, or peaks generated by K$\alpha_{1,2}$ which overlap with satellite-generated peaks due to other

electronic levels, the non-monochromatic character of the x-ray source must be taken into account. For such non-monochromatized x-ray sources, the primary limiter of instrumental resolution is thus the natural linewidth of the K$\alpha_{1,2}$ line. As judged by the full width at half maximum intensity (FWHM), this resolution limit is approximately 0·4 eV for NaK$\alpha_{1,2}$,[35] 0·7 eV for MgK$\alpha_{1,2}$,[35] 0·8 eV for AlK$\alpha_{1,2}$,[38] and 1·0–1·2 eV for SiK$\alpha_{1,2}$.[39] This width decreases with decreasing atomic number for two reasons: the $2p_{\frac{1}{2}}$–$2p_{\frac{3}{2}}$ spin-orbit splitting decreases and the $1s$ hole lifetime increases. Materials of lower atomic number are thus favoured for width, but Mg and Al are generally utilized because of their lower chemical reactivity and vapor pressure in comparison to Na, and thus their easier fabrication and use as anodes. Although neon is expected to yield a K$\alpha_{1,2}$ line at 848·6 eV of only $\sim 0·2$–0·3 eV width, no attempts at constructing such a source for use in XPS have as yet been successful. The use of K$\alpha_{1,2}$ lines from elements below neon in atomic number is generally not possible because the valence $2p$ levels involved are broadened by bonding effects, introducing a corresponding broadening in the x-ray line. However, the K$\alpha_{1,2}$ x-rays of F in highly ionic compounds have been used recently in XPS.[40]

The monochromatization of such K$\alpha_{1,2}$ x-rays by Bragg reflection from a suitable single crystal has also been utilized to achieve narrower excitation sources, as well as to eliminate satellite lines and bremsstrahlung radiation.[3, 23, 25, 41, 42] Although the intensity loss in such reflections is considerable, photoelectron peaks as narrow as 0·4 eV have been observed with monochromatized AlKα excitation;[25, 41, 42] this width is to be compared to the $\gtrsim 0·9$ eV typically found without monochromatization. To compensate for the loss in intensity due to monochromatization, various procedures have been utilized, including the use of very high-intensity x-ray tubes involving rotating anodes,[41] monochromator systems with more than one crystal,[25, 41] multichannel detection systems,[25, 41] and dispersion-compensating x-ray- and electron-optics.[3, 25] In dispersion compensation, all photon energies within the K$\alpha_{1,2}$ linewidth are spatially dispersed by Bragg reflection and utilized for photoelectron excitation, but their line-broadening influence is nullified by the action of the dispersive electron energy analyzer; the commercial Hewlett–Packard system based upon this mode of operation yields optimum photoelectron peak widths with AlK$\alpha_{1,2}$ of $\sim 0·5$ eV FWHM.[25]

An additional type of ultra-soft x-ray transition that has been utilized successfully in XPS studies is the Mζ transition ($4p_{\frac{3}{2}} \rightarrow 3d_{\frac{5}{2}}$) in the sequential elements Y to Mo. The use of such x-rays in XPS was first suggested by Krause,[34] who pointed out that they yield sufficiently intense and monochromatic sources in the very interesting energy range of $100 \lesssim h\nu \lesssim 200$ eV, even though various satellite x-rays are present. The most narrow and thus

most used lines of this type are those for Y ($h\nu = 132 \cdot 3$ eV, FWHM $= 0 \cdot 5$ eV) and Zr ($h\nu = 151 \cdot 4$ eV, FWHM $= 0 \cdot 8$ eV), and they have been successfully applied to studies of both valence levels and outer core levels.[34-36] The ultra-soft character of these x-rays and their resultant decreased ability to penetrate through matter, as well as the significant sensitivity of their linewidths to surface chemical alterations of the anode surface, lead to several special features of tube design. Thin polymeric windows must be used. Relatively high excitation voltages as compared to $h\nu$ of ~ 4–6 kV are also beneficial to maximize the intensity originating in the metallic anode interior (as distinct from its oxidized exterior).[35] And, in the highest resolution designs, a continuous deposition of fresh anode material is provided during operation.[34, 36]

A final rather new development in x-ray sources by Hovland[43] that deserves mention here leads to what has been termed *scanning* XPS. A thin layer of specimen material is directly deposited on one side of a thin Al foil (~ 6 μm thick). A high-resolution scanning electron beam is directed at the other side of this foil, so that, at any given time, AlKα x-rays are produced over only a very small spot with dimensions comparable to the beam diameter. These x-rays readily pass through the thin foil and specimen, exciting photoelectrons from a corresponding spot near the specimen surface. Lateral spatial resolutions of as low as 20 μm have so far been achieved, and a number of potential applications for such scanning XPS measurements exist.[43] The only significant limitation is that it must be possible to prepare sufficiently thin specimens (~ 1000–10,000 Å) that x-ray attenuation in penetrating to the surface is not appreciable.

The x-ray sources discussed up to this point thus permit high-resolution measurements to be carried out in the two approximate photon-energy ranges 100–200 eV and 1000–2000 eV, with a relatively little explored region from ~ 200–1000 eV separating them. Another source of radiation in the photon energy region from 100 to 2000 eV of principal interest here is the so-called synchrotron radiation that is emitted in copious quantities by centripetally-accelerated electrons moving with highly relativistic velocities.[15, 44] This continuous spectrum of radiation is sufficiently intense to permit selection of a narrow range on the order of tenths of eV or lower with a suitable monochromator (usually a grating) while still maintaining fluxes adequate for photoemission studies. A number of excellent photoemission studies have by now been performed using such radiation,[15] although these have so far been restricted to photon energies between approximately 10 and 350 eV, principally because of the difficulty of achieving adequate monochromatization without severe intensity loss for soft x-rays of $\gtrsim 350$ eV. Such radiation has the advantages of being both continuously variable in energy, as well as linearly polarized to a high degree;[44] thus, the exploration of phenomena dependent upon photon energy and/or polarization are much more easily

studied than with more standard ultraviolet or soft x-ray sources. By contrast the soft x-ray tubes discussed previously emit radiation that is randomly polarized to a very good approximation.

B. Specimen Preparation

1. *Introduction.* X-ray photoelectron spectra have been obtained from specimens present as gases, solids, or liquids. The preparation and handling of any specimen requires considering two important factors: (1) In order to avoid excessive inelastic scattering during photoelectron traversal through the energy analyzer, pressures between the specimen and the detector must be maintained at $\lesssim 10^{-4}$ torr. This limit is easily estimated by considering a typical path length during analysis of 100 cm, and requiring that the total number of atoms/molecules encountered along this path be no greater than the analogous number encountered along the mean no-loss distance of emission from a typical solid specimen of ~ 20 Å. (2) As the emission of photoelectrons, Auger electrons, and secondary electrons from any specimen constitutes a net loss of negative charge, it is also necessary to minimize or in some other way correct for the possible occurrence of a significant positive potential build-up in the emitting region. One way in which this is accomplished to some degree in any system is by the flux of similar electrons emitted *toward* the specimen by various portions of the specimen chamber and holder which are also in general exposed to exciting x-rays and/or electrons, although this can in fact lead to the opposite problem: a negative potential build-up.[45] The charging potential V_c produced by any net imbalance between charge input and output may vary throughout the specimen volume and in effect cause a range of energy level shifts from the values corresponding to the limiting situation in which no charging occurs. Thus, if $\mathbf{r}$ is the spatial coordinate of the emission point within the specimen, and $E_b{}^V(k, \mathbf{r})^0$ and $E_{kin}{}^0$ are the binding energy and kinetic energy expected for emission from level k in the absence of charging, the photoelectric equation [Eq. (1)] can be rewritten as

$$h\nu = E_b{}^V(k, \mathbf{r}) + E_{kin}(\mathbf{r})$$
$$= E_b{}^V(k)^0 + E_{kin}(\mathbf{r}) + V_c(\mathbf{r}) \qquad (2)$$

Thus, if $V_c(\mathbf{r})$ is significant with respect to the typical instrumental resolution of $\sim 0 \cdot 1$ eV (which it indeed can be in certain cases[4, 45]), the measured binding energies $E_b{}^V(k, \mathbf{r})$ will in general be different from $E_b{}^V(k)^0$, and peak broadening also may occur. To minimize or correct for such effects, studies of peak position versus x-ray flux can be made,[45, 46] and a variable external source of electrons can be provided.[25] For gaseous specimens, the pressure can also be varied.[4] For solids, it is also customary to connect the specimen electrically to the specimen chamber as well as possible. Also, the presence

of a certain reference atom (for example, gold or carbon) on the surface of the specimen can be used to correct for charging,[47] although this procedure is often not completely unambiguous. A method recently developed by Grunthaner[48] involves floating a solid specimen at a variable negative potential and noting that potential at which an external source of mono-energetic electrons just begins to reach the surface; although not widely used as yet, this method seems to provide a very direct way of measuring surface potential distributions and thus correcting for them.

2. *Gaseous Specimens.* The basic requirement for gas-phase studies is a chamber to contain the gas with an x-ray-transparent window separating it from the x-ray source and a small opening or slit to permit photoelectron exit into the energy analyzer.[4, 33, 47, 49-51] Typical gas pressures required in the chamber are from 10^{-2} to 1 torr, and therefore some form of differential pumping is generally necessary between the exit slit and the analyzer in order to minimize gas-phase inelastic scattering effects,[4] as discussed previously. Typical specimen volumes are of the order of 1 cm^3. The first gas-phase XPS studies were performed by Krause and Carlson,[49] followed shortly thereafter by the more extended investigations of Siegbahn *et al.*[4] The gas in the chamber can be provided by a room-temperature gas-phase source, or can be the result of heating liquid-[4] or solid-[33] phase reservoirs. With such devices, metals and other vaporizable solids can be studied by photoelectron spectroscopy in the gas phase.[33, 50] In certain studies, rather significant changes in peak positions and relative intensities due to the combined effects of charging and kinetic energy-dependent inelastic scattering have been noted,[4] but, in general, these are relatively small, especially at lower pressures.

For gas-phase spectra, the vacuum level is the naturally-occurring reference level, so that Eqs (1) and (2) are directly related to measurable quantities.

3. *Solid Specimens.* There are various methods of preparing solid specimens suitable for study by XPS. Typical specimen areas are ~1 cm^2 or smaller, and, because inelastic scattering effects limit the no-loss emission to a mean depth of only 10–80 Å below the surface (as discussed in more detail in Section III.E), this corresponds to an active specimen volume of only approximately 10^{-6} cm^3. Thus, total masses of only 1–10 μg are involved, and amounts of material on the order of 10^{-9} g can be detected under certain circumstances. Any change of the chemical composition in the first few atomic layers near the surface can thus also have a significant influence on results.

Machineable solids can simply be cut, cleaved, and/or polished into shapes suitable for mounting in the specimen position. For materials that can be prepared as fine powders at room temperature, specimens can also be prepared by pressing the powder into a uniform pellet (perhaps supported by an imbedded conducting-wire mesh) or by dusting the powder onto an adhesive backing such as that provided by double-sided tape (although this procedure

has the rather undesirable characteristics of limiting temperature excursions and providing a steady source of surface-contaminating carbonaceous volatiles). In order to minimize atmospheric contamination or alteration of specimens, final preparation in an inert-atmosphere glove box or bag, perhaps attached to the specimen chamber, can be useful. Elements and certain compounds can also be heated *in situ* and vapor-deposited on a supporting substrate to form specimens. Alternatively, dissolved materials can be deposited from solution on a substrate, either by evaporating off the solvent or by selectively electroplating out various components.[52] Materials that normally exist as liquids or gases can also be condensed onto suitably cooled substrates for study in the solid state.[4] A broad range of specimen temperatures has by now been investigated, ranging from near that of liquid helium (4 K)[53] to several thousand degrees Kelvin.[54]

The extreme surface sensitivity of XPS also leads in many applications to the requirement that the specimen region be held at pressures of $\lesssim 10^{-9}$ torr in order to permit adequate control of surface composition. For example, for O_2 at 10^{-9} torr and 25 °C, the gas-phase collision rate with a surface will be such that, if each molecule striking the surface remains there (corresponding to a sticking coefficient of 1·0), a full atomic layer will be deposited in approximately 50 min.[55] This minimum monolayer coverage time varies inversely with pressure, so that pressures of the order of 10^{-10} torr are necessary to insure the maintenance of a highly reactive surface in a clean state over the period of time of several hours usually required for a series of XPS measurements. In preparing such surfaces, *in situ* cleaning by vapor deposition, cleaving, scraping, or inert-gas ion bombardment is thus often used.[55]

For the case of solid specimens, an electrical connection is made to the spectrometer in an attempt to minimize charging effects and maintain a well-defined and fixed potential during photoemission. For the simplest possible case of a metallic specimen in a metallic spectrometer, the energy levels and kinetic energies which result are as shown in Fig. 3. Thermodynamic equilibrium between specimen and spectrometer requires that their electron chemical potentials or Fermi levels be equal as shown. In a metal at absolute zero, the Fermi level E_F has the interpretation of being the highest occupied level, as indicated in the figure; this interpretation of E_F is also very nearly true for metals at normal experimental temperatures. For semiconductors and insulators, however, it is not so simple to locate the Fermi level, which lies somewhere between the filled valence bands and the empty conduction bands. The work function ϕ_s for a solid is defined to be the energy separation between the vacuum level and the Fermi level. When connected as shown in Fig. 3, the respective vacuum levels for specimen and spectrometer need not be equal, however, so that in passing from the surface of the specimen into the spectrometer, an electron will feel an accelerating or retarding potential
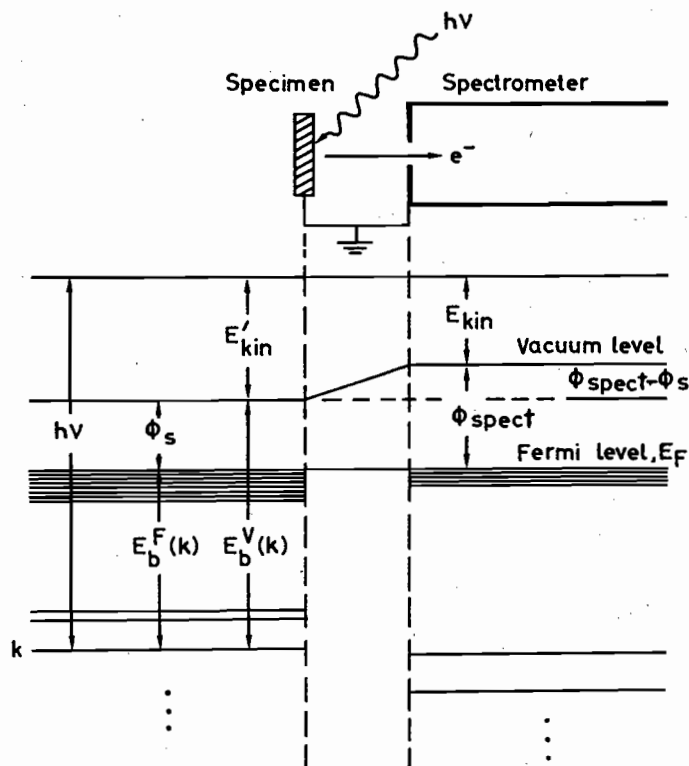
Fig. 3. Energy level diagram for a metallic specimen in electrical equilibrium with an electron spectrometer. The closely spaced levels near the Fermi level E_F represent the filled portions of the valence bands in specimen and spectrometer. The deeper levels are core levels. An analogous diagram also applies to semi-conducting or insulating specimens, with the only difference being that E_F lies somewhere between the filled valence bands and the empty conduction bands above.

equal to $\phi_s - \phi_{spect}$, where ϕ_s is the specimen work function and ϕ_{spect} is the spectrometer work function. Thus, an initial kinetic energy E_{kin}' at the surface of the specimen becomes E_{kin} inside the spectrometer, and

$$E_{kin} = E_{kin}' + \phi_s - \phi_{spect} \qquad (3)$$

From Fig. 3 it is thus clear that binding energies in a metallic solid can be measured quite easily relative to the identical Fermi levels of specimen and spectrometer. The pertinent equation is

$$h\nu = E_b^F(k) + E_{kin} + \phi_{spect} \qquad (4)$$

where the superscript F indicates a Fermi level reference. Provided that it is also possible to determine the specimen work function ϕ_s from some other

measurement, vacuum-referenced binding energies can then be obtained from

$$E_b^V(k) = E_b^F(k) + \phi_s \qquad (5)$$

In fact, photoelectron spectra can be used to derive vacuum-referenced binding energies by measuring the position of the zero-kinetic-energy cut-off of the usually very intense secondary electron peak. Such a cut-off is shown in Fig. 4 in XPS data obtained for metallic Au by Baer.[56] This procedure for determining work functions has been used extensively in UPS studies,[57] but only in a more limited way in XPS[56, 58] due to the greater range of
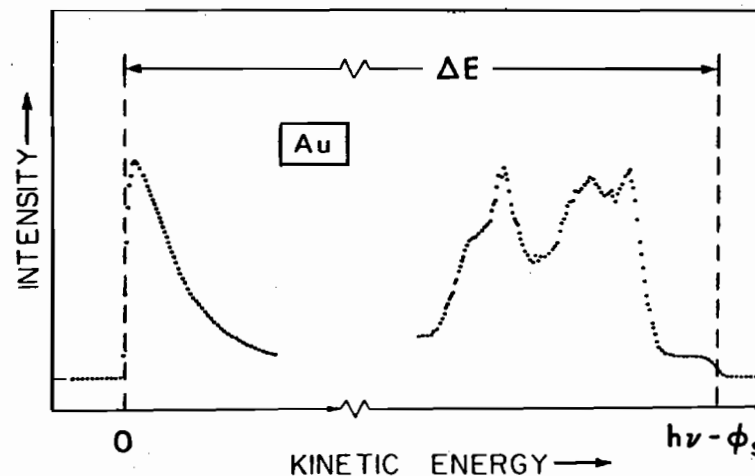
Fig. 4. Full XPS spectral scan for a polycrystalline Au specimen, showing both the cut-off of the secondary electron peak at zero kinetic energy and the high-energy cut-off for emission from levels at the metal Fermi level. The measurable distance ΔE thus equals $h\nu - \phi_s$, provided that suitable specimen biasing has been utilized. For this case, $h\nu$ was 1253·6 eV and ϕ_s was 5·1 eV. (From Baer, ref. 56.)

energies involved. In the simplest situation, both specimen and spectrometer are metallic and the energy diagram of Fig. 3 applies. All electrons emitted from the specimen are thus accelerated or decelerated by the same work function difference or contact potential $\phi_s - \phi_{spect}$ before analysis. With no voltage bias between specimen and spectrometer, the zero-energy cut-off corresponds to electrons propagating in final states exactly at the *spectrometer* vacuum level. For the implicit decelerating sign of $\phi_s - \phi_{spect}$ shown in Fig. 3, electrons propagating in final states at the *specimen* vacuum level are thus not observed. However, if the specimen is biased negatively with respect to the spectrometer by an amount greater than $\phi_s - \phi_{spect}$, then the low-energy cut-off does represent electrons at the specimen vacuum level or what can be defined as the true zero of kinetic energy. For the opposite accelerating sign of

$\phi_s - \phi_{spect}$, the true zero is observable and negative biasing is necessary only to insure that the cut-off is easily distinguishable against other sources of low-energy electrons.[56, 58] The low-energy cut-off thus establishes the zero of kinetic energy, and a distance $h\nu$ above this on the measured spectral scale corresponds to the point at which excitation from states at the specimen vacuum level would occur. On the same scale, the high-kinetic-energy cut-off observable for metal specimens (also shown in Fig. 4) is caused by excitation from occupied states at the Fermi level, and the difference between these two positions is thus the specimen work function. That is, if the measured difference in kinetic energy between the two cut-offs is denoted by ΔE, then

$$\phi_s = h\nu - \Delta E \qquad (6)$$

In more complex situations where semiconducting or insulating specimens are involved, initial states at E_F are not occupied so as to yield the same type of high-energy cut-off, although the low-energy cut-off can still be determined. The location of E_F in spectra can in this case be determined by using a reference metal specimen under the same biasing conditions, and assuming that electronic equilibrium is fully established between specimen, reference, and spectrometer. Possible charging effects make the latter assumption uncertain in many cases, however.

Whether it is determined from photoemission measurements or not, in general some additional information concerning ϕ_s is necessary to determine $E_b{}^V(k)$ for a solid specimen. Inasmuch as ϕ_s is also very sensitive to changes in surface composition, it is thus often Eq. (4) that is used in analyzing data for metals and other solid specimens. From this discussion, it is clear that Fermi-referenced binding energies are operationally very convenient for solid specimens, although they may not always be the most directly comparable to the results of theoretical calculations, in which the vacuum level often emerges as the natural reference.

4. *Liquid Specimens.* The requirement that pressures in the analyzer region be maintained at reasonably low levels of $\lesssim 10^{-4}$ torr means that measurements on common liquids with relatively high vapor pressures can be performed only with difficulty. However, Siegbahn and co-workers[41, 59] have developed techniques for carrying out such studies; these involve a continuously-replenished liquid source in the form of either a free jet or a thin film carried on a translating wire, together with a high-speed differential pumping system between specimen chamber and analyzer. With such an apparatus, it has been possible to study relatively non-volatile liquids such as formamide ($HOCNH_2$), as well as solutions of the ionic solid KI dissolved in formamide. Certain liquid metals and other very low vapor pressure materials can, on the other hand, be studied with relatively little special equipment.[60]

C. Electron Energy Analysis

1. *Brief Overview.* The various specific types of energy analyzers utilized in electron spectroscopy are discussed in detail in the literature,[10, 61, 62] as well as in a special chapter in this series.[63] Thus, only certain salient features relevant to x-ray photoelectron studies will be reviewed here. In general, there are several criteria that an analyzer should satisfy: (1) A resolution capability of $\Delta E_{kin}/E_{kin} \approx 0.01\%$. This corresponds to 0·1 eV for 1000 eV electrons. Most XPS spectrometers presently operate in the 0·01–0·10% range. (2) The highest possible efficiency (sensitivity, intensity). That is, the highest possible fraction of electrons leaving the sample should be energy-analyzed and detected at the same time. (3) Unrestricted physical access to the sample and detector regions. This permits a wide variety of excitation sources, specimen geometries, and detector systems to be used.
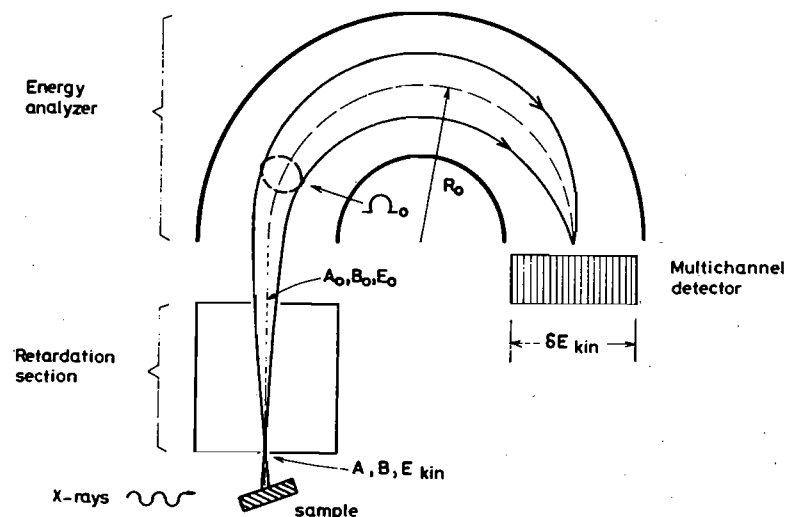
Fig. 5. Schematic illustration of an XPS spectrometer system indicating the primary components of radiation source, sample, electron energy analyser, and detector. For the specific example shown here, the energy analysis is accomplished by a pre-retardation section followed by a hemispherical electrostatic analyzer. A multichannel detector is also shown for generality.

(4) Ultra-high-vacuum capability for work on solid samples if surface composition is to be precisely controlled. (5) Ease of construction. One design philosophy often used for increasing the ease of construction is to insert a retardation section before the analyzer as shown schematically in Fig. 5, so that the energy of a given electron can be reduced from its initial value of E_{kin} to the final value at which it is analyzed of E_0. For a given *absolute* resolution of ΔE_{kin}, the *relative* resolution required from the analyzer is thus

reduced from $\Delta E_{kin}/E_{kin}$ to $\Delta E_{kin}/E_0$, thereby permitting looser tolerances on many mechanical and electrical components. The net effects of such retardations on intensity may or may not be deleterious, however, and are discussed in more detail in the next section. (6) Relative insensitivity to external environment, particularly as regards the shielding of extraneous magnetic fields. The vast majority of spectrometers currently in use are based on interaction with electrostatic fields and for these, μ-metal shielding is generally used to exclude extraneous magnetic fields. Only for the relatively few magnetic spectrometers in use are Helmholtz-coil systems required for magnetic field cancellation.[3, 4] Quantitative estimates of the degrees to which extraneous magnetic fields must be excluded for a given resolution have been calculated previously.[64] (7) If angular distribution studies are intended, well-defined, and perhaps also variable, angles of electron exit and x-ray incidence. This requirement generally acts counter to that for high efficiency, as it implies detecting only electrons emitted in a relatively small element of solid angle, thus reducing the total number that can be analyzed and detected.

With these constraints, there are several possible analyzer configurations,[61, 62] but the three that have been most used in XPS are all of the spatially dispersive type, and consist of the hemispherical electrostatic (schematically shown in cross-section in Fig. 5),[3, 61, 65] the cylindrical mirror electrostatic (CMA),[61, 66–68] and the double-focussing magnetic with a $l/\sqrt{r}$ field form.[3, 64, 69] In all of these analyzers, electrons are dispersed on the basis of kinetic energy along a radial or axial coordinate. For reasons of both ease of construction and magnetic shielding, the two electrostatic analyzers are much more common than the double-focussing magnetic, although a number of important early studies were performed on such instruments,[3, 33] and a fully-optimized spectrometer based upon the $l/\sqrt{r}$ field form is presently under construction.[64, 70] In addition to these dispersive analyzers, limited use has also been made in XPS of non-dispersive analyzers based upon the retarding grid principle.[71–73] Such analyzers are usually of relatively limited resolution (~1%), however, so that their use has been restricted to the obtaining of chemical composition information similar to that derived from Auger spectra. Such low-resolution Auger and XPS spectra can, in fact, be generated by using the spherical grids of a low-energy electron diffraction (LEED) system as a retarding grid analyzer. A further type of commercial analyzer developed specifically for XPS studies by the DuPont Corporation[24] is a hybrid with both dispersive and non-dispersive characteristics. Its first stage consists of an electrostatic deflection section that selects a band of energies in a dispersive mode; two subsequent retarding grid sections act as low-pass and high-pass filters with the net result that only a narrow band of energies is detected after the high-pass filter. A final type of XPS spectrometer with certain unique features is that formerly produced by

the Hewlett Packard Company,[25] which makes use of dispersion-compensating x-ray- and electron-optics.[3, 74] In this system, an x-ray monochromator is matched to a retarding-lens/hemispherical-electrostatic-analyzer unit in such a way as to maximize intensity and minimize linewidths without the use of any slits in the x-ray optics; the detailed performance of this spectrometer has been analyzed recently.[74]

2. *Spectrometer Efficiency and Retardation.* The resolution and efficiency of any spectrometer are of critical importance. These properties are highly dependent upon one another, since for operation at lower resolution (higher $\Delta E_{kin}/E_{kin}$), a higher fraction of electrons can usually be energy-analyzed and detected. For operation at a given resolution, the overall efficiency E of a dispersive analyzer can be written as proportional to the following product[64]

$$E \propto BA\Omega \cdot \delta E_{kin} \qquad (7a)$$

in which B is the brightness or intensity of the electron source for the energy analyzer in electrons per unit area *and* per unit solid angle, A is the area of the source, Ω is the solid angle over which electrons from the source are accepted into the energy analyzer and detected, and δE_{kin} is the range of electron energies or spectral width which can be analyzed at one time (as, for example, by a multi-channel detector). B, A, and Ω in general depend on E_{kin} for a given spectrometer. δE_{kin} will thus be proportional to N, the number of distinct energy channels simultaneously detected. If B and A vary over the area of the source, then a more correct statement of this efficiency involves an integration over the surface as

$$E \propto (\int B\Omega \cdot dA) \cdot \delta E_{kin} \qquad (7b)$$

The effective electron source as seen by the analyzer is often defined by an aperture in front of the photoemitting sample, and, depending upon the system, B, A, and Ω may refer to this aperture or to the true specimen surface. If a multichannel detector is utilized, δE_{kin} may in principle be as large as 10% of E_{kin},[25, 64] whereas the resolution ΔE_{kin} will be $\gtrsim 0.01\%$ of E_{kin}. In this case, the detector would correspond to $\lesssim 1000$ channels. The notation used in this discussion is indicated in the schematic drawing of Fig. 5, where subscript zeros have been used on all quantities after a hypothetical retarding section. Such a retarding section may or may not be present, according to the specific system under consideration.

Helmer and Weichert[75] first pointed out that, for the general class of dispersive analyzers used in XPS, it is possible to retard before analysis, and, for a given absolute resolution ΔE_{kin}, to *gain* in overall efficiency in a system with single-channel detection (for which $\delta E_{kin} \approx \Delta E_{kin}$ and $N=1$), and this result has proven useful in several specific spectrometer designs.[23, 25, 27, 28, 30]

Their analysis (which has also been extended to apply to systems with multi-channel detection by Hagström and Fadley[6]) compares the operation of a given dispersive analyzer with and without retardation for a fixed resolution ΔE_{kin}, and with a primary electron source of fixed brightness B (cf. Fig. 5). It also requires that the source area A_0 and solid angle Ω_0 utilized at the analyzer entrance (and thus perhaps after the retardation section) be adjusted to the maximum values consistent with a resolution of ΔE_{kin} in either mode of operation *and* that the primary source (for example, a first entrance aperture) be capable of supplying electrons over sufficient area and solid angle to fill or illuminate both A_0 and Ω_0 with electrons. There are then two factors to be considered: (1) *The loss of brightness with retardation.* This loss of brightness has been derived for a few geometries involving a source and a *non-absorbing* retardation (or acceleration) section. If θ is defined to be the angle between the electron emission direction and a planar source surface, these geometries include a source emitting with a $\sin \theta$ intensity distribution into an arbitrary point-to-point imaging lens system,[76] and a source with either a $\sin \theta$ [77] or an isotropic[75] intensity distribution emitting into a uniform retarding field perpendicular to its surface. These derivations, which often (but not always) make use of the Abbe sine law[75, 76] or its paraxial-ray approximation the Langrange–Helmholtz relation,[3, 76] result in a simple brightness variation of the form:

$$B_0 = B \left(\frac{E_0}{E_{kin}} \right) \qquad (8)$$

in which B_0 and E_0 are the brightness and kinetic energy after retardation. The cases for which this relationship has been shown to hold thus represent limits that are relatively easily achieved experimentally. Without retardation, the efficiency of a spectrometer conforming to this brightness law and possessing only a single channel of detection will be

$$E \propto BA\Omega \qquad (9)$$

whereas with retardation it will be

$$E' \propto B_0 A_0 \Omega_0 \qquad (10)$$

or, from Eq. (8),

$$E' \propto B \left(\frac{E_0}{E_{kin}} \right) A_0 \Omega_0 \qquad (11)$$

(2) *The gain in efficiency associated with the increase of A_0 and Ω_0 relative to A and Ω permitted by the decrease in relative resolution from* $(\Delta E_{kin}/E_{kin})$ *to* $(\Delta E_{kin}/E_0)$. As a specific example, consider the hemispherical electrostatic analyzer, which is shown in Fig. 5. Its resolution is controlled by the radial source width s, the axial (out-of-plane) source height h, the radial detector

width d, the radial angle of emission α_r, the axial (out-of-plane) angle of emission α_z, and the optic circle radius R_0, according to [3, 61]

$$\frac{\Delta E_{kin}}{E_{kin}} = \frac{s}{4R_0} + 0 \cdot 125 \left(\frac{h}{R_0} \right)^2 + \frac{d}{4R_0} + 0 \cdot 61\alpha_r^2 + \text{smaller terms in } \alpha_r, \alpha_z^3, \text{etc.} \quad (12)$$

The system is thus first-order focussing in h and α_r, and second-order focussing in α_z. Also, $sh = A$ (or A_0 with retardation) and $\alpha_z\alpha_r \propto \Omega$ (or Ω_0 with retardation). Optimizing the selection of each of the four parameters s, h, d and α_r by the reasonable procedure of requiring an approximately equal contribution from each term to $\Delta E_{kin}/E_{kin}$[69] thus means that

$$s \propto \frac{\Delta E_{kin}}{E_{kin}}, \quad h \propto \left(\frac{\Delta E_{kin}}{E_{kin}} \right)^{\frac{1}{2}}, \quad \alpha_r \propto \left(\frac{\Delta E_{kin}}{E_{kin}} \right)^{\frac{1}{2}} \qquad (13)$$

and α_z can conservatively be assumed to be held constant. Thus, without retardation,

$$A \propto \left(\frac{\Delta E_{kin}}{E_{kin}} \right)^{\frac{3}{2}}, \quad \Omega \propto \left(\frac{\Delta E_{kin}}{E_{kin}} \right)^{\frac{1}{2}} \qquad (14)$$

whereas with retardation

$$A_0 \propto \left(\frac{\Delta E_{kin}}{E_0} \right)^{\frac{3}{2}}, \quad \Omega_0 \propto \left(\frac{\Delta E_{kin}}{E_0} \right)^{\frac{1}{2}} \qquad (15)$$

The ratio of efficiencies with and without retardation is then after cancellations

$$\frac{E'}{E} = \frac{E_{kin}}{E_0} \qquad (16)$$

Thus, a tenfold retardation yields a tenfold loss in B, but a one hundredfold increase in the useable $A\Omega$ product, so that a net tenfold gain in efficiency results. Similar considerations apply to the other dispersive analyzers used in XPS,[75] provided that an appropriate retardation section is utilized. The application of such an analysis to a spectrometer in which a maximum degree of multichannel detection is incorporated is, by contrast, found to yield an approximately constant overall efficiency with retardation.[6]

D. Detection and Control

With very few exceptions, the detectors presently used in x-ray photoelectron spectroscopy are based on continuous-dynode electron mutipliers of the "channeltron" type.[62, 78, 79] These consist of fine-bore lead-doped glass tubes treated by hydrogen reduction at high temperature to leave the surface coated with a semiconducting material possessing a high secondary-electron emissive power.[62] Tube inner diameters vary from 1 mm down

to 10 μm. A high voltage of a few kV is applied between the ends of such a tube, and multiplications of 10^6–10^8 are achieved by repeated wall collisions as electrons travel down the inside of the tube. These multipliers are available in various configurations, often involving tube curvature to minimize ion-induced after-pulsing. Stacks of parallel tubes in the so-called "channel-plate" geometry are also available for use in multichannel detection schemes. Parallel-plate multipliers based upon the same principle have also been attempted.[80]

The efficiency gains concomitant with multichannel detection have led to the use of such a system in one commercial spectrometer,[25] in which the multiplied electron pulses from a channel plate are accelerated into a phosphorescent screen, behind which (and external to vacuum) is situated a vidicon camera for translating the optical signal into countable electronic pulses. Other forms of multichannel detection system based upon channel-plate/resistive strip combinations have also been used[81] to a limited degree, and solid-state image sensors of a different type appear to offer good possibilities for future applications of this nature.[62]

As the appropriate voltages or currents in the analyzer are swept so as to generate electron counts at different kinetic energies, there are various ways of storing and outputting the data. Most simply, a ratemeter can be directly coupled to a plotter or printer during a single continuous sweep. Generally, however, it is desirable to make repeated scans over a given spectral region to average out instrument drifts and certain types of noise; this results in the closest possible approximation to a spectrum with statistically-limited noise. Such repeated scanning requires some form of multiscalar memory, which is often expanded to involve on-line computer control.[33] The use of a more or less dedicated computer has additional advantages in that it can be used to control various functions of the spectrometer in a more automated way, as well as to carry out different types of data analysis such as background subtraction and curve fitting, and commercial systems usually offer this option.

E. Data Analysis

The aim of spectral analyses in XPS is to determine the locations, intensities, and, in certain cases, also the shapes of the various peaks observed, many of which are not clearly resolved from one another. Several complexities must be allowed for in doing this: (1) All peaks will exhibit inelastic tails toward low kinetic energy and these tails may in turn exhibit structure (see, for example, Fig. 1). As a rough approximation that is useful for many solid materials, a major portion of the inelastic tail can be assumed to have a linear or constant form, with extra features perhaps superimposed on it. Valence spectra from solids have been corrected for inelastic scattering by using a close-lying core level to derive the form of the inelastic tail,[33, 82] as well as by the more

approximate procedure of assuming an asymptotically-constant tail at low kinetic energy whose value at any energy is proportional to the integrated no-loss peak intensity at higher kinetic energies.[83] (2) All peaks ride on a background of secondary electrons from higher-kinetic-energy peaks. This background also can often be approximated as linear or constant. (3) The basic peak shapes observed in XPS are a convolution of several variable factors: the exciting x-ray lineshape, contributions from weaker x-rays such as satellites in non-monochromatized sources, the analyzer lineshape, possible non-uniform specimen charging, a Lorentzian hole-state lifetime contribution, Doppler broadening in gases,[4] and various final-state effects involving many-electron excitations[84] and vibrational excitations[41, 85] (as discussed further in Section V). Thus, no universal peak shape of, for example, Gaussian, Lorentzian, or Voigt-function form can be used, and most analyses have involved a somewhat trial-and-error fit for each specific problem. One rather general least-squares program for carrying out such fits permits choosing several basic peak shapes of Gaussian or Lorentzian form, to which are smoothly added an asymptotically-constant inelastic tail of variable height.[33] The effects of satellite x-rays can also automatically be included in the basic peak shape chosen, and a variable linear background is also present. Examples of spectral analyses for atomic 4d core levels using this program are shown in Fig. 6.[86] Lorentzian shapes have been used for Xe and Yb, and Gaussians for Eu, and the overall fits to these spectra are very good.

Beyond spectral analyses involving fits of certain functional forms to the data, Wertheim[87, 88] and Grunthaner[89] have also developed techniques for *deconvoluting* XPS spectra so as to mathematically remove instrumental linewidth contributions. The form of the instrumental linewidth has, in turn, been derived from the shape of the high-energy cut-off at the Fermi energy for a metallic specimen (cf. Fig. 4). This is possible because, to a good approximation, the density of occupied states ends in a vertical step function at E_F. The term "deconvolution" is also often incorrectly used to describe the results of peak-fitting procedures.

III. THE PHOTOEMISSION PROCESS

In this section, various aspects of the basic photoemission process are discussed in detail, with the primary aim of providing a unified theoretical framework for the subsequent discussion of various experimental observations. In discussing photoelectric cross-sections for atoms, molecules, and solids, applications to the interpretation of experimental results are also presented here.

A. Wave Functions, Total Energies, and Binding Energies

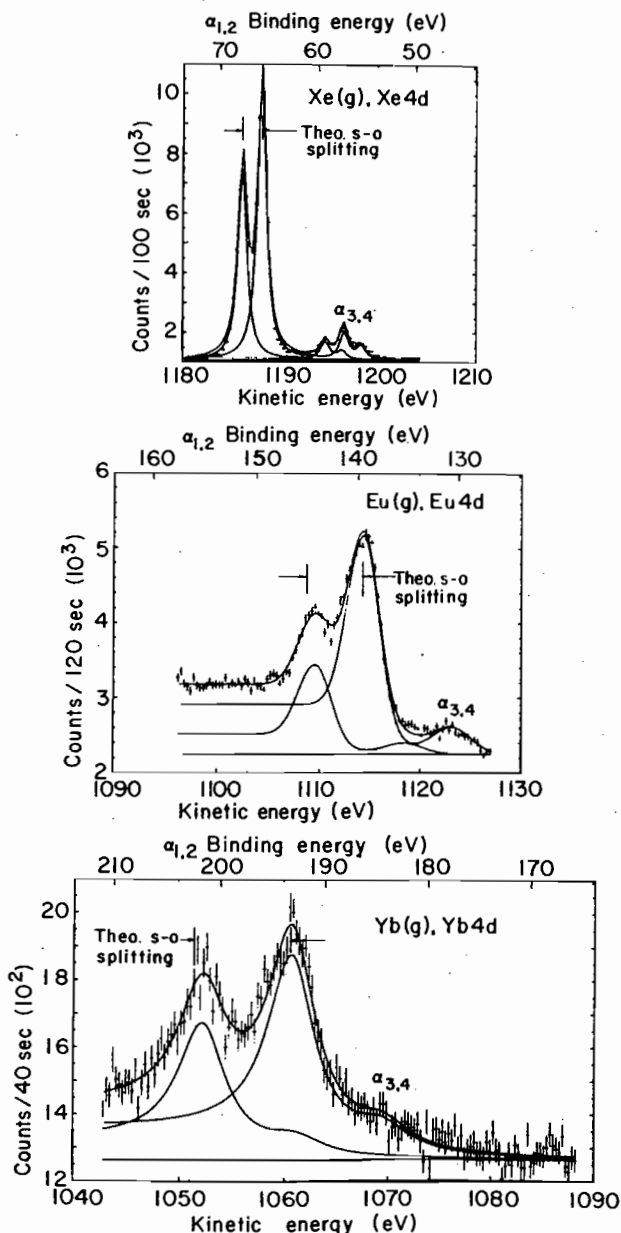In any photoelectron emission experiment, the basic excitation process

Fig. 6. $4d$ core photoelectron spectra from gaseous Xe, Eu, and Yb produced by excitation with non-monochromatized MgKα x-rays (cf. Fig. 2). The spectra have been resolved into components by least-squares fits of peak shapes including the $\alpha_{3,4}$ satellites and an asymptotically-constant inelastic tail. Lorentzian shapes were used for Xe and Yb, Gaussian for Eu. (From Fadley, ref. 33 (where the curve fitting program is described) and Fadley and Shirley, ref. 86.)

involves absorption of a photon of energy $h\nu$ according to

$$\underset{\text{Initial state}}{\Psi_{\text{tot}}{}^i(N),\ E_{\text{tot}}{}^i(N)} \xrightarrow{\ h\nu\ } \underset{\text{Final state}}{\Psi_{\text{tot}}{}^f(N, K),\ E_{\text{tot}}{}^f(N, K)} \tag{17}$$

Here $\Psi_{\text{tot}}{}^i(N)$ is the initial-state N-electron wave function corresponding to a total energy $E_{\text{tot}}{}^i(N)$, and $\Psi_{\text{tot}}{}^f(N, K)$ is the Kth final-state N-electron wave function (including the photoelectron) corresponding to a total energy of $E_{\text{tot}}{}^f(N, K)$. The relevant energy conservation equation is

$$E_{\text{tot}}{}^i(N) + h\nu = E_{\text{tot}}{}^f(N, K) \tag{18}$$

In the simplest situation, the index K thus labels the one-electron orbital k from which emission occurs (as discussed below), but in general it should describe all modes of excitation possible within the final state, including electronic, vibrational, and translational. In all forms of higher-energy photoelectron spectroscopy, it is customary to assume that the photoelectron is sufficiently weakly coupled to the $(N-1)$-electron ion left behind so as to permit separating the final state of the excitation process to yield

$$\underset{\text{Initial state}}{\Psi_{\text{tot}}{}^i(N),\ E_{\text{tot}}{}^i(N)} \xrightarrow{\ h\nu\ }$$
$$\underset{\text{Final state ion}}{\Psi_{\text{tot}}{}^f(N-1, K),\ E_{\text{tot}}{}^f(N-1, K)} + \underset{\text{Photoelectron}}{\phi^f(1)\chi^f(1),\ E_{\text{kin}}} \tag{19}$$

in which $\Psi_{\text{tot}}{}^f(N-1, K)$ and $E_{\text{tot}}{}^f(N-1, K)$ refer to the Kth $(N-1)$-electron ionic state that can be formed, E_{kin} is the kinetic energy of the Kth photoelectron peak, $\phi^f(1)$ is the spatial part of a one-electron orbital describing the photoelectron and $\chi^f(1)$ is the spin part of the photoelectron orbital ($\chi = \alpha$ or β). The form of $\phi^f(1)$ thus depends on kinetic energy. (For simplicity here, any change in kinetic energy due to work function differences between specimen and analyzer is neglected.) $\Psi_{\text{tot}}{}^f(N-1, K)$ and $\phi^f(1)$ can, if desired, be combined in a suitable sum of products to yield the correct overall antisymmetry with respect to electronic coordinates necessary in the final state. This can be written with an antisymmetrizing operator $\hat{A}$ as:[90, 91]

$$\Psi_{\text{tot}}{}^f(N, K) = \hat{A}(\phi^f(1)\chi^f(1),\ \Psi_{\text{tot}}{}^f(N-1, K)) \tag{20}$$

The energy conservation equation which then results is that most useful in analyzing XPS spectra:

$$E_{\text{tot}}{}^i(N) + h\nu = E_{\text{tot}}{}^f(N-1, K) + E_{\text{kin}} \tag{21}$$

The binding energy corresponding to leaving the ion in a state describable by $\Psi_{\text{tot}}{}^f(N-1, K)$ is thus given by

$$E_b{}^V(K) = E_{\text{tot}}{}^f(N-1, K) - E_{\text{tot}}{}^i(N) \tag{22}$$

in which the vacuum-level reference is implicit.

One inherent source of linewidth in any binding energy measurement is thus energy broadening due to lifetime effects in either the initial or final state. If the relevant lifetime is denoted by τ, uncertainty principle arguments thus lead to a broadening that is Lorentzian in shape, with a FWHM in eV given by $\sim \hbar/\tau = 6 \cdot 58 \times 10^{-16}/\tau(s)$. The initial state lifetime is usually very long, and so contributes negligible broadening. However, final-state lifetimes are estimated to be as short as 10^{-18} s in certain cases, so that such effects can play a major role in limiting XPS resolution, particularly for inner subshell excitation.

In general, for a system containing N electrons with spatial coordinates $\mathbf{r}_1, \mathbf{r}_2, ..., \mathbf{r}_N$ and spin coordinates $\sigma_1, \sigma_2, ..., \sigma_N$ and P nuclei with spatial coordinates $\mathbf{R}_1, \mathbf{R}_2, ..., \mathbf{R}_p$, any of the total wave functions considered will depend upon all of these coordinates

$$\Psi_{\text{tot}}(N) = \Psi_{\text{tot}}(\mathbf{r}_1, \sigma_1, \mathbf{r}_2, \sigma_2, ..., \mathbf{r}_N, \sigma_N; \mathbf{R}_1, \mathbf{R}_2, ..., \mathbf{R}_p) \qquad (23)$$

Nuclear spin coordinates can be neglected on the resolution scale of electron spectroscopy. In the non-relativistic limit that usually serves as the starting point for calculations on such systems, the relevant Hamiltonian in electrostatic units is

$$\hat{H}_{\text{tot}} = -\frac{\hbar^2}{2m} \sum_{i=1}^{N} \nabla_i^2 - \sum_{i=1}^{N} \sum_{l=1}^{P} \frac{Z_l e^2}{r_{il}} + \sum_{i=1}^{N} \sum_{j>i}^{N} \frac{e^2}{r_{ij}}$$
$$\underset{\substack{\text{Electron} \\ \text{kinetic}}}{} \qquad \underset{\substack{\text{Electron-} \\ \text{nuclear} \\ \text{attraction}}}{} \qquad \underset{\substack{\text{Electron-} \\ \text{electron} \\ \text{repulsion}}}{}$$
$$+ \sum_{l=1}^{P} \sum_{m>l}^{P} \frac{Z_l Z_m e^2}{r_{lm}} - \frac{\hbar^2}{2} \sum_{l=1}^{P} \frac{\nabla_l^2}{M_l} \qquad (24)$$
$$\underset{\substack{\text{Nuclear-} \\ \text{nuclear} \\ \text{repulsion}}}{} \qquad \underset{\substack{\text{Nuclear} \\ \text{kinetic}}}{}$$

Here, m is the electronic mass, Z_l is the charge of the lth nucleus, $r_{il} = |\mathbf{r}_i - \mathbf{R}_l|$, $r_{ij} = |\mathbf{r}_i - \mathbf{r}_j|$, $r_{lm} = |\mathbf{R}_l - \mathbf{R}_m|$ and M_l is the mass of the lth nucleus. To this must be added relativistic effects, usually via a perturbation approach;[92-94] the additional term in the Hamiltonian most often considered is spin–orbit splitting, which for atomic orbitals has the form:[93, 95, 96]

$$\hat{H}_{\text{so}} = \sum_{i=1}^{N} \xi(r_i) \hat{l}_i \cdot \hat{s}_i \qquad (25)$$

in which $\xi(r_i)$ is an appropriate function of the radial coordinate r_i,[95] $\hat{l}_i$ is the one-electron operator for orbital angular momentum, and $\hat{s}_i$ is the one-electron operator for spin angular momentum. The total wave function then must satisfy a time-independent Schroedinger equation of the form

$$\hat{H}_{\text{tot}} \Psi_{\text{tot}}(N) = E_{\text{tot}}(N) \Psi_{\text{tot}}(N)$$

For such an overall Hamiltonian, the Born–Oppenheimer approximation[95] permits separating the total wave function into a product of an electronic part Ψ and a nuclear part Ψ_{nuc} as

$$\Psi_{\text{tot}}(\mathbf{r}_1, ..., \mathbf{R}_p) = \Psi(\mathbf{r}_1, \sigma_1 \, \mathbf{r}_2, \sigma_2, ..., \mathbf{r}_N, \sigma_N) \Psi_{\text{nuc}}(\mathbf{R}_1, \mathbf{R}_2, ..., \mathbf{R}_p) \qquad (26)$$

In this approximation, the electronic wave function $\Psi(N)$ depends only parametrically on $\mathbf{R}_1, \mathbf{R}_2, ..., \mathbf{R}_p$ via the nuclear–nuclear Coulombic repulsion potential, and is the solution to a Schroedinger equation in which the Hamiltonian is that of Eq. (24) with the nuclear kinetic energy term subtracted off:

$$\left(\hat{H}_{\text{tot}} + \frac{\hbar^2}{2} \sum_{l=1}^{P} \frac{\nabla_l^2}{M_l} \right) \Psi(N) \equiv \hat{H}(N) \Psi(N) = E(N) \Psi(N) \qquad (27)$$

($\hat{H}_{\text{tot}}$ here can include spin–orbit effects via Eq. (25) if desired). The total energy of the system can then be written as the sum of the electronic energy E and the nuclear energy E_{nuc}, as

$$E_{\text{tot}} = E + E_{\text{nuc}} \qquad (28)$$

with E_{nuc} arising from various forms of internal nuclear motion such as vibrations, rotations, and translations (center-of-mass motions). If the various modes of nuclear motion are furthermore independent, the energy becomes

$$E_{\text{tot}} = E + E_{\text{vib}} + E_{\text{rot}} + E_{\text{trans}} + ... \qquad (29)$$

The overall quantum numbers K describing any initial or final state thus must include a complete specification of all of these modes of motion.

For example, in the limit of a diatomic molecule with a very nearly harmonic oscillator form for the curve of electronic energy, E, versus internuclear separation,

$$E_{\text{vib}} = h\nu_{\text{vib}}(v + \tfrac{1}{2}) \qquad (30)$$

in which ν_{vib} is the classical vibration frequency and $v = 0, 1, 2, ...,$ is the vibrational quantum number. Such vibrational excitations in the final state ion give rise to the pronounced vibrational bands well known in UPS studies of gas-phase molecules,[97] and have also recently been noted in XPS studies of both gases[41] and solids [85] (see Section V.E). Rotational excitations are sufficiently low in energy as to be so far unresolvable in XPS studies of molecules.

Translational motion of the center of mass of an atom or molecule can influence energies in two ways: (1) The conservation of linear momentum in the excitation process requires that

$$\mathbf{p}_{h\nu} + 0 = \mathbf{p}^f + \mathbf{p}_r \qquad (31)$$

where $\mathbf{p}_{h\nu}$ is the photon momentum and has a magnitude of $h\nu/c$, the momentum associated with E^i is taken for simplicity to be zero, $\mathbf{p}^f$ is the photoelectron momentum, and $\mathbf{p}_r$ is the recoil momentum of the atom or molecule, treated as a center-of-mass translation. If v is the magnitude of the photoelectron velocity, for $E_{kin} = 500$ eV, $v/c = 0.044$ and for $E_{kin} = 1500$ eV, $v/c = 0.076$. Thus, the photoelectrons typically encountered in XPS can be considered to a good approximation to be non-relativistic. In this approximation, it is a simple matter to show that $|\mathbf{p}_{h\nu}| \approx v/2c\,|\mathbf{p}^f|$ for the example of photoelectrons originating from valence electronic levels (for which $E_{kin} \approx h\nu$). Therefore, in general $|\mathbf{p}_{h\nu}| \ll |\mathbf{p}^f|$ and $\mathbf{p}^f \approx \mathbf{p}_r$, indicating that the ion recoils in a direction opposite to that of photoelectron emission. By conserving both energy and momentum, it can be shown that for a given $h\nu$ and E_{kin}, the recoil energy $E_r = p_r^2/2M$ increases with decreasing atomic or molecular mass M.[3] For excitation of valence shell photoelectrons with AlKα radiation ($h\nu = 1487$ eV), Siegbahn et al.[3] have calculated the following recoil energies for different atoms: H—0.9 eV, Li—0.1 eV, Na—0.04 eV, K—0.02 eV, and Rb—0.01 eV. It is thus clear that only for the lightest atoms H, He, and Li does the recoil energy have a significant magnitude in comparison with the present 0.4–1.0 eV instrumental linewidths in XPS spectra. For almost all cases, E_r can thus be neglected. (2) A more generally applicable limit on resolution in gas-phase studies is set by the Doppler broadening associated with the thermal translational motion of the emitting molecules. For center-of-mass motion of a molecule of total molecular weight M with a velocity $\mathbf{V}$, the electron kinetic energy appropriate for use in Eq. (1) is

$$E_{kin}'' = \tfrac{1}{2}m\,|\,v - \mathbf{V}\,|^2 \tag{32}$$

Thus, the measured kinetic energy $E_{kin} = \tfrac{1}{2}mv^2$ will differ from that of Eq. (32) by varying amounts, according to the thermal distribution of velocities. If the mean measured kinetic energy in a peak is denoted by $\overline{E_{kin}}$, then it can be shown using simple kinetic theory that the Doppler width ΔE_d (in eV) is given by [98]

$$\Delta E_d = 0.723 \times 10^{-3} \left(\frac{T \cdot \overline{E_{kin}}}{M} \right)^{\tfrac{1}{2}} \tag{33}$$

in which $\overline{E_{kin}}$ is in eV, T is the absolute temperature in °K and M is the molecular weight. At room temperature and a typical XPS energy of 1000 eV, ΔE_d is thus $\lesssim 0.10$ eV for molecules with $M \geqslant 10$. In general, such Doppler broadening is thus not a significant factor in comparison to typical XPS resolutions of ~ 0.4–1.0 eV, although they can be important in limiting gas-phase UPS resolution.

In many instances, it is adequate to neglect nuclear motion entirely, and use Eqs (17) and (19) with the quantities $\Psi^i(N)$, $E^i(N)$, $\Psi^f(N)$, $E^f(N)$, $\Psi^f(N-1, K)$, and $E^f(N-1, K)$ relating to only electronic motion. Note that this means

accurate calculations must in principle be made on both initial state and final state. The overall designations for such N-electron or $(N-1)$-electron states are obtained from the various irreducible representations of the symmetry group corresponding to the mean nuclear positions.[95] For example, in atoms for which spin–orbit coupling is small, Russell–Saunders or L, S coupling can be utilized, yielding states specified by L, S, and perhaps also M_L and M_S, where L is the quantum number for total orbital angular momentum $\mathbf{L}$, S is the quantum number for total spin angular momentum $\mathbf{S}$, and M_L and M_S relate to the z components of orbital- and spin–angular momentum. In the limit of zero spin–orbit splitting, energies depend only on L and S, yielding different L, S terms or multiplets with degeneracies of $(2L+1)(2S+1)$. Analogous overall quantum numbers apply for molecules,[95] but they are seldom used in describing total electronic wave functions in solids. Multiplet splittings such as those discussed in Section V.C are the result of energy differences between such many-electron states.

B. The Hartree–Fock Method and Koopmans' Theorem

In attempting to determine reasonably accurate approximations to N-electron wave functions, a common starting point is the non-relativistic Hartree–Fock (HF) self-consistent-field (SCF) method.[95, 99] As the Hartree–Fock method has been widely used in calculations on atoms, molecules, and solids at different levels of exactness and also serves as a reference method for several more accurate and less accurate methods of computing electronic energy levels, it is outlined here in simplest form. The wave function Ψ for an N-electron system is approximated as a single Slater determinant Φ of N orthonormal one-electron spin-orbitals. Each one-electron orbital is composed of a product of a spatial part $\phi_i(\mathbf{r})$ ($i = 1, 2, \ldots, N$) and a spin part $\chi_i(\sigma)$ which is equal to either α ($m_s = +\tfrac{1}{2}$), or β ($m_s = -\tfrac{1}{2}$), for which the orthonormality relations are

$$\int \phi_i^*(\mathbf{r})\phi_j(\mathbf{r})\,d\tau \equiv \langle \phi_i | \phi_j \rangle = \delta_{ij}$$

$$\int \chi_i^*(\sigma)\chi_j(\sigma)\,d\sigma \equiv \langle \chi_i | \chi_j \rangle = \delta_{m_{si}, m_{sj}} = \begin{cases} 1 & \text{for } \alpha\alpha \text{ or } \beta\beta \\ 0 & \text{for } \alpha\beta \text{ or } \beta\alpha \end{cases} \tag{34}$$

Ψ can then be written as a normalized determinant of the form:

$$\Psi \approx \Phi = \frac{1}{\sqrt{N!}} \begin{vmatrix} \phi_1(1)\chi_1(1) & \phi_2(1)\chi_2(1) & \cdots & \phi_{N-1}(1)\chi_{N-1}(1) & \phi_N(1)\chi_N(1) \\ \phi_1(2)\chi_1(2) & \phi_2(2)\chi_2(2) & \cdots & \phi_{N-1}(2)\chi_{N-1}(2) & \phi_N(2)\chi_N(2) \\ \cdot & \cdot & \cdot & \cdot & \cdot \\ \cdot & \cdot & \cdot & \cdot & \cdot \\ \cdot & \cdot & \cdot & \cdot & \cdot \\ \phi_1(N)\chi_1(N) & \phi_2(N)\chi_2(N) & \cdots & \phi_{N-1}(N)\chi_{N-1}(N) & \phi_N(N)\chi_N(N) \end{vmatrix} \tag{35a}$$

or in terms of the antisymmetrizer $\hat{A}$ as

$$\Phi = \hat{A}(\phi_1\chi_1, \phi_2\chi_2, ..., \phi_N\chi_N) \qquad (35b)$$

where the integers $1, ..., N$ label the space and spin coordinates $\mathbf{r}_j$ and σ_j for each orbital.

The spatial one-electron orbitals are furthermore assumed to have symmetries belonging to the set of irreducible representations of the symmetry group of the equilibrium nuclear geometry, and are in this sense often referred to as "delocalized". Thus, for example, in atoms, the orbitals have the form[95]

$$\phi_{nlm_l}(r, \theta, \phi) = R_{nl}(r) Y_{lm_l}(\theta, \phi) \qquad (36)$$

in which $R_{nl}(r)$ is the radial part and the angular part is given by the spherical harmonic $Y_{lm_l}(\theta, \phi)$. In molecules, various symmetry types arise, as, for example, $1\sigma\ 3\pi_g, 2a_1, ...,$[95] and the orbitals are often approximated as linear combinations of atomic orbitals (LCAO's). In solids, the translational periodicity of the crystal requires that all such delocalized orbitals be of the Bloch-function type:[95, 96, 99]

$$\phi_{\mathbf{k}}(\mathbf{r}) = u_{\mathbf{k}}(\mathbf{r}) \exp{(i\mathbf{k}\cdot\mathbf{r})} \qquad (37)$$

in which $\mathbf{k}$ is the electron wave vector with a quasi-continuous distribution of values and $u_{\mathbf{k}}(\mathbf{r})$ is a function characteristic of each $\phi_{\mathbf{k}}$ that has the same translational periodicity as the lattice. A free electron moving under the influence of no forces corresponds to a constant $u_{\mathbf{k}}(\mathbf{r})$, and yields a plane-wave (PW) one-electron orbital of the form

$$\phi_{\mathbf{k}}(\mathbf{r}) = C \exp{(i\mathbf{k}\cdot\mathbf{r})} \qquad (38)$$

in which C is a normalization constant and the momentum $\mathbf{p}$ and energy E are given by

$$\mathbf{p} = \hbar\mathbf{k} \qquad (39)$$

$$E = E_{\text{kin}} = p^2/2m = \hbar k^2/2m \qquad (40)$$

In the often-used spin-restricted Hartree–Fock method, each spatial orbital ϕ_i is also taken to be multiplied by either α and β in the Slater determinant (that is, to have a maximum occupation number of two). Thus only $N/2$ unique ϕ_i's are involved in describing a system with an even number of electrons in doubly-occupied orbitals.

If the Hamiltonian of Eq. (27) is used together with the variational principle to determine the optimum Φ for which the total energy $E = \langle\Phi|\hat{H}|\Phi\rangle$ is a minimum, the Hartree–Fock equations are obtained. These N equations can be used to determine a self-consistent set of orbitals ϕ_i, as well as to calculate the total energy E of the state described by Φ. In atomic units (1 a.u. = 1 Hartree = 27·21 eV, 1 Bohr = a_0 = 0·529 Å), the Hartree–Fock equations in

diagonal form are

$$\left[-\tfrac{1}{2}\nabla_1^2 - \sum_{l=1}^{P}\frac{Z_l}{r_{1l}}\right]\phi_i(1) + \left[\sum_{j=1}^{N}\int\phi_j^*(2)\frac{1}{r_{12}}\phi_j(2)\,d\tau_2\right]\phi_i(1)$$

<div align="center">Kinetic Electron–nuclear   Electron–electron
attraction   Coulombic
repulsion</div>

$$\qquad (41)$$

$$-\delta_{m_{si}, m_{sj}}\sum_{j=1}^{N}\left[\int\phi_j^*(2)\frac{1}{r_{12}}\phi_i(2)\,d\tau_2\right]\phi_j(1) = \epsilon_i\phi_i(1), \quad i = 1, 2, ..., N$$

<div align="center">Electron–electron
exchange</div>

where the ϵ_i's are termed energy eigenvalues, one-electron energies, or orbital energies. The origins of the individual terms are labelled. The exchange interaction is only possible between spin-orbitals with parallel spins (that is, $\alpha\alpha$ or $\beta\beta$), and the Kronecker delta $\delta_{m_{si}, m_{sj}}$ allows for this. It is convenient to re-express Eq. (41) more simply in terms of the Fock operator $\hat{F}(1)$ as:

$$\hat{F}(1)\phi_i(1) \equiv \left\{-\tfrac{1}{2}\nabla_1^2 - \sum_{l=1}^{P}\frac{Z_l}{r_{1l}} + \sum_{j=1}^{N}[\hat{J}_j - \delta_{m_{si}, m_{sj}}\hat{K}_j]\right\}\phi_i(1) = \epsilon_i\phi_i(1) \qquad (42)$$

by defining the Coulomb and exchange operators $\hat{J}_j$ and $\hat{K}_j$ such that

$$\hat{J}_j\phi_i(1) \equiv \int\phi_j^*(2)\frac{1}{r_{12}}\phi_j(2)\phi_i(1)\,d\tau_2 \qquad (43)$$

$$\hat{K}_j\phi_i(1) \equiv \int\phi_j^*(2)\frac{1}{r_{12}}\phi_i(2)\phi_j(1)\,d\tau_2 \qquad (44)$$

Thus, the matrix elements of these operators are the two-electron Coulomb integrals J_{ij} and exchange integrals K_{ij}:

$$J_{ij} \equiv \langle\phi_i(1)|\hat{J}_j|\phi_i(1)\rangle = \iint\phi_i^*(1)\phi_j^*(2)\frac{1}{r_{12}}\phi_i(1)\phi_j(2)\,d\tau_1\,d\tau_2 \qquad (45)$$

$$K_{ij} \equiv \langle\phi_i(1)|\hat{J}_j|\phi_i(1)\rangle = \iint\phi_i^*(1)\phi_j^*(2)\frac{1}{r_{12}}\phi_i(2)\phi_j(1)\,d\tau_1\,d\tau_2 \qquad (46)$$

From these definitions, it is clear that $J_{ij} = J_{ji}$, $K_{ij} = K_{ji}$, and $J_{ii} = K_{ii}$. Once the Hartree–Fock equations have been solved to the desired self-consistency, the orbitals energies ϵ_i can be obtained from

$$\epsilon_i = \epsilon_i^0 + \sum_{j=1}^{N}(J_{ij} - \delta_{m_{si}, m_{sj}}K_{ij}) \qquad (47)$$

where ϵ_i^0 is the expectation value of the one-electron operator for kinetic energy and electron-nuclear attraction

$$\epsilon_i^0 = \langle\phi_i(1)|-\tfrac{1}{2}\nabla_1^2 - \sum_{l=1}^{P}\frac{Z_l}{r_{1l}}|\phi_i(1)\rangle \qquad (48)$$

By comparison, the total energy of the state approximated by Φ is given by

$$E = \langle \Phi | \hat{H} | \Phi \rangle = \sum_{i=1}^{N} \epsilon_i{}^0 + \sum_{i=1}^{N} \sum_{j>i}^{N} (J_{ij} - \delta_{m_{s_i}, m_{s_j}} K_{ij}) + \sum_{l=1}^{P} \sum_{m>l}^{P} \frac{Z_l Z_m}{r_{lm}} \quad (49)$$

Note that the first two summations over electronic indices are not simply the sum of all of the one-electron energies for the N electrons in the system, as the sum of the Coulomb and exchange terms in the total energy is made with $i<j$ to avoid counting these terms twice. This means that measured binding energies (which will be shown shortly to be very close to the ϵ_i's in value) cannot be directly used to determine total energies and hence such quantities as reaction energies.

Mann[100] has compiled very useful tables of accurate Hartree–Fock calculations for all atoms in the periodic table. These include one-electron energies, Slater F^k and G^k integrals for calculating J_{ij} and K_{ij}, radial expectation values, and wave-function tabulations. Herman and Skillman[93] and Carlson et al.[101] have also calculated energies, radial expectation values, and local one-electron potentials for all atoms, using a Hartree–Fock Slater approximation with relativistic corrections.

In utilizing the Hartree–Fock method for computing binding energies, the most accurate procedure is to compute the difference between $E^f(N-1, K)$ and $E^i(N)$ corresponding to the Hartree–Fock wave functions $\Psi^f(N-1, K)$ and $\Psi^i(N)$, respectively. In the one-electron-orbital picture provided by this method, the final-state wave function can be characterized as having a hole in the kth subshell, and, for a closed-shell system with all ϕ_i's doubly occupied, the overall index K can be replaced simply by k. As the photoemission process by which this hole is formed occurs on a time scale very short compared to that of nuclear motion ($\sim 10^{-16}$ s compared to $\sim 10^{-13}$ s), the nuclear positions in $\Psi^f(N-1, K)$ can be assumed to be identical to those in $\Psi^i(N)$, and the nuclear–nuclear repulsion sum in Eq. (49) will thus cancel in an energy difference. However, the ion left behind by the exiting photoelectron may not possess a nuclear geometry consistent with the ionic ground-state vibrational motion, an effect which leads to the possibility of exciting various final vibrational states. If the excitation is also fast in comparison to the motions of the $(N-1)$ passive electrons in $\Psi^f(N-1, K)$ (a less rigorously justifiable limit termed the "sudden approximation"), it is also possible to show that various final electronic states can be reached. (See Sections III.D.1, V.D.2, and V.E for more detailed discussions.) For now, only the electronic ground state of the ion corresponding to the minimum binding energy will be considered. In this usually dominant final state, it is expected that the passive electrons will not have the same spatial distribution as those in $\Psi^i(N)$ due to relaxation or rearrangement around the k hole. Although the overall change in the spatial form of the passive orbitals due to relaxation

around an inner hole is not large (for example, the mean radius of an atomic orbital changes by only ~ 1–10%),[102] the resulting change in energy can have an appreciable effect on calculated binding energies. Such relaxation effects can have significant consequences in interpreting binding energy data such as, for example, chemical shifts, and they are discussed in more detail in Sections IV and V.B. Hole-state calculations in which initial and final states are treated with equal accuracy in the Hartree–Fock sense have been performed by various authors for atoms,[103–105] small molecules,[106–109] and inorganic clusters.[110] If binding energies determined in this way are corrected for relativistic effects where necessary, very good agreement with experimental core electron binding energies has been obtained. For example, an agreement of approximately 0.2% is found between theoretical and experimental $1s$ binding energies of Ne ($E_b{}^V(1s) = 870$ eV) and Ar ($E_b{}^V(1s) = 3205$ eV).[103]

Relativistic effects generally increase core electron binding energies, as well as leading to spin–orbit splittings, and their magnitudes depend on the ratio of the characteristic orbital velocity to the velocity of light.[93, 94] The atomic Hartree–Fock Slater calculations of Herman and Skillman[93] and Carlson and Pullen[94] provide a direct tabulation of such corrections for all atoms as determined by perturbation theory. For example, the correction for C$1s$ is only about 0.2 eV out of 290 eV ($\sim 0.08\%$), whereas for the deeper core level Ar$1s$, it is about 22 eV out of 3180 eV ($\sim 0.69\%$).

An additional type of correction which should in principle be made to any type of Hartree–Fock calculation is that dealing with electron–electron correlation. In connection with hole-state Hartree–Fock binding energy calculations, the intuitive expectation for such corrections might be that because the initial-state SCF calculation does not include favorable correlation between a given core electron and the other $(N-1)$ electrons, the calculated E^i value would be too large and thus that the binding energy $E_b{}^V(K) = E^f(N-1, K) - E^i(N)$ would be too small. However, in comparing relativistically-corrected hole-state calculations on several small atoms and ions with experimental binding energies, the remaining error due to correlation has been found to change sign from level to level within the same system.[103, 111] Such deviations from simple expectations appear to have their origins primarily in the different types of correlation possible for final hole states in different core or valence levels. For example, $E_b{}^V(1s)$ for Ne shows a correlation correction δE_{corr} in the expected direction (that is, so as to increase E_b) of approximately 0.6 eV out of 870.2 eV ($\sim +0.07\%$)[112] whereas δE_{corr} for $E_b{}^V(2s)$ acts in the opposite direction by approximately 0.9 eV out of 48.3 eV ($\sim -1.8\%$).[111] For core levels in closed-shell systems such as Ne, such corrections can be computed approximately from a sum of electron pair correlation energies $\epsilon(i, j)$ calculated for the ground state of the system.[111] For example, in computing the $1s$ binding energy in Ne, the

correction has the form of a sum over pair correlation energies between the $1s$ electron and all other electrons in the atom. Such correlation energies are dependent upon both overlap and spin orientation, as the exchange interaction partially accounts for correlation of electrons with parallel spin. For Ne$1s$, this sum is thus:

$$\delta E_{corr} = \epsilon(1s\alpha, 1s\beta) + \epsilon(1s\alpha, 2s\alpha) + \epsilon(1s\alpha, 2s\beta)$$
$$+ 3\epsilon(1s\alpha, 2p\alpha) + 3\epsilon(1s\alpha, 2p\beta) \qquad (50)$$

with values of $\epsilon(1s\alpha, 1s\beta) = +1\cdot09$ eV, $\epsilon(1s\alpha, 2s\alpha) = +0\cdot01$ eV, $\epsilon(1s\alpha, 2s\beta) = +0\cdot06$ eV, $\epsilon(1s\alpha, 2p\alpha) = +0\cdot11$ eV, $\epsilon(1s\alpha, 2p\beta) = +0\cdot15$ eV. Note the smaller magnitudes of $\epsilon(i,j)$ for electrons with parallel spins. Also, it is clear that most of the correlation correction arises from the strongly overlapping $1s$ electrons. Equation (50) is only a first approximation, however, and more exact calculations involving explicit estimates of all types of correlation in both Ne and Ne$^+$ with a $1s$ hole give better agreement with the experimental $1s$ binding energy.[112] The experimental value is $E_b{}^V(1s) = 870\cdot2$ eV, in comparison to $\delta E_{corr} = 1\cdot9$ eV, $E_b{}^V(1s) = 870\cdot8$ eV based on Eq. (50)[111] and $\delta E_{corr} = 0\cdot6$ eV, $E_b{}^V(1s) = 870\cdot0$ eV based on the more accurate calculation.[112] δE_{corr} is decreased in the latter calculation primarily because of correlation terms that are present in Ne$^+$ but not in Ne. The sum of pair correlation energies $\epsilon(i,j)$ in Ne$^+$ is larger than that in Ne by about 30%, and other terms not describable as pair interactions are present in Ne$^+$ but not Ne.

Aside from verifying that Hartree–Fock hole-state energy difference calculations can yield very accurate values for core electron binding energies in atoms and molecules, such investigations have also led to another important consideration concerning the final hole state formed by photoelectron emission. This concerns the correct extent of delocalization of the hole, which is implicitly assumed to have a symmetry dictated by the entire nuclear geometry (or to exhibit a maximum degree of delocalization) in the diagonal Hartree–Fock method discussed here. Hole-state calculations by Bagus and Schaefer[107] have shown that *core-orbital* holes will tend to be localized on one atomic center, as opposed to being distributed over all centers as might be expected in certain cases from a linear-combination-of-atomic-orbitals (LCAO) Hartree–Fock calculation including all electrons. In the simple example of O_2, a hole in the $1\sigma_g$ or $1\sigma_u$ molecular orbitals (which can be considered to a very good approximation to be made up of a sum or difference of $1s$ atomic orbitals on the two oxygen atoms, respectively) is predicted by such a calculation to result in a net charge of $+\frac{1}{2}e$ on each oxygen atom in the molecule. However, Snyder[108] has pointed out that such a state does not minimize the total energy associated with the final state Hamiltonian. Thus, the lowest energy state is found[107] to localize the $1s$ core hole entirely on

either oxygen atom. These pairs of equivalent final states (which no longer possess one-electron orbitals with the full symmetry of the molecule) yield the correct values of $E^f(N-1, K)$ for computing binding energies. For O_2, the localized hole states yield a value of $E_b{}^V(1s) = 542$ eV, in comparison with an experimental value of 543 eV, and a delocalized hole-state value of 554 eV. Thus, localizing the hole represents a large correction of 12 eV ($\sim 2\cdot2\%$). More recently, Cederbaum and Domcke[113] have shown from a more rigorous point of view why the use of such localized core-hole states is valid.

Although localization of final-state core holes is thus to be expected in general, the question of localization becomes more complex in dealing with valence electrons in molecules or solids. Molecular orbitals with lone-pair character or which exhibit a predominance of atomic-orbital make-up from a single atom in an LCAO description are inherently localized, even though they are describable in terms of the overall symmetry species of the molecule, and such orbitals would be expected to exhibit hole localization to a great degree. Other molecular valence hole states may or may not show localization that deviates significantly from a description with full-symmetry molecular orbitals. Similarly, the spatially-compact $4f$ valence levels in solid rare-earth elements and compounds are found to yield highly-localized hole states, as is evidenced by the atomic-like multiplet splittings observed[114] (see Section V.C). The valence d electrons in solid transition metals and their compounds or the valence electrons in free-electron-like metals may not always be so simply described, however. Nonetheless, Ley et al.[115] have concluded that, even for the highly delocalized valence states of free-electron metals such as Li, Na, Mg, and Al, the energy associated with final-state relaxation around a valence hole can be calculated equally well in terms of either a localized- or delocalized-hole-state description; in this case, however, the delocalized hole state is still best considered to be an itinerant localized hole propagating through the solid.

Although a localized-orbital description of the *initial* state can always be obtained from a Hartree–Fock determinant by means of a suitable unitary transformation of the various orbitals ϕ_i without changing the overall N-electron determinantal wave function or total energy,[116] the transformation is not unique. Payne[117] has also recently presented a new method for performing molecular Hartree–Fock calculations in which relatively unique localized-orbital character is built in by constraining each LCAO molecular orbital to be composed only of atomic orbitals centered on a small set of nearest-neighbor atoms. Although either of these two procedures for obtaining localized initial-state orbitals can provide chemically intuitive and transferable bonding orbitals between two or three bonding centers,[116, 117] it is not clear that they would necessarily lead to a more correct description of the final state with one electron removed. More theoretical and experimental work is thus necessary to characterize fully the best one-electron-orbital

description of the final states of many systems, if indeed such a one-electron picture is always adequate or necessary.

In order to avoid the difficulties associated with hole-state calculations in determining binding energies, a very often used approximation is to assume that Koopmans' Theorem well describes the relationship between initial and final state total energies. The basis of this theorem is the assumption that the initial one-electron orbitals ϕ_i making up the determinant $\Phi^i(N)$ are precisely equal to the final orbitals ϕ_i' making up $\Phi^f(N-1, k)$ with a single k-subshell hole. The final state total energy $E^f(N-1, k)$ can then be calculated from the formula for $E^i(N)$ [cf. Eq. (49)] simply by eliminating those terms dealing with the electron occupying the kth orbital initially. This procedure leaves as the Koopmans' Theorem value for $E^f(N-1, k)$ (neglecting nuclear repulsion):

$$E^f(N-1, k)^{\mathrm{KT}} = \sum_{i \neq k}^{N} \epsilon_i^0 + \sum_{i \neq k}^{N} \sum_{j > i, j \neq k}^{N} (J_{ij} - \delta_{m_{s_i}, m_{s_j}} K_{ij})$$
$$= \sum_{i \neq k}^{N} \epsilon_i^0 + \sum_{i=1}^{N} \sum_{j > i}^{N} (J_{ij} - \delta_{m_{s_i}, m_{s_j}} K_{ij})$$
$$- \sum_{i=1}^{N} (J_{ik} - \delta_{m_{s_i}, m_{sk}} K_{ik}) \tag{51}$$

The Koopmans' Theorem binding energy of the kth electron is then by the difference method [cf. Eq. (22)],

$$E_b^{\mathrm{V}}(k)^{\mathrm{KT}} = E^f(N-1, k)^{\mathrm{KT}} - E^i(N)$$
$$= -\epsilon_k^0 - \sum_{i=1}^{N} (J_{ik} - \delta_{m_{s_i}, m_{sk}} K_{ik})$$

or, making use of Eq. (47) for the orbital energy ϵ_k,

$$E_b^{\mathrm{V}}(k)^{\mathrm{KT}} = -\epsilon_k \tag{52}$$

Thus, the binding energy of the kth electron is in this approximation equal to the negative of the orbital energy ϵ_k. For bound-state orbitals ϵ_k is negative, so that the binding energy has the appropriate positive sign. This result is Koopmans' Theorem, as is indicated by the superscript KT. In reality, the relaxation of the $(N-1)$ passive orbitals about the k hole in the ionic ground state will tend to lower $E^f(N-1, k)^{\mathrm{KT}}$, and thus, as long as relativistic and correlation corrections are not too large, binding energies estimated with Koopmans' Theorem should be greater than the true values. If the error due to such electronic relaxation is denoted by $\delta E_{\mathrm{relax}} > 0$, then a binding energy can be written as (neglecting relativistic and correlation effects):

$$E_b^{\mathrm{V}}(k) = E_b^{\mathrm{V}}(k)^{\mathrm{KT}} - \delta E_{\mathrm{relax}}$$
$$= -\epsilon_k - \delta E_{\mathrm{relax}} \tag{53}$$

It should be noted, however, that Koopmans' Theorem as it is derived here applies only to closed-shell systems (that is, systems that are adequately represented by a single Slater determinant with doubly-occupied one-electron orbitals), or to solids which contain many electrons in highly delocalized valence orbitals with quasi-continuous energy eigenvalues. For any other case, there will in general be several possible couplings of spin- and orbital-angular momenta in the open shell or shells, and each distinct coupling will give rise to a different initial or final state energy. These states in atoms might, for example, be described in terms of L, S coupling, and would in general be represented by a linear combination of Slater determinants.[118] Although each of these determinants would have the same gross electronic configuration (for example, $3d^5$), various possible combinations of $m_s = \pm\frac{1}{2}$ and m_l would be possible within the open shells. Provided that final-state relaxation is neglected, Slater[118] has pointed out that a binding energy $E_b^{\mathrm{V}}(k)^{\mathrm{KT}}$ computed as the difference between the *average* total energy for all states within the final configuration and the *average* total energy for all states within the initial configuration is equal to the one-electron energy ϵ_k computed from an initial-state Hartree–Fock calculation utilizing Coulomb and exchange potentials averaged over all states possible within the initial configuration. This we can write as

$$\overline{E_b^{\mathrm{V}}(k)^{\mathrm{KT}}} = \overline{E^f(k)^{\mathrm{KT}}} - \overline{E^i} = -\overline{\epsilon_k} \tag{54}$$

and it represents a generalization of Koopmans' Theorem to open-shell systems. The various final states discussed here are the cause of the multiplet splittings to be considered in Section V.C.

Although the orbital energies ϵ_k in Koopmans' Theorem as stated here refer to fully delocalized orbitals, Payne[117] has recently pointed out that near-Hartree–Fock calculations in which different atomic-orbital basis sets are chosen for different molecular orbitals to yield effectively localized final results *also* yield a set of one-electron energies that can be interpreted via Koopmans' Theorem. As these one-electron energies are not the same as those for fully delocalized orbitals, it is thus of interest to determine whether any such localization effects are clearly discernible in experimental valence binding energies.

The most direct way of calculating $\delta E_{\mathrm{relax}}$ is of course to carry out SCF Hartree–Fock calculations on both the initial and final states and to compare $E_b^{\mathrm{V}}(k)$ as calculated by a total energy difference method with $E_b^{\mathrm{V}}(k)^{\mathrm{KT}} = -\epsilon_k$. Such calculations have been performed by various authors on both atoms and molecules.[3, 104–109] As representative examples of the magnitudes of these effects, for the neon atom, $E_b^{\mathrm{V}}(1s) = 868 \cdot 6$ eV and $E_b^{\mathrm{V}}(1s)^{\mathrm{KT}} = 891 \cdot 7$ eV, giving $\delta E_{\mathrm{relax}} \approx 23$ eV ($\sim 2 \cdot 6\%$), and $E_b^{\mathrm{V}}(2s) = 49 \cdot 3$ eV and $E_b^{\mathrm{V}}(2s)^{\mathrm{KT}} = 52 \cdot 5$ eV, giving $\delta E_{\mathrm{relax}} \approx 3$ eV ($\sim 6 \cdot 0\%$). Effects of similar magnitude are

found in the 1s levels of molecules containing first-row atoms.[106, 109] Also, in certain cases, the presence of a localized hole may cause considerable valence electron polarization relative to the initial state.[106, 107, 110] Thus δE_{relax} lies in the range of 1–10 % of the binding energy involved, with greater *relative* values for more weakly bound electrons. Several procedures have also been advanced for estimating δE_{relax}[105, 119–121] and these are discussed in more detail in Section V.B. It has also been pointed out by Manne and Åberg[90] that a Koopmans' Theorem binding energy represents an average binding energy as measured over all states K associated with emission from the kth orbital, including those describable as both "one-electron" and "multi-electron" in character. This analysis is discussed in more detail in Section III.D.1. Implicit in the use of Koopmans' Theorem is the idea of a predominantly one-electron transition in which the $(N-1)$ passive electrons are little altered.

To summarize, the use of Hartree–Fock theory and Koopmans' Theorem permits writing any binding energy approximately as

$$E_b{}^V(k) = -\epsilon_k - \delta E_{relax} + \delta E_{relat} + \delta E_{corr} \qquad (55)$$

in which δE_{relax}, δE_{relat}, and δE_{corr} are corrections for relaxation, relativisitic effects, and correlation effects, respectively.

C. More Accurate Wave Functions via Configuration Interaction

In explaining certain many-electron phenomena observed in XPS spectra it is absolutely essential to go beyond the single-configuration Hartree–Fock approximation, and the most common procedure for doing this is by the configuration interaction (CI) method.[122] In this method, an arbitrary N-electron wave function $\Psi(N)$ is represented as a linear combination of Slater determinants $\Phi_j(N)$ corresponding to different N-electron configurations:

$$\Psi(N) = \sum_{j=1} C_j \Phi_j(N) \qquad (56)$$

The coefficients C_j, and perhaps also the set of one-electron orbitals ϕ_i used to make up the Φ_j's, are optimized by seeking a minimum in total energy to yield a more accurate approximation for $\Psi(N)$. In the limit of an infinite number of configurations, the exact wave function is obtained by such a procedure. In practice, the dominant C_j's are usually those multiplying determinants with the same configurations as those describing the Hartree–Fock wave function for the system.

For example, for Ne, a highly accurate CI calculation by Barr involving 1071 distinct configurations of spatial orbitals[123] yields the following absolute values for the coefficients multiplying the various members of a few more

important configurations: $\Phi_1 = 1s^22s^22p^6 =$ Hartree–Fock configuration—0·984; $\Phi_2 = 1s^22s^12p^63s^1$—0·005; $\Phi_3 = 1s^22s^22p^53p$—0·009; $\Phi_4 = 1s^22s^22p^44p^2$—0·007–0·030; and $\Phi_5 = 1s^22s^22p^43p4p$—0·007–0·022. Approximately 70 distinct configurations have coefficients larger than 0·010 in magnitude, but only that for Φ_1 is larger than 0·030.

Manson[91] has discussed the influence of configuration interaction on the calculation of photoelectron peak intensities (see the more detailed discussion in the next section), and in particular has noted that it may be important to allow for CI effects in both initial and final states. Specific effects of configuration interaction in XPS spectra are also discussed in Sections V.C and V.D, as well as in the chapter by Martin and Shirley[14] in this series.

D. Transition Probabilities and Photoelectric Cross-sections

1. *General Considerations and the Sudden Approximation.* In order to predict the intensities with which various photoelectron peaks will occur, it is necessary to calculate their associated transition probabilities or photoelectric cross-sections. The photoelectric cross-section σ is defined as the transition probability per unit time for exciting a single atom, single molecule, or solid specimen from a state $\Psi^i(N)$ to a state $\Psi^f(N)$ with a unit incident photon flux of $1 \text{ cm}^{-2} \text{ s}^{-1}$. If the direction of electron emission relative to the directions of photon propagation and polarization is specified in $\Psi^f(N)$, as well as perhaps its direction of emission with respect to axes fixed in the specimen, such a cross-section is termed differential, and is denoted by $d\sigma/d\Omega$. The differential solid angle $d\Omega$ is that into which electron emission occurs, and it is indicated in Fig. 7. From $d\sigma/d\Omega$ for a given system, the total cross-section for electron excitation into any direction is given by

$$\sigma = \int \frac{d\sigma}{d\Omega} \, d\Omega \qquad (57)$$

Such differential or total cross-sections can be calculated by means of time-dependent perturbation theory, utilizing several basic assumptions that are discussed in detail elsewhere[124–131] and reviewed briefly below.

In a semi-classical treatment of the effect of electromagnetic radiation on an N-electron system, the perturbation $\hat{H}'$ due to the radiation can be approximated in a weak-field limit as:[131]

$$\hat{H}' = -\frac{e}{2mc} (\hat{p} \cdot \mathbf{A} + \mathbf{A} \cdot \hat{p}) \qquad (58)$$

in which $\hat{p} = -i\hbar\nabla$ and $\mathbf{A} = \mathbf{A}(\mathbf{r}, t)$ is the vector potential corresponding to the field. For an electromagnetic wave traveling in a uniform medium, it is possible to choose $\mathbf{A}$ such that $\nabla \cdot \mathbf{A} = 0$ and thus $\hat{p} \cdot \mathbf{A} = 0$, so that in all applications to XPS it is appropriate to consider only the $\mathbf{A} \cdot \hat{p}$ term in Eq.

(58). (In UPS studies of solids, it has, however, been pointed out that the change in properties near a surface can result in a "surface photoeffect" due to the $\hat{p} \cdot \mathbf{A}$ term.[132]) The electromagnetic wave is further assumed to be a traveling plane wave of the form:

$$\mathbf{A}(\mathbf{r}, t) = \mathbf{e} A_0 \exp [i(\mathbf{k}_{h\nu} \cdot \mathbf{r} - 2\pi\nu t)] \tag{59}$$

where $\mathbf{e}$ is a unit vector in the direction of polarization ($\mathbf{e}$ is parallel to the electric field $\mathbf{E}$), A_0 is an amplitude factor, $\mathbf{k}_{h\nu}$ is the wave vector of propagation, $|k_{h\nu}| = 2\pi/\lambda$, and λ is the wavelength of the radiation. Within this approximation the transition probability per unit time for a transition from $\Psi^i(N)$ to $\Psi^f(N)$ can be shown to be proportional to the following squared matrix-element[124, 131]

$$|M_{if}|^2 = \left| \langle \Psi^f(N)| \sum_{i=1}^{N} \mathbf{A}(\mathbf{r}_i) \cdot \hat{p}_i |\Psi^i(N)\rangle \right|^2$$

$$= \hbar^2 A_0^2 \left| \langle \Psi^f(N)| \sum_{i=1}^{N} \exp(i\mathbf{k}_{h\nu} \cdot \mathbf{r}_i) \mathbf{e} \cdot \nabla_i |\Psi^i(N)\rangle \right|^2 \tag{60}$$

in which the time dependence of $\mathbf{A}$ has been integrated out and the integration remaining in the matrix element is over the space and spin coordinates of all N electrons. The intensity or photon flux of the incident radiation is proportional to A_0^2. If the final state $\Psi^f(N)$ corresponds to electron emission with a wave vector $\mathbf{k}^f$ (or momentum $\mathbf{p}^f = \hbar\mathbf{k}^f$) oriented within a solid angle $d\Omega$ (cf. Fig. 7), the differential cross-section can then be shown to be:[124]

$$\frac{d\sigma}{d\Omega} = C\left(\frac{1}{h\nu}\right) \left| \langle \Psi^f(N)| \sum_{i=1}^{N} \exp(i\mathbf{k}_{h\nu} \cdot \mathbf{r}_i) \mathbf{e} \cdot \nabla_i |\Psi^i(N)\rangle \right|^2 \tag{61}$$

in which C is a combination of fundamental constants, and A_0^2 is eliminated in the normalization to unit photon flux. In dealing with atoms and molecules, it is often necessary to sum further over various experimentally-indistinguishable symmetry-degenerate final states, *and* to average over various symmetry-degenerate initial states to determine a correct cross-section. If the degeneracy of the initial state is g_i and if each such initial state is equally populated, this yields

$$\frac{d\sigma}{d\Omega} = \frac{C}{g_i}\left(\frac{1}{h\nu}\right) \sum_{i,f} \left| \langle \Psi^f(N)| \sum_{i=1}^{N} \exp(i\mathbf{k}_{h\nu} \cdot \mathbf{r}_i) \mathbf{e} \cdot \nabla_i |\Psi^i(N)\rangle \right|^2 \tag{62}$$

Also, if unpolarized radiation is utilized for excitation, a summation or integration over the various possible orientations of $\mathbf{e}$ is necessary in deriving $d\sigma/d\Omega$, yielding finally a summation $\sum_{i,f,\mathbf{e}}$ in Eq. (62). Furthermore, for a randomly oriented set of atoms or molecules as appropriate to studies of gaseous- or polycrystalline-specimens, $d\sigma/d\Omega$ must also be averaged over all

possible orientations of the target system with respect to each possible relative geometry of the radiation and the emitted electron.

A final point of general concern is the influence of nuclear motion, specifically vibration, on such cross-sections. If the Born–Oppenheimer approximation [Eq. (26)] is valid and the influence of the perturbing radiation on
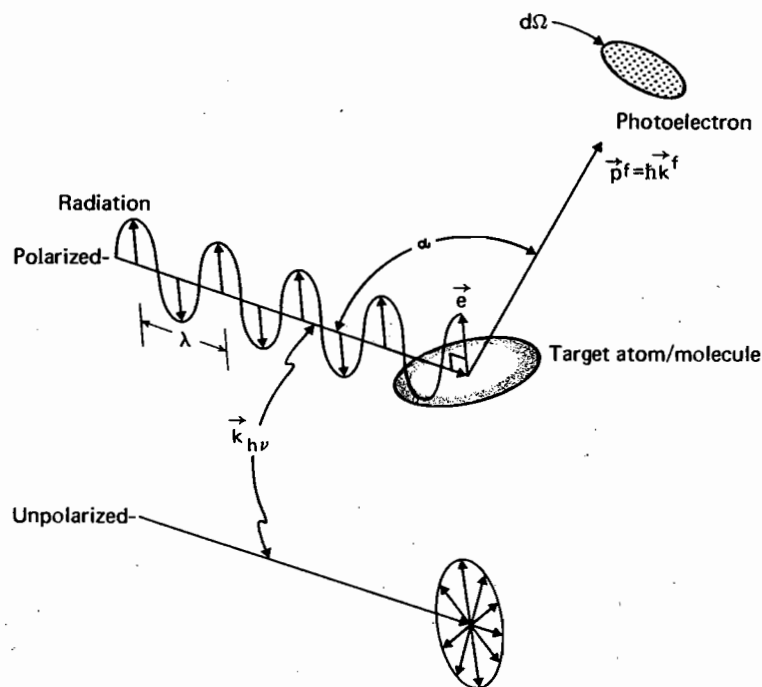

Fig. 7. General geometry for defining the differential cross-section $d\sigma/d\Omega$, showing both polarized and unpolarized incident radiation. The polarization vector $\mathbf{e}$ is parallel to the electric field $\mathbf{E}$ of the radiation. In order for the dipole approximation to be valid, the radiation wave length λ should be much larger than typical target dimensions (that is, the opposite of what is shown here).

the nuclear coordinates is neglected, the differential cross-section [Eq. (62)] becomes:

$$\frac{d\sigma}{d\Omega} = \frac{C}{g_i}\left(\frac{1}{h\nu}\right) \sum_{i,f} \left| \langle \Psi^f(N)| \sum_{i=1}^{N} \exp(i\mathbf{k}_{h\nu} \cdot \mathbf{r}_i) \mathbf{e} \cdot \nabla_i |\Psi^i(N)\rangle \right|^2$$
$$\left| \langle \Psi_{vib}^f(P)|\Psi_{vib}^i(P)\rangle \right|^2 \tag{63}$$

in which the squared overlap between the initial and final vibrational wave functions is simply a Franck–Condon factor. Vibrational effects in XPS spectra are discussed in Section V.E. Only the electronic aspects of matrix elements and cross-sections are considered further here.

In proceeding further, it is assumed that the photon wavelength λ is much larger than the typical dimensions of the system, which will generally be of the order of a few Å. This is a reasonably good, although borderline, approximation for MgKα or AlKα x-rays with $\lambda \approx 10$ Å. This assumption permits treating $\exp(i\mathbf{k}_{h\nu} \cdot \mathbf{r}_i)$ as unity in the integration, yielding for Eq. (62):

$$\frac{d\sigma}{d\Omega} = \frac{C}{g_i}\left(\frac{1}{h\nu}\right) \sum_{i,f} \left| \mathbf{e} \cdot \langle \Psi^f(N) | \sum_{i=1}^{N} \boldsymbol{\nabla}_i | \Psi^i(N)\rangle \right|^2 \qquad (64)$$

and is termed "neglect of retardation" or "the dipole approximation". A further convenience that thus arises is being able to write the matrix element in Eq. (64) in any of the three forms:[124]

$$\langle \Psi^f(N)| \sum_{i=1}^{N} \boldsymbol{\nabla}_i |\Psi^i(N)\rangle = \frac{i}{\hbar} \langle \Psi^f(N)| \sum_{i=1}^{N} \hat{p}_i |\Psi^i(N)\rangle$$

$$= \frac{m(h\nu)}{\hbar^2} \langle \Psi^f(N)| \sum_{i=1}^{N} \mathbf{r}_i |\Psi^i(N)\rangle$$

$$= \frac{1}{h\nu} \langle \Psi^f(N)| \sum_{i=1}^{N} \boldsymbol{\nabla}_i V |\Psi^i(N)\rangle \qquad (65)$$

The equality of these three forms can be proven by means of commutation relations for the exact wave functions corresponding to any Hamiltonian of the form of Eq. (24); the first form is denoted "momentum" or "dipole-velocity", the second "dipole-length", and the third "dipole-acceleration". In the last form, $V = V(\mathbf{r}_1, \mathbf{r}_2, ..., \mathbf{r}_N)$ is the potential represented by the electron–electron repulsion and electron–nuclear attraction terms in the Hamiltonian.

There are several levels of accuracy that can be used for the evaluation of matrix elements such as those in Eq. (64). The most often used approximation begins by assuming a strongly "one-electron" character for the photoemission process, and represents the initial state as an antisymmetrized product of the "active" kth orbital $\phi_k(1)$ from which emission is assumed to occur and an $(N-1)$-electron remainder $\Psi_R(N-1)$ representing the "passive" electrons:

$$\Psi^i(N) = \hat{A}(\phi_k(1)\chi_k(1), \Psi_R(N-1)) \qquad (66)$$

In the weak-coupling limit, the final state is further given very accurately by

$$\Psi^f(N) = \hat{A}(\phi^f(1)\chi^f(1), \Psi^f(N-1)) \qquad (67)$$

where for brevity the index K (or most simply k) on the ionic wave function $\Psi^f(N-1)$ has been suppressed, and f specifies the kinetic energy and any additional quantum numbers necessary for the continuum orbital $\phi^f(1)$. If it is further assumed that the primary $k \to f$ excitation event is rapid or

"sudden" with respect to the relaxation times of the passive-electron probability distribution, the evaluation of N-electron matrix elements for a general one-electron transition operator $\hat{t}$ depending only on spatial coordinates (such as any of those in Eq. 65)) yields:[90, 131]

$$\langle \Psi^f(N)| \sum_{i=1}^{N} \hat{t}_i |\Psi^i(N)\rangle = \langle \phi^f(1)|\hat{t}|\phi_k(1)\rangle \langle \Psi^f(N-1)|\Psi_R(N-1)\rangle \qquad (68)$$

The use of this expression is often termed the "sudden approximation", and it has proven to be very successful for predicting the intensities of various types of many-electron fine structure observed in XPS spectra (see, for example, Sections V.C, and V.D). Transition probabilities and cross-sections are thus in this limit proportional to

$$|\langle \phi^f(1)|\hat{t}|\phi_k(1)\rangle|^2 |\langle \Psi^f(N-1)|\Psi_R(N-1)\rangle|^2 \qquad (69)$$

and involve a one-electron matrix element and an $(N-1)$-electron overlap integral between the ionic wave function and the passive-electron remainder $\Psi_R(N-1)$. It should be noted that $\Psi_R(N-1)$ is thus not a valid ionic wave function, but rather a non-unique "best" representation of the initial-state passive electrons. In order for the overlap integral to be non-zero, symmetry requirements further dictate that both $\Psi^f(N-1)$ and $\Psi_R(N-1)$ must correspond to the same overall irreducible representation; this is the origin of the so-called "monopole selection rule", which is discussed in more detail in Section V.D.2.

It is necessary also to consider criteria for determining whether the sudden approximation can be used or not.[133, 134] If the excitation from a given subshell k gives rise to a set of final state energies $E^f(N-1, K)$; $K = 1, 2, ...,$ then the simplest criterion for the validity of the sudden approximation is that[133]

$$[E^f(N-1, K) - E^f(N-1, K')]\tau'/\hbar \ll 1 \qquad (70)$$

where τ' is the time required for the $k \to f$ photoelectron to leave the system, and K and K' can range over any pair of final energies with significant intensity in the set. As an indication of the orders of magnitude occurring in this inequality, for a typical x-ray photoelectron of $E_{kin} = 1000$ eV, $v/c \approx 0.06$ or $v \approx 2 \times 10^9$ cm/s. For a typical atomic diameter of 2 Å, the escape time can thus be roughly estimated as $\tau' \approx (2 \times 10^{-8})/2 \times 10^9) \approx 10^{-17}$ s. Thus, $\tau'/h \approx 1/65$ eV^{-1}, and for final state separations much larger than 10 eV, the sudden approximation would appear to be violated. However, calculations by Åberg[133] and by Carlson, Krause, and co-workers[135] using the sudden approximation have given reasonable agreement with experiment for several systems for which this inequality was not fully satisfied. On the other hand, Gadzuk and Sunjic[134] have considered in more detail the question of transit

times and relaxation times in XPS, and have concluded that even the typical excitation energies in XPS of $\sim 1 \cdot 5$ keV may not be sufficient to reach fully the sudden limit. This question thus requires further study.

An alternative, and in certain respects more general, description of the initial and final states in the transition matrix element is to use single-determinant Hartree–Fock wave functions. If these are calculated accurately for both states, thus including relaxation effects, the relevant wave functions are

$$\Psi^i(N) = \hat{A}(\phi_1\chi_1, \phi_2\chi_2, ..., \phi_k\chi_k, ..., \phi_N\chi_N) \tag{71}$$

$$\Psi^f(N) = \hat{A}(\phi_1'\chi_1, \phi_2'\chi_2, ..., \phi^f\chi^f, ..., \phi_N'\chi_N) \tag{72}$$

and the transition matrix element becomes[136, 137]

$$\langle \Psi^f(N) | \sum_{i=1}^{N} \hat{t}_i | \Psi^i(N) \rangle = \sum_m \sum_n \langle \phi_m'(1) | \hat{t} | \phi_n(1) \rangle D^{fi}(m|n) \tag{73}$$

where the double sum on m and n is over *all* occupied orbitals and $D^{fi}(m|n)$ is an $(N-1) \times (N-1)$ passive-electron overlap determinant. $D^{fi}(m|n)$ is thus equal to the signed minor formed by removing the mth row and nth column from the $N \times N$ determinant D^{fi} whose elements are overlaps between initial- and final-state one-electron orbitals. That is, the pq element is $(D^{fi})_{pq} = \langle \phi_p'\chi_p | \phi_q\chi_q \rangle$. Many of the N^2 matrix elements contributing to Eq. (73) are zero or near-zero for three reasons: (1) one-electron matrix-element selection rules associated with $\langle \phi_m'(1) | \hat{t} | \phi_n(1) \rangle$; (2) monopole selection rules arising from the one-electron overlaps $\langle \phi_p'\chi_p | \phi_q\chi_q \rangle$, since ϕ_p' and ϕ_q must have the same spatial symmetry and the spin functions χ_p and χ_q must be equal for the overlap to be non-zero; and (3) the near ortho-normality of the passive-orbital sets $\phi_1, ..., \phi_{k-1}, \phi_{k+1}, ..., \phi_N$ and $\phi_1', ..., \phi_{k-1}', \phi_{k+1}', ..., \phi_N'$, so that $\langle \phi_p' | \phi_p \rangle \approx 1 \cdot 0$ and $\langle \phi_p' | \phi_q \rangle \approx 0$ for $p \neq q$. Additional matrix elements corresponding to transitions other than $k \to f$ that cannot be ruled out on these bases have furthermore been shown by Åberg[133] to be negligible for a high-excitation-energy limit, which leaves finally a first-order result analogous to the sudden-approximation expression

$$\langle \Psi^f(N) | \sum_{i=1}^{N} \hat{t}_i | \Psi^i(N) \rangle = \langle \phi^f(1) | \hat{t} | \phi_k(1) \rangle D^{fi}(f|k) \tag{74}$$

Various methods for calculating such overlap determinants for atoms have been investigated by Mehta *et al.*,[102] and it has been concluded that the use of a diagonal-element product is accurate to within ~ 1–2%:

$$\langle \Psi^f(N) | \sum_{i=1}^{N} \hat{t}_i | \Psi^i(N) \rangle = \langle \phi^f(1) | \hat{t} | \phi_k(1) \rangle \sum_{j=1, j \neq k}^{N} \langle \phi_j' | \phi_j \rangle \tag{75}$$

Proceeding one step further to an unrelaxed, "frozen orbital", or "Koopmans' Theorem" final state in which $\phi_j' = \phi_j$ for $j \neq k$ finally leads to the simplest approximation for such matrix elements:

$$\langle \Psi^f(N) | \sum_{i=1}^{N} \hat{t}_i | \Psi^i(N) \rangle = \langle \phi^f(1) | \hat{t} | \phi_k(1) \rangle \tag{76}$$

The majority of matrix element and cross-section calculations to date have used this last form.

At the level of sudden approximation calculations utilizing Eq. (68) or (74), two experimentally useful spectral sum rules have been pointed out. The first states that the weighted-average binding energy over all final ionic states $\Psi^f(N-1, K)$ associated with a given primary $k \to f$ excitation is simply equal to the Koopmans' Theorem binding energy of $-\epsilon_k$. That is, if I_K is the intensity of a transition to $\Psi^f(N-1, K)$ corresponding to a binding energy $E_b(K)$, then

$$-\epsilon_k = \sum_K I_K E_b(K) \Big/ \sum_K I_K = \sum_K |\langle \Psi^f(N-1, K) | \Psi_R(N-1) \rangle|^2 E_b(K) \tag{77}$$

This was first pointed out in connection with XPS by Manne and Åberg,[90] and has also been derived in a somewhat different context by Lundquist.[138] The significance of this sum rule is illustrated in Fig. 8, and it requires that,

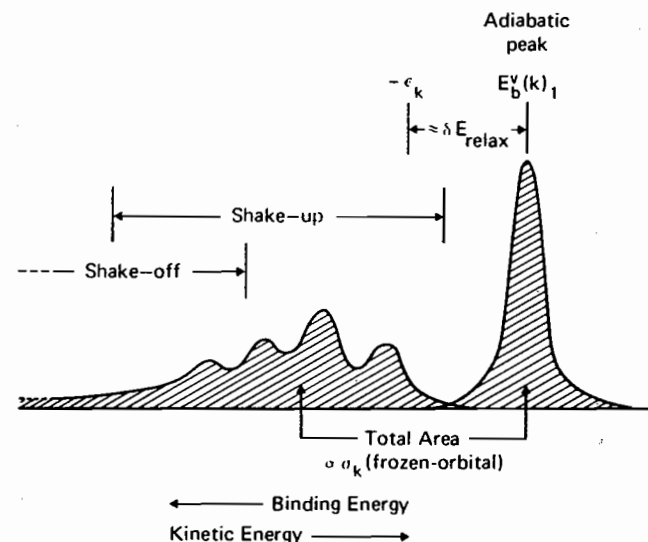Fig. 8. Schematic illustration of a photoelectron spectrum involving shake-up and shake-off satellites. The weighted average of all binding energies yields the Koopmans' Theorem binding energy $-\epsilon_k$ [sum rule (77)], and the sum of all intensities is proportional to a frozen-orbital cross section σ_k [sum rule (78)]. The adiabatic peak corresponds to formation of the ground state of the ion $[E_b(k)_1 \equiv E_b(K=1)]$.

in order for relaxation to occur in forming the lowest-binding-energy "primary" or "adiabatic" final state corresponding to the ionic ground state, excited ionic states corresponding to binding energies higher than $-\epsilon_k$ must also arise. The peaks due to these states have been variously called "shake-up", "shake-off", "many-electron transitions", "configuration-interaction satellites", or "correlation peaks", and more specific illustrations are given in Section V.D. The high-intensity lowest-binding-energy peak has often been associated with a "one-electron transition", although this name is unduly restrictive in view of the inherently many-electron nature of the photoemission process. Thus, the intimate relationship between relaxation and correlation is demonstrated, although it still is possible to determine uniquely a relaxation energy with initial- and final-state Hartree–Fock wave functions that are often assumed to be uncorrelated in the sense that E_{corr} is measured relative to them. The second sudden-approximation sum rule deals with intensities, and it states that the sum of all intensities associated with the states $\Psi^f(N-1, K)$ is given by

$$I_{tot} = \sum_K I_K = C \sum_K \left| \langle \phi^f(1) | \hat{t} | \phi_k(1) \rangle \right|^2 \left| \langle \Psi^f(N-1, K) | \Psi_R(N-1) \rangle \right|^2$$

$$= C \left| \langle \phi^f(1) | \hat{t} | \phi_k(1) \rangle \right|^2 \tag{78}$$

where C is a constant for a given photon energy. One experimental consequence of this sum rule is that matrix elements and cross-sections calculated with unrelaxed final-state orbitals and thus using Eq. (76) apply only to absolute intensities summed over all states $\Psi^f(N-1, K)$, as was first pointed out by Fadley.[137] Thus, absolute photoelectron intensities for the usually-dominant ionic-ground-state peaks may be below those predicted by unrelaxed or frozen-orbital cross-sections, as has been noted experimentally by Wuilleumier and Krause;[139] by contrast, x-ray absorption coefficients, which inherently sum over all final states for a given $k \rightarrow f$ excitation, are well predicted by unrelaxed cross-sections.[137]

At a higher level of accuracy than any of the approximations discussed up to this point, configuration-interaction wave functions can also be used in the calculation of matrix elements and cross-sections.[91, 127] In particular, Manson[91] has discussed in a general way the effects that this can have, pointing out several mechanisms by which calculated intensities can be significantly modified by the inclusion of CI in the initial-state wave function and the final-state wave function. For computational convenience, it is customary (although not essential) to use the same set of orthonormal one-electron orbitals $\phi_1, \phi_2, ..., \phi_M$ ($M > N$) in making up the configurations of both initial and final states. This apparent lack of allowance for relaxation in the final state can be more than compensated by using a large number of configurations with mixing coefficients $C_j{}^i$ and $C_j{}^f$ that are optimized for

both states:

$$\Psi^i(N) = \sum_j C_j{}^i \Phi_j{}^i(N) \tag{79}$$

$$\Psi^f(N) = \sum_m C_m{}^f \Phi_m{}^f(N) \tag{80}$$

The exact expressions for matrix elements determined with such wave functions are rather complex, particularly if more than one continuum orbital is included, corresponding to an allowance for continuum CI (also referred to as interchannel coupling or close coupling).[91] Although such continuum effects may be important in certain special cases (see Section V.D.5), several many-electron phenomena noted in XPS spectra can be well explained in terms of only initial-state CI and final-state-ion CI. In visualizing these effects, it is thus useful to take a sudden approximation point of view, in which a single primary $k \rightarrow f$ transition is considered and the individual configurations $\Phi_j{}^i(N)$ and $\Phi_m{}^f(N)$ are thus written as antisymmetrized products with forms analogous to Eqs (66) and (67):

$$\Phi_j{}^i(N) = \hat{A}(\phi_k(1)\chi_k(1), \Phi_j{}^i(N-1)) \tag{81}$$

$$\Phi_m{}^f(N) = \hat{A}(\phi^f(1)\chi^f(1), \Phi_m{}^f(N-1)) \tag{82}$$

In these equations, the $(N-1)$-electron factors can if desired be indexed identically, so that, for the fixed one-electron basis set, $\Phi_j{}^i(N-1) = \Phi_m{}^f(N-1)$ if $j = m$ and thus also $\langle \Phi_j{}^i(N-1) | \Phi_m{}^f(N-1) \rangle = \delta_{jm}$. Matrix elements in this limit are then given by repeated application of Eq. (68) as

$$\langle \Psi^f(N) | \sum_{i=1}^{N} \hat{t}_i | \Psi^i(N) \rangle = \langle \phi^f(1) | \hat{t} | \phi_k(1) \rangle [\sum_j (C_j{}^f)^* C_j{}^i] \tag{83}$$

Thus, the mixing of various configurations into either the initial or final states can affect the observed intensity of a given final state appreciably, as it is only if a certain configuration has a non-zero coefficient in both states that it will contribute a non-zero $(C_j{}^f)^* C_j{}^i$ product. For the useful limiting case in which a single configuration $j = 1$ dominates the initial state, then $C_j{}^i \approx 1 \cdot 0$, $C_j{}^i \approx 0$ for $j \neq 1$, and the square of the matrix element (83) for transitions to a given final state is simply

$$\left| \langle \Psi^f(N) | \sum_{i=1}^{N} \hat{t}_i | \Psi^i(N) \rangle \right|^2 \propto |C_1{}^f|^2 \tag{84}$$

(If relaxation is permitted in the final-state one-electron orbitals, then overlap integrals of the form $\langle \Phi_m{}^f(N-1) | \Phi_j{}^i(N-1) \rangle \equiv S_{jm}$ must be computed,[14] and Eqs (83) and (84) become more complex. However, in general $S_{jm} \approx \delta_{jm}$.) Such CI effects are important in understanding the simplest forms of multiplet

splittings (Section V.C), many-electron effects in multiplet splittings (Section V.C), and the intensities of various many-electron satellites (Section V.D).

The inherent requirement of relaxed final-state orbitals in sudden approximation calculations using single-determinant Hartree–Fock wave functions has led to a certain amount of confusion when comparing this model with the results of CI calculations. Manson,[91] for example, has pointed out that the use of relaxed final-state orbitals in such single-determinant calculations yields matrix elements of no higher accuracy than those resulting from the inclusion of only a limited form of initial-state configuration interaction. Thus, there are several types of effects that can only be adequately discussed in terms of a more complete CI treatment.

In the next three sections, matrix element and cross-section calculations for atoms, molecules, and solids are discussed at the often-used level of unrelaxed final-state orbitals that results in Eq. (76).

2. *Atoms.* For a closed-shell atom in the limit of no final-state passive-electron relaxation and a non-relativistic Hamiltonian, each emission event is characterized by a well-defined transition from spin-orbital $\phi_k \chi_k = \phi_{nlm_l} \chi_{m_s}$ to spin-orbital $\phi^f \chi^f = \phi_{E^f l^f m_l^f} \chi_{m_s^f}$, where E^f is the photoelectron kinetic energy $h\nu - E_b^V(nl)$. The usual dipole selection rules then require that

$$\Delta l = l^f - l = \pm 1 \qquad (85)$$

$$\Delta m_l = m_l^f - m_l = 0, \pm 1 \qquad (86)$$

$$\Delta m_s = m_s^f - m_s = 0$$

Photoemission is thus divided into two "channels" for $l^f = l+1$ and $l^f = l-1$, with the $l+1$ channel usually being much more important at XPS energies.

The most commonly encountered experimental situation is a collection of atoms whose orientations are random with respect to one another that is exposed to a flux of unpolarized radiation with an angle α between the propagation directions of the radiation and photoelectron (cf. Fig. 7). For this situation, the total photoelectric cross-section for all events involving emission from a given nl subshell can be calculated by summing transition probabilities for all possible one-electron events according to Eq. (63). A general derivation[124, 126, 127, 140] then shows that the total subshell cross section σ_{nl} is, in the dipole-length form,[141] given by

$$\sigma_{nl}(E^f) = \frac{4\pi\alpha_0 a_0^2}{3} (h\nu)[l R_{l-1}^2(E^f) + (l+1)R_{l+1}^2(E^f)] \qquad (87)$$

in which α_0 is the fine structure constant, a_0 is the Bohr radius, and the $R_{l\pm1}(E^f)$ are radial matrix elements common to all one-electron dipole matrix elements between ϕ_{nlm_l} and $\phi_{E^f l^f m_l^f}$. (ϕ_{nlm_l} and $\phi_{E^f l^f m_l^f}$ both have

the general form of Eq. (36).) These radial integrals are given by

$$R_{l\pm1}(E^f) = \int_0^\infty R_{nl}(r) r R_{E^f, l\pm1}(r) r^2 \, dr = \int_0^\infty P_{nl}(r) r P_{E^f, l\pm1}(r) \, dr \qquad (88)$$

where $P_{nl}(r)/r \equiv R_{nl}(r)$ is the radial part of the ϕ_{nlm_l} orbital and $P_{E^f, l\pm1}(r)/r \equiv R_{E^f, l\pm1}(r)$ is the radial part of the continuum photoelectron orbital $\phi_{E^f l^f m_l^f}$. The differential photoelectric cross-section for a given subshell is furthermore given by the expression [124, 127, 140]

$$\frac{d\sigma_{nl}}{d\Omega}(E^f) = \frac{\sigma_{nl}}{4\pi} [1 - \tfrac{1}{2}\beta_{nl}(E^f) P_2(\cos \alpha)]$$

$$= \frac{\sigma_{nl}}{4\pi} [1 + \tfrac{1}{2}\beta_{nl}(E^f)(\tfrac{3}{2}\sin^2 \alpha - 1)] \qquad (89)$$

where $\beta_{nl}(E^f)$ is termed the asymmetry parameter, α is the angle between photon propagation direction and electron emission direction, and $P_2(\cos \alpha) = \tfrac{1}{2}(3\cos^2 \alpha - 1)$. $\beta_{nl}(E^f)$ can in turn be calculated from the radial integral $R_{l\pm1}(E^f)$ and certain continuum-orbital phase shifts $\delta_{l\pm1}(E^f)$ that represents the shift in the sinusoidally oscillating character of $R_{E^f, l\pm1}(r)$ at large radii relative to the continuum wave functions for a hydrogen atom at energy E^f. The equation for $\beta_{nl}(E^f)$ is

$$\beta_{nl}(E^f) = \frac{\{l(l-1)R_{l-1}^2(E^f) + (l+1)(l+2)R_{l+1}^2(E^f) - 6l(l+1)R_{l+1}(E^f)R_{l-1}(E^f)\cos[\delta_{l+1}(E^f) - \delta_{l-1}(E^f)]\}}{(2l+1)[l R_{l-1}^2(E^f) + (l+1)R_{l+1}^2(E^f)]} \qquad (90)$$

and the term in $\cos[\delta_{l+1} - \delta_{l-1}]$ represents an interference between outgoing $l+1$ and $l-1$ waves. Such phase shifts are illustrated for C2p emission into s and d waves at different $h\nu$ in Figs 9(d) and 9(e).

The allowed range for β_{nl} is $-1 \leq \beta \leq +2$. A positive value of β indicates that photoelectrons are preferentially emitted at angles perpendicular to the photon direction ($\alpha = 90°$), whereas a negative value indicates preferential emission either parallel or anti-parallel to this direction ($\alpha = 0°$ or $180°$). A value of $\beta = 0$ yields an isotropic distribution. For s-electron emission, $l = 0$, and only transitions to $l^f = 1$ waves are possible. β is always $+2$ for this case, yielding a differential photoelectric cross-section of the form:

$$\frac{d\sigma_{ns}(E^f)}{d\Omega} = \frac{\sigma_{ns}(E^f)}{4\pi} \cdot \sin^2\alpha \qquad (91)$$

with maximum intensity at $\alpha = 90°$ and zero intensity at $\alpha = 0°$ and $180°$. For the other limiting case of $\beta = -1$,

$$\frac{d\sigma_{nl}(E^f)}{d\Omega} = \frac{\sigma_{nl}(E^f)}{4\pi} \cdot \cos^2\alpha \qquad (92)$$
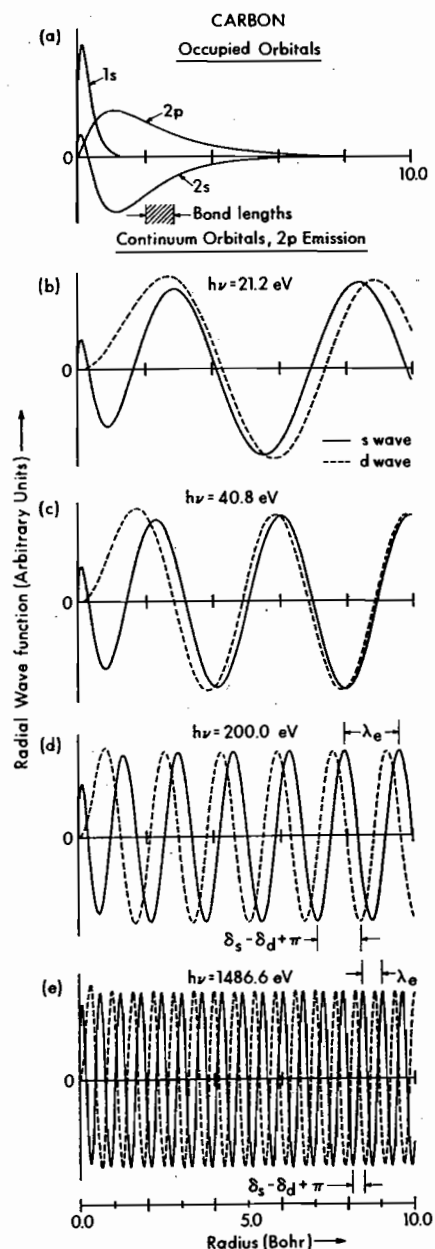
Fig. 9. Radial functions $P(r) = r \cdot R(r)$ for (a) the occupied orbitals of atomic carbon and (b)–(e) the continuum photoelectron orbitals resulting from C2p excitation at different photon energies as indicated. Continuum wave functions for both allowed emission channels are shown ($l+1 \to d$ wave, $l-1 \to s$ wave). Note the non-sinusoidal character near the nucleus, and the decrease in the electron deBroglie wavelength λ_e with increasing kinetic energy. The definition of the phase shift $\delta_s - \delta_d + \pi$ is also indicated for $h\nu = 200 \cdot 0$ eV and 1486·6 eV. In (a), the range of typical bond lengths between carbon and low-to-medium Z atoms is also shown for comparison. (S. M. Goldberg and C. S. Fadley, unpublished results.)

the photoelectron intensity is zero at $\theta = 90°$, and has its maximum value at $\theta = 0°$ and 180°. No matter what the value of β is, the form of Eq. (89) dictates that the distribution should be cylindrically symmetric about the photon propagation direction.

Equation (89) is also equivalent to

$$\frac{d\sigma_{nl}(E^f)}{d\Omega} = A + B \sin^2 \alpha \qquad (93)$$

where A and B are constants given by $A = (\sigma_{nl}/4\pi)(1 - \beta_{nl}/2)$ and $B = (\sigma_{nl}/4\pi) \cdot 3\beta_{nl}/4$. From an empirical determination of A and B, β can thus be calculated from $\beta_{nl} = 4B/(3A + 2B)$. A comparison between the function predicted by Eq. (93) and experimental results made by Krause[142] is shown in Fig. 10. The parameters A and B have in this case been empirically adjusted to give the best fit to data obtained for photoemission from Kr3s, Kr3p, and Kr3d levels with MgKα x-rays. The data are reasonably well described by Eq. (93), although a slight systematic deviation is apparent; this has been associated with effects due to the breakdown of the dipole approximation
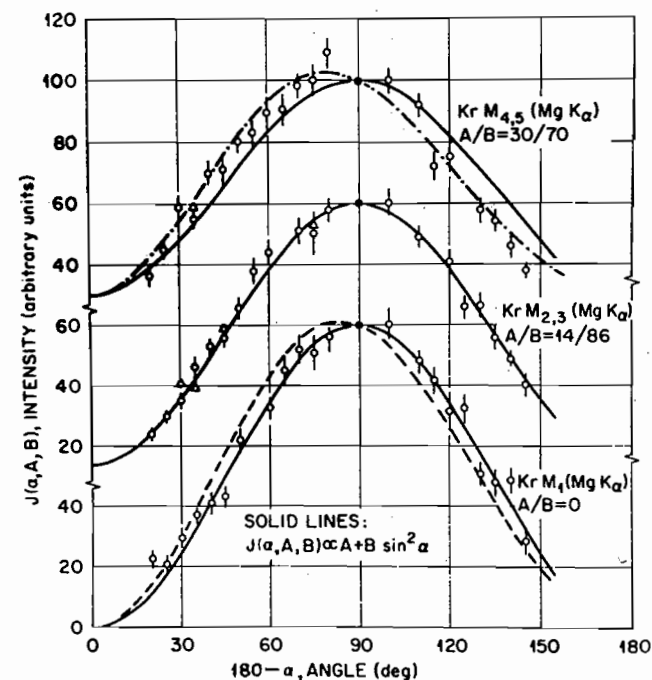

Fig. 10. Experimental angular distributions of $3s$ ($= M_1$), $3p$ ($= M_{2,3}$), and $3d$ ($= M_{4,5}$) photoelectrons excited from gaseous Kr with MgKα x-rays. The curves represent least-squares fits to the data points of a relationship of the form of Eq. (93), in which A and B were treated as empirical constants. (From Krause, ref. 142.)

(neglect of retardation).[142] Note that the $3s$ data are consistent with Eq. (91) as expected. Also, a decrease in β with increasing orbital angular momentum is observed, although β is clearly positive for all three cases presented in Fig. 10. Wuilleumier and Krause[139] have also presented a similar analysis for Ne$2p$ emission that extends up to XPS excitation energies.

Total atomic subshell cross-sections for photon energies relevant to XPS have been calculated in various studies.[126, 143–151] These calculations have made use of both the non-relativistic theory outlined above, as well as relativistic methods based upon the Dirac equation.[144, 145, 151] In the non-relativistic calculations, the method introduced by Cooper and Manson[126, 146, 147] has been most utilized: cross-sections are calculated from matrix elements between initial-state orbitals determined in a Hartree–Fock–Slater approximation (as those generated by Herman and Skillman for all atoms)[93] and final-state orbitals determined from a one-electron radial Schroedinger equation with a central potential $V(r)$ representing the interaction with the nucleus and $(N-1)$ electrons in the ion (again of the form determined by Herman and Skillman). More recently, Scofield[151] has used a relativistic analogue of this procedure to calculate MgKα and AlKα total subshell cross sections σ_{nl}, $j=l\pm\frac{1}{2}$ for all elements in the periodic table; spin–orbit effects split each subshell into two j components with occupancy $2j+1$. The use of such a cross-section tabulation in analyzing XPS spectral intensities is discussed below in Section III.F.3.

In general, it is found that for $h\nu$ well above threshold, as is the case in XPS measurements, transitions to $l^f=l+1$ are much more probable than those to $l^f=l-1$.[126, 147] Thus, the term $(l+1)R_{l+1}^2(E^f)$ dominates the term $lR_{l-1}^2(E^f)$ in Eq. (87). Also, $\sigma_{nl}(E^f)$ is generally a decreasing function of E^f for $h\nu$ well above threshold. However, large oscillations and minima in the cross-section may occur as $h\nu$ is increased above threshold.[126, 146, 147] Such oscillations can be explained in terms of the changing overlap character of an oscillatory $P_{nl}(r)$ and an oscillatory $P_{E^f, l\pm1}(r)$ with changing E^f.[126] As E^f is increased, the effective wavelength of the radial oscillations in $P_{E^f, l\pm1}$ decreases and the oscillations penetrate more deeply into the region of non-zero $P_{nl}(r)$ "within" the atom. This effect is illustrated quantitatively in Fig. 9 for continuum orbitals corresponding to emission from a C$2p$ subshell at $h\nu=21\cdot2$, $40\cdot8$, 200, and $1486\cdot6$ eV, as calculated by Goldberg and Fadley using the Manson/Cooper program. For a given $h\nu$, the matrix element $R_{l\pm1}(E^f)$ thus may consist of contributions due to the constructive overlap of one or more lobes in $P_{nl}(r)$ and $P_{E^f, l\pm1}$. If, as E^f is varied, the relative signs of the overlapping lobes change, $R_{l\pm1}(E^f)$ may change sign, and therefore at some kinetic energy intermediate between the sign change, a zero or minimum in $E_{l\pm1}(E^f)$ and $\sigma_{nl}(E^f)$ can result. A corollary of this argument is that atomic orbitals $P_{nl}(r)$ which exhibit no oscillations with r

should show cross-sections which decrease smoothly with increasing E^f and exhibit no zeroes or minima.[126] Examples of such orbitals would be $1s$, $2p$, $3d$, and $4f$.

Comparisons of total cross-section calculations with experiment are often made through the total atomic absorption coefficient for x-rays, which at lower x-ray energies of $\lesssim 10$ eV consists essentially of a sum over the several subshell cross-sections. Such comparisons yield reasonably good agreement between experiment and theory (~ 5–10%) except near threshold where $h\nu \approx E_b^V(nl)$.[137, 143, 145, 150, 152] Cooper and Manson[147] have also calculated relative subshell cross-sections in XPS which compare favorably with the experimental values of Krause[142] shown in Fig. 10.

Asymmetry parameter calculations have also been performed for various atoms at the Manson/Cooper level, and the values obtained for $\beta_{nl}(E^f)$ are also in reasonable agreement with experiment ($\sim \pm 5\%$).[147] Manson[153] and Kennedy and Manson[149] have also pointed out that for certain subshells, theory predicts that $\beta_{nl}(E^f)$ may exhibit large oscillations with E^f. Finally, Reilman et al.[154] have calculated β values spanning all elements in the periodic table for the two common XPS x-rays MgKα and AlKα; interpolations in this table can be made to any atomic subshell. Thus, the use of Scofield's σ_{nlj} values[151] together with the β_{nl} tables of Reilman et al.[154] permits determining a reasonably accurate differential cross-section for any situation encountered in typical XPS experiments (even though it does represent a mixture of relativistic and non-relativistic calculations). The data of Fig. 10 make it clear that in order for comparisons of peak intensities in photoelectron spectra to be meaningful, the angular geometry of the experiment must be known and allowed for via $d\sigma/d\Omega$. Neglecting the effect of the asymmetry parameter is equivalent to assuming

$$\frac{d\sigma}{d\Omega} = \frac{\sigma}{4\pi} \qquad (94)$$

a relationship that is only rigorously true for a "magic-angle" experimental geometry with $P_2(\cos \alpha)=0$ or $\alpha=54\cdot74°$.

A further important point in connection with atomic cross-sections is that, for systems initially possessing an open shell, the calculations outlined above will represent a sum of cross-sections leading to the various allowed final multiplet states (generally describable as L, S terms).[125] Provided that these multiplets are degenerate, no observable effects are suppressed by such a summation. However, in many cases of both core-level and valence-level emission, these multiplets are resolvable from one another, so that some procedure within a one-electron-transition model is needed for predicting the partitioning of the cross-section into the various multiplets. For emission from a closed inner subshell, the weight of each multiplet is just its total

multiplicity,[155] so that

$$\text{Intensity} \propto (2S^f + 1)(2L^f + 1) \qquad (95)$$

For emission from a partially-filled valence subshell, more complex expressions involving fractional parentage coefficients arise; these have been discussed in detail by Cox and co-workers,[155, 156] and by Bagus, Freeouf, and Eastman.[157] These references include extensive numerical tables. It has also recently been pointed out by Dill et al.[158] that for emission from a given nl subshell β_{nl} may vary from mutliplet to multiplet, but such effects are small enough to be neglected in first approximation.

Finally, it should be noted that, although all of the foregoing has assumed randomly oriented atoms (as would be characteristic of gas-phase or polycrystalline specimens), the situation of an array of atoms with definite orientation can be important for the case of chemical bonding at a well-defined single-crystal surface. Gadzuk[159] has considered the theoretical expressions resulting for oriented transition-metal atoms on surfaces, and finds potentially significant effects on the angular dependence of photoelectron emission from such atoms.

3. *Molecules and Molecular-orbital Studies*. In general, less is known both experimentally and theoretically about molecular cross-sections, primarily due to the greater difficulty of accurately calculating either the initial-state orbitals or especially the final-state orbitals involved.

For core-level emission to typical XPS energies of a few hundred eV or more, the use of atomic subshell cross-sections is probably a very good approximation at the level of a one-electron model of photoemission, because the initial-state orbital is very little altered by chemical bonding and the final-state hole is highly localized and atomic-like, thus leading to a continuum orbital with very nearly atomic properties. (At very low energies of excitation, it is interesting to note however, that even core levels are predicted to show cross-section resonances due to molecular geometry.[160]) Based upon theoretical calculations by Nefedov et al.,[161] changes in the magnitudes of core-level cross-sections with ionization state are further expected to be very small (~ 0–1% per unit charge), although in some cases such effects could be significant.

In valence-level emission, the determination of cross-sections becomes more complex. The initial-state orbital ϕ_k is usually written as a linear combination of atomic orbitals (LCAO):

$$\phi_k = \sum_{A\lambda} C_{A\lambda k}\phi_{A\lambda} \qquad (96)$$

in which k represents a symmetry label appropriate for the molecule (e.g. $2\sigma_g$ or $1\pi_u$ in O_2), $\phi_{A\lambda}$ is an atomic orbital (AO) for which A designates the atom and λ the symmetry (e.g. $A=$ oxygen and $\lambda = 1s$ in O_2), and the $C_{A\lambda k}$'s

are expansion coefficients. Such an LCAO description can be made at any of various levels of accuracy, as is common in quantum-chemical calculations. The final-state orbital ϕ^f presents more of a problem, however, as it must be computed so as to take account of the full molecular geometry, even though at high excitation energies and large distances from the center of mass it will look very much like an atomic continuum orbital of the same kinetic energy. Various approximations have been used for such final states in cross-section calculations relevant to XPS: (1) A simple plane-wave (PW) of the form $\exp(i\mathbf{k}\cdot\mathbf{r})$ has been used in several studies,[162, 163] although it seems doubtful that highly quantitative results can be achieved in this approximation because the plane-wave is in no way sensitive to the true potential near the atomic centers and neither is it properly orthogonal to the initial-state orbital. By analogy with the atomic case, one would expect correct final states to show behavior near the nucleus much like that shown in Fig. 9. (2) Plane-waves orthgonalized to the occupied core- and valence-orbitals (OPW's) have also been utilized, for example, by Rabalais, Ellison, and co-workers,[162] but doubts concerning their quantitative accuracy at high energies have also been raised by Ritchie.[164] Also, the use of either PW or OPW approximations in the atomic case has been shown by Williams and Shirley[165] to be grossly inadequate. (3) Ritchie[164] has used an expansion in terms of partial waves of different l character, noting that the non-spherical symmetry of the molecular geometry may mix these, introducing complexities not found in the atomic case. (4) More recently, Dill,[160] Dehmer,[160] and Davenport[166] have discussed the use of the multiple-scattering $X\alpha$[167] method in molecular cross-section calculations and, at this point, it shows considerable promise of being able to provide very useful and reasonably accurate numerical results. The calculation of molecular cross-sections has been reviewed recently by Dehmer,[168] as well as by Huang and Rabalais[130] elsewhere in this series.

An additional factor that must be considered in molcular cross-section and lineshape analyses is that various final vibrational states may be reached in a given photoemission event, even in the simple case for which only a single vibrational mode is initially populated. These vibrational excitations are responsible for the bands observed in gas-phase UPS spectra,[97] for example, and similar effects have been noted in core-level XPS emission (see Section V.E). If the Born–Oppenheimer approximation is used, then the electronic cross-section (differential or total) can be partitioned among the various vibrational states simply by multiplying by appropriate Franck–Condon factors, as indicated previously in Eq. (63).

Whatever initial- and final-state approximations are utilized, it is nonetheless a general consequence of the conservation of parity and angular momentum that the overall form of the differential photoelectric cross-section of a randomly oriented collection of Born–Oppenheimer molecules exposed

to unpolarized radiation will have the same form as that for the atomic case,[140, 168] namely, Eqs (89) or (93). The calculation of σ_k and β_k proceeds by a different method from that in atoms, of course. The UPS angular distributions of a number of small molecules have been measured by Carlson et al.[169, 170] and they are found to follow the predicted form $A + B\sin^2\alpha$, with all members of each valence vibrational band showing very nearly the same distinct β value (with a few exceptions perhaps indicative of a partial breakdown of the Born–Oppenheimer approximation).

As in atoms, molecular cross-sections for open-shell systems also may represent emission into several non-degenerate multiplet states. Cox and Orchard[155] have derived the relative probabilities of reaching different final electronic states for emission from both filled and unfilled subshells. (A specialization of their results to filled-subshell emission from atoms yields Eq. (95).)

As a final general point concerning molecular cross-sections, it should be noted that, although all of the foregoing results assumed random orientation, the situation of surface chemical bonding on an atomically-ordered substrate may yield a set of molecules with a definite orientation. Dill[171] has presented a general theoretical formalism for evaluating such oriented-molecule differential cross-sections, and Davenport[166] has performed numerical calculations for oriented carbon monoxide based upon the $X\alpha$ method. Primary emphasis in all such theoretical studies to date has been on ultra-violet excitation, however.

In analyzing XPS emission from molecular valence levels, much use has also been made of an approximation first suggested by Gelius.[172] Although originally derived by assuming a plane-wave final state $\exp(i\mathbf{k}\cdot\mathbf{r})$, a slightly different procedure will be used here that both leads to the same result and also automatically includes certain correction terms that are often omitted. The initial-state molecular orbital (MO) ϕ_k is assumed to be of LCAO form [Eq. (96)] with the implicit restriction (not always stated) that the atomic orbitals $\phi_{A\lambda}$ be reasonable representations of *true* atomic orbitals, not just single-radial-lobe basis functions, for example, of Slater or Gaussian type. Consider a hypothetical final-state orbital ϕ^f corresponding to $E^f = h\nu - E_b{}^V(k)$ that has somehow been determined with arbitrary accuracy. The matrix element for photoemission from the molecular orbital will then be given by

$$\langle\phi^f|\mathbf{r}|\phi_k\rangle = \langle\phi^f|\mathbf{r}|\sum_{A\lambda} C_{A\lambda k}\phi_{A\lambda}\rangle$$

$$= \sum_{A\lambda} C_{A\lambda k}\langle\phi^f|\mathbf{r}|\phi_{A\lambda}\rangle \tag{97}$$

The photoelectric cross-section will be proportional to the square of this matrix element. If the atomic orbitals and LCAO coefficients are assumed to

have been constructed as real, this square will be given by

$$|\langle\phi^f|\mathbf{r}|\phi_k\rangle|^2 = \sum_{A'\lambda'}\sum_{A\lambda} C_{A'\lambda'k}C_{A\lambda k}\langle\phi^f|\mathbf{r}|\phi_{A'\lambda'}\rangle\langle\phi^f|\mathbf{r}|\phi_{A\lambda}\rangle$$

$$= \sum_{A\lambda} |C_{A\lambda k}|^2|\langle\phi^f|\mathbf{r}|\phi_{A\lambda}\rangle|^2$$

$$+ 2\sum_{A'\lambda'}\sum_{\substack{A\lambda \\ (A\lambda > A'\lambda')}} C_{A'\lambda'k}C_{A\lambda k}\langle\phi^f|\mathbf{r}|\phi_{A'\lambda'}\rangle\langle\phi^f|\mathbf{r}|\phi_{A\lambda}\rangle \tag{98}$$

The MO cross-section thus depends on matrix elements between a true molecular final state ϕ^f, and good approximations to atomic orbitals $\phi_{A\lambda}$. The strongly attractive potential near each atomic center will furthermore tend to make ϕ^f in the near-nuclear region look very much like the final-state orbital for photoemission from an isolated atom at the same kinetic energy. At XPS energies, the atomic continuum orbitals for all valence AO's should furthermore be very similar in oscillatory behavior, as the kinetic energies are all very close for a given $h\nu$. It can further be argued that it is the region near the nucleus in which most of the non-zero contributions to the matrix elements $\langle\phi^f|\mathbf{r}|\phi_{A\lambda}\rangle$ arise, because as the distance from each nucleus is increased, ϕ^f rapidly becomes an oscillatory function with periods of only ~ 0.35 Å (the de Broglie wavelength λ_e of the photoelectron). This is illustrated for C$2p$ emission from atomic carbon in Fig. 9. Thus, it is only near the nucleus that the initial-state AO's have sufficiently dense spatial variations to yield a largely non-cancelling contribution to the matrix element; in the diffuse, slowly-varying tails of the valence AO's between the atoms, the oscillations in ϕ^f will yield an approximate cancellation in the matrix element integration. (This same argument is made by Gelius[172] using the more approximate plane-wave final state.) The squares of each of the matrix elements in Eq. (98) are therefore expected to be approximately proportional to the corresponding atomic cross-section:

$$|\langle\phi^f|\mathbf{r}|\phi_{A\lambda}\rangle|^2 \propto d\sigma_{A\lambda}{}^{(AO)}/d\Omega$$

or

$$\langle\phi^f|\mathbf{r}|\phi_{A\lambda}\rangle \propto \pm(d\sigma_{A\lambda}{}^{(AO)}/d\Omega)^{\frac{1}{2}} \tag{99}$$

and the final result for the molecular cross-section can be rewritten as

$$d\sigma_k{}^{(MO)}/d\Omega \propto \sum_{A\lambda} |C_{A\lambda k}|^2(d\sigma_{A\lambda}{}^{(AO)}/d\Omega)$$

$$+ 2\sum_{A'\lambda'}\sum_{\substack{A\lambda \\ (A\lambda > A'\lambda')}} (\pm)C_{A'\lambda'k}C_{A\lambda k}(d\sigma_{A'\lambda'}{}^{(AO)}/d\Omega)^{\frac{1}{2}}(d\sigma_{A\lambda}{}^{(AO)}/d\Omega)^{\frac{1}{2}} \tag{100}$$

The cross-terms in Eq. (100) are generally neglected, yielding the most commonly-used form of this model:

$$d\sigma_k{}^{(MO)}/d\Omega \propto \sum_{A\lambda} |C_{A\lambda k}|^2(d\sigma_{A\lambda}{}^{(AO)}/d\Omega) \tag{101}$$

$|C_{A\lambda k}|^2$ is the net population of atomic orbital Aλ in molecular orbital k. In applications of Eq. (101), the net population is often replaced by the gross population $P_{A\lambda k}$ defined as

$$P_{A\lambda k} = |C_{A\lambda k}|^2 + \sum_{\substack{A'\lambda' \\ (A' \neq A)}} C_{A\lambda k} C_{A'\lambda'k} \langle \phi_{A\lambda} | \phi_{A'\lambda'} \rangle \qquad (102)$$

although Eq. (100) makes it clear that this is only a very crude way of allowing for overlap affects. Discussions of additional theoretical complexities have also appeared in several studies.[172–176]

The model summarized in Eqs (101) and (102) has been used with reasonable success in analyzing valence spectra of both molecules[172, 173] and solids in which quasi-molecular units (for example, polyatomic ions) exist.[174–176] In general, empirical relative atomic cross-sections are determined for atoms or simple molecules, and then used, together with an LCAO calculation for the system under study, to generate a theoretical spectrum. One such example for CF_4 is shown in Fig. 11, and it is clear that it correctly predicts relative intensities to a very high accuracy.
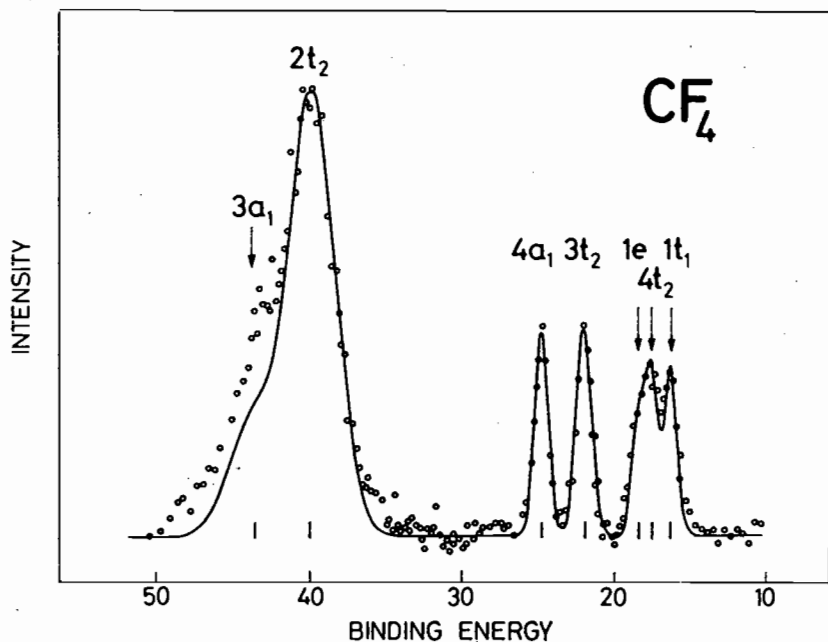

Fig. 11. Experimental XPS spectrum for the valence levels of gaseous CF_4 (points) in comparison with a theoretical curve based upon Eqs (101) and (102). Relative atomic subshell cross-sections were determined experimentally. MgKα radiation was used for excitation. (From Gelius, ref. 172.)

4. *Solids and Valence-band Studies.* X-ray photoemission from solids has been very successfully analyzed in terms of a three-step model first utilized in ultraviolet photoemission studies by Berglund and Spicer.[177] The steps involved are: (1) a one-electron excitation occurring somewhere below the solid surface from an initial-state orbital ϕ_k at energy E to a final-state orbital ϕ^f with an energy E^f greater by $h\nu$, (2) electron transport via ϕ^f to the surface, during which elastic and inelastic scattering events may occur, and (3) passage of the electron through the surface, at which a small potential barrier may cause refraction or back-reflection to occur. The electron states involved are generally assumed to be characteristic of the bulk material. The one-electron energies E and E^f may be measured with respect to the Fermi energy, the vacuum level, or some other reference; in any case E^f can be easily connected with the measured kinetic energy E_{kin}. An additional zeroth step involving penetration of the exciting radiation to the depth where excitation occurs might also be added to this model, but this has no significant consequence for XPS except at grazing incidence angles for which significant refraction and reflection begin to occur.[17, 178, 179] As x-ray photoelectron escape depths are only of the order of 10–30 Å, the assumption of an initial excitation involving pure bulk electronic states might be questioned, and one-step theoretical models in which the surface is explicitly included in the photoemission process have been presented.[180, 181] However, the bulk photoemission model correctly predicts most of the features noted in both UPS and XPS measurements on semiconductors and transition metals,[57, 182] and also permits separating out the various important physical aspects of photoemission. The presence of distinct surface effects on the photoemission process cannot be discounted, however,[132] with one much-discussed example being a surface-state peak observed in UPS spectra and other measurements on tungsten.[183] Primary emphasis here will be placed upon the excitation step in the three-step model, as it contains those elements of the problem that are most clearly related to the ground-state electronic structure of the system.

For emission from non-overlapping, highly-localized, core orbitals, the use of an atomic cross-section (differential or total) is a reasonable approximation for predicting the excitation strength. For emission from valence levels involved in only slightly overlapping quasi-molecular units, the methods discussed in the last section can be used. For emission from highly-overlapping band-like valence levels, a distinctly different procedure is necessary, as outlined below.

In a crystalline solid, both initial and final orbitals will be Bloch functions with wave vectors $\mathbf{k}$ and $\mathbf{k}^f$, respectively, so that $\phi_k(\mathbf{r}) \equiv \phi_\mathbf{k}(\mathbf{r}) = u_\mathbf{k}(\mathbf{r}) \exp(i\mathbf{k} \cdot \mathbf{r})$ and $\phi^f(\mathbf{r}) \equiv \phi_{\mathbf{k}^f}(\mathbf{r}) = u_{\mathbf{k}^f}(\mathbf{r}) \exp(i\mathbf{k}^f \cdot \mathbf{r})$, consistent with Eq. (37). Such an excitation is shown in Fig. 12 on a plot of one-electron potential energy versus distance from the surface. In traversing the surface barrier, the electron

$$\phi^f(\vec{r}) \simeq \exp(i\vec{k}^f \cdot \vec{r}) \quad\text{---}\quad \phi^f(\vec{r}) = \exp(i\vec{K}^f \cdot \vec{r})$$

Solid   Surface   Vacuum
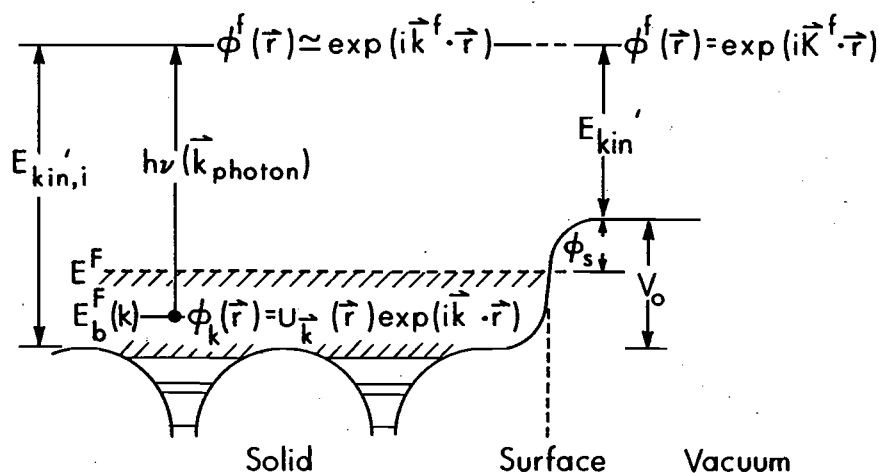
$$(1) \quad E_{kin,i}' = h\nu - E_b^F(k) + V_0 - \phi_s \cong \frac{\hbar^2(k^f)^2}{2m}$$

$$(2) \quad E_{kin}' = E_{kin,i}' - V_0 = \frac{\hbar^2(K^f)^2}{2m}$$

$$(3) \quad \vec{k} + \vec{k}_{photon} + \vec{g} = \vec{k}^f$$

Fig. 12. One-electron model of photoemission in a metallic solid, shown as an energy-level diagram superimposed on the one-electron potential energy curve near the surface. The initial and final states inside the solid are assumed to have Bloch-wave character. Applicable conservation relations on energy and wave vector are also shown.

kinetic energy is reduced from its value inside the surface of E_{kin}', i by an amount equal to the barrier height or inner potential V_0. V_0 is generally measured with respect to the least negative portion of the potential energy inside the crystal which occurs midway between the strongly attractive atomic centers. Detection of an electron propagating in a definite direction outside of the surface implies a free-electron orbital $\phi_{K^f}(\mathbf{r}) = C \exp(i\mathbf{K}^f \cdot \mathbf{r})$ with momentum $\mathbf{P}^f = \hbar\mathbf{K}^f$, but it should be noted that $\mathbf{K}^f$ need not be precisely equal to $\mathbf{k}^f$. One obvious source of a difference between $\mathbf{K}^f$ and $\mathbf{k}^f$ is refraction effects at the surface barrier, which are only expected to conserve the component of wave vector parallel to the surface ($\mathbf{k}_{\parallel}^f = \mathbf{K}_{\parallel}^f$), but such effects are rather small in XPS except for grazing-angles of electron emission with respect to the surface.[17] A convenient convention for describing the electron wave vectors involved in such a transition is to choose the initial $\mathbf{k}$ to lie inside the first or reduced Brillouin zone and the final $\mathbf{k}^f$ to be expressed in an extended-zone scheme. Thus, initial states at several different energies may

possess the same reduced $\mathbf{k}$ value, but each final state is associated with a unique $\mathbf{k}^f$ value.

The basic one-electron matrix element associated with the cross-section for excitation is most generally written as $\langle \phi_{k^f} | \mathbf{A} \cdot \nabla | \phi_k \rangle$. This represents the one-electron analogue of Eq. (60). It is then a simple matter to show[184] that the translational symmetry properties of Bloch functions [Eq. (37)] imply that this matrix element can only be non-zero when $\mathbf{k}$ and $\mathbf{k}^f$ are related by a reciprocal lattice vector $\mathbf{g}$:

$$\mathbf{k}^f = \mathbf{k} + \mathbf{g} \tag{103}$$

Transitions satisfying this selection rule are termed "direct", and have been found to be very important in the analysis of UPS spectra and other optical absorption experiments from a variety of materials.[57, 182] At the higher energies of excitation involved in XPS, it has been pointed out by Baird et al.[185] that the wave vector $\mathbf{k}_{h\nu}$ associated with the exciting x-ray in XPS has a magnitude sufficiently large that it must be included in this wave-vector conservation equation:

$$\mathbf{k}^f = \mathbf{k} + \mathbf{g} + \mathbf{k}_{h\nu} \tag{104}$$

For example, with $h\nu = 1486\cdot6$ eV, $|\mathbf{k}^f| \approx 2\pi/\lambda_e \approx 19\cdot7$ Å^{-1} for valence emission, $|\mathbf{k}_{h\nu}| = 2\pi/\lambda \approx 0\cdot7$ Å^{-1}, and typical magnitudes of the reduced wave vector are $|\mathbf{k}| \lesssim 2\cdot0$ Å^{-1}. Transitions violating such selection rules are termed "non-direct", and can be induced in various ways, for example, by interaction with lattice vibrations (phonons), by the introduction of atomic disorder, or by considering emission from very localized valence levels (for example, rare-earth $4f$) for which the localized initial and final hole states suppress the effects of translational symmetry. Shevchik[186] has recently made the important observation that phonon effects may lead to an almost total obscuring of direct-transition effects in the XPS spectra of most materials at room temperature. Phonons with a range of wave vectors $\mathbf{k}_{phonon}$ are created or annihilated during the excitation process in a manner completely analogous to thermal diffuse scattering in x-ray diffraction,[187] with the net effect that only a certain fraction of the transitions are simply describable in terms of Eq. (104) (for which $\mathbf{k}_{phonon} \ll \mathbf{k}$). This fraction is most simply estimated from the Debye–Waller factor, as discussed in more detail in Section VI.D.2. Further study of such phonon effects is needed to assess quantitatively their importance, but they do appear to provide a likely mechanism whereby all occupied $\mathbf{k}$ values can contribute to XPS spectra, even if electrons are collected along only a finite solid-angle cone with respect to the axes of a single-crystal in an angle-resolved experiment (see further discussion in Section VI.D.2).

If it is assumed for the moment (as in most prior XPS studies) that direct transitions *are* important, the total rate of excitation of electrons to a given

energy E^f will be given by a summation over all allowed $\mathbf{k} \to \mathbf{k}^f$ transitions in which energy and wave vector conservation are satisfied. Also, for experiments at non-zero temperature each transition must be weighted by the probability of occupation of the initial state, as given by the Fermi function:

$$F(E) = \frac{1}{\exp\,[(E-E_{\mathrm{F}})/kT]+1} \qquad (105)$$

This function allows for the thermal excitation of electrons lying within $\sim kT$ of the Fermi level. Finally, each transition can be weighted by an average probability $\bar{T}$ for escape without inelastic scattering or back reflection at the surface, which will depend on both E^f and $\mathbf{k}^f$ and can be denoted $\bar{T}(E^f, \mathbf{k}^f)$. The average indicated is over various depths of excitation below the surface. The final result will be proportional to the no-loss photoelectron spectrum finally observed, and is thus given by

$$\begin{aligned} N(E_{\mathrm{kin}}) &= N(E^f+\Delta) = N(E+h\nu+\Delta) \\ &\propto \sum_{\substack{\text{Occupied}\\ \text{bands}}} \int |\langle \phi_{\mathbf{k}}{}^f(E')|\mathbf{A}\cdot\boldsymbol{\nabla}|\phi_{\mathbf{k}}(E)\rangle|^2 \\ &\quad \times F(E)\bar{T}(E^f, \mathbf{k}^f)\delta(E^f-E-h\nu)\delta(\mathbf{k}^f-\mathbf{k}-\mathbf{g}-\mathbf{k}_{h\nu})\, d^3k \end{aligned} \qquad (106)$$

where Δ is a trivial energy-scale shift that allows for the binding-energy reference chosen, as well as any work function difference between specimen and spectrometer.

In evaluating the matrix elements in this equation to permit comparisons with XPS spectra, Kono et al.[176] have assumed an orthogonalized plane wave for the final state $\phi_{\mathbf{k}}{}^f$ and a tight-binding (or LCAO) initial state $\phi_{\mathbf{k}}$. Similar analyses have also been carried out more recently by Aleshin and Kucherenko,[188] and in Section VI.D.2, the application of a simpler form of this model to the analysis of angle-resolved XPS valence spectra from single crystals is discussed.

Several basic simplifications of Equation (106) have often been made so as to obtain a rather direct relationship between observed XPS spectra and the initial density of electronic states $\rho(E)$.[82] Most of these simplifications cannot be made in considering UPS spectra, by contrast. The average no-loss escape function $\bar{T}(E^f, \mathbf{k}^f)$ will be essentially constant for all of the high-energy electrons in the XPS valence spectral region, and so can be eliminated. In UPS however, $\bar{T}(E^f, \mathbf{k}^f)$ can vary considerably over the spectrum. The Fermi function produces only relatively small effects within $\sim \pm kT$ of the Fermi energy, so that in either UPS or XPS carried out at or below room temperature, it is adequate to set it equal to a unit step function. A further simplification that can be justified in several ways for XPS but not UPS is

that the summation and integration in Eq. (106) ultimately yield *for a polycrystalline specimen* a result of the approximate form

$$N(E_{\mathrm{kin}}) \propto \bar{\sigma}_E(h\nu)\rho(E) \qquad (107)$$

in which $\bar{\sigma}_E(h\nu)$ is a mean photoelectric cross section for the initial states at energy E and $\rho(E)$ is the density of occupied initial states at energy E. The steps in this justification involve first noting the highly free-electron character of the very high energy final states in XPS (that is $\phi_{\mathbf{k}}{}^f \approx \exp\,(i\mathbf{k}^f\cdot\mathbf{r})$). Because the free-electron density of states is proportional to $(E^f)^{\frac{1}{2}}$, this results in an essentially constant total density of final states into which valence emission can occur.[82] Furthermore, the relatively short electron mean free paths in XPS have been argued by Feibelman and Eastman[181] to introduce an uncertainly-principle smearing in the surface-normal component of $\mathbf{k}^f$ that is larger than the mean $\Delta\mathbf{k}$ spacing between final-state bands at a given energy, and so permits all initial states in a polycrystalline specimen to be equally involved in direct transitions as far as k-conservation is concerned. Phonon effects also may lead to a uniform sampling of all initial states, as suggested by Shevchik.[186] Finally, Baird, Wagner, and Fadley have carried out model direct-transition calculations for single crystals of Au[185] and Al[189] in which all matrix elements were assumed to be equal and the only $\mathbf{k}^f$ smearing included was associated with a finite spectrometer acceptance aperture; summing spectra predicted for all mean emission directions with respect to the crystal axes gave results essentially identical to the density of occupied states, suggesting again that all initial states are equally sampled. Thus, there are several reasons to expect XPS spectra from polycrystalline materials to have a form given approximately by Eq. (107).

XPS has been utilized to study the valence electronic structures of many solids.[82, 190–193] Examples of comparisons between experiment and theory for the three principal classes of solids (metal, semiconductor, and insulator) are shown in Figs 13,[191] 14,[192] and 15.[193] Here, total densities of initial states $\rho(E)$ are compared directly with experiment, in some cases after a suitable broadening has been applied to theory to simulate natural and instrumental linewidth contributions. These comparisons show that all of the main features noted in the experimental spectra are also seen in the theoretical densities of states, although peak intensities are not always well predicted, probably due to non-constant cross-section effects. For example, in Fig. 15, the dotted curve indicates an empirical estimate by Ley et al.[193] of the relative cross-section variation that would be necessary to yield agreement between experiment and Eq. (107) for diamond. The form of this curve is furthermore consistent with the increasing C2s character expected toward higher binding energies in the diamond valence bands, as the C2s atomic cross-section is expected to be considerably larger than that for C2p.[151] Similar conclusions have also been

reached for diamond in a recent more quantitative calculation of the matrix elements involved.[188] Cross-section variations over the valence bands thus clearly can play an important role in the analysis of such XPS data, but it is very encouraging that observed peak positions in general agree very well with those in the density of states. Thus, XPS has proven to be a very direct method for studying the density of states.

In summary, for studies of densities of states in solids, both UPS and XPS exhibit certain unique characteristics and advantages. Somewhat better resolution is possible in a UPS measurement, primarily due to the narrower
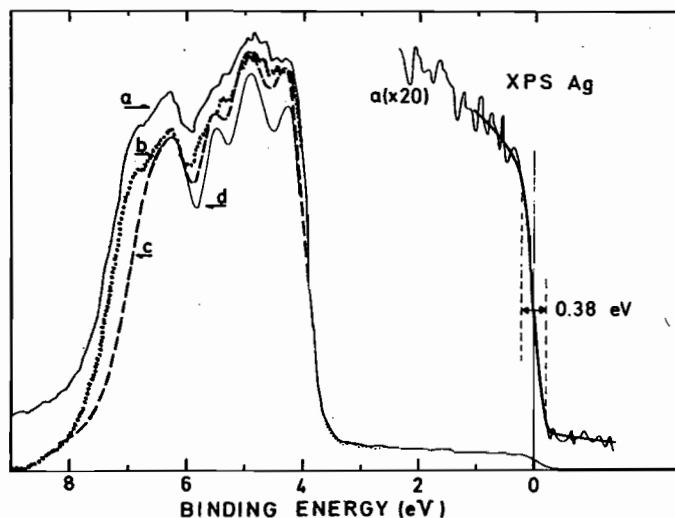

Fig. 13. XPS valence spectrum for polycrystalline silver excited by monochromatized AlKα radiation in comparison with a theoretical density of states. Curve a is the raw XPS data, curve b is the data after a smooth inelastic background correction has been subtracted, and curves c and d represent two different lineshape broadenings of the total theoretical density of states according to Eq. (158). These broadenings thus include effects due to both lifetime and shake-up type excitations in the metal. Note the steep cut-off in the data near $E_F = 0$, which can be used to determine the instrumental resolution function. (From Barrie and Christensen, ref. 191.)

radiation sources presently available. Also, UPS spectra contain in principle information on both the initial and final density of states functions, together with certain k-dependent aspects of these functions. The interpretation of an XPS spectrum in terms of the initial density of states appears to be more direct, however. Also, the effects of inelastic scattering are more easily corrected for in an XPS spectrum (cf. Section II.E). Finally, the two techniques are very complementary in the sense that they are controlled by cross-sections which may have different relative values for different bands, thereby providing further information on the types of states involved.
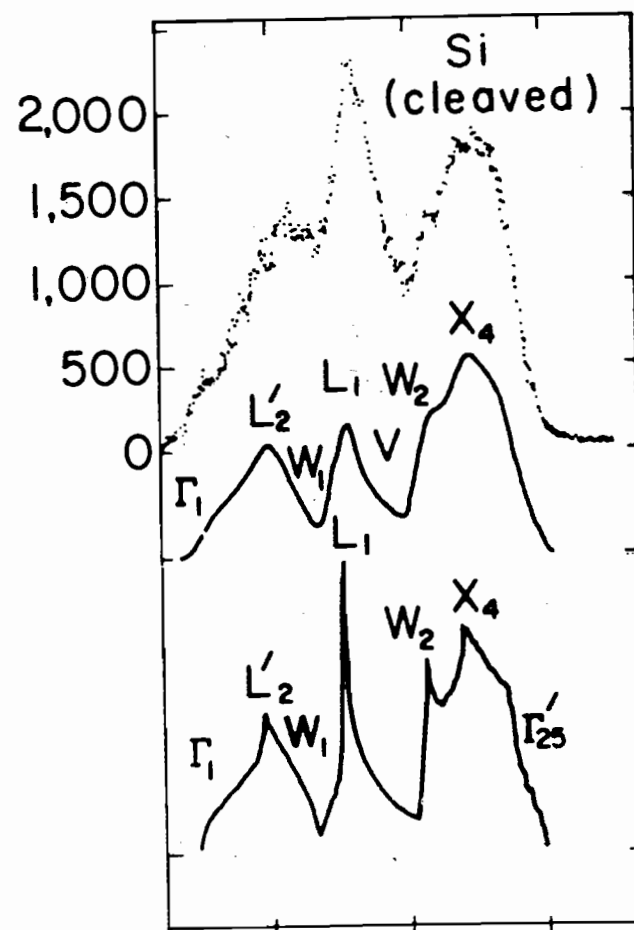
Fig. 14. XPS valence spectrum for a silicon single crystal cleaved in vacuum (points), together with a calculated total density of states (bottom curve), and a density of states broadened by the instrumental resolution function. Excitation was with monochromatized AlKα. The spectrum has been corrected for inelastic scattering. The energy locations of state density primarily due to various high-symmetry points in the reduced Brillouin zone are also indicated. (From Ley et al., ref. 192.)

E. Inelastic Scattering in Solids

Inelastic scattering acts to diminish the no-loss photoelectron current for any type of specimen (gas, liquid, or solid). The processes involved can be one-electron excitations, vibrational excitations, or, in certain solids, plasmon excitations. As it is in measurements on solids that inelastic scattering plays the most significant role in limiting no-loss emission to a mean depth of only a few atomic layers, only such effects will be considered in detail here.
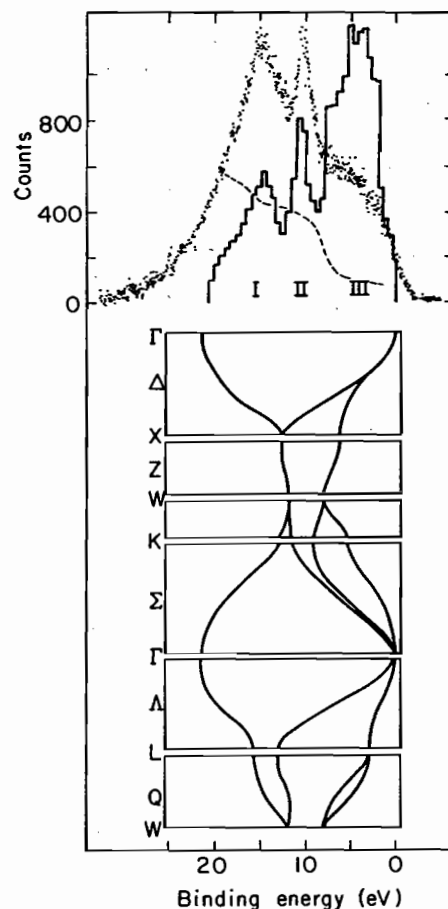
Fig. 15. Valence spectrum for diamond (points) in comparison with a calculated density of states (solid histogram). The dotted curve is an empirical estimate of the mean cross-section variation with energy that would be required to reconcile the spectrum and the density of states according to Eq. (107). Also shown in the lower portion of the figure is the detailed theoretical band structure along various high-symmetry directions in the reduced zone. The incident radiation was monochromatized $AlK\alpha$. The spectrum has been corrected for inelastic scattering. (From Cavell et al., ref. 193.)

Inelastic scattering in solids is generally discussed in terms of a characteristic length for decay of the no-loss intensity. Specifically, if a monoenergetic flux N_0 at energy E_{kin} is generated at a given point, the no-loss flux N remaining after traveling a distance l is assumed to be given by an exponential decay law

$$N = N_0 \exp\left[-l/\Lambda_e\left(E_{kin}\right)\right] \tag{108}$$

where Λ_e is termed the electron attenuation length, mean free path, or penetration depth. Implicit in this definition is the idea that inelastic scattering

occurs *after* photoelectron excitation by means of what are often referred to as "extrinsic" loss processes. "Intrinsic" losses can however occur *during* excitation[194] and are discussed further in Section VI.B.

Such attenuation lengths are usually determined by measuring Auger or photoelectron peak intensities from uniform overlayers with varying thicknesses comparable in magnitude to Λ_e. Powell[20] and Lindau and Spicer[21] have recently presented very thorough reviews of attenuation length measurements in the 40–2000 eV range of most interest in XPS, and an on-going compilation of Λ_e values is also available through the National Physical Laboratory, U.K.[195] Powell's summary of experimental values obtained in various studies is shown in Fig. 16. (Note the log–log scales.) All data points
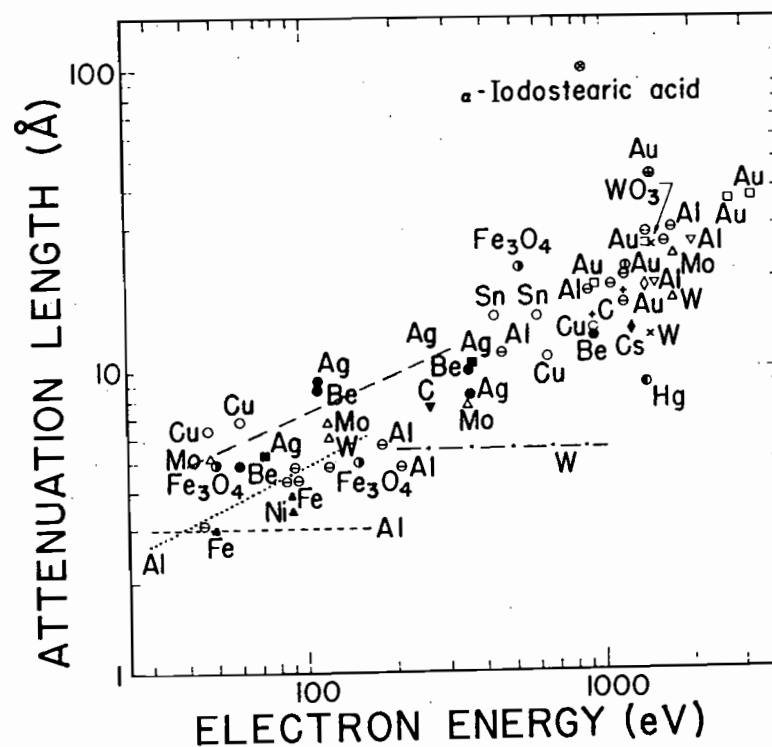
Fig. 16. Summary of experimental values for the electron inelastic attenuation length Λ_e for various solids. (From Powell, ref. 20.)

lie roughly on a common curve, which has been termed the "universal curve" of attenuation lengths (although it should be noted that it is universal to within only a factor of two to five). Extending a plot such as Fig. 16 to lower energies[21] reveals a minimum in Λ_e at ~ 30–100 eV and an increase at lower energies corresponding to typical UPS experiments. Thus, surface sensitivity

is a maximum in the 30–100 eV kinetic-energy range. For the log–log plot of Fig. 16, the higher energy data are fairly well described by a single straight line that ultimately yields an empirical energy dependence of the form

$$\Lambda_e(E_{kin}) \propto (E_{kin})^{0.52} \qquad (109)$$

This relationship is useful in rough estimates of Λ_e variation from peak to peak in a given specimen, although between different materials it is certainly not very reliable.

Powell[20] and Penn[196] have also recently discussed various theoretical models that can be used to predict attenuation lengths at XPS kinetic energies in terms of microscopic system electronic properties. Penn divides the attenuation length up into two parts involving core- and valence-level excitations according to a reciprocal addition procedure expected if the two types of losses are independent of one another:

$$\frac{1}{\Lambda_{e,\,total}} = \frac{1}{\Lambda_{e,\,core}} + \frac{1}{\Lambda_{e,\,valence}} \qquad (110)$$

$\Lambda_{e,\,core}$ is determined from an equation of the form given by Powell:[20]

$$\Lambda_{e,\,core} = 2.55 \times 10^{-3}\, M E_{kin} \Big/ \rho \sum_i \frac{N_i}{E_i} \ln\left[\frac{4E_{kin}}{\Delta E_i}\right] \qquad (111)$$

in which M is the atomic or molecular weight of the solid, E_{kin} is in electron volts, ρ is the density in g/cm³, N_i is the number of electrons in the ith subshell at energy E_i, and ΔE_i is the mean energy loss involving these electrons (always greater than $E_i = E_b^F(i)$). $\Lambda_{e,\,valence}$ is determined by assuming that plasmon excitations are the dominant loss processes,[196] a situation that can also be shown to yield an overall relationship very similar to Eq. (111),[20] and the final results permit estimating XPS Λ_e values for all elements and compounds, albeit by means of a rather simplified model. In connection with such estimates, it is expected that *ratios* of Λ_e values for a given element or compound will be much more accurately determined than absolute values; this is a very useful result, as it is such ratios that are involved in quantitative analyses of homogeneous systems by XPS, as discussed further in the next section.

As a final comment concerning electron attenuation lengths, it has also been pointed out by Feibelman[197, 198] that Λ_e may vary in magnitude from the bulk of a specimen to its surface because of changes in the dominant mode of extrinsic inelastic scattering (for example, from bulk- to surface-plasmon excitation). Thus, Λ_e need not be an isotropic constant of the material, although it does not much deviate from this for a free electron metal.[197]

F. Photoelectron Peak Intensities

1. *Introduction.* The quantitative interpretation of x-ray photoelectron peak intensities requires developing a model for predicting their magnitudes from various properties of the excitation source, specimen, electron analyzer, and detection system. Detailed discussions of such models have been presented previously by Krause and Wuilleumier[199] for emission from gases and by Fadley[17] for emission from polycrystalline solids. A brief outline of the essential assumptions involved will be presented here, followed by a summary of several important special cases for emission from solids in the next section.

In general, the photoelectron peak intensity N_k produced by subshell k can be calculated within a three-step-like model by integrating the differential intensities dN_k originating in the various volume elements of the specimen. Each of these differential intensities can be written as the following product, in which x, y, z denotes position within the specimen:

$$
dN_k = \begin{bmatrix} \text{X-ray flux} \\ \text{at } x, y, z \end{bmatrix} \times \begin{bmatrix} \text{Number of atoms (molecules)} \\ \text{in } dx\, dy\, dz \end{bmatrix}
$$
$$
\times \begin{bmatrix} \text{Differential cross-} \\ \text{section for } k \text{ subshell} \end{bmatrix} \times \begin{bmatrix} \text{Acceptance solid angle of} \\ \text{electron analyzer at } x, y, z \end{bmatrix}
$$
$$
\times \begin{bmatrix} \text{Probability for no-loss} \\ \text{escape from specimen} \\ \text{with negligible} \\ \text{direction change} \end{bmatrix} \times \begin{bmatrix} \text{Instrumental} \\ \text{detection} \\ \text{efficiency} \end{bmatrix} \qquad (112)
$$

In most spectrometer systems, a non-monochromatized x-ray source with a broad flux emission pattern is utilized, and for this case it is reasonable to set the x-ray flux equal to some constant value I_0 over the entire specimen volume that is active in producing detectable photoelectrons. This assumption is valid because the exciting radiation is attenuated much more slowly with distance of travel into the specimen than are the electrons as they escape from the specimen. Thus, the region active in producing no-loss electrons is exposed to an essentially constant flux. Exceptions to this situation are mono-chromatized x-ray sources for which a focused beam is produced,[74] as well as grazing-incidence experiments on solid specimens in which x-ray refraction at the surface much increases the x-ray attenuation with distance below the surface.[17, 178, 179] Neither of these special cases will be considered further here, but refraction effects are discussed in Section VI.C.

The acceptance solid angle Ω of the electron analyzer will vary over the specimen volume, becoming zero for those points from which emission is totally prohibited by the electron optics. Ω, as well as the effective specimen

area A over which $\Omega \neq 0$, also may vary with electron kinetic energy, as discussed previously in Sections II.C.1 and II.C.2.

The probability for no-loss escape from the specimen, which can in the present context be written as $T(E_{kin}, \mathbf{k}^f, x, y, z)$, is most simply given by an expression such as Eq. (108) involving the electron attenuation length, provided that elastic scattering events that change direction but not energy are neglected. $\mathbf{k}^f$ thus specifies the direction of electron motion along the path length l from the excitation point x, y, z. In gases, such an escape probability must also take into account variations in density (and thus also Λ_e) along the electron trajectories.

The instrumental detection efficiency D_0 is defined to be the probability that a no-loss electron escaping from the specimen in a direction encompassed by the acceptance solid angle will yield a single final count (or equivalent current). This efficiency thus allows for all non-idealities in the analysis and detection system, and it can also depend on E_{kin}.

If the atomic or molecular density in cm^{-3} is denoted $\rho(x, y, z)$, the differential intensity element thus becomes

$$dN_k = I_0 \cdot \rho(x, y, z) \, dx \, dy \, dz \cdot \frac{d\sigma_k}{d\Omega} \cdot \Omega(E_{kin}, x, y, z)$$

$$\cdot T(E_{kin}, \mathbf{k}^f, x, y, z) \cdot D_0(E_{kin}) \qquad (113)$$

or for a uniform-density, but bounded, specimen:

$$dN_k = I_0 \cdot \rho \, dx \, dy \, dz \cdot \frac{d\sigma_k}{d\Omega} \cdot \Omega(E_{kin}, x, y, z)$$

$$\exp\left[-l/\Lambda_e(E_{kin})\right] \cdot D_0(E_{kin}) \qquad (114)$$

where l is the path length to escape from the specimen surface into vacuum.

2. *Peak Intensities from Solids.* With a few simplifying assumptions, Eq. (114) is readily integrated to obtain useful expressions for total peak intensity N_k for the idealized spectrometer shown in Fig. 17.[17, 178] The specimen surface is assumed to be atomically flat. The specimen is taken to be polycrystalline to avoid single-crystal anisotropies in emission[200] (see discussion in Section VI.D.1). An exponential inelastic attenuation law as in Eq. (108) is assumed, and elastic electron scattering effects are neglected. For a given kinetic energy, the electron spectrometer is further assumed to act as though a mean solid angle Ω_0 is applicable over all specimen volume included in the projection of an effective aperture A_0 along the mean electron emission direction (dotted lines in Fig. 17). Both Ω_0 and A_0 may be functions of the kinetic energy E_{kin}. The mean emission direction is assumed to be at an angle θ with respect to the surface. The exciting radiation is incident at an angle ϕ_x with respect to the surface, and, due to refraction, the internal
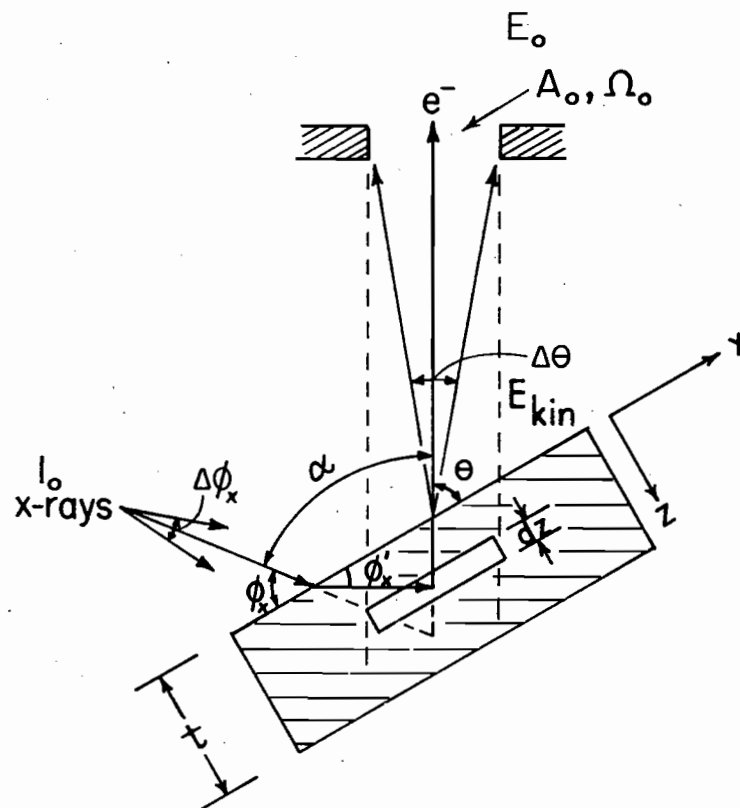
Fig. 17. Idealized spectrometer geometry for calculating photoelectron peak intensities from solid specimens.

angle ϕ_x' may be less than ϕ_x. Such refraction (and reflection) effects only occur for $\phi_x \lesssim 1°$,[178, 179] and will not be included here, although they are briefly discussed in Section VI.C. The angle α between the mean incidence- and exit-directions is held fixed at between approximately 45° and 105° in most current XPS spectrometers.

Within the approximations quoted above (which are very nearly achieved in a number of practical spectrometer systems), it is possible to derive intensity expressions for several important cases: [17, 178, 201]

(a) Semi-infinite specimen, atomically clean surface, peak k with $E_{kin} \equiv E_k$:

$$N_k(\theta) = I_0 \Omega_0(E_k) A_0(E_k) D_0(E_k) \rho \, d\sigma_k/d\Omega \, \Lambda_e(E_k) \qquad (115)$$

This case corresponds to an optimal measurement on a homogeneous specimen for which no surface contaminant layer is present. The expression given permits predicting the absolute peak intensities resulting for a given

specimen, or, of much more interest in practice, the relative intensities of the various peaks. If absolute intensities are to be derived, then the incident flux I_0 must be determined, as well as the kinetic energy dependences of effective solid angle Ω_0, effective specimen area A_0, and detection efficiency D_0. In relative intensity measurements in which the quantity of interest is N_k/N_k, for two peaks k and k', I_0 will cancel, although $\Omega_0 A_0 D_0$ need not due to its kinetic energy dependence. The density ρ of the atoms or molecules on which subshell k or k' is located may be known beforehand, or may also be the desired end result in quantitative analyses using XPS. The differential cross-section $d\sigma_k/d\Omega$ can be calculated by the various methods discussed in Sections III.D.2–III.D.4. For core levels, the tabulations of σ_{nlj} by Scofield,[151] combined with the β_{nl} values given by Reilman et al.,[154] provide a suitable means for estimating $d\sigma_k/d\Omega$ with good accuracy within the framework of a one-electron-transition model. Possible effects of multi-electron processes on the use of such cross-sections are discussed in Sections III.D.1 and V.D. Within a given specimen, $\Lambda_e(E_k)$ can be estimated from Penn's treatment,[191] or, more simply, its dependence on kinetic energy can be assumed to follow the empirical square-root dependence of Eq. (109). Note that there is no θ dependence in N_k within this simple model, a prediction that has been verified experimentally by Henke;[178] this behavior is expected to hold as long as θ is not made so small that the edges of the specimen lie within the aperture A_0.[17, 222]

(b) Specimen of thickness t, atomically clean surface, peak k with $E_{\text{kin}} \equiv E_k$:

$$N_k(\theta) = I_0 \Omega_0(E_k) A_0(E_k) D_0(E_k) \rho \; d\sigma_k/d\Omega \; \Lambda_e(E_k)$$
$$\times [1 - \exp(-t/\Lambda_e(E_k) \sin \theta)] \qquad (116)$$

Here, the intensity of a peak originating in a specimen of finite thickness is predicted to increase with decreasing θ (again with the proviso that θ not be so small that the specimen edges lie within A_0).

(c) Semi-infinite substrate with uniform overlayer of thickness t—Peak k from substrate with $E_{\text{kin}} \equiv E_k$:

$$N_k(\theta) = I_0 \Omega_0(E_k) A_0(E_k) D_0(E_k) \rho \; d\sigma_k/d\Omega \; \Lambda_e(E_k)$$
$$\times \exp(-t/\Lambda_e'(E_k) \sin \theta) \qquad (117)$$

Peak l from overlayer with $E_{\text{kin}} \equiv E_l$:

$$N_l(\theta) = I_0 \Omega_0(E_l) A_0(E_l) D_0(E_l) \rho' \; d\sigma_l/d\Omega \; \Lambda_e'(E_l)$$
$$\times [1 - \exp(-t/\Lambda_e'(E_l) \sin \theta)] \qquad (118)$$

where

$\Lambda_e(E_k) =$ an attenuation length in the substrate

$\Lambda_e'(E_k) =$ an attenuation length in the overlayer

$\rho =$ an atomic density in the substrate

$\rho' =$ an atomic density in the overlayer.

Overlayer/substrate ratio:

$$\frac{N_l(\theta)}{N_k(\theta)} = \frac{\Omega_0(E_l) A_0(E_l) D_0(E_l) \rho'(d\sigma_l/d\Omega) \Lambda_e'(E_l)}{\Omega_0(E_k) A_0(E_k) D_0(E_k) \rho \; d\sigma_k/d\Omega \; \Lambda_e(E_k)}$$
$$\times [1 - \exp(-t/\Lambda_e'(E_l) \sin \theta] \exp(t/\Lambda_e'(E_k) \sin \theta \qquad (119)$$

This case represents a much more common experimental situation in which the primary specimen acts as substrate and possesses an intentional or unintentional contaminant overlayer (for example, oxide on a metal or a layer deposited from the spectrometer residual gases). Substrate peaks are attenuated by inelastic scattering in the overlayer, an effect that is much enhanced at low θ. The overlayer/substrate ratio is thus predicted to increase strongly as θ decreases, an effect that suggests a general method for increasing surface sensitivity by using grazing angles of electron escape; such angular-dependent studies are discussed in more detail in Section VI.B.

(d) Semi-infinite substrate with a non-attenuating overlayer at fractional monolayer coverage—Peak k from substrate: Eq. (115).

Peak l from overlayer:

$$N_l(\theta) = I_0 \Omega_0(E_l) A_0(E_l) D_0(E_l) \sigma'(d\sigma_l/d\Omega)(\sin \theta)^{-1} \qquad (120a)$$

Overlayer/substrate ratio:

$$\frac{N_l(\theta)}{N_k(\theta)} = \frac{\Omega_0(E_l) A_0(E_l) D_0(E_l) s'(d\sigma_l/d\Omega)}{\Omega_0(E_k) A_0(E_k) D_0(E_k) s \; d\sigma_k/d\Omega \; (\Lambda_e(E_k) \sin \theta/d)}$$
$$= \left[\frac{s'}{s}\right] \cdot \frac{D_0(E_l) \Omega_0(E_l) A_0(E_l)(d\sigma_l/d\Omega)d}{D_0(E_k) \Omega_0(E_k) A_0(E_k) \; d\sigma_k/d\Omega \; \Lambda_e \sin \theta} \qquad (120b)$$

with

$s' =$ the mean surface density of atoms in which peak l originates in cm^{-2}

$s =$ the mean surface density of substrate atoms in cm^{-2}

$s'/s =$ the fractional monolayer coverage of the atomic species in which peak l originates

$d =$ the mean separation between layers of density s in the substrate (calculable from s/ρ).

These expressions are useful in surface-chemical studies at very low exposures to adsorbate molecules ($s'/s \lesssim 1$), as they permit an estimation of the fractional monolayer coverage from observed peak intensities. The assumption of no inelastic attenuation in the overlayer is an extreme one, but is justified because the macroscopic Λ_e' of case (c) is both difficult to estimate and dubious in its application to such thin, non-macroscopic layers, and also because it represents a correct limiting form for zero coverage.

The basic model presented here assumes an atomically-flat surface. As this will obtain only very rarely in actual experiments, assessments of the potential effects of surface roughness on XPS peak intensities have been made by Fadley et al.[17, 202] It is found that roughness can appreciably affect both absolute and relative intensities, especially for systems with inhomogeneity as measured vertical to the surface,[17, 203] with much depending upon the dimensional scale of the roughness relative to the attenuation lengths for x-rays and electrons involved. Roughness effects on angular-resolved measurements are discussed further in Section VI.B, and in considerably greater detail in other sources.[17, 202, 203]

As a final comment concerning the equations presented here, it should be noted that, for complete generality, an angle-dependent instrument response function $R(E_k, \theta)$ must be included as a further factor in all of Eqs (115)–(120). The definition and determination of this response function are discussed elsewhere.[17, 202] It is unity for the idealized geometry treated here (as long as θ is not too small). It has also been calculated and measured for one particular spectrometer system.[74] A further important property of this function is that it will generally be only weakly dependent on kinetic energy, and so will cancel to a very good approximation in peak intensity ratios obtained at a given angle θ. Thus, relative intensity measurements can be made in most cases without the necessity of evaluating the instrument response with θ.

3. *Applications to Quantitative Analysis.* The first detailed experimental tests of the simplest model for intensities originating in a uniform specimen represented by Eq. (115) above were carried out by Nefedov et al.[161] and Carter et al.[204] The study by Carter et al. made use of Eq. (94) to avoid the need of evaluating symmetry parameters, Eq. (109) for the energy dependence of attenuation lengths, and an empirically-determined instrument factor $\Omega_0(E_k)A_0(E_k)D_0(E_k)$. The Scofield calculations[151] provided the cross-sections required. Theoretical relative intensities were calculated for subshells in a number of elements and comparisons were made with several sets of experimental data, including tabulations of measured relative intensities (or elemental sensitivities) by Wagner[205] and Jorgensen and Berthou.[206] In general, agreement to within $\pm 10\%$ was found. Powell and Larson[207] have more recently considered the use of the same model from a somewhat more exact viewpoint, including a discussion of potential errors associated with determining experimental peak areas that are directly relatable to all of the processes involved in the differential photoelectric cross-section. Specifically, from 20% to 50% of the one-electron differential photoelectric cross-section is expected to appear as low-energy satellite intensity due to many-electron effects (cf. discussions in Sections III.F.1 and V.D.2). All of the factors in Eq. (115) were considered in detail, with the most accurate approximations being made whenever possible; for three pure compounds with carefully

cleaned surfaces, the agreement between experimental and theoretical relative intensities was $\sim \pm 5\%$. Thus, there are good reasons to be optimistic that XPS can be used for quantitative analyses of well-prepared homogeneous specimens with this accuracy. For systems exhibiting inhomogeneity near the surface (for example, a substrate/overlayer geometry), additional problems are encountered because at least two regions are involved, but, especially when coupled with angular-dependent measurements,[17] accuracies of $\sim \pm 10\%$ again seem achievable (see also discussion in Section VI.B). Thus, XPS does have considerable analytical potential, particularly as a near-surface probe that is at least complementary to, and probably somewhat more quantitative and less destructive than, electron-excited Auger electron spectroscopy (AES). Powell[208] has recently comparatively reviewed the use of XPS and AES in surface analysis.

IV. CORE ELECTRON BINDING ENERGY SHIFTS

A considerable fraction of XPS studies to date has been involved primarily with the precise measurement of core electron binding energies, and in particular with the measurement of chemical shifts in these binding energies. Such chemical shifts in fact provided much of the recent impetus for the development of XPS.[3] The technique is rather uniquely qualified for such studies, as the usual x-rays utilized (MgKα = 1254 eV and AlKα = 1487 eV) can penetrate to levels well below the vacuum level. The more common ultraviolet radiation sources presently limit UPS to valence levels and weakly bound core levels within ~ 40 eV of the vacuum level, on the other hand. Synchrotron radiation is also now beginning to be used to excite outer core levels with $E_b^V \lesssim 300$ eV.[15,209]

The core levels of any atom can by definition be considered to represent filled subshells, and are found in XPS spectra to be relatively sharp in energy, with typical experimental widths of approximately 1–10 eV. The width observed for a core photoelectron peak depends upon several factors of both inherent and instrumental type. The most important inherent sources of width are:

(1) the lifetime of the k-subshell core hole created by photoemission,

(2) various possible values for the final state energy $E^f(N-1, K)$, as represented for example by multiplet splittings, multi-electron effects, or vibrational broadening (see Section V), and

(3) unresolvable chemically-shifted peaks.

For the present discussion, the final-state complexities of item (2) will be neglected so as to yield a description analogous to that for a simple, closed-shell system. The most important instrumental sources and their typical

magnitudes are:

(1) the exciting x-ray linewidth (approximately $1 \cdot 0$ eV for AlKα without monochromatization and approximately $0 \cdot 4$ eV with),

(2) the finite resolving power of the electron spectrometer (for example, $0 \cdot 3$ eV for $0 \cdot 03\%$ resolution at $E_{\text{kin}} = 1000$ eV), and

(3) non-uniform charging of the specimen (variable magnitude, as discussed in connection with Eq. (2)).

The minimum core linewidths observed to date have been a few tenths of an eV.[41, 210] Thus, provided that the various inherent sources of linewidth and non-uniform charging are not too large, it is possible in principle to measure chemical shifts of the order of $0 \cdot 1$ eV between two or more photoelectron peaks resulting from emission from the same subshell.

If the same atom A is considered as existing either in two chemically inequivalent sites in the same compound labelled 1 and 2 *or* in two different compounds which can be similarly labelled 1 and 2, then the chemical shift ΔE_b of the k electron binding energy can be written simply as the difference of two binding energies. For gaseous specimens with vacuum-referenced binding energies, this means that

$$\Delta E_b{}^V(A, k, 1\text{--}2) = (E_b{}^V(k))_1 - (E_b{}^V(k))_2$$
$$= (E_{\text{kin}})_2 - (E_{\text{kin}})_1 \quad \text{(gases)} \tag{121}$$

where A, k, 1–2 represent the minimum number of parameters required to specify a chemical shift, that is, the atom and level, and the two chemical sites or compounds involved. Here, we have neglected charging effects. For solids with Fermi-referenced binding energies, the corresponding equation is

$$\Delta E_b{}^F(A, k, 1\text{--}2) = (E_b{}^F(k))_1 - (E_b{}^F(k))_2$$
$$= (E_{\text{kin}})_2 - (E_{\text{kin}})_1 + (\phi_{\text{spect}})_2 - (\phi_{\text{spect}})_1 + (V_c)_2 - (V_c)_1 \tag{122}$$

where possible effects due to spectrometer work function changes or differences in charging potential have been included. Provided that both of the latter effects are negligible, Eq. (122) simplifies to a form identical to that of Eq. (121),

$$\Delta E_b{}^F(A, k, 1\text{--}2) = (E_b{}^F(k))_1 - (E_b{}^F(k))_2$$
$$= (E_{\text{kin}})_2 - (E_{\text{kin}})_1 \quad \text{(solids)} \tag{123}$$

As has been noted previously, many theoretical calculations of chemical shifts have an implicit vacuum reference level. This is quite satisfactory for gas-phase work, but not necessarily for work on solids. For the latter case, the relationship between vacuum-referenced and Fermi-referenced chemical shifts is, from Eq. (5):

$$\Delta E_b{}^V(A, k, 1\text{--}2) = \Delta E_b{}^F(A, k, 1\text{--}2) + (\phi_s)_1 - (\phi_s)_2 \tag{124}$$

Thus, in directly comparing vacuum-referenced theoretical calculations and Fermi-referenced experimental values, it is required to neglect the work function difference between the two solids, $(\phi_s)_1 - (\phi_s)_2$. In most work to date, no serious effects of work function differences have been observed, although there is generally more scatter on a plot of measured chemical shifts against calculated chemical shifts for solids than on a corresponding plot for gases.[3, 4, 7, 211] This additional scatter could be connected with reference level effects or specimen charging or both. Both of these effects deserve further study.

The theoretical interpretation of core-level chemical shifts has been attempted at various levels of sophistication, with each level providing a certain degree of agreement with experiment and interpretive utility. Several reviews of these procedures have been presented previously,[3, 4, 7, 8, 109] and therefore only a brief outline of the most important models, their uses, and their limitations will be given here. These procedures will be considered in approximate order of descending accuracy. From the outset, it is clear that the major goal of such analyses is to derive chemically-significant information concerning the initial state electronic structure of the system. Various final-state complexities (see Section V) can tend at times to obscure the initial-state chemical information, but it has nonetheless proven possible to derive it relatively straightforwardly for a number of systems.

The most accurate calculation of any binding energy shift must in general involve determining two binding energies, or a total of two initial-state calculations and two final hole-state calculations. The possible errors in shifts are thus approximately twice as large as for a single binding energy when calculations are performed at a given level. Various procedures for calculating binding energies have already been discussed in Sections III.A and III.B. Relative to a Koopmans' Theorem approach, corrections due to relaxation, relativistic, and correlation effects must be considered, as summarized in Eq. (55). A chemical shift in such binding energies between two chemically-inequivalent sites or compounds labelled 1 and 2 is thus

$$\Delta E_b{}^V(A, k, 1\text{--}2) = (E_b{}^V(k))_1 - (E_b{}^V(k))_2$$
$$= -(\epsilon_k)_1 + (\epsilon_k)_2 - (\delta E_{\text{relax}})_1 + (\delta E_{\text{relax}})_2$$
$$+ (\delta E_{\text{relat}})_1 - (\delta E_{\text{relat}})_2 + (\delta E_{\text{corr}})_1 - (\delta E_{\text{corr}})_2$$

or

$$\Delta E_b{}^V(A, k, 1\text{--}2) = -\Delta\epsilon_k - \Delta(\delta E_{\text{relax}}) + \Delta(\delta E_{\text{relat}}) + \Delta(\delta E_{\text{corr}}) \tag{125}$$

In view of the physical origins of the relativistic and correlation corrections for a given core level, they will tend to have values of approximately the same magnitude from one site or compound to another. The same should also be true, but probably to a lesser degree, for relaxation corrections. Thus,

in many cases, it would be expected that $\Delta(\delta E_{\text{relax}})$, $\Delta(\delta E_{\text{relat}})$, and $\Delta(\delta E_{\text{corr}})$ would be considerably smaller in magnitude than the individual corrections to either $(E_b^V(k))_1$ or $(E_b^V(k))_2$, and therefore that the Koopmans' Theorem value $-\Delta\epsilon_k$ would represent a quite good approximation to the chemical shift $\Delta E_b^V(A, k, 1\text{-}2)$.[105] (This need not always be true, however, and we discuss both below and in Section V.B a few special examples in which $\Delta(\delta E_{\text{relax}})$ is very large.) For similar reasons, the quality of the wave function utilized in obtaining ϵ_k is often not as critical as might be imagined. That is, approximate wave functions with the same degree of self-consistency for both systems 1 and 2 may yield a reasonably accurate value of $\Delta\epsilon_k$ (which is, after all, a small perturbation primarily due to changes in valence electron charge distribution). Thus, the use of Koopmans' Theorem in conjunction with various approximate calculation procedures such as minimal-basis-set- or double-zeta-basis-set Hartree–Fock calculations has met with success in analyzing much chemical shift data. It appears that molecular wave functions of double-zeta quality can be utilized to predict chemical shifts from $-\Delta\epsilon_k$ which agree with experiment to within $\sim \pm 1$ eV for a carefully-chosen set of molecules not too much different in size, in spite of the fact that the orbital energies for such levels as C1s and N1s tend to be as much as 10–20 eV higher than the experimental binding energies due to relaxation. In Fig. 18, experimental C1s binding energies for different gaseous molecules are compared to 1s orbital energies from various theoretical calculations of roughly double-zeta accuracy. Although the two scales are shifted relative to one another by about 15 eV, the points lie very close to a straight line of unit slope. Thus, for sets of molecules chosen to minimize $\Delta(\delta E_{\text{relax}})$, $\Delta(\delta E_{\text{relat}})$, and $\Delta(\delta E_{\text{corr}})$, chemical shifts should be calculable from these orbital energies with an accuracy roughly equal to the scatter of points about the straight line or ± 1 eV.[7, 8, 109]

Although the use of Koopmans' Theorem in estimating binding energy shifts from reasonably accurate molecular-orbital calculations can thus be expected to yield fairly reliable values for well-chosen compounds, it is especially important to be able to include the effects of relaxation in such calculations. Such effects are treated in more detail in Section V.B, but at this point it is appropriate to mention a calculation procedure that lies intermediate between those of Koopmans' Theorem and doing accurate SCF calculations on both initial and final states. This method was developed by Goscinski et al.[212, 213] and is termed the transition-state or transition-operator method. In this method, relaxation effects are allowed for to second order in perturbation theory by solving a set of Hartree–Fock equations in which the Fock operator on the left-hand side of Eq. (42) is adjusted so as to involve an effective 1/2 occupation number as far as electron–electron interactions involving the kth spin-orbital from which emission is to occur. For
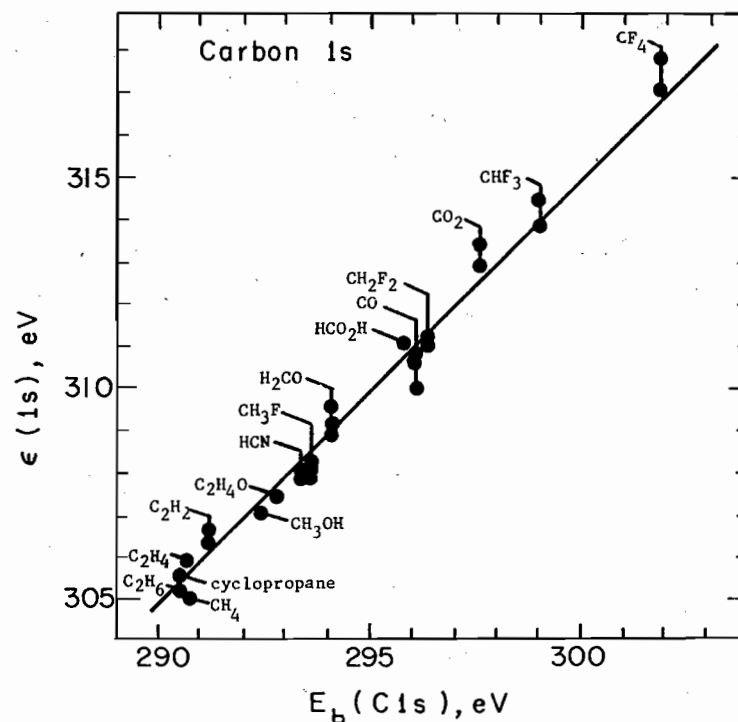
Fig. 18. Plot of carbon 1s binding energies calculated via Koopmans' Theorem against experimental binding energies for several carbon-containing gaseous molecules. For some molecules, more than one calculated value is presented. The slope of the straight line is unity. The two scales are shifted with respect to one another by 15 eV, largely due to relaxation effects. All of the theoretical calculations were of roughly double-zeta accuracy or better. (From Shirley, ref. 7.)

the fictitious "transition state" thus calculated for each initially-occupied spin-orbital, negatives of the one-electron energy eigenvalues yield estimates for binding energies that should include relaxation effects to second order. Comparisons of core- and valence-electron binding energy calculations for He, Li, Be, Ne, and Ar [212, 213] do indeed show that this method yields results in very good agreement with the more laborious procedure of calculating and subtracting accurate total energies for both the initial and final states.

The next approximation moving away from the Koopmans' Theorem method for calculating chemical shifts is the potential model that was used in the earliest quantitative discussions of chemical shifts by Siegbahn et al.[3] and Fadley et al.[105] In this model, the interaction of a given core electron with all other electrons and nuclei in a molecule or solid is divided into an intra-atomic term and an extra-atomic term. Furthermore, the assumption is made that each atom in the array has associated with it a net charge consistent with

overall electroneutrality. These net changes thus account in some way for the displacement of electronic charge which occurs in the formation of chemical bonds. In very covalent systems, this model is of questionable utility, but several variations of it have been applied to a wide variety of systems with considerable success.[3, 4, 105, 214–219] More recently, it has been termed a ground-state-potential model (GPM)[215] to emphasize its usual neglect of final-state effects (especially relaxation). Consider an atom A with a charge q_A situated in an array of atoms to which it is somehow bonded. The binding energy of the kth electron in this atom can then be expressed as a sum of two terms, one intra-atomic free-ion term and one extra-atomic potential:

$$\underset{\text{Compound}}{E_b{}^V(k)} = \underset{\substack{\text{Free ion of} \\ \text{charge } q_A}}{E_b{}^V(k, q_A)} + \underset{\substack{\text{Potential due} \\ \text{to all other atoms}}}{V} \qquad (126)$$

The first term is a binding energy for the kth electron in a free-ion of charge q_A and the second term is the total potential due to all other atoms in the array. The first term might be evaluated by means of a free-ion Hartree–Fock calculation, for example (although much simpler procedures for dealing with it will also be discussed). The simplest way to calculate the second term is to assume that the other atoms behave as classical point charges in creating the potential V. Thus,

$$V = e^2 \sum_{i \neq A} \frac{q_i}{r_{iA}} \qquad (127)$$

where the summation is over all atoms except that of interest in the array. If the array is a crystal, then V represents a convergent infinite sum that is closely related to the Madelung energy of the solid.[105] Thus, both terms in Eq. (126) may be relatively easy to obtain for a number of systems. Calculating a chemical shift using Eq. (126) gives

$$\Delta E_b{}^V(A, k, 1\text{–}2) = E_b{}^V(k, q_{A, 1}) - E_b{}^V(k, q_{A, 2}) + V_1 - V_2 \qquad (128)$$

where $q_{A, 1}$ and $q_{A, 2}$ are the net charges on atom A in the sites 1 and 2, respectively. It is instructive to consider the predictions of this model for several simple systems, as it is found to explain qualitatively and semi-quantitatively several basic features of chemical shifts.

The difference of free-ion terms in Eq. (128) represents a change in binding energy concomitant with a change in the valence electron orbital occupation of the atom such that the net charge is altered from $q_{A, 2}$ to $q_{A, 1}$. In the first analyses based upon the potential model, Fadley et al.[105] calculated such changes for removal of successive valence electrons from various ionic states of I, Br, Cl, F, and Eu, using a minimum-basis-set Hartree–Fock calculation

and Koopmans' Theorem. These results are presented in Figs 19–23, where the shifts are plotted against the location of the maximum magnitude of the radial function for each orbital. Several systematic features of these results can be noted. For iodine, all core levels shift by very nearly the same amount. This is basically true also for Br and Cl, although as the atomic size decreases there is less constancy in the core shifts, with outer orbitals showing slightly
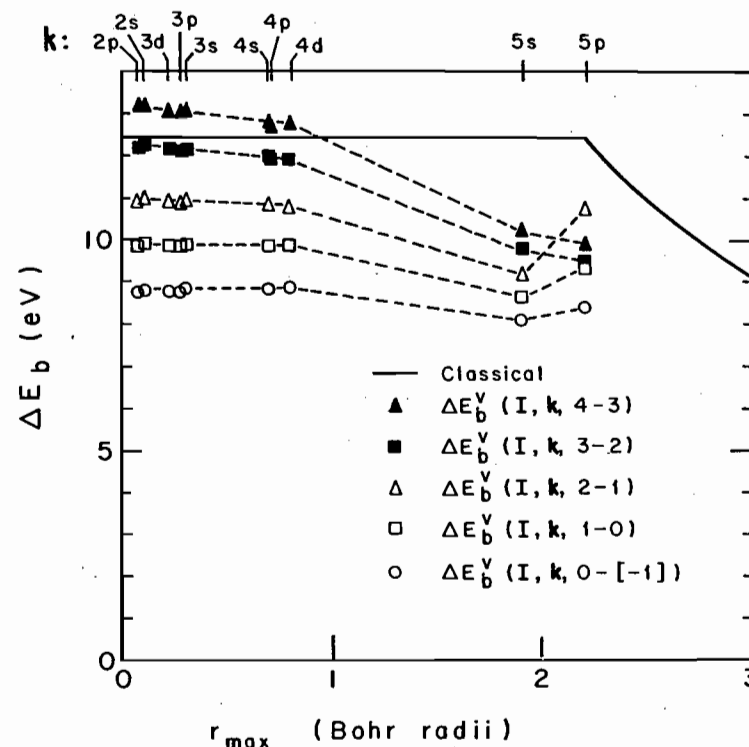

Fig. 19. Koopmans' Theorem free-ion binding energy shifts caused by the removal of a valence $5p$ electron from various configurations of iodine, plotted against the location of the radial maxima for the various orbitals. The configurations are: $+4 = 5s^2 5p$, $+3 = 5s^2 5p^2$, $+2 = 5s^2 5p^3$, $+1 = 5s^2 5p^4$, $0 = 5s^2 5p^5$, and $-1 = 5s^2 5p^6$. The solid curve shows the classical shift resulting from the removal of an electron from a thin spherical shell of charge with the radius of the $5p$ maximum. (From Fadley et al., ref. 105.)

lower shifts. In all of the halogens, the p valence electrons are largely external to the core, as is evidenced by the location of the core- and valence-orbital radial maxima. For Eu, which by contrast has valence $4f$ electrons overlapping considerably with the core electrons, the core shifts are not at all constant, and furthermore can be about twice as large per unit change in valence shell occupancy as for the halogens. All of these results are qualitatively consistent with a very simple classical model of the interaction between core
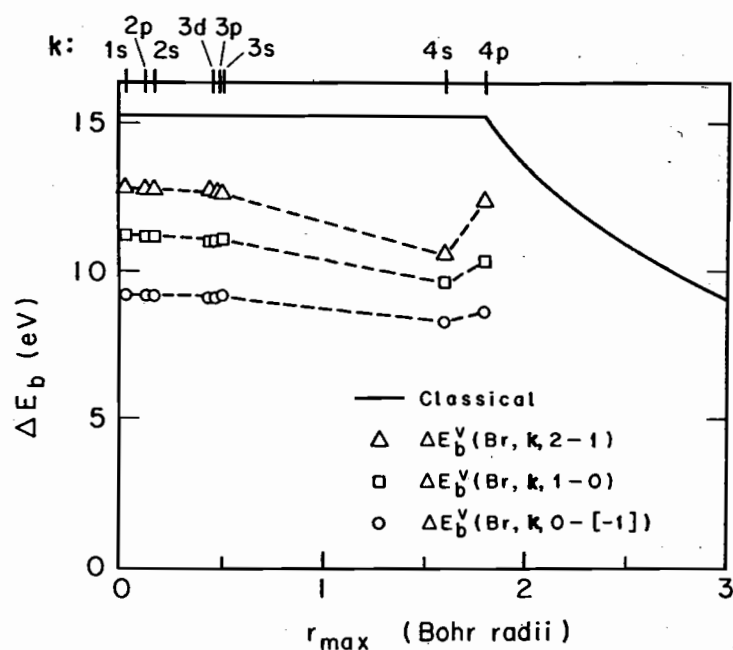
Fig. 20. Calculated free-ion binding energy shifts caused by the removal of a valence $4p$ electron from bromine, plotted as in Fig. 19. The configurations are: $+2 = 4s^2 4p^3$, $+1 = 4s^2 4p^4$, $0 = 4s^2 4p^5$, and $-1 = 4s^2 4p^6$. (From Fadley et al., ref. 105.)

and valence electrons. The valence electron charge distribution can be approximated by a spherical charged shell of radius r_v, where r_v can reasonably be taken to be the average radius of the valence orbitals or the location of their radial function maximum. The classical potential inside this spherical shell will be constant and equal to q/r_v, where q is the total charge in the valence shell. If the charge on this shell is changed by δq, the potentials, and thus binding energies, of all the core electrons located well inside the shell will shift by an amount $\delta E_b{}^V = \delta q / r_v$. Such classical calculations are shown as the solid lines in Figs 19–23 and are found to give results that correctly predict the trends in relative shifts from subshell to subshell, as well as being in semi-quantitative agreement with the absolute magnitudes of the more accurate Hartree–Fock calculations. In general then, all core electrons which overlap relatively little with the valence shell are predicted to shift by approximately the same amount, and this prediction is verified experimentally.[105] The magnitude of the shift per unit change in charge should also increase as the valence shell radius r_v decreases, as is illustrated for the case of Eu. A more accurate estimate of $\delta E_b{}^V / \delta q$ for any atom is given by the change in Hartree–Fock ϵ_k upon removal of one valence electron. From Eq. (47),

Fig. 21. Calculated free-ion binding energy shifts caused by the removal of a valence $3p$ electron from chlorine, plotted as in Fig. 19. The configurations are: $+2 = 3s^2 3p^3$, $+1 = 3s^2 3p^4$, $0 = 3s^2 3p^5$, and $-1 = 3s^2 3p^6$. (From Fadley et al., ref. 105.)

this will be given by $J_{k\text{–valence}} - K_{k\text{–valence}}$ (spins parallel) or $J_{k\text{–valence}}$ (spins anti-parallel). As the core-valence exchange integral $K_{k\text{–valence}}$ will be of significant magnitude only if there is appreciable overlap between the core and valence orbitals, we can neglect $K_{k\text{–valence}}$ in comparison to $J_{k\text{–valence}}$. (For example, in carbon, $J_{1s,\,2s} = 22 \cdot 1$ eV, $K_{1s,\,2s} = 1 \cdot 4$ eV, $J_{1s,\,2p} = 20 \cdot 8$ eV, and $K_{1s,\,2p} = 0 \cdot 6$ eV.) Thus, $\delta E_b{}^V / \delta q$ should be approximately equal to $J_{k\text{–valence}}$, the core-valence Coulomb integral. The magnitude of such Coulomb integrals are, in fact, found to be in good agreement with the shifts calculated in Figs 19–21 for I, Br, and Cl. As a final point, the free ion term $\delta E_b{}^V / \delta q$ is of the order of 10–20 eV/electron charge for essentially all elements.

If the potential term V in Eq. (126) is now considered, it is found that its value also will be of the order of 10–20 eV for a transfer of unit electron charge from one atom to its nearest neighbors,[3, 105] as, for example, in a highly ionic alkali halide crystal. Furthermore, for a given molecule or solid the free-ion term $(\delta E_b{}^V / \delta q) \cdot \delta q$ will be opposite in sign to V, as V must account for the fact that charge is not displaced to infinity, but only to adjacent atoms during chemical bond formation. Thus, both the free-ion and potential terms
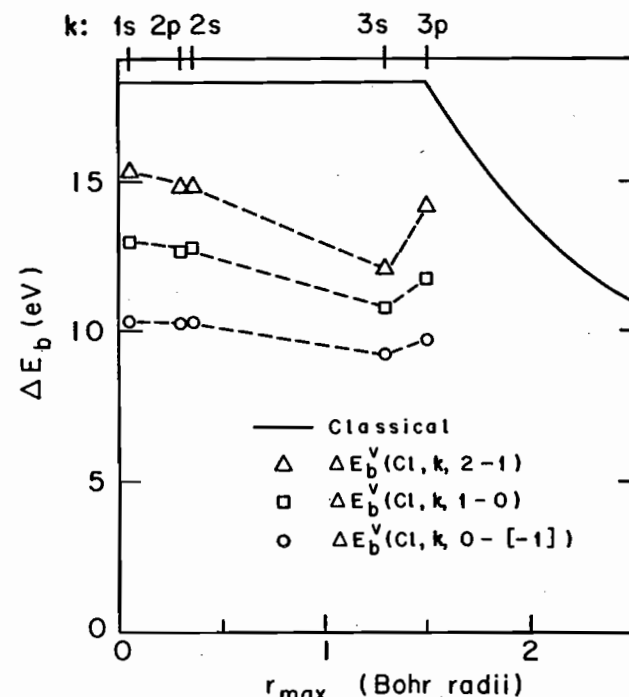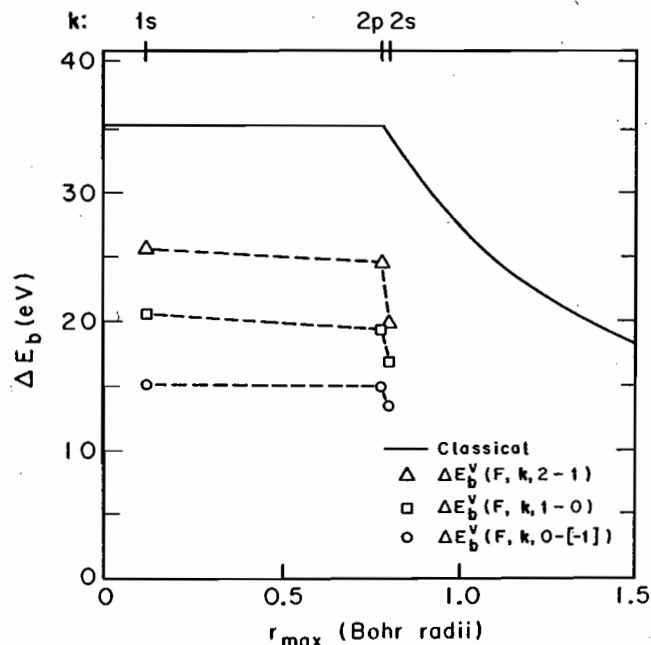
Fig. 22. Calculated free-ion binding energy shifts caused by the removal of a valence $2p$ electron from fluorine, plotted as in Fig. 19. The configurations are: $+2=2s^2 2p^3$, $+1=2s^2 2p^4$, $0=2s^2 2p^5$, and $-1=2s^2 2p^6$. (From Fadley et al., ref. 105.)

in Eq. (126) must be calculated with similar accuracy if the resultant binding energy (or chemical shift) value is to have corresponding accuracy. This represents one of the possible drawbacks of such potential models.

Several other models based essentially on Eq. (126) have been utilized in analyzing core electron chemical shifts,[7, 8] and the detailed theoretical justifications for them have been discussed by Manne,[216] Basch,[217] and Schwartz.[218] For example, Siegbahn et al.[4] and Gelius et al.[211] have been able to describe the core binding energy shifts for a variety of compounds of C, N, O, F, and S with the following equation:

$$\Delta E_b{}^V(A, k, 1\text{-}2) = C_A q_A + V + l \qquad (129)$$

where 2 represents a fixed reference compound. The various atomic charges q_t in each molecule were estimated using CNDO molecular-orbital theory, and these charges were then substituted into Eq. (127) to compute V. Then the constants C_A and l were determined empirically by a least-squares fit to the experimental data. Such fits give a reasonably consistent description of the data, as is shown in Fig. 24 for various compounds of carbon, and, in particular, the parameters C_A are found to be rather close to the $1s$-valence
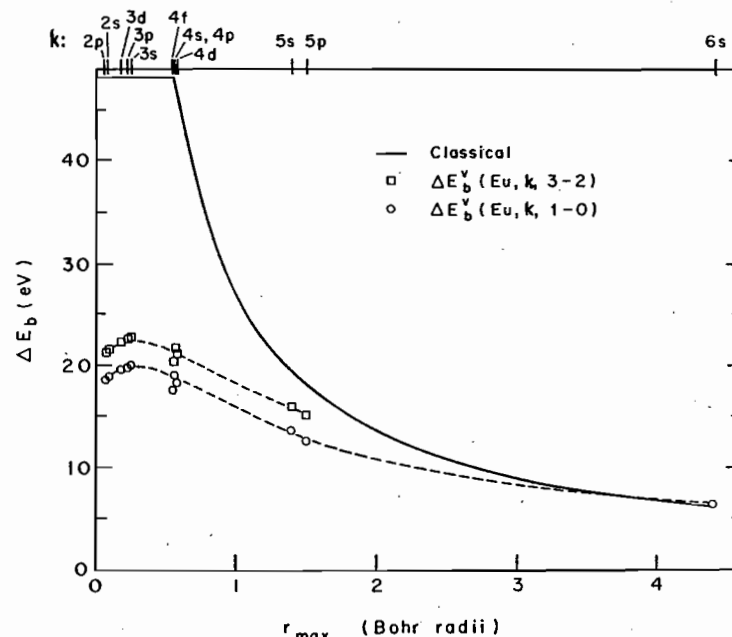
Fig. 23. Calculated free-ion binding energy shifts caused by the removal of a valence $4f$ electron from europium, plotted as in Fig. 19. The configurations are: $+3=4f^6$, $+2=4f^7$, $+1=4f^6 6s^2$, and $0=4f^7 6s^2$. Note the non-constancy of the core-level shifts by comparison to Figs 19-22. (From Fadley et al., ref. 105.)

Coulomb integral $J_{1s\text{-valence}}$ computed for atom A. Thus, Eq. (129) as utilized in this semi-empirical way is consistent with a somewhat more exact theoretical model. Note, however, that all molecules are not adequately described by this model and that, for example, the points for CO and CS_2 lie far from the straight line predicted by Eq. (129). As might be expected, if an orbital energy difference based on near Hartree–Fock wave functions is used for the calculated shift of CO, much better agreement with experiment is obtained, as is shown in Fig. 18.

In another variant of the potential model proposed by Davis et al.,[219] a series of chemical shift measurements on core levels in all the atoms of several related molecules are used to derive a self-consistent set of atomic charges. For each atom in each molecule, the measured chemical shift is written in terms of undetermined atomic charges as

$$E_b{}^V(A, k, 1\text{-}2) = C_A' q_A + e^2 \sum_{i \neq A} \frac{q_t}{r_{At}} \qquad (130)$$

where C_A' is set equal to $J_{1s\text{-valence}}$ for atom A. The resultant set of equations is solved self-consistently for the q_A values on each atom. Such calculations
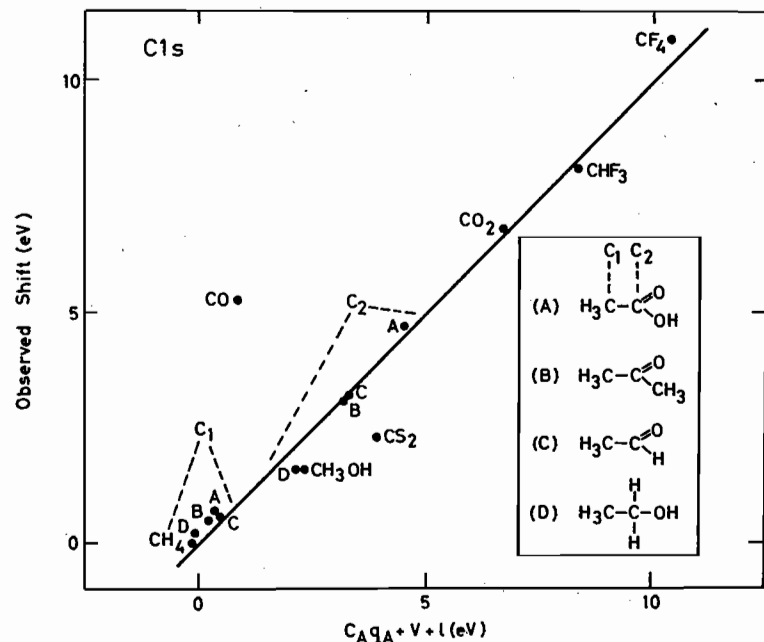
Fig. 24. A comparison of the experimental carbon 1s chemical shift values for several molecules with shifts calculated using the potential model of Eq. (129). The shifts were measured relative to CH_4. The parameters of the straight line were $C_A = 21 \cdot 9$ eV/unit charge and $l = 0 \cdot 80$ eV. (From Siegbahn *et al.*, ref. 4.)

on a series of fluorinated benzenes[219] give charges which agree rather well with charges obtained from calculations based upon the CNDO/2 method, as is apparent in Fig. 25.

Another procedure for analyzing chemical shift data that can be at least indirectly related to the various potential models is based on summing empirically determined shifts associated with each of the groups bonded to the atom of interest, and has been developed primarily by Gelius, Hedman, and co-workers.[211, 220] Each group shift is assumed to be constant and independent of the other groups present and is determined from a series of chemical shift measurements on reference compounds representing suitable combinations of the groups. The chemical shift associated with atom A in a given compound is thus written as

$$\Delta E_b(A, k, 1\text{-}2) = \sum_{groups} \Delta E_b(group) \qquad (131)$$

where 2 constitutes some reference compound against which all of the group shifts are determined. The applicability of this procedure has been demonstrated on a large number of carbon- and phosphorous-containing compounds,[211, 220] and a summary of results obtained for phosphorus compounds
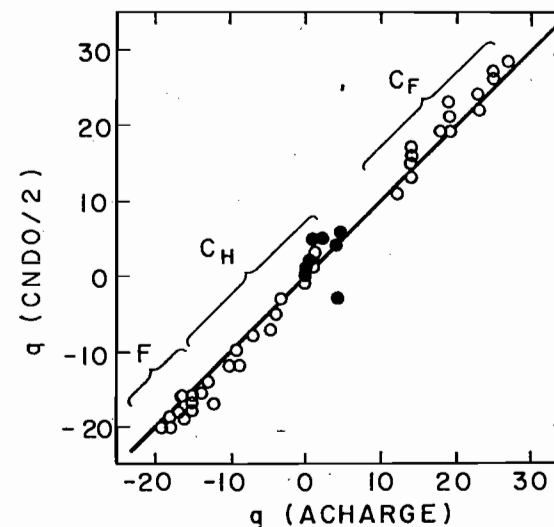
Fig. 25. Atomic charges for the various fluorinated benzenes as calculated by the CNDO/2 method and as derived experimentally ("ACHARGE") from chemical shift measurements on carbon and fluorine and Eq. (130). Charges are in units of 1/100 of an electronic charge. The filled circles represent average hydrogen charges. (From Davis *et al.*, ref. 219.)

is shown in Fig. 26. The relationship of this procedure to a potential model is possible if it is assumed that each group induces a valence electron charge change of δq(group) on the central atom and also possesses essentially the same intragroup atomic charge distribution regardless of the other groups present. Then both the free-ion and potential terms in Eq. (126) become simply additive for different groups, as is required in Eq. (131). In addition, however, the group shift can be considered to include empirically an approximately constant intragroup relaxation correction, thus going somewhat beyond a ground-state potential model in one sense.

Some of the first analyses of shift data were performed simply by plotting ΔE_b against atomic charges which were estimated by various procedures, among them CNDO or extended-Hückel calculations, or most crudely by electronegativity arguments. The implicit neglect of the potential terms of Eqs (126) and (128) in such a correlation of ΔE_b against q_A can, however, lead to a rather wide scatter of the points about a straight line or curve drawn through them. Hendrickson *et al.*,[221] for example, found two rather distinct clusters of data points described by two different curves in comparing nitrogen 1s shifts with charges calculated via CNDO. However, there *is* in general a systematic increase in E_b with increasing q_A for most compounds, particularly if the compounds are chosen to be rather similar in bonding type. One such series of compounds for which a simple electronegativity correlation has proven adequate is the halomethanes. Thomas[222] expressed the C1s
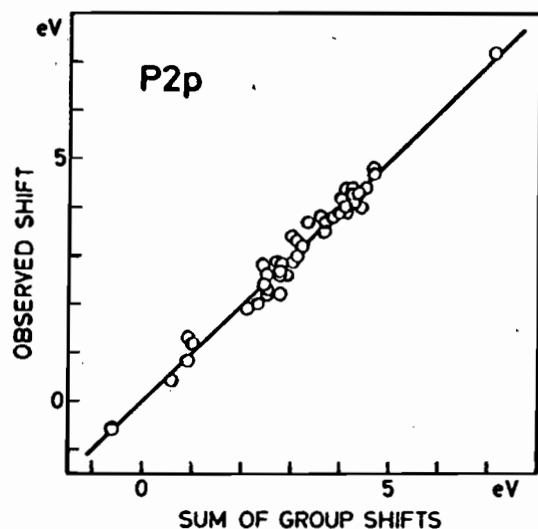
Fig. 26. A comparison of measured phosphorous $2p$ chemical shifts with shifts calculated using the group shift model of Eq. (131). The compounds were studied as solids. (From Hedman *et al.*, ref. 220.)

shifts between CH_4 and a given halomethane as a linear combination of the electronegativity differences between the various ligands present and hydrogen:

$$\Delta E_b{}^V(C1s, \text{halomethane–}CH_4) = C \sum_l (X_l - X_H) \qquad (132)$$

where C is an empirical constant, X_l is the ligand electronegativity, and X_H is the electronegativity of hydrogen. Such a correlation is shown in Fig. 27. The explanation for the success of this correlation would seem to be as a further simplification of the group shift approach, in which each monatomic ligand induces a charge transfer δq_l proportional to $X_l - X_H$, and the potential term involved is also simply proportional to δq_l for a nearly constant carbon–ligand bond length. Thus, the potential model of Eq. (128) can be reduced to the form of Eq. (132). Such correlations should be used very cautiously, however, as exceptions are relatively easy to encounter: for example, in the series of molecules generated by adding successive methyl groups to ammonia (NH_3, $NH_2(CH_3)$, $NH(CH_3)_2$, and $N(CH_3)_3$), the N1s binding energy is observed to *decrease* with the addition of CH_3 groups,[223] in complete disagreement with the greater positive charge expected on the central nitrogen because $X_C > X_H$. The major cause of this discrepancy is believed to be the greater relaxation energy associated with the polarization of the $-CH_3$ group around the N1s hole,[223] a type of effect discussed in more detail in Section V.B.
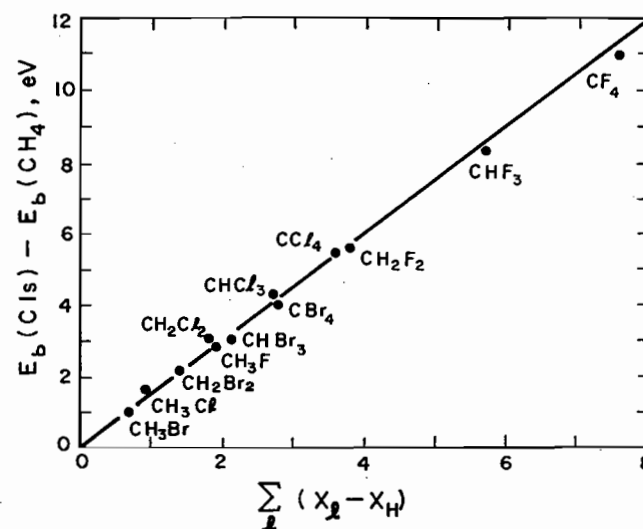
Fig. 27. Carbon $1s$ chemical shifts for halogenated methanes measured relative to CH_4 and plotted against shifts calculated on the basis of a sum of ligand-hydrogen electronegativity differences, as in Eq. (132). (From Thomas, ref. 222.)

Among the other methods utilized to analyze chemical shift data, mention should also be made of a procedure introduced by Jolly and Hendrickson[224, 225] for relating chemical shifts to thermochemical data. In this method, it is noted that to a good approximation the atomic core of an atom with nuclear charge Z and a single core-level hole acts on any surrounding electrons in an equivalent way to the filled core of an atom with nuclear charge $Z+1$. If the core electron overlap with the outer electrons is small, then the nuclear shielding should be nearly complete and this assumption is reasonable. As a more quantitative indicator of how good this approximation is for a medium-Z atom, Table I summarizes the results of highly-accurate numerical Hartree–Fock calculations by Mehta, Fadley, and Bagus[102] for atomic Kr with various core-level holes and its equivalent-core analogue Rb^{+1}. With neutral Kr as a reference, the fractional decreases in average subshell radii $1 - \langle r_{nl} \rangle / \langle r_{nl} \rangle_0$ are tabulated for different core-hole locations in Kr^{+1} and for the equivalent-core species Rb^{+1}. For the equivalent-core approach to be fully valid, these fractional changes should be nearly identical between true Kr hole states and Rb^{+1}, thus indicating the same degree of inward relaxation around both a core hole and a nuclear charge that is incremented from Z to $Z+1$. For the various true hole states in subshells that can be designated $n_{hole}l_{hole}$, the fractional decreases in $\langle r_{nl} \rangle$ range from ~ 0 for subshells with $n \lesssim n_{hole}$ up to 11% for the outermost $4p$ orbital. The equivalent-core Rb^{+1} orbitals by contrast show significant relaxation in all

TABLE I

Average radii for the various subshells of neutral Kr $\langle r_{nl}\rangle_0$, together with the fractional changes in average radii between neutral Kr and all possible core-hole states. The changes between neutral Kr and the equivalent-core ion Rb^+ are also given. The units for $\langle r_{nl}\rangle_0$ are bohrs. The Kr^+ values are divided into those for $n \leqslant n_{hole}$ and $n > n_{hole}$ (from Mehta et al., ref. 102)
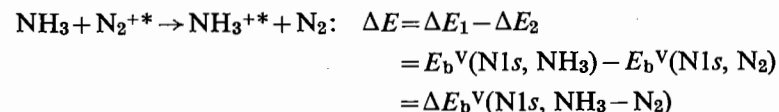
Atom	L,S term	$\langle r_{1s}\rangle_0 =$ 0.0424 $1-\frac{\langle r_{1s}\rangle}{\langle r_{1s}\rangle_0}$	$\langle r_{2s}\rangle_0 =$ 0.1873 $1-\frac{\langle r_{2s}\rangle}{\langle r_{2s}\rangle_0}$	$\langle r_{2p}\rangle_0 =$ 0.1619 $1-\frac{\langle r_{2p}\rangle}{\langle r_{2p}\rangle_0}$	$\langle r_{3s}\rangle_0 =$ 0.5378 $1-\frac{\langle r_{3s}\rangle}{\langle r_{3s}\rangle_0}$	$\langle r_{3p}\rangle_0 =$ 0.5426 $1-\frac{\langle r_{3p}\rangle}{\langle r_{3p}\rangle_0}$	$\langle r_{3d}\rangle_0 =$ 0.5509 $1-\frac{\langle r_{3d}\rangle}{\langle r_{3d}\rangle_0}$	$\langle r_{4s}\rangle_0 =$ 1.6294 $1-\frac{\langle r_{4s}\rangle}{\langle r_{4s}\rangle_0}$	$\langle r_{4p}\rangle_0 =$ 1.9516 $1-\frac{\langle r_{4p}\rangle}{\langle r_{4p}\rangle_0}$
$Kr^+(-1s)$	^2S	0.0049	0.0185	0.0267	0.0273	0.0381	0.0558	0.0722	0.1142
$Kr^+(-2s)$	^2S	0.0000	0.0010	0.0087	0.0194	0.0268	0.0534	0.0662	0.1078
$Kr^+(-2p)$	^2P	0.0008	0.0074	0.0026	0.0209	0.0304	0.0542	0.0683	0.1083
$Kr^+(-3s)$	^2S	0.0000	-0.0009	0.0004	0.0016	0.0105	0.0251	0.0606	0.1007
$Kr^+(-3p)$	^2P	0.0001	0.0006	-0.0006	0.0077	0.0028	0.0248	0.0617	0.1019
$Kr^+(-3d)$	^2D	0.0000	0.0003	0.0003	0.0089	0.0119	0.0272	0.0618	0.1003
Rb^+	^1S	0.0275	0.0294	0.0306	0.0366	0.0403	0.0537	0.0799	0.1150

subshells, with a range between 3% for $1s$ and 11% for $4p$. Relaxation for subshells with $n \ll n_{hole}$ is thus much overestimated by the use of an equivalent core, whereas for $n > n_{hole}$, the overestimates range from only ~ 0–1% in absolute fractional radius change. Thus, the equivalent-core model is a reasonable and useful first approximation, although it is certainly expected to overestimate relaxation effects due to core-hole formation.
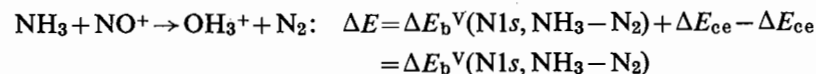
In applying the equivalent-core model to chemical-shift analyses, it is assumed[224, 225] that an exchange of cores can be made in the final-state ion without appreciably altering the valence electron charge distribution *or* equilibrium nuclear geometry. (The results in Table I for the $4s$ and $4p$ subshells suggest that this is a good approximation.) Thus, in considering core-level emission from a species containing nitrogen, an $O^{+6}\ 1s^2$ core can be exchanged for the $N^{+6}\ 1s = N^{+6*}$ core, where the asterisk denotes the presence of the $1s$ core hole. Such core exchanges can be utilized to write binding energy shifts in terms of thermodynamic heats of reaction, and hence to predict either shifts from thermodynamic data or thermodynamic data from shifts. As one example of the application of this procedure, let us consider $1s$ photoelectron emission from gaseous NH_3 and N_2 as chemical reactions in which the electron is assumed to be formed exactly at the vacuum level and therefore with no kinetic energy:

$$NH_3 \to NH_3^{+*} + e^-: \quad \Delta E_1 = E_b^V(N1s, NH_3)$$
$$N_2 \to N_2^{+*} + e^-: \quad \Delta E_2 = E_b^V(N1s, N_2)$$
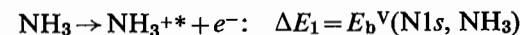
These reactions are endothermic with internal energy changes ΔE_1 and ΔE_2 given by the $1s$ binding energies in NH_3 and N_2. Subtracting the second reaction from the first gives

$$NH_3 + N_2^{+*} \to NH_3^{+*} + N_2: \quad \Delta E = \Delta E_1 - \Delta E_2$$
$$= E_b^V(N1s, NH_3) - E_b^V(N1s, N_2)$$
$$= \Delta E_b^V(N1s, NH_3 - N_2)$$

with an internal energy change precisely equal to the $N1s$ chemical shift between NH_3 and N_2. However, this reaction involves the unusual and very short-lived species N_2^{+*} and NH_3^{+*}. Now, it is assumed that the N^{6+*} core can be replaced by the O^{6+} core in either N_2^{+*} or NH_3^{+*} with only a small gain or loss of energy that can be termed the core-exchange energy ΔE_{ce}. As long as the core-exchange energy is very nearly the same in both N_2^{+*} and NH_3^{+*}, then the overall energy change associated with the reaction is not affected by core exchange. That is, we have a final reaction of

$$NH_3 + NO^+ \to OH_3^+ + N_2: \quad \Delta E = \Delta E_b^V(N1s, NH_3 - N_2) + \Delta E_{ce} - \Delta E_{ce}$$
$$= \Delta E_b^V(N1s, NH_3 - N_2)$$

Therefore, the chemical shift is equal to a thermodynamic heat of reaction involving well-known species. This procedure has been applied to an analysis of 1s shifts in compounds of N, C, O, B, and Xe, and very good agreement is obtained between experimental ΔE_b values and thermochemical estimates of these shifts. Such a comparison for nitrogen 1s is shown in Fig. 28. This analysis is closely related to the isodesmic processes discussed by Clark,[9] and is also reviewed in more detail by Jolly[13] in this series.

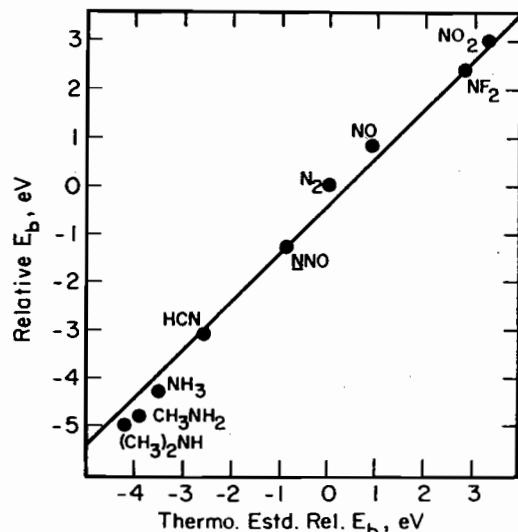Fig. 28. Plot of experimental N1s binding energy shifts relative to N_2 for several molecules versus values calculated using equivalent-core exchange and thermodynamic data. The slope of the line is unity. (From Jolly, ref. 225.)

Finally, a few other methods in which core electron binding energy shifts can be used should be mentioned:

(1) Attempts have been made to derive bonding information from relative binding energy shifts of different levels in the same atom. From Figs 19–23, it is clear that the outer core and valence levels of a given atom need not shift by the same amount as inner core levels, especially if relatively penetrating valence levels are present as in Eu. Such *relative* shifts of different levels can for certain cases be simply related to the basic Coulomb and exchange integrals involved, and then utilized to determine properties of the valence electron charge distribution. In particular, the relative shifts of the inner core $3d_{\frac{5}{2}}$ and valence $5p_{\frac{3}{2}}$ levels have been measured for iodine in various alkyl iodides and HI, and these shifts have been found by Hashmall *et al.*[226] to be consistent with a simple bonding model of the compounds involved. More

recently, Aono *et al.*[227] have carried out a similar relative shift study of rare-earth compounds that quantitatively confirms the non-constancy of the intra-atomic free-ion shifts as predicted, for example, for Eu in Fig. 23.

(2) In another type of analysis, core-level chemical shifts for several homologous series of the form RXH with X=O, N, P, and R=various substituent groups have also been found to be approximately equal to relative proton affinities.[228] Martin *et al.*[228] have explained this correlation by noting that the removal of a core electron from atom X to form a positive hole involves very nearly the same set of R-group relaxation energies (and to a less important degree also potential energies) as the addition of a proton. Thus, changes in X-atom core binding energy with R are expected to be approximately equal to changes in proton affinity with R, even though the absolute magnitudes of the two quantities are very different; this has been found to be true for a rather large number of small molecules.[228]

(3) It has also been proposed by Wagner[229] that the difference in kinetic energy between a core photoelectron peak and an Auger electron peak originating totally via core-level transitions in the same atom can be used as a sensitive indicator of chemical state that is free of any uncertainty as to binding energy reference or variable specimen surface charging. This difference, which has been termed the "Auger parameter",[229] changes with alterations in chemical environment because Auger energies are influenced much more strongly than photoelectron energies by final-state relaxation.[230, 231] In fact, Auger energy chemical shifts are roughly 3–4 times as large as corresponding core binding energy shifts.[229] Although a precise theoretical calculation of such extra-atomic relaxation effects may be difficult (see, for example, Section V.B), the Auger parameter appears to have considerable potential as a fingerprint for different chemical states.

(4) Finally, attempts have been made to correlate core binding energy shifts with the results of nuclear spectroscopic measurements such as NMR[232, 233] and Mössbauer spectroscopy,[234] as reviewed elsewhere by Carlson.[10] NMR diamagnetic shielding factors have been compared with core shifts, but the difficulty of separating out diamagnetic and paramagnetic contributions to shielding have prevented extensive application of this type of analysis. Also, binding energy shifts for a closely related set of tin compounds correlate reasonably well with Mössbauer chemical shift values,[234] but no detailed theoretical justification for this correlation has been presented.

It is clear that the theoretical interpretation of core electron binding energies or chemical shifts in these energies can be attempted in several ways at varying levels of sophistication. When binding energies are calculated by the most rigorous total-energy-difference method, including perhaps corrections for relativistic effects and electron–electron correlation, values in very good agreement with experiment have been obtained for several atoms and

small molecules. This agreement verifies that all of the basic physical effects involved have been recognized and can be accounted for quantitatively. If binding energies are calculated from orbital energies via Koopmans' Theorem, errors primarily due to neglect of final state relaxation are incurred. Such errors can be from 1 % to 10 % of the total binding energy and can be estimated in several ways. In calculating chemical shifts of binding energies between two different sites or compounds by means of Koopmans' Theorem, however, a fortuitous cancellation of a large fraction of the relativistic, correlation, and relaxation corrections occurs. Thus, orbital energies can be used with reasonable success in predicting shifts, although anomalously large final-state relaxation around a localized hole represents an ever-present source of error in such analyses (see also Section V.B). The interaction of a core electron with its environment can be simplified even further, giving rise to several so-called potential models with varying degrees of quantum-mechanical and/or empirical input. All of these models can be useful in interpreting shifts, although it may be necessary to restrict attention to a systematic set of compounds for the most approximate of them. The direct connection of chemical shifts with thermochemical heats of reaction via the equivalent-core approximation is also possible. Finally, it is worthwhile to note that one of the primary reasons that chemical shifts can be analyzed by such a wide variety of methods is that their origin is so simply and directly connected to the molecular charge distribution. In turn, it is very often this charge distribution that is of primary interest in a given chemical or physical investigation.

V. FINAL-STATE EFFECTS

A. Introduction

In this section, several effects arising because of complexities in the final state of the photoemission process will be considered. Considerable use will be made of the theoretical developments of Sections III.A–D, from which it is already clear that unambiguously distinguishing various final-state effects in the electronic wave function may not always be possible, primarily due to many-electron effects that might, for example, be described by a configuration-interaction approach. Thus, the first four topics to be dealt with here (relaxation phenomena, multiplet splittings, shake-up and shake-off effects, and other many-electron effects) are all very much interrelated, as will become evident from subsequent discussion. However, for both historical and heuristic reasons, it is reasonable to consider them separately, using several examples for which distinctions can be made relatively easily. (Such final-state electronic effects have also been reviewed by Martin and Shirley[13] in more detail in this series.) The last subject to be treated here involves the influence

of exciting various final vibrational states, for which theoretical background has already been presented in Sections III.A and III.D.

B. Relaxation Effects

The importance of relaxation corrections in accurately predicting binding energies has been emphasized in several prior discussions in this chapter. As a further example of how large such effects can be, it has been suggested by Ley et al.[235] that relaxation is the primary reason why free-atom vacuum-referenced core binding energies are higher by ~ 5–15 eV than corresponding vacuum-referenced binding energies in the pure elemental solid. Also, inert gas atoms implanted in noble metal lattices have been shown by Citrin and Hamann[236] to exhibit core binding energies 2–4 eV lower than in the free-atom state, again primarily due to relaxation. In a systematic study of the $C1s$ binding energy in a set of linear alkanes C_nH_{2n+2} ($n = 1, 2, ..., 13$), Pireaux et al.[237] noted a monotonically increasing $C1s$ chemical shift $\Delta E_b(C1s, CH_4 - C_nH_{2n+2})$ with n, and a small overall shift of $0 \cdot 6$ eV between CH_4 and $C_{13}H_{28}$ with sign such that $C_{13}H_{28}$ has the lowest binding energy. Transition-operator calculations for these alkane molecules indicate that the relaxation energy increases by almost $2 \cdot 0$ eV in going from the smallest CH_4 to $C_{13}H_{28}$; thus, relaxation is a major contributing factor in producing these small chemical shifts, although it must act in conjunction with certain other effects with opposite sign to reduce the overall shift to $0 \cdot 6$ eV. Relaxation shifts of ~ 1–3 eV are also noted in UPS spectra of the valence levels of molecules chemisorbed on surfaces,[238] with the binding energies of molecular orbitals not directly involved in bonding to the surface being lower than in the free molecule, presumably due to extra relaxation in the substrate. In general for these systems, then, it is found that the more near-neighbor atoms there are surrounding a given final-state hole, the more relaxation can occur and the lower is the observed binding energy.

The relaxation energy δE_{relax} can be unambiguously defined as the difference between a Koopmans' Theorem binding energy $-\epsilon_k$ and a binding energy calculated by means of a difference of self-consistent Hartree–Fock total energies for both the initial and final states. Various methods have been utilized for estimating this energy in atoms, molecules, and solids,[119-121, 235, 239-242] but principal emphasis here will be on a relatively straightforward, yet easily visualized, procedure first used extensively by Shirley and co-workers.[121, 235, 239]

In this procedure,[121, 235, 239] the relaxation energy for a given core-level emission process is divided into two parts: an intra-atomic term (the only term present in the free-atom case) and an extra-atomic term that is important in molecules or solids. The extra-atomic term thus includes all relaxation

involving electrons primarily situated *in the initial state* on other atomic centers. Thus,

$$\delta E_{relax} = \delta E_{relax}^{intra} + \delta E_{relax}^{extra} \qquad (133)$$

(This division of the relaxation correction was, in fact, made in the first discussion of the potential model for analyzing chemical shifts.[105]) The calculation of these two terms makes use of a general result derived by Hedin and Johansson,[120] which states that, for emission from an initial orbital ϕ_k in an atom of atomic number Z, the relaxation energy is given to a good approximation by

$$\delta E_{relax} = \tfrac{1}{2} \langle \phi_k | \hat{V}(N-1, Z) - \hat{V}(N, Z) | \phi_k \rangle \qquad (134)$$

in which $\hat{V}(N-1, Z)$ is the total electronic Hartree–Fock potential operator acting on the kth orbital in the $(N-1)$-electron final state and $\hat{V}(N, Z)$ is the analogous total Hartree–Fock potential operator for the N-electron initial state. (For a neutral atom, of course $N=Z$.) The expectation value in Eq. (134) thus involves sums over Coulomb and exchange integrals between ϕ_k and $(N-1)$ other spin-orbitals $\phi_j \neq \phi_k$. Two sets of orbitals ϕ_j are also needed, an initial-state set $\{\phi_j\}$ in $\hat{V}(N, Z)$ and a relaxed set $\{\phi_j'\}$ in $\hat{V}(N-1, Z)$. The determination of the relaxed orbitals is now further simplified by using the equivalent-core approximation, such that the integrals involving $\hat{V}(N-1, Z)$ are replaced by integrals for $\hat{V}(N+1, Z+1)$, the neutral atom with next higher atomic number; correspondingly, ϕ_k is taken to be an orbital in atom $Z+1$ in evaluating these integrals. This procedure is reasonable because the orbitals at larger mean radii than ϕ_k produce most of the relaxation and such orbitals in neutral atom $Z+1$ are very little different from those in atom Z with a hole in the k subshell (cf. Table I). Furthermore, even though inner-orbital relaxation occurs (including relaxation of ϕ_k), this inner-orbital relaxation is smaller (again see Table I), and thus the Coulomb and exchange integrals between inner and outer orbitals change little in atom $Z+1$ relative to the true hole state in atom Z.[121] Thus, the overall relaxation energy becomes finally

$$\delta E_{relax} = \tfrac{1}{2} (\langle \phi_k | \hat{V} | \phi_k \rangle_{Z+1} - \langle \phi_k | \hat{V} | \phi_k \rangle_Z) \qquad (135)$$

with all relevant Coulomb and exchange integrals available from existing tabulated data for atoms.[100] Applying this calculation procedure to core emission from noble-gas atoms, Shirley[121] obtained very good estimates for relaxation energies as compared to direct total-energy-difference calculations.

The same procedure has also been applied to metals by Ley *et al.*,[235] for which the separation of Eq. (135) into intra-atomic and extra-atomic terms yields formally

$$\delta E_{relax} = \tfrac{1}{2} (\langle \phi_k | \hat{V} | \phi_k \rangle_{Z+1} - \langle \phi_k | \hat{V} | \phi_k \rangle_Z)^{intra}$$
$$+ \tfrac{1}{2} (\langle \phi_k | \hat{V} | \phi_k \rangle_{Z+1} - \langle \phi_k | \hat{V} | \phi_k \rangle_Z)^{extra} \qquad (136)$$

The intra-atomic term in Eq. (136) is calculable as described previously. If a free atom A is placed into a pure solid lattice of the same species and it is further assumed that placement in the lattice has a small influence on the initial-state Hartree–Fock energy eigenvalues ϵ_k (corresponding to an extra-atomic potential effect of approximately zero), then the difference between free-atom and solid binding energies is given simply by the extra-atomic relaxation term for the solid:

$$E_b{}^V(A, k, \text{atom}) - E_b{}^V(A, k, \text{solid})$$
$$= \tfrac{1}{2} (\langle \phi_k | \hat{V} | \phi_k \rangle_{Z+1} - \langle \phi_k | \hat{V} | \phi_k \rangle_Z)^{extra} \qquad (137)$$

These extra-atomic terms have been derived[235] for a metal by assuming that the conduction electrons polarize to such an extent that a screening charge of approximately unit magnitude occupies an atomic-like orbital centered on the atom containing the core hole. As a reasonable choice for this orbital, that possessing the dominant character of the lowest unoccupied valence band in the solid is used, again together with an equivalent-cores approximation. Although this procedure overestimates screening because the orbital chosen is too localized, it does give approximately correct magnitudes for atom-solid shifts such as those in Eq. (137), as is illustrated in Fig. 29 for the $3d$ transition-metal series. Note the break in values at $Z=29$ (Cu) when the screening orbital changes from $3d$ to the more diffuse $4s$ because of filling of

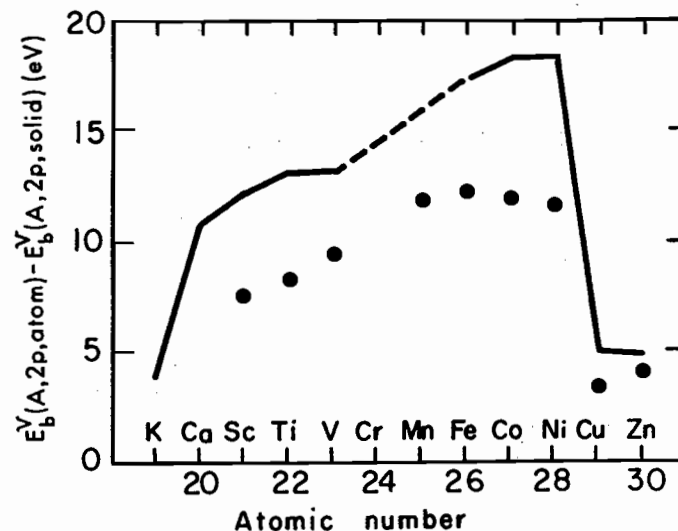Fig. 29. Differences between vacuum-referenced free-atom $2p$ core binding energies and analogous binding energies in the corresponding elemental metal. The points represent experimental values and the line calculations based upon Eq. (137), which assumes that extra-atomic relaxation is the main cause of such differences. The break at $Z=29$ is caused by the filling of the $3d$ valence bands. (From Ley *et al.*, ref. 215 and 235).

the $3d$ bands. Alternate calculation procedures of a somewhat more rigorous nature have also been proposed to explain such atom-solid shifts[236, 240-242], including especially discussions of possible initial-state shifts in the solid. However, the scheme presented here clearly yields a semi-quantitative approximation for one of the most important factors, extra-atomic relaxation, as well as being very easy to apply to various systems.

As noted previously (Section III.B), it has also been pointed out by Ley et al.[115] that a localized-hole description can be used to estimate relaxation energies associated with *valence-level* excitations in free-electron metals. Such relaxation energies are calculated by assuming that in the final state a full single-electron screening charge occupies an initially unoccupied atomic-like valence orbital. Then, because there is minimal inner-orbital relaxation, the difference operator $\hat{V}(N-1, Z) - \hat{V}(N, Z)$ in Eq. (134) reduces to the single terms $\hat{J}_{valence} + \hat{K}_{valence}$, and the final relaxation energy is given by $\frac{1}{2}\langle\phi_{valence}|\hat{J}_{valence} + \hat{K}_{valence}|\phi_{valence}\rangle \approx \frac{1}{2}\langle\phi_{valence}|\hat{J}_{valence}|\phi_{valence}\rangle = \frac{1}{2}J_{valence, valence}$.

As a final comment concerning relaxation, the discussion surrounding Eq. (77) and Fig. 8 should be recalled. That is, the occurrence of relaxation requires by virtue of the Manne–Åberg–Lundqvist sum rule given in Eq. (77) that additional photoelectron intensity arises at kinetic energies below that of the relaxed or adiabatic peak position. Thus, relaxation is very closely associated with various kinds of low-energy satellite structure of types to be discussed in Section V.D.

C. Multiplet Splittings

Multiplet splittings arise from the various possible non-degenerate total electronic states that can occur in the final hole states of open-shell systems, whether they be atoms, molecules, or solids with highly localized unfilled valence levels. The way in which multiple final states can be produced has already been briefly introduced in Section III.A, and for most systems it is adequate to consider a total spatial symmetry designation (e.g. $L=0, 1, 2, \ldots$ in atoms), a total spin designation (e.g. $S=0, 1, 2, \ldots$ in atoms or molecules), and perhaps also the perturbation of these via the relativistic spin–orbit interaction. The simplest interpretation of atomic multiplet splittings is thus in terms of various L, S terms. Such effects can occur in any system in which the outer subshell or subshells are only partially occupied. The partial occupation provides certain extra degrees of freedom in forming total final states relative to the closed-shell case via coupling with the unfilled shell left behind by photoelectron emission. Multiplet effects can occur for both core and valence emission, as long as the valence subshell(s) are not totally occupied initially. Multiplet splittings also possess the important feature of being describable *in first order* in terms of a single set of ground-state Hartree–Fock

one-electron orbitals. Thus, electron–electron correlation effects beyond the ground-state Hartree–Fock approximation are not essential for predicting that multiplet effects will exist, although, as will be shown, the inclusion of correlation effects is absolutely essential for quantitatively describing these phenomena in certain instances.

Multiplet effects involving core-level holes are very commonly encountered in interpretations of the fine structure arising in x-ray emission spectra[243-245] and Auger electron spectra.[3, 246-248] However, it is more recently that such effects were first recognized and studied in detail in connection with core x-ray photoelectron spectra of paramagnetic free molecules[4, 249] and transition-metal compounds.[86, 250] Subsequently, numerous studies have been carried out, including applications to systems containing both transition-metal atoms[86, 157, 250-257] and rare-earth atoms,[156, 258-261] and a few comprehensive reviews have appeared.[262-265] Primary emphasis here will be on the elucidation of a few examples to illustrate the types of effects noted and their modes of interpretation.

As an introductory example of one type of multiplet splitting found in XPS studies,[86, 250] consider first the ground-state Hartree–Fock description of photoemission from the $3s$ level of a Mn^{2+} free ion, as shown on the left-hand side of Fig. 30. The ground state of this ion can be described in L, S (Russell–Saunders) coupling as $3d^5\ ^6S$ (that is, $S=\frac{5}{2}$, $L=0$). In this state, the five $3d$ spins are coupled parallel. Upon ejecting a $3s$ electron, however, two final states may result: $3s3d^5\ ^5S$ ($S=2$, $L=0$) or $3s3d^5\ ^7S$ ($S=3$, $L=0$). The basic difference between these two is that in the ^5S state, the spin of the remaining $3s$ electron is coupled anti-parallel to those of the five $3d$ electrons, whereas in the ^7S state the $3s$ and $3d$ spins are coupled parallel. Because the exchange interaction acts only between electrons with parallel spins, the ^7S energy will be lowered relative to the ^5S energy because of the favorable effects of $3s$–$3d$ exchange. The magnitude of this energy separation will be proportional to the $3s$–$3d$ exchange integral $K_{3s, 3d}$, and will be given by[118]

$$\Delta[E_b(3s)] = E^f(3s3d^5\ ^5S) - E^f(3s3d^5\ ^7S) = \Delta E^f(3s3d^5)$$

$$= 6K_{3s, 3d}$$

$$= \frac{6e^2}{5} \int_0^\infty \int_0^\infty \frac{r_<^2}{r_>^3} P_{3s}(r_1)P_{3d}(r_2)P_{3s}(r_2)P_{3d}(r_1)\ dr_1\ dr_2 \qquad (138)$$

where e is the electronic charge, $r_<$ and $r_>$ are chosen to be the smaller and larger of r_1 and r_2 in performing the integrations, and $P_{3s}(r)/r$ and $P_{3d}(r)/r$ are the radial wave functions for $3s$ and $3d$ electrons. The factor $1/5$ results from angular integrations involved in computing $K_{3s, 3d}$. A Hartree–Fock calculation of the energy splitting in Eq. (138) for Mn^{3+} gives a value of $\Delta E^f(3s3d^5) \approx 13$ eV.[86, 250] As this predicted splitting is considerably larger

Fig. 30. The various final state L, S multiplets arising from $3s$ and $3p$ photoemission from a Mn^{2+} ion. Within the S and P manifolds, separations and relative intensities have been computed using simple atomic multiplet theory as discussed in the text. The separation and relative intensity of the ^7S and ^7P peaks were fixed at the values observed for $3s(1)$ and $3p(1)$ in the MnF_2 spectrum of Fig. 31 to facilitate comparison with experiment. (From Fadley, ref. 262.)

than typical XPS linewidths, it is not surprising that rather large $3s$ binding energy splittings have in fact been observed in solid compounds containing Mn^{2+}, and such splittings are clearly evident in the $3s$ regions of the first data of this type obtained by Fadley et al.,[86, 250] as shown in Fig. 31. Roughly the left half of each of these spectra represents $3s$ emission, and the splittings observed in MnF_2 and MnO are approximately one-half of those predicted from Eq. (138). The primary reason for this large discrepancy in magnitude appears to be correlation effects due to the highly overlapping character of the $3s$ and $3d$ orbitals, as discussed in more detail below.

In considering further such core binding energy splittings in non-relativistic atoms, it is worthwhile to present a more general discussion of the photoemission process, including the relevant selection rules.[8, 262, 263] If the photoelectron is ejected from a filled nl subshell containing q electrons, and an unfilled $n'l'$ valence subshell containing p electrons is present, the overall photoemission process can be written as

$$\underset{\substack{\text{(filled)} \ (L, S)}}{(nl)^q(n'l')^p} \xrightarrow{h\nu} \underset{(L^f, S^f)}{(nl)^{q-1}(n'l')^p} + \text{photoelectron} \qquad (139)$$

Fig. 31. XPS spectra from three solid compounds containing Mn, in the kinetic energy region corresponding to emission of $Mn3s$ and $3p$ electrons. The initial-state ions present are $Mn^{+2}3d^5$ (MnF_2, MnO) and $Mn^{+4}3d^3$ (MnO_2). Peaks due to multiplet splittings are labelled $3s(1)$, $3s(2)$, etc. $K\alpha_{3, 4}$ x-ray satellite structures are also indicated. (From Fadley and Shirley, ref. 86.)

Here, L and S denote the total orbital and spin angular momenta of the initial N-electron state and L^f and S^f represent the same quantities for the final ionic state with $(N-1)$ electrons. As $(nl)^p$ is a filled subshell, its total orbital and spin angular momenta must both be zero and therefore L and S correspond to the orbital and spin momenta of the valence subshell $(n'l')^p$. In the final state, L^f and S^f represent momenta resulting from the coupling of $(nl)^{q-1}$ (or, equivalently, a single core-electron hole) with $(n'l')^p$. The transition probability per unit time for photoelectron excitation is proportional to the square of a dipole matrix element between the initial and final state wave functions (see Section III.D.1 for a detailed discussion). In a nearly one-electron model of photoemission, this matrix element can be simplified to the sudden approximation forms given in Eqs (68) and (74). The selection rule on one-electron angular momentum is $\Delta l = l^f - l = \pm 1$, as stated previously. Conservation of total spin and total orbital angular

momenta requires that

$$\Delta S = S^f - S = \pm \tfrac{1}{2} \qquad (140)$$

and

$$\Delta L = L^f - L = 0, \pm 1, \pm 2, ..., \pm l \text{ or } L^f = L+l, L+l-1, ..., |L-l| \qquad (141)$$

Also, the overlap factors in Eqs (68) and (74) yield an additional *monopole* selection rule on the passive electrons, as introduced in Section III.D.1. This rule implies that the coupling of the unfilled valence subshell $(n'l')^p$ in the final state must be the same as that in the initial state: that is to total spin and orbital angular momenta of L and S. Finally, any coupling scheme for $(nl)^{q-1}$ or $(n'l')^p$ must of course be consistent with the Pauli exclusion principle. Since $(nl)^{q-1}$ is assumed to represent a single hole in an otherwise filled subshell, it must therefore couple to a total spin of $\tfrac{1}{2}$ and a total orbital angular momentum of l. Within this model, it has been shown by Cox and Orchard[155] that the total intensity of a given final state specified by L^f, S^f will be proportional to its total degeneracy, as well as to the one-electron matrix element squared. Thus, in Russell–Saunders coupling

$$I_{\text{tot}}(L^f, S^f) \propto (2S^f+1)(2L^f+1) \qquad (142)$$

For the special case of atomic s-electron binding energy splittings, the relevant selection rules are thus:

$$\Delta S = S^f - S = \pm \tfrac{1}{2} \qquad (143)$$

$$\Delta L = L^f - L = 0 \qquad (144)$$

and the total intensity of a given peak is predicted to be proportional to the spin degeneracy of the final state:

$$I_{\text{tot}}(L^f, S^f) \propto 2S^f + 1 \qquad (145)$$

Thus, only two final states are possible corresponding to $S^f = S \pm \tfrac{1}{2}$, and the relative intensities of these will be given by the ratio of their multiplicities, or

$$\frac{I_{\text{tot}}(L, S+\tfrac{1}{2})}{I_{\text{tot}}(L, S-\tfrac{1}{2})} = \frac{2S+2}{2S} \qquad (146)$$

The energy separation of these two states can further be calculated from simple atomic multiplet theory and is given by a result often referred to as the Van Vleck Theorem:[118]

$$\Delta[E_b(ns)] = E^f(L, S-\tfrac{1}{2}) - E^f(L, S+\tfrac{1}{2}) \qquad (147)$$

$$\Delta[E_b(ns)] = (2S+1)K_{ns,n'l'} \quad \text{for } S \neq 0 \qquad (148)$$

$$\Delta[E_b(ns)] = 0 \quad \text{for } S = 0 \qquad (149)$$

Here $K_{ns,n'l'}$ is the $ns - n'l'$ exchange integral and can be calculated from

$$K_{ns,n'l'} = \frac{e^2}{2l'+1} \int_0^\infty \int_0^\infty \frac{r_<^{l'}}{r_>^{l'+1}} P_{ns}(r_1) P_{n'l'}(r_2) P_{ns}(r_2) P_{n'l'}(r_1)\, dr_1\, dr_2 \qquad (150)$$

where the same notation as that in Eq. (138) has been used. Equations (146)–(150) indicate that such s-electron binding energy splittings should yield a doublet with a more intense component at lower binding energy (corresponding to an exchange-favored final state of $S^f = S + \tfrac{1}{2}$) and a component separation that is directly associated with both the initial state spin and the spatial distributions of the core and valence electrons as reflected in the exchange integral. Thus, the potential for extracting certain types of useful and unique information from such splittings exists.

That Eq. (148) provides a good description of the systematics of such s-level multiplet splittings has been nicely demonstrated in studies of the $4s$ and $5s$ splittings in rare-earth metals and compounds with varying outer $4f$ subshell occupation numbers and spins S,[258, 259] as summarized in Fig. 32.
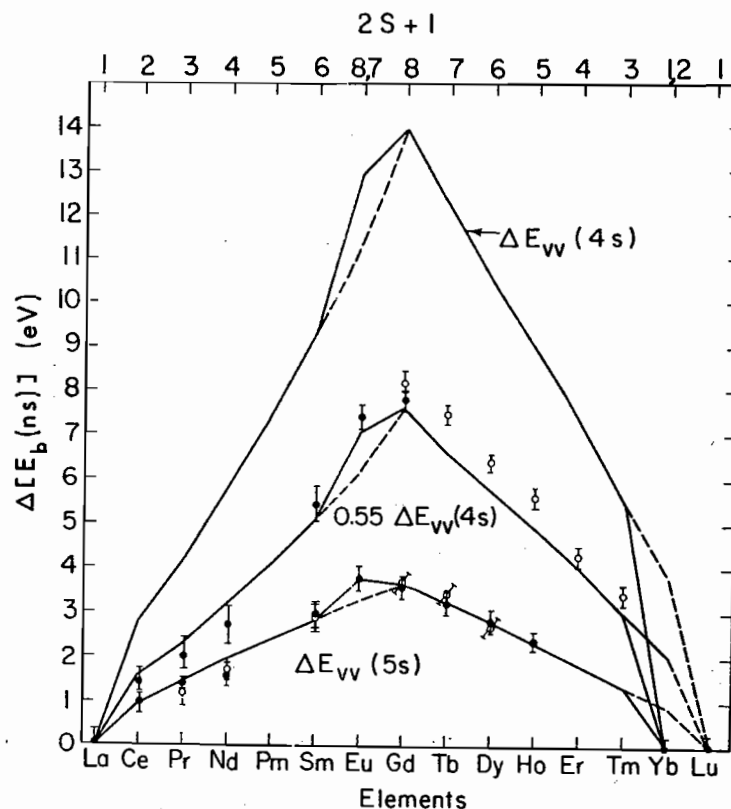

Fig. 32. Experimental (points) and theoretical (lines) $4s$ and $5s$ binding energy splittings in various rare-earth ions. The ΔE_{VV} values are calculated using Van Vleck's Theorem [Eq. (148)]. Experiment and theory are in excellent agreement for $5s$, but the theoretical splittings must be reduced by a factor of 0·55 to agree with the $4s$ data because of correlation effects. (From McFeely *et al.*, ref. 259.)

The solid lines connect calculated values based upon Eq. (148) and are in excellent agreement with experiment for the $5s$ splittings, whereas for the $4s$ splittings, this simple theory must be reduced by a factor of ~ 0.55 to agree with experiment. These results also suggest that the $4s$ discrepancy may be due to the same type of correlation correction involved in Mn$3s$, as the $4s$–$4f$ spatial overlap is high, increasing correlation, whereas the $5s$–$4f$ overlap is much lower, decreasing it.

Configuration interaction calculations on Mn^{3+} by Bagus et al.[252] first provided a more quantitative understanding of such correlation corrections to intrashell s-level splittings such as $3s$–$3d$ and $4s$–$4f$. They pointed out that, in a CI description of the true Mn^{3+} final states corresponding to $3s$ emission, several configurations would be of special importance in addition to the usual one-electron-transition final configuration as shown in the left half of Fig. 30. (In writing such configurations below, numbers in parentheses will denote the L, S coupling of the subshell to the left.) The ^7S final state is found to be composed almost completely of $3s^1(^2S)3p^6(^1S)3d^5(^6S)$, the one-electron configuration, and so is not much perturbed by CI. Another way of saying this is that there is already strong exchange correlation in ^7S, so that the addition of CI is not so significant. The ^5S final state is by contrast expected to have significant contributions from not only the one-electron configuration $\Phi_1(^5S) = 3s^1(^2S)3p^6(^1S)3d^5(^6S)$, but also from configurations in which it formally appears that one $3p$ electron has been transferred down to a $3s$ orbital while another $3p$ electron has been transferred up to a $3d$ orbital: $\Phi_2(^5S) = 3s^2(^1S)3p^4(^3P)3d^6(^3P_1)$, $\Phi_3(^5S) = 3s^2(^1S)3p^4(^3P)3d^6(^3P_2)$ and $\Phi_4(^5S) = 3s^2(^1S)3p^4(^1D)3d^6(^5D)$. (The notations $3d^6(^3P_1)$ and $3d^6(^3P_2)$ stand for two independent ways in which $3d^6$ can couple to ^3P.) Thus, there will be at least a fourfold manifold of ^5S states, and the lowest-energy member is expected to be lowered significantly (that is, to move toward ^7S). In fact, the ^5S state nearest ^7S is found to be only 4.71 eV away, in much better agreement with the experimental splitting for MnF$_2$ of 6.5 eV than the estimate of ~ 13 eV obtained from Eq. (138). Such intrashell s-level multiplet splittings can thus only be predicted accurately when correlation is allowed for, whereas intershell s-level splittings are, by contrast, well predicted by Eq. (148). A further significant effect predicted by these CI calculations for the Mn^{3+} ^5S states is the existence of additional experimental fine structure. Specifically, there are four ^5S states at E_1, E_2, E_3, and E_4, that can be written to a good approximation as

$$\Psi_1(^5S) = C_{11}\Phi_1(^5S) + C_{12}\Phi_2(^5S) + C_{13}\Phi_3(^5S) + C_{14}\Phi_5(^5S)$$

$$\Psi_2(^5S) = C_{21}\Phi_1(^5S) + C_{22}\Phi_2(^5S) + C_{23}\Phi_3(^5S) + C_{24}\Phi_1(^5S)$$

$$\Psi_3(^5S) = C_{31}\Phi_1(^5S) + C_{32}\Phi_2(^5S) + C_{33}\Phi_3(^5S) + C_{34}\Phi_4(^5S) \qquad (151)$$

$$\Psi_4(^5S) = C_{41}\Phi_1(^5S) + C_{42}\Phi_2(^5S) + C_{43}\Phi_3(^5S) + C_{44}\Phi_4(^5S)$$

As the initial state is rather well described by a single configuration $3s^2(^1S)3p^6(^1S)3d^5(^6S)$ possessing the d-electron coupling of Φ_1, the sudden approximation result of Eq. (84) can immediately be used to show that the four ^5S intensities will be given by

$$I_1 \propto |C_{11}|^2, \quad I_2 \propto |C_{21}|^2, \quad I_3 \propto |C_{31}|^2, \quad I_4 \propto |C_{41}|^2 \qquad (152)$$

with the total intensity $I_1 + I_2 + I_3 + I_4$ still being proportional to the spin degeneracy of 5. Evaluating the energies and relative intensities in this way yields a prediction of a total of only *three* observable ^5S peaks (one is too weak to be seen easily) and one observable ^7S peak in the Mn^{2+} spectrum. Weak structures in good agreement with these predictions have, in fact, been observed by Kowalczyk et al.,[253] and their experimental results are shown in Fig. 33. These CI calculations also explain a peak intensity discrepancy noted relative to simple multiplet theory: namely that the intensity ratio $^5S(1)/^7S$ in Fig. 31 or Fig. 33 is significantly below the 5/7 predicted by
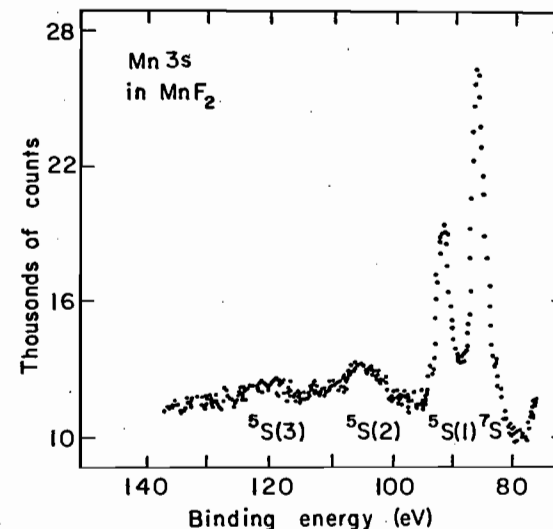

Fig. 33. Higher resolution Mn$3s$ spectrum from MnF$_2$ obtained with monochromatized AlKα radiation (cf. Fig. 31). The peaks $^5S(2)$ and $^5S(3)$ arise from final-state configuration interaction (correlation effects) according to Eq. (151). (From Kowalczyk et al., ref. 253.)

Eq. (146). It is thus clear, that, although a first-order description of multiplet effects is possible within a non-correlated Hartree–Fock approach, a detailed description of the numbers, positions, and relative intensities of peaks may require including correlation effects, especially where intrashell interactions dominate.

The first observations of s-electron core binding energy splittings analogous to those described by Eqs (146)–(150) were in gaseous, paramagnetic
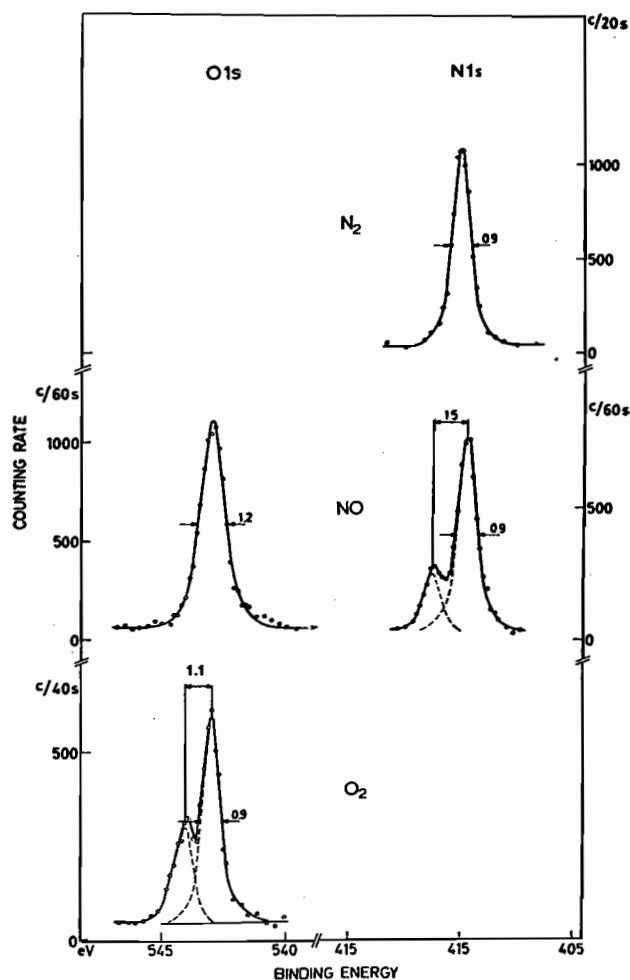
Fig. 34. XPS spectra from the $1s$ core electrons of the gaseous molecules N_2, NO, and O_2. The $1s$ peaks from the paramagnetic molecules NO and O_2 are split due to final-state multiplets. Diamagnetic N_2 shows no splitting. (From Siegbahn et al., ref. 4.)

molecules.[4, 249] Hedman et al.[249] found splittings as large as $1\cdot5$ eV in the $1s$ photoelectron spectra of the molecules NO and O_2. These results are shown in Fig. 34 along with an unsplit $1s$ spectrum from the diamagnetic molecule N_2. In each case, it can be shown that the observed energy splitting should be proportional to an exchange integral between the unfilled valence molecular orbital and the $1s$ orbital of N or O,[4] in analogy with Eq. (148). Theoretical estimates of these splittings from molecular orbital calculations give values in good agreement with experiment,[4, 107] as expected for such

intershell interactions in which correlation effects are much decreased. The observed intensity ratios of the peaks are furthermore very close to the ratios of the final-state degeneracies, also in agreement with simple theory.

The analysis of binding energy splittings in emission from non-s core levels is not as straightforward as for s-level emission, primarily due to the fact that the core-electron hole represented by $(nl)^{q-1}$ (which now has associated with it a spin of $\frac{1}{2}$ and a non-zero orbital angular momentum of l) can couple in various ways with the valence subshell $(n'l')^p$ (which can have various spins S'' and orbital angular momenta L'', including the initial values S and L) to form a final state with a given total spin S^f and total orbital angular momentum L^f. Thus, the number of allowed final states increases and their energy separations will in general be determined by both Coulomb and exchange integrals through different coupling schemes. Additional complexities arising for non-s levels are caused by spin–orbit coupling and crystal-field splittings.

The simplest procedure for calculating such non-s energy separations is again to use non-relativistic atomic multiplet theory.[86, 250, 262, 263] As an illustrative example, consider $3p$ electron emission from Mn^{2+}, as indicated in the right-hand portion of Fig. 30. For this case, $(nl)^{q-1} = 3p^5$, $(n'l')^p = 3d^5$ and the initial state, as before, is ^6S $(S = \frac{5}{2}, L = 0)$. The previously stated selection rules imply that the allowed final states correspond to $^7P(S = 3, L = 1)$ and ^5P $(S = 2, L = 1)$. Although a ^5S $(S = 2, L = 0)$ final state would be consistent with selection rule (141), it requires changing the coupling of $3d^5$ from its initial ^6S and so is not allowed. There is only one way for $3p^5$ to couple with $3d^5$ to form a ^7P state, that being with $3p^5$ (always coupled to total spin $= s = \frac{1}{2}$ and total orbital angular momentum $= l = 1$) coupled with $3d^5$ in its initial state coupling of ^6S $(S = \frac{5}{2}, L = 0)$. However, there are three ways to form the allowed ^5P final state by coupling

$$3p^5(s = \tfrac{1}{2}, l = 1) \quad \text{with} \quad 3d^5 \; ^6S(S'' = \tfrac{5}{2}, L'' = 0)$$
$$3p^5(s = \tfrac{1}{2}, l = 1) \quad \text{with} \quad 3d^5 \; ^4D(S'' = \tfrac{3}{2}, L'' = 2)$$

and

$$3p^5(s = \tfrac{1}{2}, l = 1) \quad \text{with} \quad 3d^5 \; ^4P(S'' = \tfrac{3}{2}, L'' = 1)$$

Thus, four distinct final states are possible for $3p$ emission from Mn^{2+}, one ^7P and three ^5P. As there are off-diagonal matrix elements of the Hamiltonian between the various ^5P coupling schemes,[118] they do not individually represent eigenfunctions. The eigenfunctions describing the ^5P final states will thus be linear combinations of the three schemes:

$$\Psi_1(^5P) = C_{11}\Phi(^6S) + C_{12}\Phi(^4D) + C_{13}\Phi(^4P)$$
$$\Psi_2(^5P) = C_{21}\Phi(^6S) + C_{22}\Phi(^4D) + C_{23}\Phi(^4P) \tag{153}$$
$$\Psi_3(^5P) = C_{31}\Phi(^6S) + C_{32}\Phi(^4D) + C_{33}\Phi(^4P)$$

where each ^5P configuration has been labelled by the $3d^5$ coupling involved and the C_{ij}'s are the usual expansion coefficients. The energy eigenvalues corresponding to these eigenfunctions will give the separations between the ^5P states. Such eigenfunctions and eigenvalues can most easily be determined by diagonalizing the 3×3 Hamiltonian matrix for the ^5P states, where each matrix element is expressed as some linear combination of $J_{3d,\,3d}$, $K_{3d,\,3d}$, $J_{3p,3d}$, and $K_{3p,\,3d}$.[33, 118] If Coulomb and exchange integrals from a Hartree–Fock calculation on Mn^{2+} are used, such matrix diagonalization calculations yield the relative separations indicated on the right-hand side of Fig. 30.[86, 250] Once again, the sudden approximation result of Eq. (84) indicates that, because the initial state is rather purely $3d^5(^6S)$, only those components of the ^5P states represented by $C_{11}\Phi(^6S)$ are accessible. Thus, the individual intensities of Ψ_1, Ψ_2, and Ψ_3 can be computed from $|C_{11}|^2$, $|C_{21}|^2$, and $|C_{31}|^2$, respectively. In determining the total intensity ratios for the ^5P and ^7P states, Eq. (142) can be used to give:

$$I_{tot}(^5P) : I_{tot}(^7P) = [I_1(^5P) + I_2(^5P) + I_3(^5P)] : I_{tot}(^7P) = 5 : 7$$

The relative peak heights in Fig. 30 have been calculated in this way, and the experimental $3s(1)$–$3p(1)$ separation and relative intensity for MnF_2 were used to empirically fix the scales between the $3s$ and $3p$ regions. The separations and relative intensities of the peaks observed are found to be at least semi-quantitatively predicted by this simple, atomic L, S coupling model,[86, 250] and these results have been confirmed in more detail by later experimental[255] and theoretical[256] studies. The remaining discrepancies between theory and experiment for this $3p$ case could be caused by a combination of effects due to correlation, spin–orbit coupling, and crystal-field splitting, although calculations by Gupta and Sen[256] indicate that the latter two are probably not so significant. Ekstig et al.[245] have carried out matrix diagonalization calculations like those described here but for more complex sets of final $3p$-hole states in $3d$ transition metal atoms in an attempt to interpret soft x-ray emission spectra from solids. The theoretical aspects of calculating such non-s splittings have also recently been reviewed by Freeman et al.[263]

Deeper non-s core levels in $3d$ atoms should also exhibit similar splittings, although the magnitudes will be reduced because of the decreased interaction strengths between the core and $3d$ orbitals. For example, Fadley and Shirley[86] first noted that the $Mn2p$ levels in MnF_2 are broadened by $\sim 1{\cdot}5$ eV relative to those in low-spin (filled subshell) compounds, and suggested multiplet splittings as the origin of this broadening. Subsequent measurements at higher resolution by Kowalczyk et al.,[255] coupled with theoretical calculations by Gupta and Sen,[257] have confirmed this suggestion, and also verified the existence of peak asymmetries and anomalous $2p_{\frac{1}{2}}$–$2p_{\frac{3}{2}}$ separations. For this

$2p$ case, both multiplet effects and spin–orbit coupling are of similar magnitude, and were included in calculations that successfully predicted the observed spectra.[257]

Analogous non-s core-level splittings have also been studied in systems with partially-filled f subshells,[86, 260, 266] and the anomalous shape and decreased spin–orbit splitting in the $Eu4d$ spectrum of Fig. 6 is, in fact, attributable to such effects.[86]

Although only multiplet effects on core-level binding energies have been considered up to this point, such phenomena can play a considerable role in determining the fine structure observed in valence spectra (as has been apparent for some time in UPS studies of free molecules[97]). In particular, XPS valence spectra obtained from solids containing highly localized d levels or f levels are expected to be influenced by such multiplet effects,[82, 156, 157, 261, 266, 267] with the relative intensities of various allowed final states being determined by fractional parentage coefficients, as described in Section III.D.2 and elsewhere.[156, 157, 262] Heden et al.[267] first observed such effects in valence spectra of $4f$ metals. As an example of the occurrence and use of such splittings in studies of rare-earth compounds, the XPS results of Campagna et al.[261] and Chazalviel et al.[266] show strong multiplet splittings in the valence spectra of Sm-chalcogenides and a mixture of two markedly different multiplet structures in certain Sm compounds that are thought to exhibit valence fluctuations between Sm^{+2} $4f^7$ and Sm^{+3} $4f^6$. Some of these results for SmB_6[266] are presented in Fig. 35, in which the L, S multiplets expected for both Sm^{+2} and Sm^{+3} are labelled. Theoretical intensities have been calculated using fractional parentage coefficients,[156] and the agreement between the theoretically simulated spectrum and experiment is excellent. Baer[268] has also presented very high-resolution XPS spectra for various $4f$ metals that further confirm the existence of these atomic-like multiplet effects. In analogous multiplet effects in valence d orbitals, the inclusion of crystal-field effects is also expected to be important, as has been emphasized in a recent discussion by Bagus et al.[157]

In comparison to chemical shifts of core-electron binding energies, multiplet splittings of core- or valence-energies thus represent higher-order effects yielding a different type of information. In their simplest interpretation, chemical shift measurements detect a change in the spatially-averaged potential experienced by an electron, whereas analyses of multiplet effects have the capability of determining the valence electron configuration or the detailed strengths of various higher-order electronic interactions. The two types of measurements are thus complementary. Numerous applications of multiplet splittings measurements are thus possible in the study of the transition series metals, the rare earths, the transuranium elements, and open-shell systems in general.
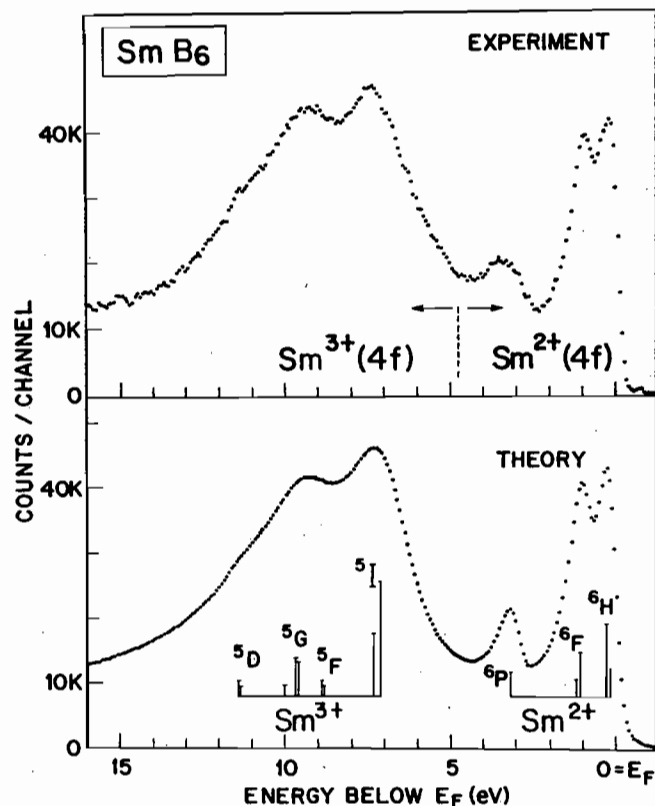
Fig. 35. Experimental and theoretical $4f$ valence spectra from SmB₆, a "mixed-valence" metallic compound believed to contain both $Sm^{+2}\,4f^6$ and $Sm^{+3}\,4f^5$. The intensities of the various final-state multiplets for $Sm^{+2} \rightarrow Sm^{+3}$ and $Sm^{+3} \rightarrow Sm^{+4}$ were computed using fractional parentage coefficients and are indicated as vertical bars. These calculations were broadened by an empirically-derived function of the form of Eq. (158) to generate the final theoretical curve. Monochromatized AlKα was used for excitation. (From Chazalviel et al., ref. 266.)

D. Multi-electron Excitations

1. *Introduction.* In this section, several types of final-state effects (and, to a lesser degree, initial-state effects) that involve what appear to be "multi-electron" excitations during the photoemission process are considered. The term multi-electron is judged against a purely one-electron description in which no final-state relaxation occurs. From the outset, it is clear that relaxation *does* occur, so that all transitions are indeed N-electron. Also, in a configuration interaction picture, the various mixtures of initial- and final-state configurations involved could easily make it impossible to distinguish clearly a one-electron component of photoemission. Nonetheless, all effects discussed here do somehow represent final states that deviate in a well-defined

way from the single initial-state Hartree–Fock determinant that best approximates the one-electron photoemission event. The discussion begins with relatively simple forms of multi-electron excitation (shake-up and shake-off), but then comes to involve more complex phenomena that are important in XPS studies of certain atoms, molecules, and solids.

2. *Shake-up, Shake-off, and Related Correlation Effects.* Multi-electron processes in connection with x-ray photoemission were first studied in detail by Carlson, Krause, and co-workers.[135] In these studies, gaseous neon and argon were exposed to x-rays with energies in a range from 270 eV to 1·5 keV. Measurements were then made of both the charge distributions of the resulting ions and the kinetic energy distributions of the ejected photoelectrons. From these measurements, it was concluded that two-electron and even three-electron transitions occur in photo-absorption, with total probabilities which may be as high as 20% for each absorbed photon. By far the most likely multi-electron process is a two-electron transition, which is approximately ten times more probable than a three-electron transition. Two types of two-electron transitions can further be distinguished, depending upon whether the second electron is excited to a higher bound state ("shake-up"[4]) or to an unbound continuum state ("shake-off"[135]). These are indicated in the transition below (cf. the corresponding one-electron transition in relation Eq. (139)):

Shake-up:

$$\underset{(L,\,S)}{(nl)^q(n'l')^p} \xrightarrow{h\nu} \underset{(L',\,S')}{(nl)^{q-1}(n'l')^{p-1}(n''l'')^1} + \text{photoelectron} \qquad (154)$$

Shake-off:

$$(nl)^q(n'l')^p \xrightarrow{h\nu} (nl)^{q-1}(n'l')^{p-1}(E_{kin}''l'')^1 + \text{photoelectron} \qquad (155)$$

Here $(n'l')^p$ represents some outer subshell from which the second electron is excited; it can be filled or partially filled. Either shake-up or shake-off requires energy that will lower the kinetic energy of the primary photoelectron. Thus, such multi-electron processes lead to satellite structure on the low-kinetic energy side of the one-electron photoelectron peak, as shown schematically in Fig. 8.

Higher resolution XPS spectra have been obtained more recently for neon and helium by Carlson et al.[269] and for neon by Siegbahn et al.[41, 270] A high-resolution N₁s spectrum obtained by Gelius et al.[270] is shown in Fig. 36. The two-electron transitions that are believed to be responsible for the observed spectral features labelled 2 to 14 occurring at relative energies from 33 to 97 eV below the one-electron peak are listed in Table II. The total two-electron shake-up intensity in this spectrum is thus estimated to be approximately 12% of that of the one-electron peak. Both shake-up and shake-off together account for ~30% of all emission events.

TABLE II

Summary of data concerning multi-electron transitions accompanying the formation of a 1s hole in atomic neon by AlKα or MgKα x-rays (compare Fig. 36)

(a) Shake-up transitions

Line no.	Type of process	Final state	Experimental[a] excitation energy (eV)	Calculated[a,b] excitation energy (eV)	Experimental relative intensity (%)	Calculated[c] relative intensity (%)	Calculated[d] relative intensity (%)
0	One-electron transition	$1s2s^22p^6$ ^2S	(870·37)	(870·37)	100·00	100	100
1	Energy loss	$1s^22s^22p^53s$ ^2P	16·89 (6)	16·93			
2	Dipole shake-up	$1s^22s^22p^53s$ ^2P lower	33·35 (9)				
3	Monopole shake-up	$1s^22s^22p^53p$ ^2S lower	37·35 (2)	37·39	0·06 (1)	2·3	2·47
4	Monopole shake-up	$1s^22s^22p^53p$ ^2S upper	40·76 (3)	41·26	3·15 (8)	2·9	2·60
5	Monopole shake-up	$1s^22s^22p^54p$ ^2S lower	42·34 (4)	42·30	3·13 (10)		1·48
6	Monopole shake-up	$1s^22s^22p^55p$ ^2S lower	44·08 (5)	44·18	2·02 (10)		0·43
7	Monopole shake-up	$1s^22s^22p^56p$ ^2S lower	45·10 (7)		0·42 (6)		0·09
8	Monopole shake-up	$1s^22s^22p^54p$ ^2S upper	46·44 (5)	46·42	0·50 (15)		0·70
9	Monopole shake-up	$1s^22s^22p^55p$ ^2S upper	48·47 (7)	48·40	0·96 (11)		0·11
10	Monopole shake-up	$1s^22s2p^63s$ ^2S lower	59·8 (1)	59·75	0·17 (5)		
11	Monopole shake-up	$1s^22s2p^63s$ ^2S upper	65·9 (1)	65·93	0·57 (5)		
12	Two electron shake-up	} $1s^22s^22p^43p^2$ ^2S	93·14 (7)		0·49 (6)		
13	Two electron shake-up		95·9 (1)		0·08 (2)		
14	Two electron shake-up		97·23 (5)		0·10 (4)		
					0·24 (4)		
					11·89% = Partial sum of shake-up		
	Onset of shake-off	$1s^22s^22p^5$ ^3P	47·4 (5)	46·96			
	Onset of shake-off	$1s^22s^22p^5$ ^1P	51·7 (5)	51·27			

[a] From Gelius, ref. 270.
[b] All calculated excitation energies have been increased by 1·8 eV to allow for errors due to relativistic and correlation effects, particularly in the $1s2s^22p^6$ one-electron-transition final state.
[c] Calculated using one-electron wave functions only from Eq. (156) by Carlson et al., ref. 269.
[d] Calculated using initial-state configuration interaction and Eq. (83) by Martin and Shirley, ref. 14.

TABLE II (cont.)

(b) Shake-off transitions

	Experimental[e] relative intensity (%)	Calculated[e] relative intensity (%)
Total intensity for shake-off of one electron from Ne 2s and 2p subshells (Ne→Ne²⁺)	16·5	16·1
Total intensity for shake-off of two electrons from Ne 2s and 2p subshells (Ne→Ne³⁺)	0·8	

[e] From Carlson, Krause, and co-workers, ref. 135. Intensity calculated using an extension of Eq. (156).
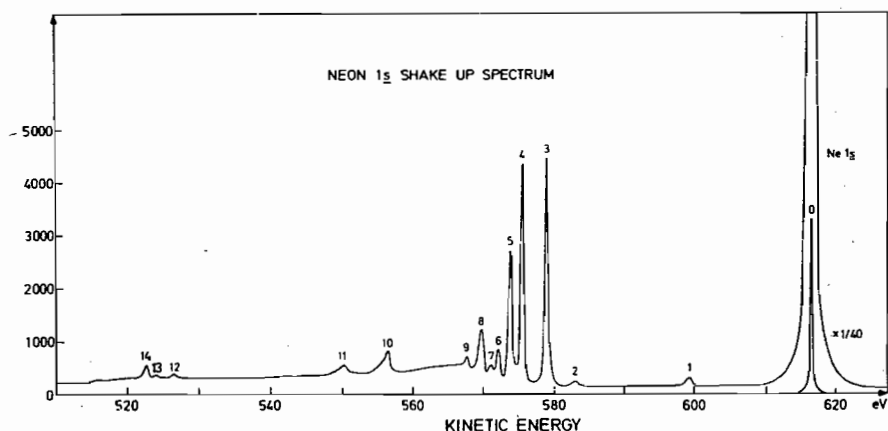
Fig. 36. High-resolution shake-up spectrum associated with excitation from Ne1s in gaseous neon. Table II lists the origins of the various satellite peaks labelled 1–14. The Ne1s FWHM was reduced to 0·4 eV in these measurements by using a monochromatized AlKα source. (From Gelius, ref. 270.)

Note that the initial and final states given in Table II are assumed to be composed of a single electronic configuration. This assumption, together with the sudden approximation as outlined in Section III.D.1, permits predicting such shake-up and shake-off peak intensities in a very straight-forward way.[135] Namely, Eq. (75) is used for the relevant matrix element and it is noted that, in the passive-electron manifold, the only major change occurring for a two-electron transition is $\phi_{n'l'} \to \phi_{n''l''}$, with all other passive orbitals remaining in very nearly the same form. Thus, $\langle \phi_j' | \phi_j \rangle \approx 1 \cdot 0$ unless the overlap involved is $\langle \phi_{n''l''} | \phi_{n'l'} \rangle$, and the probability of a given transition is in simplest approximation[269]

$$P_{n'l' \to n''l''} \propto N_{n'l'} |\langle R_{n''l''} | R_{n'l'} \rangle|^2 \qquad (156)$$

where $N_{n'l'}$ is the occupation number of the $n'l'$ subshell, and allows for a summation on $m_{l'} m_{s'}$ (which must equal $m_{l''} m_{s''}$). Here the radial function $R_{n''l''}$ must be calculated in the final-state ionic potential, and $R_{n'l'}$ is a radial function for the initial state. By virtue of symmetry, the overlap in Eq. (156) will only be non-zero if $l'' = l'$, a result that is often termed a one-electron monopole selection rule. Thus, for example, only $2s \to ns$ and $2p \to np$ monopole transitions yield large intensities as quoted in Table II (although a single, weak $2p \to 3s$ dipole transition is also thought to be present). The total symmetries for the $(N-1)$ passive electrons are also predicted to follow a monopole rule of the form predicted by Eq. (69)

$$\Delta J = \Delta L = \Delta S = \Delta M_J = \Delta M_L = \Delta M_S = \Delta \pi = 0 \qquad (157)$$

where J is the quantum number for $\mathbf{L} + \mathbf{S}$, and π is the overall state parity.

Equation (156) has been used with reasonable success in predicting shake-up and shake-off intensities in core-level emission from rare gases,[4, 135, 269, 270 271] as well as from alkali-halides[271] for which the component ions possess rare-gas configurations. Some previous results for Ne1s emission are summarized in Table II, where calculated two-electron peak separations and relative intensities are compared with experiment. The various final-state configurations are noted and for this case the $\Psi_R(N-1)$ of Eq. (69) corresponds to an *unrelaxed* Ne+ $1s2s^22p^6$ with an overall L, S coupling of ^2S. There is reasonable agreement between theoretical and experimental separations, but the theoretical values are uniformly high by about 1·8 eV out of 40 eV, and have been back-corrected by this amount before entry in the table.[270] The necessity for this correction has been explained as a $2p$–$2p$ correlation and relativistic error in the Hartree–Fock calculation for the one-electron $2p^6$ final state that is of much lower magnitude in the various $2p^5np$ two-electron final states because of the reduced $2p$–np overlap. Theoretical and experimental relative intensities are also in fair agreement. It should also be noted in connection with these data that the various L, S multiplets formed as final states must be considered. For example, the peaks indicated as "lower" and "upper" in Table II are due to a multiplet splitting of the same type noted on the right-hand side of Fig. 30 for the ^5P states of Mn^{3+}. In the case of Ne+, ^2S states can be formed in two ways from the same total configuration $1s2s^22p^5np$: one in which the $1s$ electron is coupled with $2s^22p^5np(^1S)$ and one in which it is coupled with $2s^22p^5np(^3S)$.[4, 135] A similar effect occurs in $1s2s2p^6ns$ final states. Thus, there may be considerable interaction between multi-electron processes and multiplet splittings, and a complete specification of the final state must include possible multiplet effects.

The assumption of single-configuration final states used in the previous analysis clearly is open to question, especially since the best description of all states would presumably be via a complete configuration-interaction treatment. Martin and Shirley[14] have performed CI calculations for Ne and the isoelectronic molecule HF that do indeed indicate that configuration-interaction effects can be significant. Their analysis proceeds via an equation analogous to Eq. (83), from which it is clear that both final-state CI and initial-state CI can complicate the calculation of intensities by opening up new options for non-zero $(C_j^f)^* C_j^t$ products. In particular, the mixing of both the $1s^22s^22p^6$ and $1s^22s^22p^53p$ configurations into the initial state *and* the final states corresponding to the observed peaks 0, 3, and 4 is found to significantly alter the calculated intensities so as to yield better agreement with experiment, as shown in Table II.

It should also be noted that the total shake-up intensities associated with *valence-level* emission are generally observed to be higher than predicted by

the simple theory outlined above, a result that is consistent with much stronger intrashell correlation effects.[135, 269] For example, Chang and Poe[272] have recently performed theoretical calculations for Ne2p excitation at $h\nu \lesssim 200$ eV using more accurate many-body perturbation theory. Their results are in good agreement with available experimental data.

Similar core-level shake-up phenomena are also well known in molecules[4, 269, 270] and the same type of sudden approximation analysis as represented by Eqs (69) to (74) has been used with some success to predict intensities.[273, 274] In connection with valence-level emission a recent CI analysis of low-energy satellite structure in CO by Bagus and Viniikka[275] indicates that higher-order correlation effects are also highly significant, in agreement with the similar conclusions reached previously for atomic valence-level shake-up.

3. *Multi-electron Excitations in Metals.* Processes analogous to shake-up and shake-off are also expected to occur during core-level emission from solid metals, where the form of the density-of-states curve above the Fermi energy provides a continuous range of allowed one-electron excitation energies, rather than the discrete set available in atoms or molecules. Thus, rather than a sharp set of satellite lines below a roughly symmetric one-electron-transition peak (cf. Fig. 36), what is expected is an asymmetric tailing of the main peak. The detailed line shapes associated with such processes in XPS core-level emission were first discussed by Doniach and Sunjic[276] and are predicted to have the form:

$$I(E) = \frac{\cos\left[\pi\alpha/2 + (1-\alpha)\tan^{-1}(E/\gamma)\right]}{(E^2 + \gamma^2)^{(1-\alpha)/2}} \qquad (158)$$

where

$E =$ kinetic energy measured from the threshold of the unbroadened one-electron-transition peak

$\gamma =$ the lifetime of the core hole

$\alpha =$ an asymmetry parameter

$$= 2\sum_l (2l+1)(\delta_l/\pi)^2 \qquad (159)$$

$\delta_l =$ the phase shift of the lth partial wave for electrons at the Fermi energy scattering from the core hole.

2γ is thus the natural FWHM of the core-level. If $\alpha = 0$ (as it is for insulators), then $I(E)$ merely reduces to a Lorentzian lifetime broadening. The phase shift δ_l thus has a meaning very close to those discussed in connection with atomic differential cross-sections in Section III.D.2 (cf. Fig. 9).

Citrin[277] first pointed out that XPS metal spectral shapes exhibited an asymmetry suggestive of Eq. (158). The first quantitative tests of the applicability of this line shape for describing such spectra were performed by Hüfner, Wertheim and co-workers.[84] They fitted Eq. (158) to core spectra for various simple metals and transition metals, empirically choosing the best values of γ and α. The spectra were corrected for instrumental resolution effects, but not for inelastic scattering. Examples of such a comparison between theory and experiment for Au and Pt[84] are shown in the right-hand panels of Fig. 37. It is significant here that Au with a low density of states near the Fermi level shows a much lower degree of asymmetry than Pt with a high density of states near the Fermi level. Hüfner, Wertheim *et al.*[84] concluded that this line shape does well describe the peaks observed in these metals, and that the values of γ and α obtained were physically reasonable. Similar conclusions have been reached in several other studies,[115, 191] and it thus seems likely that such shake-up-like effects do exert a significant influence on line shapes in metals.

A further closely-related effect that has been predicted to occur in metals is the creation of plasmon excitations during the formation of a core hole.[194, 278] Such "intrinsic" plasmons are distinguished from the "extrinsic" plasmons created during photoelectron escape from the material, although they occur at the same energy and are thus rather difficult to resolve from the experimental inelastic tail. Debate still continues as to how important intrinsic plasmons are in XPS spectra,[279] and some angular-resolved XPS results bearing on this question are discussed in Section VI.B.

4. *Core-peak Satellites in Transition-metal and Rare-earth Compounds.* Very strong low-kinetic-energy satellite lines were first observed in a study of Cu2p core levels in compounds such as CuS and Cu$_2$O by Novakov[280]. Similar results obtained more recently by Frost *et al.*[281] are shown in Fig. 38, and it is clear that the satellite peaks have intensities comparable to those of what might be referred to as the one-electron-transition peaks at lowest apparent binding energy. The appearances of these satellites also depend strongly on chemical state, being most intense in cupric compounds containing Cu^{+2} 3d^9 ions, and almost unobservable in cupric compounds containing Cu^{+1} 3d^{10} ions. Similar strong satellites also occur in the core spectra of other open-shell transition-metal and rare-earth compounds.[114, 282–286] They are thus much higher in relative intensity than the 10–30% expected from typical atomic-like shake-up processes, and a great deal of discussion has gone on concerning their origins. Summaries of experimental data, as well as analyses of various proposed models, appear in several prior publications.[114, 280–286]

The most plausible explanation that has emerged for such effects is a significant involvement in the final state of a ligand-to-metal charge transfer
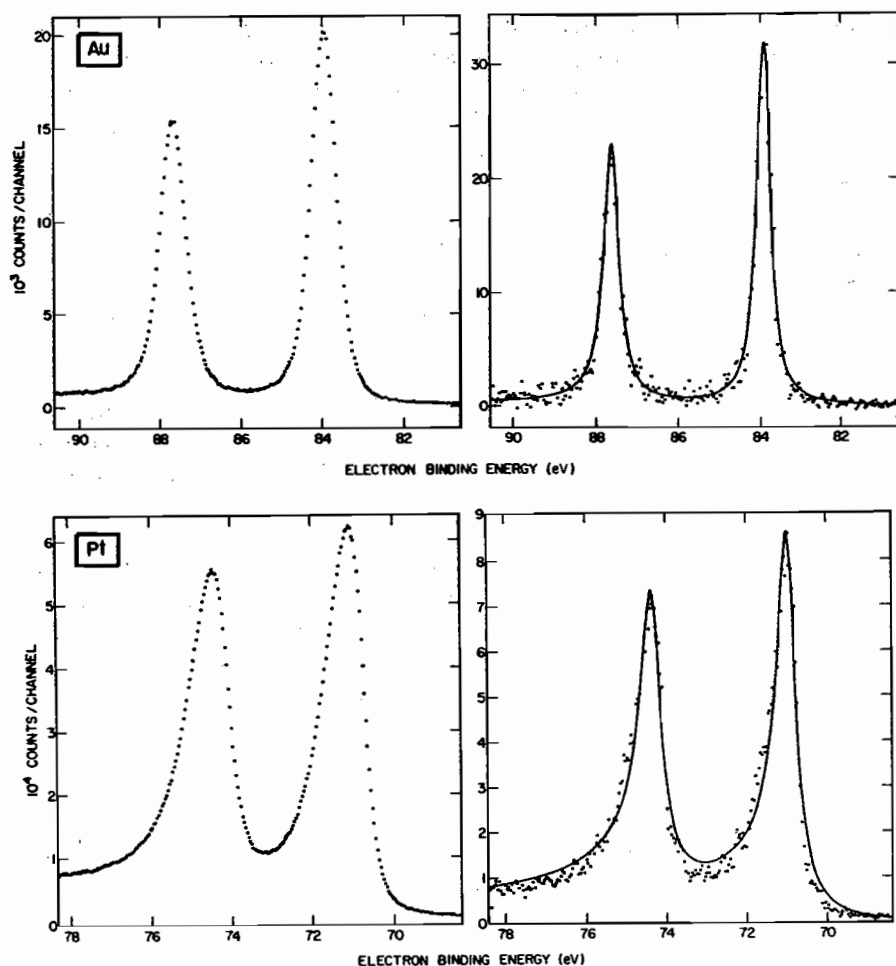
Fig. 37. $4f$ core spectra from polycrystalline Au and Pt (points) in comparison to a best fit of the asymmetric line shape predicted by Eq. (158) (curves). In the right panels, the data have been corrected by deconvolution of the instrumental line shape, but no correction for inelastic scattering effects has been made. The instrumental line shape was derived from the form of the cut-off near E_F (cf. Fig. 13). (From Hüfner and Wertheim, ref. 84.)

that results in a $3d$ or $4f$ configuration with one more d or f electron than in the initial state.[114, 282, 283, 285, 286] This idea was first suggested and qualitatively discussed by Wertheim et al.[114] for satellites in $4f$ compounds and by Kim[283] for $3d$ satellites. The importance of such $3d^n \rightarrow 3d^{n+1}$ and $4f^n \rightarrow 4f^{n+1}$ configurations is not surprising, since they represent an attempt to screen very effectively the core hole formed during final-state relaxation. In fact, there is a high degree of similarity between such final-state configurations
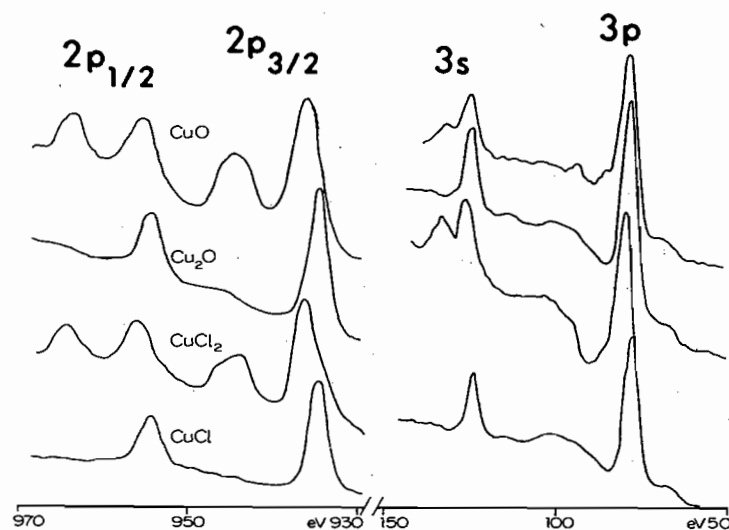
Fig. 38. $2p\frac{3}{2}$, $\frac{1}{2}$ and $3s$, $3p$ core-level spectra from the copper compounds CuO, Cu$_2$O, CuCl$_2$, and CuCl. The low-energy satellites are very strong in Cu^{+2} $3d^9$ compounds (CuO, CuCl$_2$), and very weak in Cu^{+1} $3d^{10}$ compounds (Cu$_2$O, CuCl). (From Frost et al., ref. 281.)

and those used by Ley et al.[235] to describe conduction-electron screening in metals (cf. Fig. 29 and discussion in Section V.B). The absence of satellites for closed-shell d or f systems is immediately explained in this picture, as such relaxation mechanisms are not possible. The most quantitative discussions of this model as applied to $3d$-compound satellites have been presented by Larsson[285] and Asada and Sugano.[286] A two-configuration manifold is used to describe the final-state core-hole wave functions, with one configuration Φ_1 being the simplest final-state determinant with no change in valence-subshell occupations and the other Φ_2 being a determinant in which a single-electron ligand-to-metal transfer has occurred. Specifically, in an octahedrally-coordinated system, the transfer is ascribed to a monopole-allowed excitation of the type:[283, 285, 286] e_g(bonding)$\equiv e_g^b \rightarrow e_g$(anti-bonding)$\equiv e_g^a$. Both orbitals are expressed as linear combinations of metal d and ligand valence, with e_g^a being primarily metal $3d$. The crystal-field-split octahedral symmetry designations are used, and the sudden approximation one-electron monopole selection rule must here be applied to these symmetries. If only the active orbitals are considered, the two final-state configurations can thus be written as:[286]

$$\Phi_1 = (\text{core hole}) \, (e_g^b)^n (e_g^a)^m$$

$$\Phi_2 = (\text{core hole}) \, (e_g^b)^{n-1} (e_g^a)^{m+1} \tag{160}$$

Mixing these configurations produces two final states with differing degrees of charge transfer:

$$\Psi_1{}^f = C_{11}\Phi_1 + C_{12}\Phi_2 \quad \text{at} \quad E_1{}^f$$
$$\Psi_2{}^f = C_{21}\Phi_1 + C_{22}\Phi_2 \quad \text{at} \quad E_2{}^f \tag{161}$$

The "main" line occurs at lower E^f and thus higher kinetic energy and lower binding energy. If $\Psi_1{}^f$ is chosen to represent this main line, it is found to correspond to a net transfer of $\gtrsim 0.5$ electrons to the metal site.[110, 285] Thus, hole screening is predicted to be very appreciable as far as this state is concerned, and the mixing represented by Eq. (161) is highly significant. If the degree of one-electron-orbital relaxation is small, then Φ_1 is approximately equal to the $(N-1)$-electron remainder $\Psi_R(N-1)$ in Eq. (69), and the sudden approximation yields peak intensities via Eq. (84) of

$$I_1 \propto |C_{11}|^2, \quad I_2 \propto |C_{21}|^2 \tag{162}$$

Additional splittings due to crystal-field effects, multiplet effects, and spin–orbit interactions cause further fine structure in the predicted energies, and one-electron orbital relaxation has furthermore been included by means of the equivalent-core approximation.[286] With a limited degree of empirical parameter choice, numerical results based upon this model are in good agreement with experimental satellite data for $3d$ compounds as to intensities, widths, positions, and systematic trends with ligand character and d-orbital occupations.[285, 286] Finally, it is important to note that Viniikka and Bagus[110] have carried out more accurate self-consistent Hartree–Fock calculations with configuration interaction on fully-relaxed core-hole states in the cluster $[NiO_6]^{-10}$. These results also show that a significant ligand-to-metal charge transfer of ~ 0.5 electrons is present in the state representing the main line. It is also concluded that the two primary final states contain significant admixtures of both configurations ($C_{11} \approx 0.9$, $C_{12} \approx 0.3$; $C_{21} \approx 0.3$, $C_{22} \approx 0.9$).

The occurrence of such two-configuration charge-transfer satellites has also been suggested in connection with the adsorption of CO on transition-metal surfaces.[287] In this case, satellites observed in the O$1s$ spectrum are attributed to the strong involvement of a metal-to-molecule charge transfer (that is, the reverse of the direction discussed previously).

Thus, such satellites and the charge-transfer they represent can be extremely important considerations in the analysis of spectra in many systems. The term "shake-up" has been applied to these effects,[283, 285, 286] but such nomenclature can be a bit misleading in the sense that the final states are not pure configurations that are as simply related to the initial state as for the neon case of Table II. The most correct view would seem to be

simply that a strong configuration interaction occurs in the final state due to relaxation about the inner hole.

It is finally worth noting that the presence or absence of such satellites has potential for use in a "'fingerprint" mode for determining the oxidation state and/or valence configuration of $3d$ or $4f$ atoms in different chemical environments.

5. Other Multi-electron Effects. As a final example of multi-electron effects, we consider the observation first made by Gelius[270] that, for a series of elements with $Z \approx 50$–60, the $4p$ binding energy broadens into a many-electron resonance with complex structure, as shown in later data obtained by Kowalczyk et al.[215] in Fig. 39. This rather unique occurrence has been observed in both gases[270] and solids,[215] and has been explained by Wendin et al.[288, 289] as being caused by the particular one-electron energy-level spacings involved. Specifically, the single-configuration final-state after $4p$ emission is $\ldots 4p^5 4d^{10} 5s^2 \ldots$, with the remaining outer occupancies depending upon Z. However, the $4d$ binding energy is approximately $\frac{1}{2}$ that of $4p$ in this region of the periodic table, so that one $4d$ electron can be moved into the lower-energy $4p$ orbital and another $4d$ electron can be placed in a low-energy unoccupied bound orbital or continuum orbital to yield a set of configurations like $\ldots 4p^6 4d^8 5s^2 \ldots (n''l'')^1$ or $\ldots 4p^6 4d^8 5s^2 \ldots (E_{\text{kin}}''l'')^l$ respectively that are nearly degenerate with the one-electron final-state configuration. Strong mixing thus occurs among these configurations, with a resultant smearing of the final states into a broad resonance with fine structure. The mixing in of continuum configurations can also be considered to result from a Coster–Kronig Auger de-excitation of the $4p$ hole via $4d \to 4p$, $4d \to$ continuum. The form of the interactions further dictates that orbitals with $l'' = 2$ are dominant.[288, 289] (Note the similarity between the configurational degeneracy discussed here and that noted by Bagus et al.[252] in their analysis of $3s$ emission from Mn^{2+}, cf. Section V.C). It is thus rather fortunate that such resonances are rare phenomena throughout the periodic table, as one-electron energy levels would otherwise be a much less useful concept.

E. Vibrational Effects

The effects of exciting various final vibrational states on XPS spectra were first clearly observed in gas-phase data obtained with monochromatized radiation by Gelius and co-workers.[270] A C$1s$ spectrum obtained from gaseous CH_4 is shown in Fig. 40, and it exhibits a three-component structure that can be explained as arising from the excitation of three different vibrational states of the symmetric C–H stretch type.[270] The relative intensities and positions of these peaks are furthermore found to be in good agreement with a theoretical model based upon the Born–Oppenheimer approximation as expressed in Eq. (63), provided that it is noted that the C$1s$ hole alters
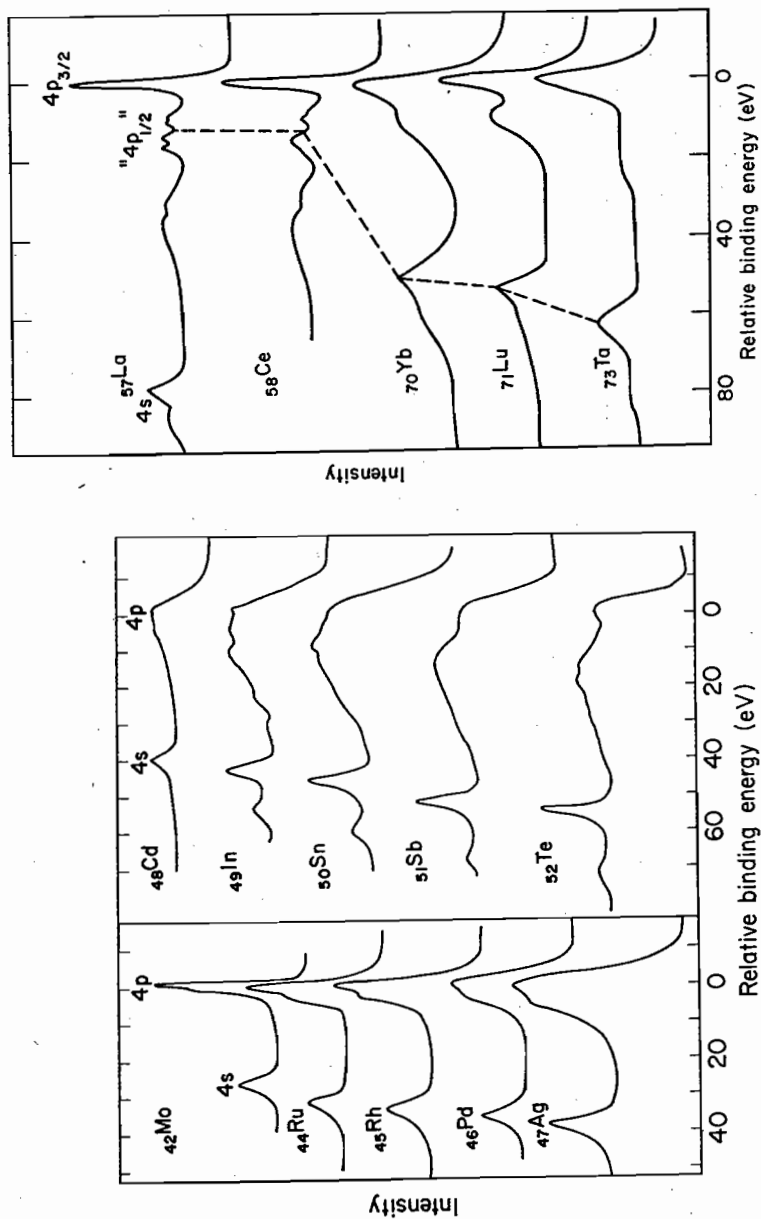
Fig. 39. 4s, 4p core-level spectra for a series of metals from Mo (Z=42) to Ta (Z=73). Note the broad 4p resonance that exists from Z≈49 to Z≳60. (From Shirley et al., ref. 215.)

vibrational energies and wave functions appreciably in the final state. Similar vibrational effects appear to be present in other small molecules, and it is thus clear that XPS peak widths and positions can be significantly affected by final-state vibrational excitations.

Vibrational effects have also been noted in XPS studies of solids by Citrin et al.[85] In this work, core peaks in alkali halides were found to exhibit temperature-dependent line widths consistent with the excitation of lattice
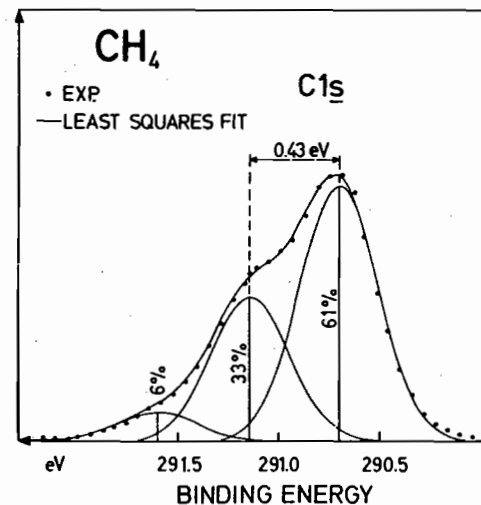
Fig. 40. A C1s spectrum from gaseous CH_4 obtained with very high instrumental resolution (FWHM ≈ 0·3 eV). The lowest-binding-energy primary peak shown here is found to exhibit three components due to vibrational excitations in the final state. (From Gelius, ref. 270.)

vibrations (phonons) during photoemission as shown in Fig. 41. A solid-state analysis based upon the Born–Oppenheimer approximation and Franck–Condon factors yields the proper variation with temperature, provided that the effects of specimen charging due to low conductivities at low temperatures are corrected for, as shown in the figure. Such effects are thus expected to be important in all polar solids for which electronic relaxation around the core hole cannot be complete enough to leave final vibrational states of very nearly the same form as the initial vibrational states. In metals, on the other hand, conduction electron screening is expected to be complete enough to leave the initial- and final-vibrational manifolds nearly identical. Thus, in metals the distribution of phonon excitation probabilities or Franck–Condon envelope is sharply peaked around the initial states (as can be seen by considering Eq. (63) for a single set of orthonormal functions); therefore, very little extra broadening is expected.
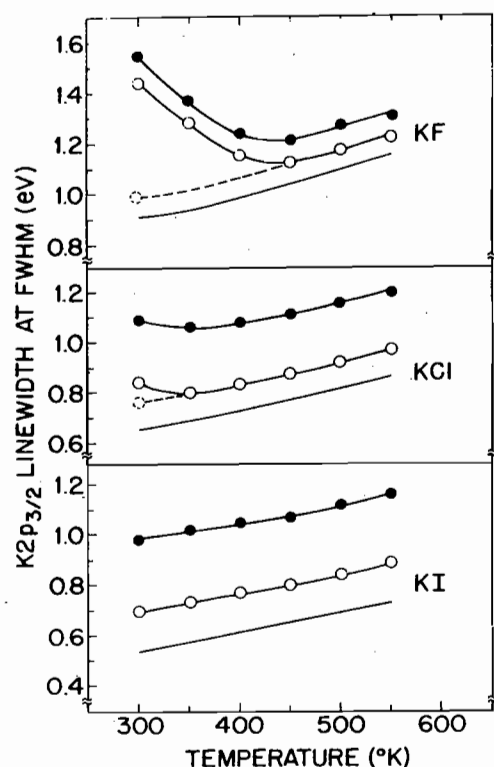
Fig. 41. Variation of the $K2p_{\frac{1}{2}}$ FWHM with temperature in solid KF, KCl, and KI. the curves —●—●— are the unaltered experimental data. The curves —○—○— have been corrected for lifetime and instrumental width contributions. The dotted curves represent further corrections for specimen charging that occurred in KF and KI at low temperatures. The solid curves are theoretical calculations based upon final-state vibrational broadening. (From Citrin *et al.*, ref. 85.)

VI. ANGULAR-RESOLVED MEASUREMENTS ON SOLIDS

A. Introduction

Angular-resolved XPS studies of solids have very recently been reviewed by the author,[17] so only a brief outline of the most significant aspects and certain very new results will be presented here. The most generally occurring types of effects are those involving surface sensitivity enhancement for grazing angles of electron exit *or* x-ray incidence with respect to the surface and two types of anisotropies observed in the angular distributions of photoelectron intensities from single-crystal specimens.

The schematic geometry shown in Fig. 42 both reiterates the definitions of various angles as discussed previously here (cf. Figs 7 and 17) and also indicates that the electron emission direction can be made to have any
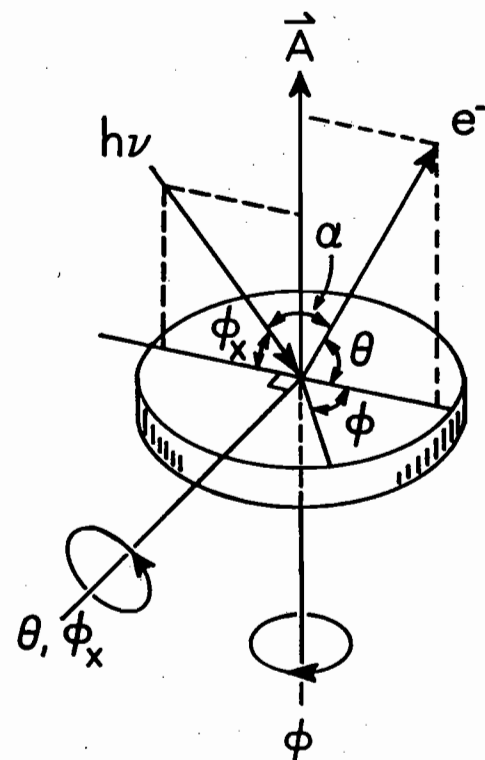
Fig. 42. General geometry for an angular-resolved XPS experiment. Rotations on the two perpendicular axes shown vary θ, ϕ_x and ϕ over their full allowed ranges. The angle α also may be varied, but is most commonly held constant.

orientation with respect to a set of axes fixed in the specimen if externally-accuated rotation is possible on the two perpendicular axes shown. Rotation on the axis perpendicular to the plane containing the photon and electron propagation directions varies the angles θ and ϕ_x describing electron exit and x-ray incidence, respectively. Rotation about the second axis parallel to the specimen surface normal varies the azimuthal angle ϕ as measured with respect to a specimen-fixed reference. Low ϕ or low ϕ_x thus corresponds to a grazing condition. The angle α is held fixed in most current XPS systems. Two-axis specimen goniometers for this purpose have been specially built for use in XPS studies, and various instrumental aspects of carrying out such measurements have been reviewed elsewhere.[17, 74, 202, 290]

B. Surface Sensitivity Enhancement at Grazing Electron Exit Angles

The achievement of greater relative surface sensitivity at conditions of grazing electron exit angles has already been discussed in connection with the

θ-dependent relationships describing peak intensities in Section III.F.2. The application of this procedure in XPS was first demonstrated by Fadley and Bergström,[291] and first quantitatively applied by Fraser et al.[201] As a simple illustration of the fundamental mechanism, Fig. 43 illustrates the way in which the mean depth of no-loss emission varies for a homogeneous, semi-infinite substrate. If Λ_e is assumed to be a direction-independent property of the material, this mean depth is given at any angle by $\Lambda_e \sin \theta$, so it is clear that a decrease of θ from say 90° to 5° will decrease the mean depth by about a factor of 6. This is a highly significant change that has by now been used in numerous studies to enable selectively altering the surface sensitivity of the XPS measurement.[17]
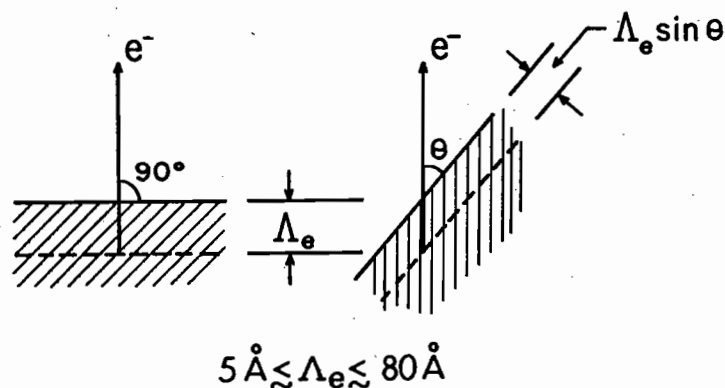
Fig. 43. Illustration of the basic mechanism producing surface sensitivity enhancement for low electron exit angles θ. The average depth for no-loss emission as measured perpendicular to the surface is given by $\Lambda_e \sin \theta$.

The only significant moderating factor that may in certain circumstances render such low-θ measurements somewhat less dramatic in capability is the presence of surface roughness. Surface roughness in general causes the local microscopic true angles of emission θ^t to differ from the experimental value θ as measured relative to the macroscopic planar average of the specimen surface. In general, for low θ values, roughness is expected to cause θ^t to be greater than θ, so that surface sensitivity enhancement is expected to be diminished.[17, 202, 290-294] Roughness further has the effect of shading certain portions of the surface from x-ray incidence and/or electron exit. Such effects have been studied both experimentally and theoretically for a few systems,[17, 202, 203, 290-294] and, although it is clear that large-scale roughness can significantly alter the type of surface enhancement achieved,[203] it has also been found for one system that, even with pressed powder pellets of the type often used as specimens in XPS, a usefully large surface enhancement can be achieved at low θ.[293] Thus, although roughness effects always need

to be considered in any quantitative analysis of such XPS data and the preparation of highly planar specimens is essential for some work,[294] there are good reasons to expect very general utility of the low-θ surface enhancement procedure. We now consider a few examples of the application of this method.

In Fig. 44, broad-scan spectra are shown at various angles for a highly-polished silicon specimen with an oxide overlayer 1–2 atomic layers in
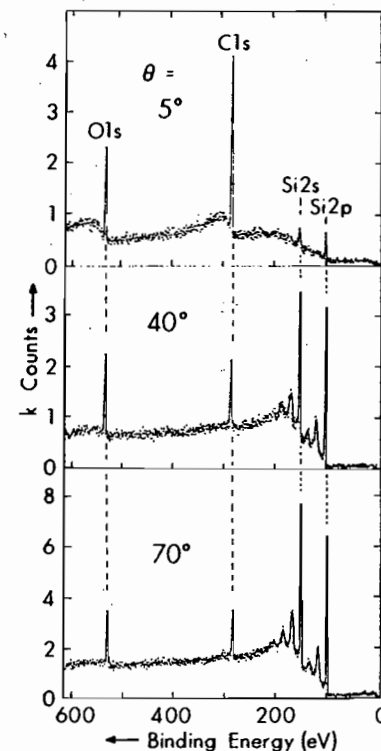

Fig. 44. Broad-scan core spectra at low and high exit angles for a Si specimen with a thin oxide overlayer (~ 4 Å) and an outermost carbon contaminant overlayer approximately 1–2 monolayers in thickness. The C1s and O1s signals are markedly enhanced in relative intensity at low θ due to the general effect presented in Fig. 43. (From Fadley, ref. 17.)

thickness, and an outermost overlayer of carbon-containing residual gas impurities of approximately the same thickness. (These thicknesses were estimated using Eqs such as (117) and (118).) Pronounced peaks due to the O1s, C1s, Si2s, and Si2p core levels are observed. At the higher emission angles of 40° and 70°, plasmon loss structure is also found to be associated with the Si peaks (cf. also Fig. 1 for Al). As θ is lowered to a grazing exit condition, marked changes occur in the relative intensities of all peaks, in

fact causing a complete inversion in ordering. At high θ where maximum bulk sensitivity is expected (Λ_e in Si is ~ 37 Å and Λ_e' in SiO$_2$ is ~ 27 Å[294]), the intensity order is Si$2s$, $2p \gg$ O$1s >$ C$1s$, where at low θ with maximum surface sensitivity, it is C$1s >$ O$1s \gg$ Si$2s$, $2p$. Such a three-angle scan thus clearly establishes the mean vertical displacement of all dominant species with respect to the surface, yielding very directly a qualitative concentration profile. If the Si$2p$ region for this specimen is examined more closely, it is further found to exhibit a chemical shift between oxide and element, as shown in Fig. 45. However, the thin oxide layer present yields only a very weak relative intensity in the Si$2p$ (oxide) peak at the relatively high angle of $\theta = 49°$.

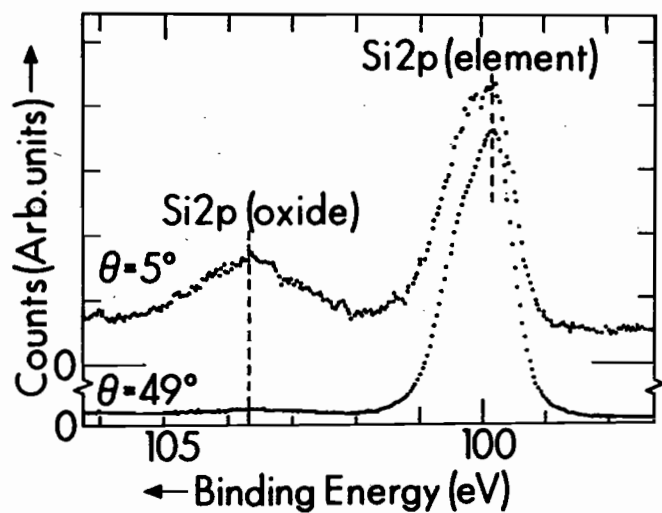Fig. 45. Si$2p$ core spectra at $\theta = 5°$ and 49° for the specimen of Fig. 44. The chemically-shifted Si$2p$ (oxide) peak is enhanced in relative intensity by approximately a factor of 20 between 49° and 5°. (From Fadley, ref. 17.)

The spectrum obtained at $\theta = 5°$ by contrast exhibits marked enhancement by a factor of ~ 20 in the oxide relative intensity. More quantitative studies of such relative intensity changes with angle have also been made by Hill et al.,[294] and, although certain discrepancies are found to occur at low θ values with respect to the simple intensity expressions given in Section III.F.2, case (c), it nonetheless appears possible to extract highly quantitative data concerning specimen geometry and electron attenuation lengths.

An additional effect that is of interest in connection with the enhanced surface sensitivity achievable at low θ is a change in the relative intensities of various inelastic loss processes. For example, for an atomically clean surface of aluminium (which exhibits well-defined surface- and bulk-plasmon excitations at different energies), it has been found by Baird et al.[295] that

the surface plasmon losses are markedly enhanced in relative importance at low θ. Some data from this study are shown in Fig. 46. The reason for this enhancement is that the surface- and bulk-plasmons are spatially orthogonal.[197] Because decreasing the angle of exit also decreases the mean depth of emission, the relative probability of exciting a surface plasmon is thus also increased at low exit angles. Comparisons of such data with theoretical calculations for a free electron metal[194] furthermore yield good agreement with experimental relative intensities and further suggest that the creation of plasmons occurs by means of both extrinsic (after excitation) and intrinsic
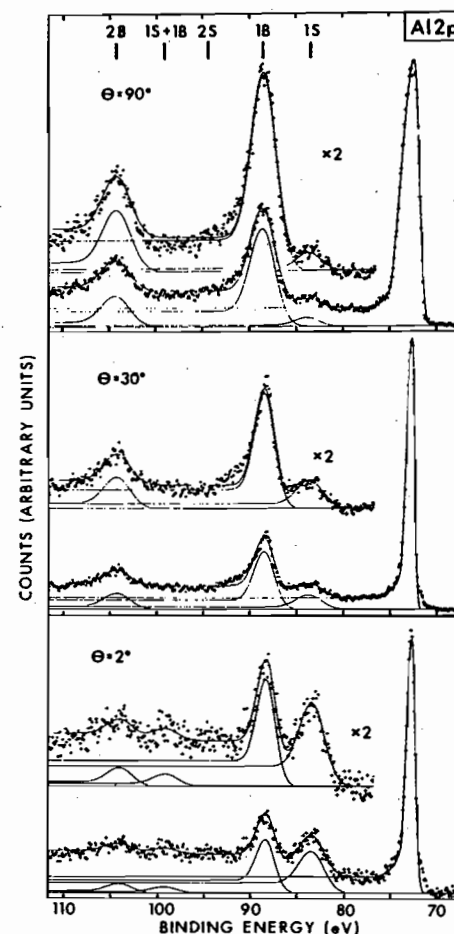

Fig. 46. Al$2p$ plasmon loss spectra from a clean surface of polycrystalline aluminium at $\theta = 90°$, 30°, and 2°. The positions of various combinations of surface and bulk losses are denoted 1S, 1B, etc. Note the marked enhancement of the relative intensity of the surface plasmon loss (1S) for grazing exit angles. (From Baird et al., ref. 295.)

(during excitation) processes.[295] An additional interesting feature of such angular-dependent loss measurements is that they can be used to determine the locations of adsorbed molecules relative to a surface. Specifically, the O1s loss spectrum for an ~0·2 monolayer coverage of oxygen on aluminium exhibits only surface plasmon peaks at grazing electron exit, indicating that the oxygen has not penetrated significantly below the surface plane.[295, 296] Thus, the angular dependence of such absorbate loss structures should provide useful complementary information concerning adsorption geometries and near-surface electronic structure.

The ground-state valence electronic structure of a solid is also predicted theoretically to change near its surface,[297] and it is of interest to determine whether angle-resolved XPS studies can detect this. One effect that should occur in transition metals is a narrowing of the FWHM of the d-bands near the surface due to reduced coordination number.[297] Such effects have been studied quantitatively by Mehta and Fadley[298] for the case of clean polycrystalline copper surfaces, and the experimental and theoretical d-band
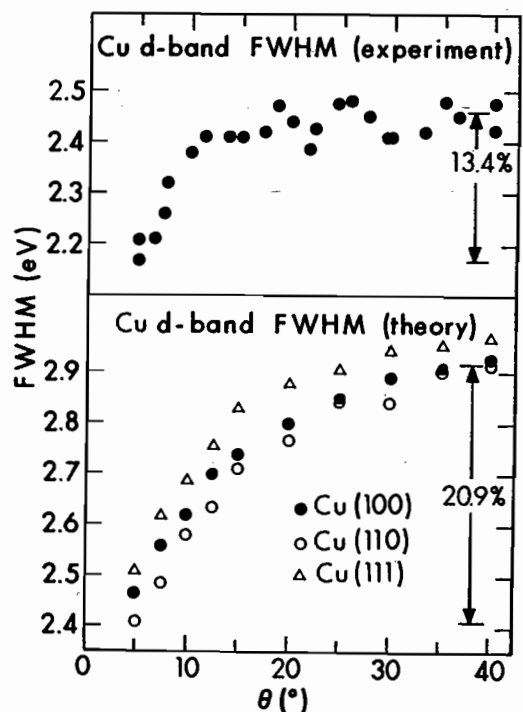
FWHM values determined are summarized in Fig. 47. The small, but unambiguous decreases in FWHM observed at low θ are consistent with the theoretical calculations, with theory showing somewhat larger relative changes that could easily be explained by several effects.[298] Thus, such low-θ measurements can also be used to probe alterations in the near-surface valence electronic structure.

C. Surface Sensitivity Enhancement at Grazing X-ray Incidence Angles

A second mechanism producing enhanced surface sensitivity involves measurements carried out at very low x-ray incidence angles ϕ_x. For $\phi_x \lesssim 1°$, it was first noted by Henke[178] that the mean x-ray penetration depth in a typical XPS experiment (which is 10^3–10^5 Å for $\phi_x \gg 1°$) decreases markedly to values of the same order as the electron attenuation length Λ_e. This further suggests that surface-atom signals will be enhanced in relative intensity at low ϕ_x, as was first demonstrated by Mehta and Fadley.[179] The reason for this decrease in x-ray penetration depth is the onset of significant refraction such that $\phi_x' \ll \phi_x$ (cf. Fig. 17) and reflection at the solid surface. The interactions of typical XPS x-rays with a homogeneous medium are furthermore well described by a macroscopic classical treatment,[178] and detailed expressions for predicting penetration depths and expected surface sensitivity

Fig. 47. Experimental and theoretical angular dependence of the FWHM of the Cu3d valence-band peak. The width decreases at low θ due to d-band narrowing near the surface that is in turn caused by reduced coordination number. (From Mehta and Fadley, ref. 298.)
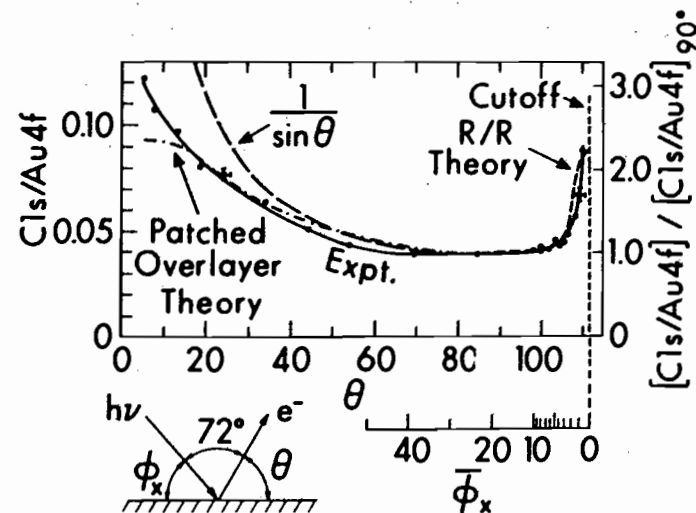

Fig. 48. Angular dependence of the C1s/Au4f intensity ratio for a gold specimen with a thin carbon-containing overlayer. Enhancement of the near-surface carbon signal is found for both grazing electron exit (low θ) and grazing x-ray incidence (low ϕ_x). The low-ϕ_x enhancement is well predicted by classical calculations allowing for x-ray refraction and reflection (R/R) at the surface, as shown by the dashed curve. (From Mehta and Fadley, ref. 179.)

enhancements in terms of the material optical constants and other parameters have been presented elsewhere.[17, 178, 179]

As an example of the surface sensitivity enhancement occuring at low ϕ_x, Fig. 48 shows data obtained from a gold specimen with ~ 2 atomic layers of carbon-containing material as an overlayer. The C1s/Au4f intensity ratio thus serves as a measure of relative surface sensitivity, and it is observed to increase at both low θ (for reasons discussed in the last section) and low ϕ_x. The increase at low ϕ_x is comparable to that at low θ (approximately a factor of 2–3), and there is good agreement between experiment and theoretical calculations including refraction and reflection effects. Note the very sharp onset of the low-ϕ_x enhancement over a region of only a few degrees near $\phi_x=0$. Similar effects have also been noted in the Si2p(oxide)/Si2p(element) ratio for silicon with varying oxide overlayer thicknesses.[299] Also, the optical properties of several solids at XPS energies of ~ 1.5 keV have been used to predict that such phenomena should be of very general occurrence.[17]

It should be noted in connection with low-ϕ_x studies, however, that surface roughness effects can be very important in any attempt at quantitatively analyzing such data.[299] This is due to the very small incidence angles involved, so that if the true microscopic incidence angle $\phi_x{}^t$ deviates by even $\sim 0.1°$ from the macroscopically measurable ϕ_x, a significant change occurs in the degree of refraction and reflection. Thus, surface preparation and accurate angle measurement are both very critical. A further practical problem is that surface shading by any roughness present will generally act to much diminish absolute photoelectron intensities at low ϕ_x. Thus, low ϕ_x surface enhancements may serve as a useful complement to those at low θ, but the measurement and interpretation of low-incidence-angle data may not be as straightforward.

D. Single-crystal Effects

Two rather distinct types of single-crystal effects have been noted in prior XPS studies. The physical origins and possible interpretations of these will be briefly discussed.

1. *Electron Channeling and Kikuchi Bands.* In measurements of core peak intensities or energy-integrated valence-spectral intensities from single-crystal specimens as a function of the emission angles θ and ϕ in Fig. 42, pronounced fine structure is noted. The first effects of this type were observed by Siegbahn et al.[300] in NaCl and by Fadley and Bergström[291] in Au. Baird et al.[200] have obtained the most detailed set of such data to date for Au4f emission from a Au crystal with (001) orientation and this is summarized in the stereographic projection intensity contour plot of Fig. 49(a). Considerable fine structure is evident in this plot, with many features possessing angular FWHM values of only ~ 5–$10°$ and peak height : background ratios as high as $\sim 2 : 1$. It is

thus clear that no peak intensity analysis involving a single crystal can neglect such effects.

The origin of this fine structure is primarily electron diffraction from the various sets of planes in the crystal. These effects are furthermore very closely related to the Kikuchi bands seen in low-energy electron diffraction (LEED) experiments carried out with $E_{kin} \gtrsim 300$ eV,[301] as well as to channeling phenomena seen in the emission of high-energy electrons ($\sim 10^4$–10^6 eV) from radioactive nuclei imbedded in single crystals.[302] Based upon prior experimental and theoretical studies in these two areas,[301, 302] the qualitative expectation is for each set of planes denoted by Miller indices (hkl) to have associated with it a band of enhanced intensity for photoelectron emission that is parallel with the planes to within plus or minus the first-order Bragg angle θ_{hkl}, as defined from
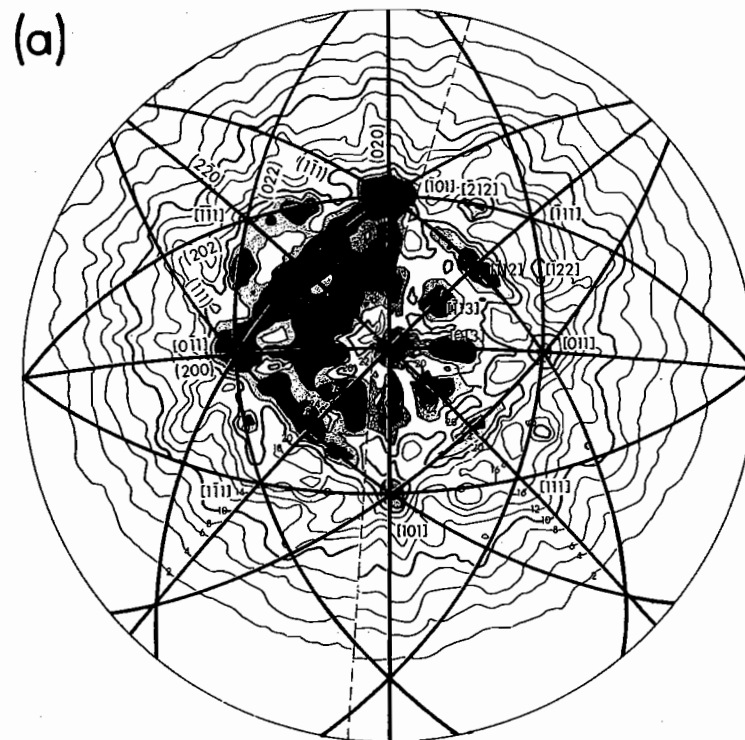
$$\lambda_e = 2d_{hkl} \sin \theta_{hkl} \qquad (163)$$

Fig. 49. (a) Experimental photoelectron intensity contours for Au4f emission from a Au(001) single-crystal surface. The contours are plotted in stereographic projection with various low-index directions indicated as [hkl]. The normal to the surface therefore lies in the centre of the figure. The arcs represent low-index planes available for electron diffraction or channelling.
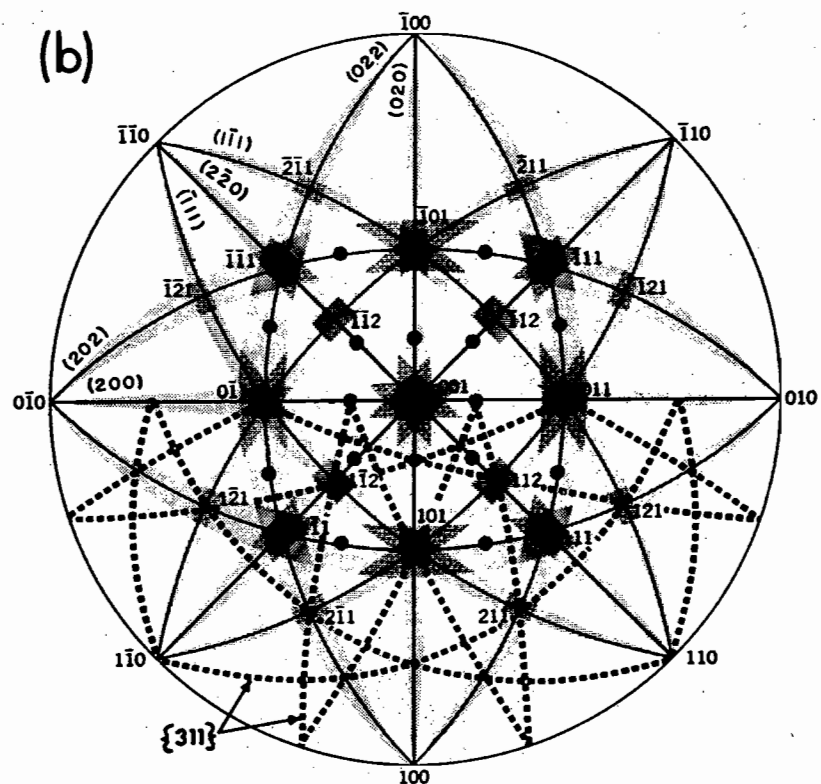
Fig. 49. (b) Qualitative theoretical simulation of the intensity pattern of (a) based on shaded rectangular Kikuchi bands of the form given by the dashed line in Fig. 50. The dotted lines in the lower half of the figure represent the centres of weaker, broader bands from lower-index planes that would also appear at mirror-symmetry-related points in the upper half. (From Baird et al., ref. 200.)

with

$$\lambda_e \text{ (in Å)} = \text{electron deBroglie wavelength}$$

$$= [150/E_{kin} \text{ (in eV)}]^{\frac{1}{2}} \qquad (164)$$

$$d_{hkl} = \text{the interplanar spacing}$$

Such Kikuchi bands are furthermore expected to be approximately uniform in intensity over the $\pm \theta_{hkl}$ range, and to drop off rather sharply at the limits of this range, as shown schematically in Fig. 50. For typical higher-energy XPS photoelectrons and lower-index metal crystal planes, θ_{hkl} is found to lie in the range 3–15°. The overall photoelectron intensity distribution above a single-crystal surface is thus expected to be approximately given by a super-position of such bands for the various low-index planes within the crystal.
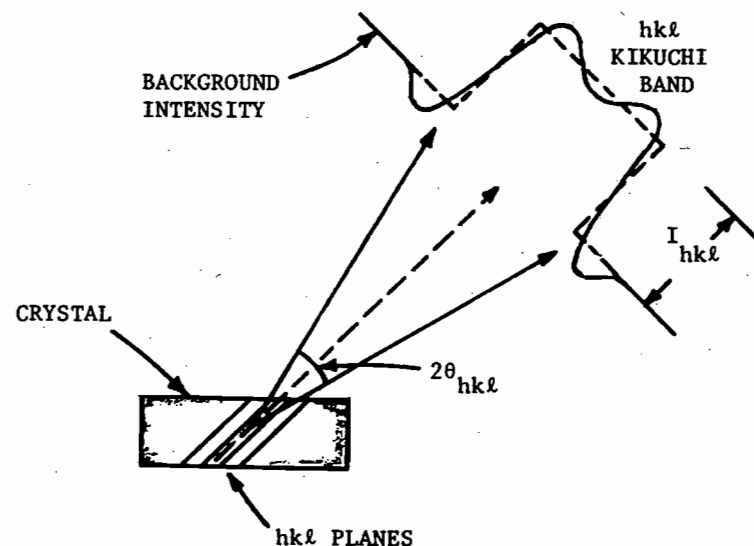
Fig. 50. The approximate form expected for a Kikuchi band from the (hkl) set of planes in a single crystal.

As a qualitative test of this interpretation, Fig. 49(b) presents a stereo-graphic projection on which shaded bands corresponding in width and placement to those expected for the lowest index planes in Au have been inserted. Dotted lines in the lower half of the figure also indicate the centres of broader and weaker bands expected from higher-index planes. Comparison of Figs 49(a) and 49(b) indicates that there is good correspondence between experiment and theory as to the locations of high-intensity regions and fine structure. Recently, more quantitative calculations for copper have been carried out by Baird et al.[303] in which each band is given a height proportional to the Fourier coefficient V_{hkl} in the crystal potential; these calculations yield very good agreement with similar intensity contours for copper. Thus, the basic systematics of such effects is well established and relatively easily predicted, and such measurements can provide rather direct information concerning the near-surface atomic order and crystal orientation. Further-more, in the very near future, more highly accurate theoretical calculations of such effects utilizing methods developed for LEED analyses should become available.[304]

A final important point in connection with such core-level angular distri-bution measurements is that it may be possible to utilize them for determining the bonding geometries of atoms or molecules adsorbed on single-crystal surfaces. That is, if core-level emission from an adsorbed atom does exhibit angular anisotropy, it must be primarily associated with final-state scattering effects that should, in turn, be strongly related to the nearest-neighbor

atomic geometry. Very recent measurements in our laboratory do in fact indicate that such anisotropies exist.

2. *Valence Spectra.* It was first noted by Baird et al.[185, 305] that XPS valence spectra from a single crystal exhibit considerable changes in fine structure as the electron emission direction is varied with respect to the crystal axes. As an example of these effects, Fig. 51 presents Au valence
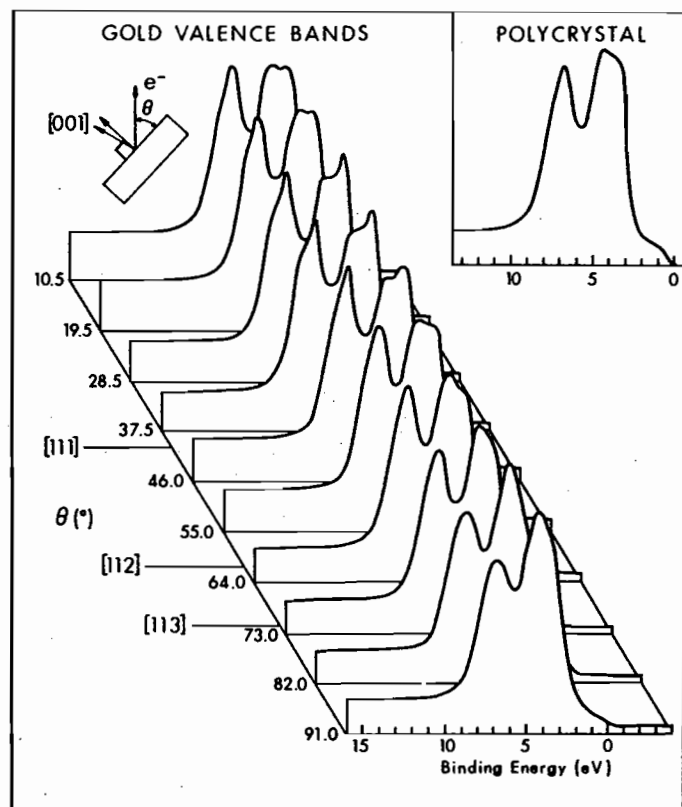

Fig. 51. Au valence spectra from a (001) single-crystal surface obtained at various θ values in a single polar scan passing through the [111], [112], and [113] directions. A polycrystalline spectrum is shown for reference. (From Baird et al., ref. 200.)

spectra obtained with electron emission along various directions in a single θ scan. Although the basic two-peak structure in the dominant d-band peak is present for all directions, there are pronounced changes in the relative intensities and shapes of the two components. In particular, Au spectra obtained with emission along the [001], [101], and [111] directions exhibit probably the most pronounced differences relative to one another, as shown in Fig. 52. Similar changes in single-crystal XPS valence spectra with direction

have by now also been noted in Ag,[306] Cu,[307, 308] Pt,[309] and the layer compounds MoS_2, $GaSe_2$, and $SnSe$.[310]

The occurrence of such anisotropic effects thus means minimally that considerable care must be exercised in interpreting any XPS valence spectrum from a single crystal in terms of quantities such as the total density of states. That is, the total density of states $\rho(E)$ is by definition a non-directional quantity, as is the mean cross-section $\bar{\sigma}_E(h\nu)$, so that clearly such single-crystal effects add an element beyond the model summarized in Eq. (107). For example the Si spectrum shown in Fig. 14 may well exhibit an extra strength in the peak labelled "L_1" due to such effects.[305] As noted in Section III.D.4, the connection of XPS spectra to the density of states in a direct way implies a type of uniform averaging over initial states that need not be possible in a directionally-sensitive single-crystal experiment.

As it is reasonable to expect that the anisotropies noted in XPS valence emission from single crystals are associated somehow with the basic
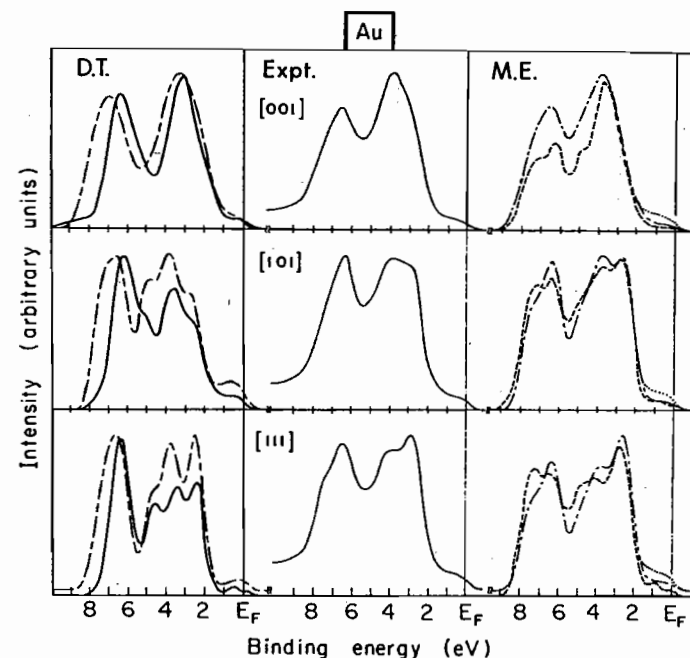
Fig. 52. Experimental and theoretical angular-resolved XPS Au valence spectra for electron emission along the [001], [101], and [111] directions. The data were obtained with monochromatized AlKα radiation. "D.T." represents calculations based upon the direct-transition model. "M.E." represents plane-wave matrix-element calculations. The band structures utilized in the theoretical calculations were: ——, Christensen's RAPW[315] and — —, — — —, two slightly different choices for the spin–orbit parameter in Smith's tight-binding interpolation scheme.[316] (From refs 185, 311, and 317.)

symmetries of the initial states involved, it is of considerable interest to develop theoretical models for the interpretation of such effects. Two different approaches to this problem have been proposed.[185, 306-312] Both of these models begin with the basic direct-transition expression given in Eq. (106), but the different assumptions made in each yields final predictions of a much different form. These two models are:

(1) *The Direct Transition Model.* In this model, the wave-vector conservation embodied in Eq. (104) is primarily emphasized. This viewpoint has been used previously to analyze angular-dependent UPS data from single crystals,[182, 313] and suitable modifications to permit its direct application to higher-energy photoemission experiments were first discussed by Baird *et al.*[185] Rigorous wave-vector conservation is used to connect each observed final-state wave vector $\mathbf{k}^f$ with a unique initial-state wave vector $\mathbf{k}$ within the reduced Brillouin zone by means of a suitable (and unique) reciprocal lattice vector $\mathbf{g}$. The *magnitude* of $\mathbf{k}^f$ is determined from the internal kinetic energy $E_{\text{kin}, i'}$ (cf. Fig. 12) by assuming that the free-electron dispersion relation $E_{\text{kin}, i'} = \hbar^2 (k^f)^2/2m$ is valid at high excitation energies. At XPS energies, k^f furthermore varies very little over the valence spectrum: for example, in gold with lattice constant $a = 4 \cdot 08$ Å, it is found that $12 \cdot 84 (2\pi/a) \leqslant k^f \leqslant 12 \cdot 88 (2\pi a)$, where $2\pi/a$ is approximately the reduced zone radius. The *direction* of $\mathbf{k}^f$ (or, equivalently, the direction of the photoelectron momentum) with respect to the crystal axes is determined from the known crystal orientation relative to the spectrometer acceptance solid angle. (Small direction corrections due to electron refraction in crossing the surface barrier V_0 are necessary only for very low angles of electron exit.[17, 307]) The finite solid angle of acceptance of the electron energy analyzer distributes the
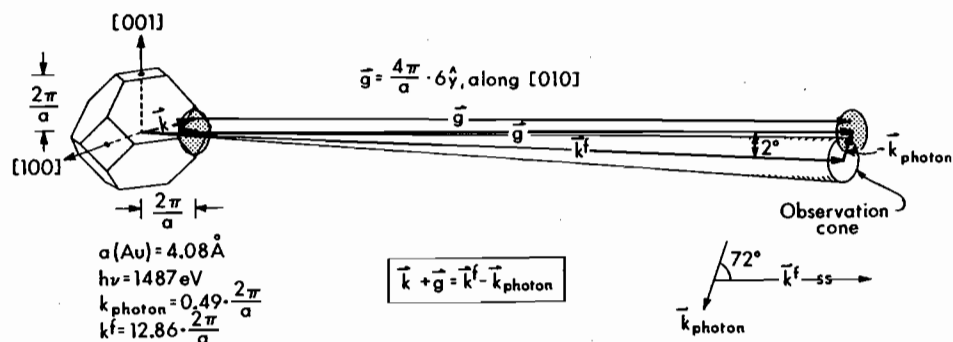

Fig. 53. Scale drawing in k-space of the direct transitions that would be involved in XPS emission along the [010] direction in a Au single crystal. The initial states from which emission could occur are represented by those k values in the shaded disc near the face of the reduced Brillouin zone at left. The additional involvement of variable-magnitude phonon wave vectors due to vibrational effects appears, however, to lead to rather full zone averaging in angular-resolved XPS spectra from Au at room temperatures, as discussed in the text.

observed $\mathbf{k}^f$ values over a disc-like region in k-space, as shown in the scale drawing for gold in Fig. 53, where the acceptance solid angle is taken for illustration to be conical with a $2 \cdot 0°$ half angle. Each $\mathbf{k}^f$ value can then be corrected by the non-negligible $\mathbf{k}_{h\nu}$ associated with the photon to yield a set of vectors $\mathbf{k}^f - \mathbf{k}_{h\nu} = \mathbf{k} + \mathbf{g}$ (shown as the right-hand shaded disc in the figure) that permits uniquely determining the set of $\mathbf{k}$ values in the reduced zone from which allowed transitions can occur (shown as the left-hand shaded disc lying coincidentally very near a reduced-zone face). Due to the finite size of the disc (cf. its size to that of the reduced zone in Fig. 53), more than one $\mathbf{g}$ may be involved, depending on the exact placement of the disc in k-space or, equivalently, the observation direction in real space. It is further assumed in this model that the matrix elements for all $\mathbf{k} \rightarrow \mathbf{k}^f$ transitions are approximately equal, so that an angular-resolved spectrum is finally predicted to be proportional to the density of electronic states over the allowed $\mathbf{k}$ region (*not* the total density of states).

This model has been unambiguously demonstrated by Wagner *et al.*[314] to predict correctly all of the major spectral changes occurring with emission direction and photon energy for copper in the intermediate photon energy range $40 \lesssim h\nu \lesssim 200$ eV. XPS calculations based upon this model for Au with emission along [001], [101], and [111] are shown in Fig. 52, where they are indicated by "D.T." and compared with experimental spectra. Two different initial-state band structures have been utilized in the calculations,[315, 316] yielding two different sets of curves. The most accurate band structure was used for the solid curves, and comes from a relativistic augmented plane wave (RAPW) calculation by Christensen.[315] Both sets of direct-transition curves qualitatively predict the correct changes in both the relative intensities of the two main components and the shapes of each component, although the calculations do predict more change with direction than is noted experimentally. Similar agreement has been found for 9 other directions in Au,[317] as well as 6 directions in Cu,[307] leading to previous conclusions[185, 307] that the direct-transition model represents a good description of such effects in XPS. However, very recent data obtained by Hussain *et al.*[318] for Au with both MgKα and AlKα radiation are at variance witht his model: specifically, for emission along [001], [111], and [112], theory predicts large changes in the spectra of a given direction when photon energy is changed (because the disc changes position in the reduced zone due to the change in the length of $\mathbf{k}^f$), whereas negligible differences are observed experimentally. In addition,[318] for excitation with AlKα, the free-electron metal Al is found not to exhibit *any* spectral changes with emission direction, again in disagreement with direct-transition predictions. It thus appears that some form of wave-vector smearing or reduced-zone averaging is occurring, probably due to the creation or annihilation of phonons, as suggested first by Shevchik[186] and discussed

previously in Section III.D.4. The fraction of direct transitions for which phonon smearing is absent is most simply estimated from the Debye–Waller factor:[187]

$$\text{Debye–Waller factor} = \exp\left(-\tfrac{1}{3}\langle u^2 \rangle g^2\right) \qquad (165)$$

where

$\langle u^2 \rangle$ = the mean squared vibrational displacement of atoms in the lattice

$g^2 = |g|^2$, with g the reciprocal lattice vector involved in a given direct transition

$\langle u^2 \rangle$ is thus a function of material and temperature. In XPS, g^2 is of the same order as $(k^f)^2$ (cf. Fig. 53) and therefore is much larger than the corresponding quantity in UPS. Thus, the Debye–Waller factor can be very small in XPS, as, for example, 0·04 in Au at 25 °C. Such small values suggest that rather complete zone averaging may occur in room-temperature angular-resolved XPS measurements on many systems, as previously noted. (In fact, Williams et al.[319] have recently noted the disappearance of direct-transition effects in UPS spectra of Cu obtained at high temperature that very nicely confirm phonon involvement.) The direct transition model as outlined here thus may not be applicable to room-temperature XPS measurements on many materials, even though it clearly is a valid description at lower excitation energies,[313, 314] and perhaps also at lower temperatures in XPS.

(2) *The Plane-wave Matrix-element Model.* This model was first discussed in connection with angular-dependent XPS spectra by McFeely et al.[306] Although k-conserving direct transitions are used as a starting point, it is further assumed that final-state complexities somehow smear out the determination of k and k^f to such a degree that essentially all k values in the reduced zone can contribute to emission in any direction. Mixing of different plane-wave components into the final electronic states by various scattering processes was first suggested as the source of such zone averaging,[306] but such effects do not seem to be strong for copper with $h\nu \leqslant 200$ eV.[314] More likely, the creation or annihilation of phonons in the photoelectron excitation event is responsible.

In the limit of complete zone averaging, anisotropies in XPS valence spectra are then assumed by McFeely et al.[306] to be due to directional matrix elements as summed over all occupied initial states. These matrix elements are in turn calculated by assuming a plane-wave final state of the form:

$$\phi_{\mathbf{k}}{}^f(\mathbf{r}) = \exp\left(i\mathbf{k}^f\cdot\mathbf{r}\right) \qquad (166)$$

and a tight-binding or LCAO initial state of the form:[96, 99]

$$\phi_{\mathbf{k}}(\mathbf{r}) = \sum_{\mathbf{R}_i} \exp\left(i\mathbf{k}\cdot\mathbf{R}_i\right)\left\{\sum_{\mu} C_{\mu\mathbf{k}} X_{\mu}(\mathbf{r}-\mathbf{R}_i)\right\} \qquad (167)$$

in which

$\mathbf{R}_i$ = the position of an atomic center in the lattice

$X_{\mu}(\mathbf{r}-\mathbf{R}_i)$ = an atomic orbital centered at $\mathbf{R}_i$

$X_{\mu}(\mathbf{r}) = R_{\mu}(r) Y_{\mu}(\theta, \phi)$ [cf. Eq. (36)]

$C_{\mu\mathbf{k}}$ = an expansion coefficient

Computing matrix elements $\langle \phi_{\mathbf{k}}{}^f | \mathbf{A}\cdot\nabla | \phi_{\mathbf{k}} \rangle$ can then be shown[159, 306, 312] to yield a linear combination of the Fourier transforms of the various atomic orbitals making up the initial-state orbital. Such Fourier transforms furthermore exhibit the same angular dependence in $\mathbf{k}^f$ space that the atomic function has in real space, and they can thus be written as

$$X_{\mu}(\mathbf{k}^f) = f_{\mu}(k^f) Y_{\mu}(\theta_{\mathbf{k}}{}^f, \phi_{\mathbf{k}}{}^f) \qquad (168)$$

with $\theta_{\mathbf{k}}{}^f, \phi_{\mathbf{k}}{}^f$ indicating the direction of $\mathbf{k}^f$, and $f_{\mu}(k^f)$ being a radial integral dependent on $|k^f| = k^f$ only. For radiation with a polarization direction $\mathbf{e}$, it then directly results that

$$|\langle \phi_{\mathbf{k}}{}^f | \mathbf{A}\cdot\nabla | \phi_{\mathbf{k}} \rangle|^2 \propto (\mathbf{e}\cdot\mathbf{k}^f)^2 \Big| \sum_{\mu} C_{\mu\mathbf{k}} X_{\mu}(\mathbf{k}^f - \mathbf{k}_{h\nu}) \Big|^2 \qquad (169)$$

In general, $\mathbf{e}\cdot\mathbf{k}^f$ has been held constant in prior experiments, and for a closely related set of orbitals such as d functions, it can further be assumed that the factor $f_{\mu}(k^f)$ is constant. Finally, each initial state is thus predicted to contribute photoelectron intensity with a weight of $\big| \sum_{\mu} C_{\mu\mathbf{k}} Y_{\mu}(\theta_{\mathbf{k}^f - \mathbf{k}_{h\nu}}, \phi_{\mathbf{k}^f - \mathbf{k}_{h\nu}}) \big|^2$ and a summation can be carried out over all such occupied states. Thus, for example, the contribution of a $d_{x^2-y^2}$ atomic orbital to such a matrix element is predicted to be a maximum along the same directions as the orbital maxima, namely the $\pm x$ and $\pm y$ directions. Orbital symmetry is thus predicted to be very directly reflected in the angular-dependent emission probability. Calculations based upon this model are presented in Fig. 52 for Au, where they are indicated by "M.E." Two different types of tight-binding parameterizations have been utilized, and it is clear that the results are sensitive to this choice. Nonetheless, there is generally good agreement between experiment and theory for the three directions shown, as well as others in Au[306, 311] which have been investigated, and a similar set in Cu.[311] The same type of plane-wave model has also been found by Ley et al.[310] to predict correctly changes in single-crystal valence spectra of the compounds MoS_2, $GaSe_2$, and $SnSe_2$. Thus, it at present appears that the plane-wave matrix element approach is the more correct of the two discussed here for describing room temperature XPS experiments on most materials, although significant questions do still remain as to the validity of using a free-electron plane-wave final state for

computing XPS matrix elements.[165, 186, 318] More accurate theoretical calculations of such effects are thus clearly of interest.

To the degree that such measurements do directly reflect orbital symmetries, such angular-resolved XPS studies should prove to be very useful probes of valence electronic structure.
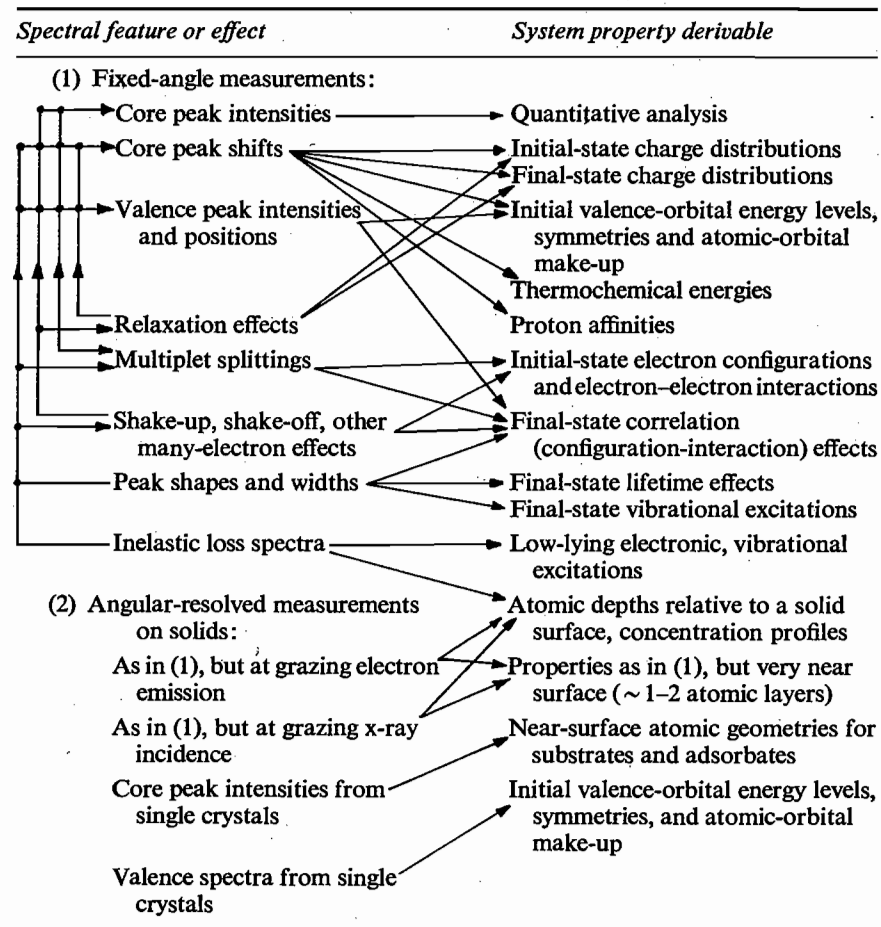
VII. CONCLUDING REMARKS

The aim of this chapter has been to discuss in some detail the basic ideas involved in both performing and interpreting XPS measurements. It is clear that a relatively large number of distinct physical and chemical effects can be related to the observed spectra. This diversity can be both an advantage and a disadvantage in using the technique, depending upon the specific problem at hand and the phenomena encountered. On the positive side, however, is the fact that at least some degree of quantitative understanding has been achieved in connection with all of the effects noted to date. The theoretical interpretation of XPS spectra also involves a liberal mixture of concepts from atomic, molecular, and solid-state physics, thus making the technique truly interdisciplinary in character. A major goal of the discussion here has been to present these diverse ideas within a single, unified framework.

As an important example of the interdependency of different phenomena, final-state effects of various types can tend in certain situations to obscure the initial-state information that is of most interest in many applications. But, on the other hand, final-state effects can also be used to determine additional characteristics of the system. The essential reason for this initial-state/final-state dichotomy is that the photoemission event is inherently very disruptive to the system, leaving it with a hole in a certain subshell and thus a significantly altered set of electron–electron interactions. The interpretive material presented in Sections III–V therefore begins with a rather general discussion of the photoemission process that emphasizes the importance of both initial and final states (as well as inelastic scattering effects). However, the first areas of application considered are intentionally those which for many systems can exhibit the strongest initial-state component: valence-level studies in molecules and solids (Sections III.D.3 and III.D.4), quantitative analysis (Section III.F.3), and core-level binding energy shifts (Section IV). Nonetheless, care must always be exercised in analysing data in order to avoid having the different final-state effects discussed in Section V introduce a significant error in any conclusions concerning initial-state properties.

The potential range of information derivable from XPS spectra is indeed very broad, and a schematic summary of the interrelationships between various observable quantities or effects and basic system properties is presented in Table III. In this table, the possible interactions between different observables are also indicated.

TABLE III

Schematic illustration of the interrelationships between various observable XPS spectral features or their associated effects and the basic system properties potentially derivable from an analysis of such observations

Spectral feature or effect	System property derivable
(1) Fixed-angle measurements:	
Core peak intensities	Quantitative analysis
Core peak shifts	Initial-state charge distributions
	Final-state charge distributions
Valence peak intensities and positions	Initial valence-orbital energy levels, symmetries and atomic-orbital make-up
	Thermochemical energies
Relaxation effects	Proton affinities
Multiplet splittings	Initial-state electron configurations and electron–electron interactions
Shake-up, shake-off, other many-electron effects	Final-state correlation (configuration-interaction) effects
Peak shapes and widths	Final-state lifetime effects
	Final-state vibrational excitations
Inelastic loss spectra	Low-lying electronic, vibrational excitations
(2) Angular-resolved measurements on solids:	Atomic depths relative to a solid surface, concentration profiles
As in (1), but at grazing electron emission	Properties as in (1), but very near surface ($\sim$1–2 atomic layers)
As in (1), but at grazing x-ray incidence	Near-surface atomic geometries for substrates and adsorbates
Core peak intensities from single crystals	Initial valence-orbital energy levels, symmetries, and atomic-orbital make-up
Valence spectra from single crystals	

XPS has been and will no doubt continue to be fruitfully utilized for the study of free atoms, free molecules, and the *bulk* properties of solids and liquids. However, the inherent *surface* sensitivity of the technique when applied to solids and liquids leads to what is certainly one of the most significant areas of application, namely in studying the physics and chemistry of surfaces and interfaces. In this context, the relatively newly developed angular-resolved studies of solids have also clearly been demonstrated to enhance significantly the amount of information derivable, as is also indicated

in Table III. Two separate procedures exist for selectively increasing surface sensitivity by angle variations. For single-crystal specimens, information concerning both detailed atomic geometries and valence-orbital symmetries can also be derived from angular-distribution measurements.

No exhaustive elucidation of specific areas of application for XPS has been attempted here, but it is sufficient to note that by now the technique has been used in problems related to physical chemistry, inorganic chemistry, organic chemistry, biochemistry, solid-state physics, surface chemistry, surface physics, industrial chemistry, and environmental science. Future developments will no doubt involved all of these areas, but with special emphasis on problems related to surface science. A further significant component of future work will no doubt be the more extended use of XPS in combination with other spectroscopic methods such as, for example, the other surface-sensitive techniques of UPS, photoelectron spectroscopy utilizing synchrotron radiation sources, low-energy electron diffraction (LEED), Auger electron spectroscopy (AES), and secondary ion mass spectrometry (SIMS).

Thus, x-ray photoelectron spectroscopy is by now a relatively mature and well-established experimental tool. However, various major problems still remain to be solved concerning both the measurement and the analysis of XPS spectra. These include the ever-present and conflicting needs for higher resolution and higher intensity, which are at present being sought by means of more efficient x-ray monochromators combined with multichannel detection systems. More novel radiation sources and analyzer/detector systems might also provide a further solution to this problem. From the point of view of theory, more quantitative treatments of various final-state effects and electron–electron correlation effects are needed. More accurate calculations of both wave functions and photoelectric cross-sections for molecules and solids would also be very helpful, especially as related to angular-resolved studies of atoms and molecules interacting with solid surfaces.

Acknowledgements

REFERENCES

1. H. Robinson and W. F. Rawlinson, *Phil. Mag.* **28**, 277 (1914).
2. R. G. Steinhardt and E. J. Serfass, *Anal. Chem.* **25**, 697 (1953); and R. G. Steinhardt, F. A. D. Granados, and G. I. Post, *Anal. Chem.* **27**, 1046 (1955).
3. K. Siegbahn, C. Nordling, A. Fahlman, R. Nordberg, K. Hamrin, J. Hedman, G. Johansson, T. Bergmark, S.-E. Karlsson, I. Lindgren, and B. Lindberg, "ESCA: Atomic, Molecular, and Solid State Structure Studied by Means of Electron Spectroscopy", Nova Acta Regiae Soc. Sci. Upsaliensis, Ser. IV, Vol. 20 (Almqvist and Wiksells, Stockholm, 1967), also available as National Technical Information Service Report No. AD 844315, 1968, Dept of Commerce, Springfield, Va, U.S.A. See also earlier references therein, particularly S. Hagström, C. Nordling, and K. Siegbahn, *Z. Physik*, **178**, 439 (1964), in which the first association of core-binding energy shifts with chemical state was made.
4. K. Siegbahn, C. Nordling, G. Johansson, J. Hedman, P.-F. Hedén, K. Hamrin, U. Gelius, T. Bergmark, L. O. Werme, R. Manne, and Y. Baer, "ESCA Applied to Free Molecules" (North-Holland, Amsterdam, 1969).
5. The extensive XPS literature has been reviewed, for example, in D. M. Hercules, *Anal. Chem.* **44**, 106R (1972); W. E. Schwartz, *Anal. Chem.* **45**, 789A (1973); D. M. Hercules and J. C. Carver, *Anal. Chem.* **46**, 133R (1974), and D. M. Hercules, *Anal. Chem.* **48**, 294R (1976); A. D. Baker, M. Brisk and D. Liotta, *Anal. Chem.* **50**, 328, 1978R. Also, from 1972 on, numerous publications have appeared in the *Journal of Electron Spectroscopy and Related Phenomena*.
6. S. B. M. Hagström, and C. S. Fadley in "X-ray spectroscopy", L. V. Azaroff, ed. (McGraw-Hill, New York, 1974).
7. D. A. Shirley, *Adv. Chem. Phys.* **23**, 85 (1973).
8. C. S. Fadley in "Electron Emission Spectroscopy", W. Dekeyser *et al.*, eds (Reidel, Dordrecht, Netherlands, 1973).
9. D. T. Clark in "Electron Emission Spectroscopy", W. Dekeyser *et al.*, eds (Reidel, Dordrecht, Netherlands, 1973).
10. T. A. Carlson, "Photoelectron and Auger Spectroscopy" (Plenum Press, New York, 1975).
11. D. A. Shirley, ed., "Electron Spectroscopy" (North-Holland, Amsterdam, 1972). The proceedings of an international conference held at Asilomar, California, in September 1971.
12. R. Caudano and J. Verbist, eds, "Electron Spectroscopy: Progress in Research and Applications" (Elsevier, Amsterdam, 1974). The proceedings of an international conference held in Namur, Belgium, in April 1974. Also available as Volume 5 in the *Journal of Electron Spectroscopy* (1974).
13. W. L. Jolly in "Electron Spectroscopy: Theory, Techniques, and Applications", C. R. Brundle and A. D. Baker, eds (Academic Press, London and New York, 1977), Chapter 3, Vol. 1.
14. R. L. Martin and D. A. Shirley in "Electron Spectroscopy: Theory, Techniques, and Applications", C. R. Brundle and A. D. Baker, eds (Academic Press, London and New York, 1977), Chapter 2, Vol 1; and *Phys. Rev.* A13, 1475 (1976).
15. Detailed discussions of the application of synchrotron radiation to photoelectron spectroscopy have, for example, been given in papers by D. E. Eastman, by F. C. Brown, R. Z. Bachrach, S. B. M. Hagström, N. Lien,

and C. H. Pruitt, and by others in "Vacuum Ultraviolet Physics", E. E. Koch *et al.*, eds (Pergamon Press, New York, 1974); as well as in W. E. Spicer, K. Y. Yu. I. Lindau, P. Pianetta, and D. M. Collins in "Surface and Defect Properties of Solids", J. M. Thomas and M. W. Roberts, eds (Chem. Soc., London, 1976), Vol. V.

16. The general area of spin-polarized electron emission experiments has recently been reviewed in: M. Campagna, D. T. Pierce, F. Meier, L. Sattler, and H. C. Siegmann, in *Advances in Electronics and Electron Physics*, **41**, 113 (1976).

17. C. S. Fadley, *Prog. Sol. St. Chem.* **11**, 265 (1976).

18. For discussions of energy loss measurements at approximately XPS energies, see, for example, O. Klemperer and J. P. G. Shepherd, *Adv. Phys.* **12**, 355 (1963); H. Raether, *Springer Tracts in Modern Physics*, **38**, 84 (1965); J. Daniels, C. v. Festenburg, H. Raether, and K. Zeppenfeld, *Springer Tracts in Modern Physics*, **54**, 77 (1970), and G. R. Wight and C. E. Brion, *J. Electr. Spectr.* **3**, 191 (1974).

19. C. Kittel, "Introduction to Solid State Physics", 4th edn (Wiley, New York, 1971), Chapters 7 and 8.

20. C. J. Powell, *Surf. Sci.* **44**, 29 (1974).

21. I. Lindau and W. E. Spicer, *J. Electron Spectrosc.* **3**, 409 (1974).

22. C. R. Brundle, *J. Vac. Sci. Tech.* **11**, 212 (1974).

23. Kratos, 403 S. Raymond Avenue, Pasadena, California, U.S.A. is now marketing systems formerly manufactured by AEI Scientific Apparatus Ltd.

24. E. I. DuPont de Nemours and Co., Instrument Products Division, Wilmington, Delaware, U.S.A.

25. Hewlett Packard Co., Scientific Instruments Division, 1601 California Street, Palo Alto, California, U.S.A. Although no longer marketed, the special properties of this spectrometer are discussed in K. Siegbahn, D. Hammond, H. Fellner-Felldegg, and E. F. Barnett, *Science*, **176**, 245 (1972), as well as by R. J. Baird and C. S. Fadley in reference 74.

26. GCA/McPherson Instrument Corp., 530 Main Street, Acton, Massachusetts, U.S.A.

27. Leybold-Heraus GmbH, Gaedestrasse, 5000 Köln 51, West Germany. The electron optics of this system are described in detail in H. G. Nöller, H. D. Polaschegg, and H. Schillalies, *J. Electron Spectrosc.* **5**, 705 (1974).

28. Physical Electronics Industries, Inc., 6509 Flying Cloud Drive, Eden Prairie, Minnesota, U.S.A.

29. Vacuum Generators Inc., Charlwood Road, East Grinstead, Sussex, England.

30. Varian Associates, Analytical Instrument Devices, Palo Alto, California, U.S.A. This system is no longer marketed.

31. A. H. Compton and S. K. Allison, "X-rays in Theory and Experiment" (Macmillan and Co., London, 1935).

32. B. L. Henke in "Advances in X-ray analysis", Vol. 5 (Plenum Press, New York, 1962), p. 285; and in "X-ray Optics and Microanalysis" (Academic Press, New York and London, 1963), p. 157.

33. C. S. Fadley, Ph.D. Thesis, University of California at Berkeley, 1970 (Lawrence Berkeley Laboratory *Report UCRL-19535*).

34. M. O. Krause, *Chem. Phys. Lett.* **10**, 65 (1971).

35. M. S. Banna and D. A. Shirley, *J. Electr. Spectr.* **8**, 23, 255 (1976).

36. R. Nilsson, R. Nyholm, A. Berndtsson, J. Hedman, and C. Nordling, *J. Electr. Spectr.* **9**, 337 (1976).

37. M. O. Krause and J. G. Ferreira, *J. Phys.* **B8**, 2007 (1975).

38. E. Källne and T. Åberg, *X-ray Spect.* **4**, 26 (1975).

39. J. E. Castle, L. B. Hazell, and R. D. Whitehead, *J. Electron Spectrosc.* **9**, 246 (1976).

40. A. Berndtsson, R. Nyholm, R. Nilsson, J. Hedman, and C. Nordling, *J. Electron Spectrosc.* **13**, 131 (1978).

41. K. Siegbahn, *J. Electr. Spectr.* **5**, 3 (1974) and Uppsala University, *Institute of Physics Report*, No. *UUIP–909* (1975).

42. Y. Baer, G. Busch, and P. Cohn, *Rev. Sci. Inst.* **46**, 466 (1975).

43. C. T. Hovland, *Appl. Phys. Lett.* **30**, 274 (1977).

44. R. P. Godwin, "Synchrotron Radiation as a Light Source" in *Springer Tracts in Modern Physics*, **51** (1970).

45. J. F. McGilp and I. G. Main, *J. Electron Spectrosc.* **6**, 397 (1975).

46. C. S. Fadley, G. L. Geoffroy, S. B. M. Hagström, and J. M. Hollander, *Nucl. Inst. Methods*, **68**, 177 (1969).

47. G. Johansson, J. Hedman, A. Berndtsson, M. Klasson, and R. Nilsson, *J. Electron Spectrosc.* **2**, 295 (1973), and references therein.

48. F. J. Grunthaner, N.A.S.A. Technical Brief NPO-13772, Item 57, Spring 1977.

49. M. O. Krause, *Phys. Rev.* **A140**, 1845 (1965); T. A. Carlson and M. O. Krause, *Phys. Rev.* **A137**, 1655 (1965); **A140**, 1057 (1965); **A151**, 41 (1966).

50. J. Berkowitz in "Electron Spectroscopy", D. A. Shirley, ed. (North-Holland, Amsterdam, 1972), p. 391; and in "Electron Spectroscopy: Theory, Techniques, and Applications", C. R. Brundle and A. D. Baker, eds (Academic Press, London, 1977), Chap. 7, Vol 1.

51. See, for example, early gas-phase molecular studies in T. D. Thomas, *J. Chem. Phys.* **52**, 1373 (1970); *J. Am. Chem. Soc.* **92**, 4184 (1970); and D. W. Davis, D. A. Shirley, and T. D. Thomas in "Electron Spectroscopy", D. A. Shirley, ed. (North-Holland, Amsterdam, 1972), p. 707.

52. J. S. Brinen, *J. Electron Spectrosc.* **5**, 377 (1974); *Accts Chem. Res.* **9**, 86 (1976).

53. H. P. Hughes and R. A. Pollak, *Phil. Mag.* **34**, 1025 (1976).

54. T. E. Madey, J. T. Yates, and N. E. Erickson, *Chem. Phys. Lett.* **19**, 487 (1973); *Surf. Sci.* **43**, 526 (1974).

55. P. A. Redhead, J. P. Hobson, and E. V. Kornelsen, "The Physical Basis of Ultrahigh Vacuum" (Chapman and Hall, London, 1968); D. H. Holkeboer, D. W. Jones, F. Pagano, D. J. Santeler, "Vacuum Engineering" (Boston Technical, Boston, 1967).

56. Y. Baer, *Sol. St. Comm.* **19**, 669 (1976).

57. D. E. Eastman in "Electron Spectroscopy", D. A. Shirley, ed. (North-Holland, Amsterdam, 1972), p. 487.

58. S. Evans, *Chem. Phys. Lett.* **23**, 134 (1973).

59. H. Siegbahn and K. Siegbahn, *J. Electron Spectrosc.* **2**, 319 (1972); **5**, 1059 (1974).

60. UPS measurements on liquid Au are, for example, discussed in reference 57.

61. K. D. Sevier, "Low Energy Electron Spectrometry" (Wiley–Interscience, New York, 1972).

62. H. Fellner-Felldegg, U. Gelius, B. Wannberg, A. G. Nilsson, E. Basilier, and K. Siegbahn, *J. Electron Spectrosc.* **5**, 643 (1974); B. Wannberg, U. Gelius, and K. Siegbahn, Uppsala University, *Institute of Physics Report No. UUIP-818* (1973).

63. C. E. Kuyatt, review of electron energy analyzers to appear in this series.

64. C. S. Fadley, C. E. Miner, and J. M. Hollander, *Appl. Phys. Letters*, **15**, 223 (1969); C. S. Fadley, R. N. Healey, J. M. Hollander, and C. E. Miner, *J. Appl. Phys.* **43**, 1085 (1972).
65. E. M. Purcell, *Phys. Rev.* **54**, 818 (1938).
66. H. Z. Sar-el, *Rev. Sci. Inst.* **38**, 1210 (1969).
67. S. Aksela, M. Karras, M. Pessa, and E. Suoninen, *Rev. Sci. Inst.* **41**, 351 (1970); S. Aksela, *Rev. Sci. Inst.* **42**, 810 (1971).
68. R. W. Shaw and T. D. Thomas in "Electron Spectroscopy", D. A. Shirley, ed. (North-Holland, Amsterdam, 1972), p. 105; K. Maeda, *op. cit.* p. 177.
69. K. Siegbahn in "Alpha-, Beta-, and Gamma-ray Spectroscopy", K. Siegbahn, ed. (North-Holland, 1965), Vol. 1, Chap. III.
70. K. Mills and D. A. Shirley, private communication.
71. L. B. Leder and J. A. Simpson, *Rev. Sci. Inst.* **29**, 571 (1958); J. A. Simpson, *Rev. Sci. Inst.* **32**, 1283 (1961).
72. C. N. Berglund and W. E. Spicer, *Rev. Sci. Inst.* **35**, 1665 (1964).
73. D. A. Huchital and J. D. Rigden in "Electron Spectroscopy", D. A. Shirley, ed. (North-Holland, Amsterdam, 1972), p. 79.
74. R. J. Baird and C. S. Fadley, *J. Electron Spectrosc.* **11**, 39 (1977).
75. J. C. Helmer, *Am. J. Phys.* **34**, 222 (1966); J. C. Helmer and N. H. Weichert, *Appl. Phys. Lett.* **13**, 266 (1968).
76. O. Klemperer, "Electron Optics", 3rd edn (Cambridge University Press, Cambridge, 1971), Chaps 1 and 2.
77. B. L. Henke, J. A. Smith, and D. T. Attwood, *J. Appl. Phys.* **48**, 1852 (1977).
78. Channeltron electron multipliers were originally marketed under a registered trademark of the Bendix Corporation. They are now available from various manufacturers.
79. The early development of such electron multipliers is reviewed in W. C. Wiley and C. F. Hendee, *I.R.E. Trans. Nucl. Sci.* **NS-9**, 103 (1962), D. S. Evans, *Rev. Sci. Inst.* **36**, 375 (1965).
80. Ö. Nilsson, L. Hasselgren, K. Siegbahn, S. Berg, L. P. Andersson, and P. A. Tore, *Nucl. Inst. and Meth.* **84**, 301 (1970).
81. C. D. Moak, S. Datz, F. Garcia-Santibanez, and T. A. Carlson, *J. Electron Spectrosc.* **6**, 151 (1975); M. Lampton and F. Paresec, *Rev. Sci. Inst.* **45**, 1098 (1974).
82. C. S. Fadley and D. A. Shirley, *J. Res. Nat. Bur. Stds*, **74A**, 543 (1970).
83. Various self-consistent inelastic loss subtraction procedures such as this have been utilized for XPS valence spectra, as discussed, for example, in references 82, 192, and 298.
84. S. Hüfner and G. K. Wertheim, *Phys. Rev.* **B11**, 678 (1975); *Phys. Rev.* **B11**, 5197 (1975); *Phys. Rev. Lett.* **35**, 53 (1975).
85. P. H. Citrin, P. Eisenberger, and D. R. Hamann, *Phys. Rev. Lett.* **33**, 965 (1974).
86. C. S. Fadley and D. A. Shirley, *Phys. Rev.* **A2**, 1109 (1970).
87. G. K. Wertheim, *J. Electr. Spectr.* **6**, 239 (1975). (As based on mathematical methods developed in ref. 88.)
88. P. H. van Zittert, *Z. Phys.* **69**, 298 (1931).
89. F. J. Grunthaner, Ph.D. Thesis, California Institute of Technology (1974).
90. R. Manne and T. Åberg, *Chem. Phys. Lett.* **7**, 282 (1970).
91. S. T. Manson, *J. Electron Spectrosc.* **9**, 21 (1976).
93. F. Herman and S. Skillman, "Atomic Structure Calculations" (Prentice-Hall, Inglewood Cliffs, New Jersey, 1963).
94. T. A. Carlson and B. P. Pullen, Oak Ridge National Laboratory, *Report No. ORNL-4323* (1969).

95. M. Tinkham, "Group Theory and Quantum Mechanics" McGraw-Hill, New York, 1964).
96. J. M. Ziman, "Principles of the Theory of Solids", 2nd edn (Cambridge University Press, Cambridge, 1972).
97. D. W. Turner, C. Baker, A. D. Baker, and C. R. Brundle, "Molecular Photoelectron Spectroscopy" (Wiley, London, 1970).
98. K. Siegbahn in "Electron Spectroscopy", D. A. Shirley, ed. (North-Holland, Amsterdam, 1972), p. 15.
99. J. Callaway, "Quantum Theory of the Solid State" (Academic Press, New York and London, 1974), Chap. 4.
100. J. B. Mann, Los Alamos Scientific Laboratory, *Reports LA-3690* (1967) and *LA-3691* (1968).
101. T. A. Carlson, C. C. Lu, T. C. Tucker, C. W. Nestor, and F. B. Malik, Oak Ridge National Laboratory, *Report ORNL-4614* (1970).
102. M. Mehta, C. S. Fadley, and P. S. Bagus, *Chem. Phys. Lett.* **37**, 454 (1975).
103. P. S. Bagus, *Phys. Rev.* **139**, A619 (1965).
104. A. Rosen and I. Lindgren, *Phys. Rev.* **176**, 114 (1968).
105. C. S. Fadley, S. B. M. Hagström, J. M. Hollander, M. P. Klein, and D. A. Shirley, *Science*, **157**, 1571 (1967); C. S. Fadley, S. B. M. Hagström, M. P. Klein, and D. A. Shirley, *J. Chem. Phys.* **48**, 3779 (1968).
106. M. E. Schwartz, *Chem. Phys. Lett.* **5**, 50 (1970).
107. P. S. Bagus and H. F. Schaefer, *J. Chem. Phys.* **55**, 1474 (1971); **56**, 224 (1972).
108. L. C. Snyder, *J. Chem. Phys.* **55**, 95 (1971).
109. H. Basch, *J. Electron Spectrosc.* **5**, 463 (1974).
110. E.-K. Viinikka and P. S. Bagus, extended abstract for the International Conference on the Physics of X-ray Spectra, 30 August–2 September, 1976, National Bureau of Standards, Gaithersberg, Md.
111. G. Verhaegen, J. J. Berger, J. P. Desclaux, and C. M. Moser, *Chem. Phys. Lett.* **9**, 479 (1971).
112. C. M. Moser, R. K. Nesbet, and G. Verhaegen, *Chem. Phys. Lett.* **12**, 330 (1971).
113. L. S. Cederbaum and W. Domcke, *J. Chem. Phys.* **66**, 5084 (1977).
114. G. K. Wertheim, R. L. Cohen, A. Rosencwaig, and H. J. Guggenheim in "Electron Spectroscopy", D. A. Shirley, ed. (North-Holland, Amsterdam, 1972), p. 813.
115. L. Ley, F. R. McFeely, J. G. Jenkin, and D. A. Shirley, *Phys. Rev.* **11**, 600 (1975).
116. See, for example, J. E. Lennard-Jones and J. A. Pople, *Proc. Roy. Soc.* **A202**, 166 (1950); C. Edmiston and K. Ruedenberg, *Rev. Mod. Phys.* **35**, 457 (1963).
117. P. W. Payne, *J. Am. Chem. Soc.* **99**, 3787 (1977).
118. J. C. Slater, "Quantum Theory of Atomic Structure" (McGraw-Hill, New York, 1960), Vol. II.
119. D. Liberman, *Bull. Am. Phys. Soc.* **9**, 731 (1964).
120. L. Hedin and A. Johansson, *J. Phys.* **B2**, 1336 (1969).
121. D. A. Shirley, *Chem. Phys. Lett.* **16**, 220 (1972).
122. H. F. Schaefer, "The Electronic Structure of Atoms and Molecules" (Addison-Wesley, Reading, Mass., 1972).
123. T. L. Barr, private communication.
124. H. A. Bethe and E. E. Salpeter, Quantum Mechanics of One- and Two-electron Atoms in "Handbuch der Physik" (Springer-Verlag, Berlin, 1955), Vol. 35, p. 88.
125. D. R. Bates, *Mon. Not. Roy. Astr. Soc.* **106**, 432 (1946).

126. J. W. Cooper, *Phys. Rev.* **128**, 681 (1962).
127. U. Fano and J. W. Cooper, *Rev. Mod. Phys.* **40**, 441 (1968).
128. J. W. Cooper, review in "Atomic Inner-shell Processes" (Academic Press, 1975).
129. S. T. Manson, review on atomic cross-section calculations to appear in this series, and S. T. Manson, *Advances in Electronics and Electron Physics*, **41**, 73 (1976).
130. J. J. Huang and J. W. Rabelais, review on molecular cross-sections to appear in this series.
131. See, for example, L. I. Schiff, "Quantum Mechanics" (McGraw-Hill, New York, 1968), Sections 35, 44, and 45, 3rd edn.
132. B. Feuerbacher and R. F. Willis, *J. Phys.* **C9**, 169 (1976).
133. T. Åberg, *Phys. Rev.* **156**, 35 (1967) and in "Inner-shell Ionization Phenomena and Future Applications", R. W. Fink *et al.*, eds (U.S.A.E.C., Conference–72-0404, 1973), p. 1409.
134. J. W. Gadzuk and M. Sunjic, *Phys. Rev.* **B12**, 524 (1975). See also the prior treatment of time scales in photoionization by H. W. Meldner and J. D. Preze, *Phys. Rev.* **A4**, 1388 (1971).
135. T. A. Carlson, *Phys. Rev.* **156**, 142 (1967); M. O. Krause and T. A. Carlson, *Phys. Rev.* **158**, 18 (1967); M. O. Krause, T. A. Carlson, and R. D. Dismukes, *Phys. Rev.* **170**, 37 (1968); M. O. Krause, *Phys. Rev.* **177**, 151 (1968).
136. P. O. Löwdin, *Phys. Rev.* **97**, 1474 (1955).
137. C. S. Fadley, *Chem. Phys. Lett.* **25**, 225 (1974); *J. Electr. Spectr.* **5**, 895 (1974).
138. B. I. Lundqvist, *Phys. Kondens. Materie*, **9**, 236 (1969).
139. F. Wuilleumier and M. O. Krause, *Phys. Rev.* **A10**, 242 (1974).
140. J. Cooper and R. N. Zare, *J. Chem. Phys.* **48**, 942 (1968); and in "Lectures in Theoretical Physics", S. Geltman, K. Mahanthappa, and W. Brittlin, eds (Gordon and Breach, New York, 1969), Vol. XIC.
141. In atomic cross-section calculations based upon typical approximation schemes, the three forms of the dipole operator need not give the same result. Recently, the degree of agreement between calculations using all three forms has been discussed for wave functions including correlation effects in M. S. Pindzola and H. P. Kelly, *Phys. Rev.* **A12**, 1419 (1975).
142. M. O. Krause, *Phys. Rev.* **177**, 151 (1969).
143. A. J. Bearden, *J. Appl. Phys.* **37**, 1681 (1966).
144. G. Rakavy and A. Ron, *Phys. Rev.* **159**, 50 (1967).
145. H. Brysl and C. D. Zerby, *Phys. Rev.* **171**, 292 (1968).
146. S. T. Manson and J. W. Cooper, *Phys. Rev.* **165**, 126 (1968).
147. J. W. Cooper and S. T. Manson, *Phys. Rev.* **177**, 157 (1969).
148. E. J. McGuire, *Phys. Rev.* **175**, 20 (1968).
149. D. J. Kennedy and S. T. Manson, *Phys. Rev.* **A5**, 227 (1972).
150. E. Storm and H. I. Israel, *Nuclear Data Tables* **A7**, 565 (1970).
151. J. H. Scofield, *J. Electr. Spectr.* **8**, 129 (1976).
152. B. L. Henke and E. S. Ebisu, in "Advances in X-ray Analysis" (Plenum Press, New York, 1974), Vol. 17.
153. S. T. Manson, *Phys. Rev. Lett.* **26**, 219 (1971).
154. R. F. Reilman, Alfred Msezone, and S. T. Manson, *J. Electr. Spectr.* **8**, 389 (1976).
155. P. A. Cox and F. A. Orchard, *Chem. Phys. Lett.* **7**, 273 (1970).
156. P. A. Cox, Y. Baer, and C. K. Jorgensen, *Chem. Phys. Lett.* **22**, 433 (1973); P. A. Cox, *Struct. Bonding*, **23**, 59 (1974).

157. P. S. Bagus, J. L. Freeouf, and D. E. Eastman, *Phys. Rev.* **B15**, 3661 (1977).
158. D. Dill, A. F. Starace, and S. T. Manson, *Phys. Rev.* **A11**, 1596 (1975).
159. J. W. Gadzuk, *Sol. St. Comm.* **15**, 1011 (1974); *Phys. Rev.* **B10**, 5030 (1974); *Phys. Rev.* **B12**, 5608 (1975).
160. D. Dill and J. L. Dehmer, *J. Chem. Phys.* **61**, 692 (1974); J. L. Dehmer and D. Dill, *Phys. Rev. Lett.* **35**, 213 (1975).
161. V. I. Nefedov, N. P. Sergushin, I. M. Band, and M. B. Trzhaskowskaya, *J. Electr. Spectr.* **2**, 383 (1973).
162. F. O. Ellison, *J. Chem. Phys.* **61**, 507 (1974); J. W. Rabelais, T. P. Debies, J. L. Berkosky, J. T. Huang, and F. O. Ellison, *J. Chem. Phys.* **61**, 516, 529 (1974).
163. M. J. S. Dewar, A. Komornicki, and W. Thiel, *Chem. Phys. Lett.* **31**, 286 (1975).
164. B. Ritchie, *J. Chem. Phys.* **60**, 898 (1974); **61**, 3279, 3291 (1974); **64**, 3050 (1976).
165. R. S. Williams and D. A. Shirley, *J. Chem. Phys.* **66**, 2378 (1977)
166. J. W. Davenport, *Phys. Rev. Lett.* **36**, 945 (1976).
167. K. H. Johnson in "Advances in Quantum Chemistry", P. O. Löwdin, ed. (Academic Press, New York and London, 1973), Vol. 7, p. 143.
168. J. L. Dehmer, *J. de Physique*, Coll. **C4**, 42 (1978).
169. T. A. Carlson and G. E. McGuire, *J. Electr. Spectr.* **1**, 209 (1972/73).
170. T. A. Carlson, G. E. McGuire, A. E. Jonas, K. L. Cheng, C. P. Anderson, C. C. Lu, and B. P. Pullen in "Electron Spectroscopy", D. A. Shirley, ed. (North Holland, Amsterdam, 1972), p. 207.
171. D. Dill, *J. Chem. Phys.* **65**, 1130 (1976).
172. U. Gelius in "Electron Spectroscopy", D. A. Shirley, ed. (North-Holland, Amsterdam, 1972), p. 311.
173. U. Gelius, C. J. Allen, G. Johansson, H. Siegbahn, D. A. Allison, and K. Siegbahn, *Phys. Scripta*, **3**, 237 (1971); C. J. Allen, U. Gelius, D. A. Allison, G. Johansson, H. Siegbahn, and K. Siegbahn, *J. Electr. Spectr.* **1**, 131 (1972).
174. R. Prins, *Chem. Phys. Lett.* **19**, 355 (1973).
175. A. Calabrese and R. G. Hayes, *Chem. Phys. Lett.* **27**, 376 (1974); *J. Am. Chem. Soc.* **95**, 2819 (1973); **96**, 505 (1974).
176. S. Kono, T. Ishii, T. Sagawa, and T. Kobayasi, *Phys. Rev. Lett.* **28**, 1385 (1972); *Phys. Rev.* **B8**, 795 (1973).
177. C. N. Berglund and W. E. Spicer, *Phys. Rev.* **A136**, 1030, 1044 (1964).
178. B. L. Henke, *Phys. Rev.* **A6**, 94 (1972).
179. M. Mehta and C. S. Fadley, *Phys. Lett.* **A55**, 59 (1975).
180. G. D. Mahan, *Phys. Rev.* **B2**, 4374 (1970); W. L. Schaich and N. W. Ashcroft, *Phys. Rev.* **B3**, 2452 (1970).
181. P. J. Feibelman and D. E. Eastman, *Phys. Rev.* **B10**, 4932 (1974).
182. N. V. Smith and M. M. Traum, *Phys. Rev. Lett.* **31**, 1247 (1973); M. M. Traum, N. V. Smith, and F. J. DiSalvo, *Phys. Rev. Lett.* **32**, 1241 (1974); N. V. Smith and M. M. Traum, *Phys. Rev.* **B11**, 2087 (1975), and references therein.
183. B. Feuerbacher and F. Fitton, *Phys. Rev. Lett.* **30**, 923 (1973); R. R. Tuttle and T. A. Callcott, *Phys. Rev. Lett.* **34**, 86 (1975); R. F. Willis, *Phys. Rev. Lett.* **34**, 670 (1975).
184. C. Kittel, "Quantum Theory of Solids" (Wiley, New York, 1963), Chap. 1.
185. R. J. Baird, L. F. Wagner, and C. S. Fadley, *Phys. Rev. Lett.* **37**, 111 (1976).
186. N. J. Shevchik, *Phys. Rev.* **16**, 3428 (1977); *J. Phys.* **C10**, L555 (1977).

187. R. W. James, "The Optical Principles of the Diffraction of X-rays" (Cornell University Press, Ithaca, 1967), Chap. V.
188. V. G. Aleshin and Y. N. Kucherenko, *J. Electr. Spectr.* **8**, 411 (1976).
189. L. F. Wagner and C. S. Fadley, unpublished results.
190. See, for example, R. A. Pollak, Ph.D. Thesis, University of California at Berkeley, 1972 (Lawrence Berkeley Laboratory Report LBL–1299); S. P. Kowalczyk, Ph.D. Thesis, University of California at Berkeley, 1976 (Report LBL–4319).
191. A. Barrie and N. E. Christensen, *Phys. Rev.* **B14**, 2442 (1976).
192. L. Ley, S. Kowalczyk, R. A. Pollak, and D. A. Shirley, *Phys. Rev. Lett.* **29**, 1088 (1972).
193. R. G. Cavell, S. P. Kowalczyk, L. Ley, R. A. Pollak, B. Mills, D. A. Shirley, and W. Perry, *Phys. Rev.* **B7**, 5313 (1973); F. R. McFeely, S. P. Kowalczyk, L. Ley, R. G. Cavell, R. A. Pollak, and D. A. Shirley, *Phys. Rev.* **B9**, 5268 (1974).
194. M. Sunjic, D. Sokcevic, and A. Lucas, *J. Electr. Spectr.* **5**, 963 (1974); M. Sunjic and D. Sokcevic, *Sol. St. Comm.* **15**, 165 (1974); **15**, 1703 (1974); **18**, 373 (1976).
195. This compilation of electron inelastic attenuation lengths is intended to contain all published determinations, and information concerning it is available through M. P. Seah, National Physical Laboratory, Electron Mean Free Path Versus Energy Compilation, Teddington, Middlesex, U.K.
196. D. R. Penn, *J. Electr. Spectr.* **9**, 29 (1976).
197. P. J. Feibelman, *Phys. Rev.* **B7**, 2305 (1973).
198. P. J. Feibelman, *Surf. Sci.* **36**, 558 (1973).
199. M. O. Krause and F. Wuilleumier, *Phys. Lett.* **A35**, 341 (1971), and in "Proceedings of the International Conference on Inner Shell Ionization Phenomena", Atlanta, Georgia, 1972.
200. R. J. Baird, C. S. Fadley, and L. F. Wagner, *Phys. Rev.* **B15**, 666 (1977).
201. W. A. Fraser, J. V. Florio, W. N. Delgass, and W. D. Robertson, *Surf. Sci.* **36**, 661 (1973).
202. C. S. Fadley, R. J. Baird, W. Siekhaus, T. Novakov, and S. Å. Bergström, *J. Electr. Spectr.* **4**, 93 (1974).
203. R. J. Baird, C. S. Fadley, S. Kawamoto, and M. Mehta, *Chem. Phys. Lett.* **34**, 49 (1975).
204. W. J. Carter, G. K. Schweitzer, and T. A. Carlson, *J. Electr. Spectr.* **5**, 827 (1974).
205. C. D. Wagner, *Anal. Chem.* **44**, 1050 (1972).
206. C. K. Jorgensen and H. Berthou, *Disc. Far. Soc.* **54**, 269 (1973); H. Berthou and C. K. Jorgensen, *Anal. Chem.* **47**, 482 (1975).
207. C. J. Powell and P. E. Larson, *Appl. Surf. Sci.* **1** (1977), in press.
208. C. J. Powell, in A.S.T.M. Special Technical Publication of the 1977 Symposium on Quantitative Surface Analysis, in press.
209. S. A. Flodström, R. Z. Bachrach, R. S. Bauer, and S. B. M. Hagström, *Phys. Rev. Lett.* **37**, 1282 (1976).
210. K. Siegbahn, Uppsala University, *Institute of Physics Report No. UUIP-940* (1976).
211. U. Gelius, P.-F. Heden, J. Hedman, B. J. Lindberg, R. Manne, R. Nordberg, C. Nordling, and K. Siegbahn, *Physica Scripta*, **2**, 70 (1970).
212. O. Goscinski, B. Pickup, and G. Purvis, *Chem. Phys. Lett.* **22**, 117 (1973).

213. G. Howat and O. Goscinski, *Chem. Phys. Lett.* **30**, 87 (1975).
214. P. H. Citrin, R. W. Shaw, A. Packer, and T. D. Thomas in "Electron Spectroscopy", D. A. Shirley, ed. (North Holland, Amsterdam, 1972), p. 691.
215. D. A. Shirley, R. L. Martin, F. R. McFeely, S. P. Kowalczyk, and L. Ley, *Far. Soc. Disc.* No. 60, 7 (1975).
216. R. Manne, *J. Chem. Phys.* **46**, 4645 (1967).
217. H. Basch, *Chem. Phys. Lett.* **5**, 3371 (1970).
218. M. F. Schwartz, *Chem. Phys. Lett.* **5**, 50 (1970); **6**, 631 (1970).
219. D. W. Davis, D. A. Shirley, and T. D. Thomas, *J. Chem. Phys.* **56**, 671 (1972).
220. J. Hedman, M. Klasson, B. J. Lindberg, and C. Nordling in "Electron Spectroscopy", D. A. Shirley, ed. (North-Holland, Amsterdam, 1972), p. 681.
221. D. N. Henderickson, J. M. Hollander, and W. L. Jolly, *J. Inorg. Chem.* **8**, 2642 (1969).
222. T. D. Thomas, *J. Am. Chem. Soc.* **92**, 4184 (1970).
223. P. Finn, R. K. Pearson, J. M. Hollander, and W. L. Jolly, *J. Inorg. Chem.* **10**, 378 (1971).
224. W. L. Jolly and D. N. Henderickson, *J. Am. Chem. Soc.* **92**, 1863 (1970).
225. W. L. Jolly in "Electron Spectroscopy", D. A. Shirley, ed. (North-Holland, Amsterdam, 1972), p. 629.
226. J. A. Hashmall, B. E. Mills, D. A. Shirley, and A. Streitweiser, *J. Am. Chem. Soc.* **94**, 445 (1972).
227. M. Aono, M. Okusawa, T. Sagawa, Y. Takehana, and T. Nagatani, "Proceedings of the 7th International Conference on X-ray Optics and Microanalysis" (Moscow); M. Aono, S. Kawai, S. Kono, M. Okusawa, T. Sagawa, and Y. Takehana, *Sol. St. Comm.* **16**, 13 (1975).
228. R. L. Martin and D. A. Shirley, *J. Am. Chem. Soc.* **96**, 5299 (1974); B. E. Mills, R. L. Martin, and D. A. Shirley, *J. Am. Chem. Soc.* **98**, 2380 (1976).
229. C. D. Wagner, *Far. Soc. Disc.* No. 60, 291 (1975).
230. C. D. Wagner and P. Biloen, *Surf. Sci.* **35**, 82 (1973).
231. D. A. Shirley, *Phys. Rev.* **A7**, 1520 (1973).
232. G. D. Mateescu and J. L. Riemenschneider in "Electron Spectroscopy", D. A. Shirley, ed. (North Holland, Amsterdam, 1972), p. 661; B. J. Lindberg, *J. Electr. Spectr.* **5**, 149 (1974).
233. H. Basch, *Chem. Phys. Lett.* **5**, 3371 (1970).
234. M. Barber, P. Swift, D. Cunnginham, and M. J. Frazer, *Chem. Commun.* **1970**, 1338 (1970).
235. L. Ley, S. P. Kowalczyk, F. R. McFeely, R. A. Pollak, and D. A. Shirley, *Phys. Rev.* **B8**, 2392 (1973).
236. P. H. Citrin and D. R. Hamann, *Phys. Rev.* **B10**, 4948 (1974).
237. J. J. Pireaux, S. Swensson, E. Basilier, P. A. Malmqvist, U. Gelius, R. Caudano, and K. Siegbahn, *Phys. Rev.* **A14**, 2133 (1976).
238. J. E. Demuth and D. E. Eastman, *Phys. Rev. Lett.* **32**, 1123 (1974).
239. D. W. Davis and D. A. Shirley, *Chem. Phys. Lett.* **15**, 185 (1972).
240. R. E. Watson, M. L. Perlman, and J. F. Herbst, *Phys. Rev.* **13**, 2358 (1976).
241. R. Hoogewijs, L. Fiermans, and J. Vennik, *Chem. Phys. Lett.* **37**, 87 (1976).
242. J. W. Gadzuk, *Phys. Rev.* **B14**, 2267 (1976).
243. D. Coster and M. J. Druyvesteyn, *Z. Physik*, **40**, 765 (1927).
244. V. I. Nefedov, *J. Struct. Chem.* **5**, 603, 605 (1964); **7**, 672 (1966).
245. B. Ekstig, E. Källne, E. Noreland, and R. Manne, *Physica Scripta*, **2**, 38 (1970).
246. W. N. Asaad and E. H. S. Burhop, *Proc. Phys. Soc.* **71**, 369 (1958).

247. E. H. S. Burhop, "The Auger Effect and Other Radiationless Transitions" (Cambridge University Press, London, 1952).
248. D. Stalherm, B. Cleff, H. Hillig, and W. Mehlhorn, *Naturforsch.* **24a**, 1728 (1969).
249. J. Hedman, P.-F. Heden, C. Nordling, and K. Siegbahn, *Phys. Lett.* **A29**, 178 (1969).
250. C. S. Fadley, D. A. Shirley, A. J. Freeman, P. S. Bagus, and J. V. Mallow, *Phys. Rev. Lett.* **23**, 1397 (1969).
251. J. C. Carver, T. A. Carlson, L. C. Cain, and G. K. Schweitzer, in "Electron Spectroscopy", D. A. Shirley, ed. (North-Holland, Amsterdam, 1972), p. 803.
252. P. S. Bagus, A. J. Freeman, and F. Sasaki, *Phys. Rev. Lett.* **30**, 850 (1973). These CI calculations actually use seven configurations for ^5S rather than the four discussed here, but the dominant contributors are found to be only those four.
253. S. P. Kowalczyk, L. Ley, R. A. Pollak, F. R. McFeely, and D. A. Shirley, *Phys. Rev.* **B7**, 4009 (1973).
254. S. P. Kowalczyk, F. R. McFeely, L. Ley, and D. A. Shirley in "Proceedings of the 20th Annual Conference on Magnetism and Magnetic Materials", 1974.
255. S. P. Kowalczyk, L. Ley, F. R. McFeely, and D. A. Shirley, *Phys. Rev.* **B11**, 1721 (1975).
256. R. P. Gupta and S. K. Sen, *Phys. Rev.* **B10**, 71 (1974).
257. R. P. Gupta and S. K. Sen, *Phys. Rev.* **B12**, 15 (1975).
258. R. L. Cohen, G. K. Wertheim, A. Rosencwaig, and H. J. Guggenheim, *Phys. Rev.* **B5**, 1037 (1972).
259. F. R. McFeely, S. P. Kowalczyk, L. Ley, and D. A. Shirley, *Phys. Lett.* **A49**, 301 (1974).
260. S. P. Kowalczyk, N. Edelstein, F. R. McFeely, L. Ley, and D. A. Shirley, *Chem. Phys. Lett.* **29**, 491 (1974).
261. M. Campagna, E. Bucher, G. K. Wertheim, and L. D. Longinotti, *Phys. Rev. Lett.* **33**, 165 (1974).
262. C. S. Fadley in "Electron Spectroscopy", D. A. Shirley, ed. (North-Holland, Amsterdam, 1972), p. 781.
263. A. J. Freeman, P. S. Bagus, and J. V. Mallow, *Int. J. Magnetism*, **4**, 35 (1973).
264. S. Sugano in "Proceedings of the NATO Advanced Study Institute on Spectroscopy of Excited States" (Plenum Press, New York, 1976).
265. T. A. Carlson, *Far. Soc. Disc.* No. 60, 30 (1975).
266. J. N. Chazalviel, M. Campagna, G. K. Wertheim, and P. H. Schmidt, *Phys. Rev.* **B10**, 4586 (1976).
267. P.-O. Heden, H. Löfgren, and S. B. M. Hagström, *Phys. Rev. Lett.* **26**, 432 (1971).
268. Y. Baer, *J. Electr. Spectr.* **5**, 611 (1974).
269. T. A. Carlson, M. O. Krause, and W. E. Moddeman, *J. de Physique*, **C2**, 102 (1971).
270. U. Gelius, *J. Electr. Spectr.* **5**, 985 (1974).
271. D. P. Spears, H. J. Fischbeck, and T. A. Carlson, *Phys. Rev.* **A9**, 1603 (1974).
272. T. N. Chang and R. T. Poe, *Phys. Rev.* **A12**, 1432 (1975).
273. H. Basch, *Chem. Phys.* **10**, 157 (1975); T. X. Carroll and T. D. Thomas, *J. Electr. Spectr.* **10**, 215 (1977).
274. D. T. Clark in *Far. Soc. Disc.* No. 60, 183 (1975).
275. P. S. Bagus and E.-K. Viinikka, *Phys. Rev.* **A15**, 1486 (1977).

276. S. Doniach and M. Sunjic, *J. Phys.* **C3**, 285 (1970).
277. P. H. Citrin, *Phys. Rev.* **B12**, 5545 (1973).
278. D. C. Langreth, *Phys. Rev. Lett.* **26**, 1229 (1971); J. J. Chang and D. C. Langreth, *Phys. Rev.* **B5**, 3512 (1972); **B8**, 4638 (1973); G. D. Mahan, *Phys. Stat. Solid.* **55**, 703 (1973).
279. W. J. Pardee, G. D. Mahan, D. E. Eastman, R. A. Pollak, L. Ley, F. R. McFeely, S. P. Kowalczyk, and D. A. Shirley, *Phys. Rev.* **B11**, 3614 (1975); J. C. Fuggle, D. J. Fabian, and L. M. Watson, *J. Electr. Spectr.* **9**, 99 (1976).
280. T. Novakov, *Phys. Rev.* **B3**, 2693 (1971).
281. D. C. Frost, A. Ishitani, and C. A. McDowell, *Molec. Phys.* **24**, 861 (1972).
282. T. A. Carlson, J. C. Carver, L. J. Saethre, and F. Garcia Santibanez, *J. Electr. Spectr.* **5**, 247 (1974); T. A. Carlson, J. C. Carver, and G. A. Vernon, *J. Chem. Phys.* **62**, 932 (1975).
283. K. S. Kim and R. E. Davis, *J. Electr. Spectr.* **1**, 251 (1972/73); K. S. Kim, *Phys. Rev.* **B11**, 2177 (1975).
284. L. Yin, I. Adler, T. Tsang, L. I. Matienzo, and S. O. Grim, *Chem. Phys. Lett.* **24**, 81 (1974).
285. S. Larsson, *Chem. Phys. Lett.* **32**, 401 (1975); **40**, 362 (1976).
286. S. Asada and S. Sugano, *J. Phys. Soc. Jap.* **41**, 1291 (1976).
287. E. W. Plummer and W. R. Salaneck in "Proceedings of the 5th International Conference on Vacuum Ultraviolet Radiation Physics", Montpellier, France (1977).
288. S. Lundqvist and G. Wendin, *J. Electr. Spectr.* **5**, 513 (1974).
289. G. Wendin and M. Ohno, *Physica Scripta*, **14**, 148 (1976); G. Wendin, M. Ohno, and S. Lundqvist, *Sol. St. Comm.* **19**, 165 (1976).
290. C. S. Fadley, *J. Electr. Spectr.* **5**, 725 (1974).
291. C. S. Fadley and S. Å. L. Bergström, *Phys. Lett.* **A35**, 375 (1971); in "Electron Spectroscopy", D. A. Shirley, ed. (North-Holland, Amsterdam, 1972), p. 233.
292. C. S. Fadley, *Far. Soc. Disc.* No. 60, 18 (1975).
293. R. J. Baird, C. S. Fadley, S. Kawamoto, M. Mehta, R. Alvarez, and J. A. Silva, *Anal. Chem.* **48**, 843 (1976).
294. J. M. Hill, D. G. Royce, C. S. Fadley, L. F. Wagner, and F. J. Grunthaner, *Chem. Phys. Lett.* **44**, 225 (1976).
295. R. J. Baird, C. S. Fadley, S. M. Goldberg, P. J. Feibelman, and M. Sunjic, *Surf. Sci.* **72**, 495 (1978).
296. A. M. Bradshaw, W. Domcke, and L. S. Cederbaum, *Phys. Rev.* **B16**, 1480 (1977).
297. R. Haydock and M. J. Kelly, *Surf. Sci.* **38**, 139 (1973); M. C. Dejonqueres and F. Cyrot-Lackmann, *Surf. Sci.* **53**, 429 (1975); K. S. Sohn, D. G. Dempsey, L. Kleinmann, and E. Caruthers, *Phys. Rev.* **B13**, 1515 (1976); **B14**, 3185, 3193 (1976).
298. M. Mehta and C. S. Fadley, *Phys. Rev. Lett.* **39**, 1569 (1977).
299. M. Mehta and C. S. Fadley, *Chem. Phys. Lett.* **46**, 225 (1977).
300. K. Siegbahn, U. Gelius, H. Siegbahn, and E. Olsen, *Phys. Lett.* **A32**, 221 (1970).
301. R. Baudoing, R. M. Stern, and H. Taub, *Surf. Sci.* **11**, 255 (1968); E. G. McRae, *Surf. Sci.* **44**, 321 (1974), and earlier references therein.
302. R. E. DeWames and W. F. Hall, *Acta Cryst.* **A24**, 206 (1968), and earlier experimental references therein.
303. R. J. Baird, C. S. Fadley, S. M. Goldberg, and S. Kono, to be published.

304. J. B. Pendry and R. Lindsay, private communication.
305. R. J. Baird, C. S. Fadley, and L. F. Wagner, *Far. Soc. Disc.* No. 60, 143 (1975).
306. F. R. McFeely, J. Stöhr, G. Apai, P. S. Wehner, and D. A. Shirley, *Phys. Rev.* **B14**, 3273 (1976).
307. L. F. Wagner, Z. Hussain, and C. S. Fadley, *Sol. St. Comm.* **21**, 453 (1977).
308. G. Apai, J. Stöhr, R. S. Williams, P. S. Wehner, S. P. Kowalczyk, and D. A. Shirley, *Phys. Rev.* **B15**, 584 (1977).
309. Z. Hussain, L. F. Wagner, and C. S. Fadley, to be published.
310. L. Ley, R. H. Williams, and P. Kemeny, *Bull. Am. Phys. Soc.* **24**, 942 (1976); R. H. Williams, P. C. Kemeny, and L. Ley, *Sol. St. Comm.* **19**, 495 (1976).
311. P. S. Wehner, J. Stöhr, G. Apai, F. R. McFeely, and D. A. Shirley, *Phys. Rev. Lett.* **38**, 169 (1977).
312. K.-F. Berggren and F. Martino, *Sol. St. Comm.* **20**, 1057 (1976).
313. P.-O. Nilsson and L. Ilver, *Sol. St. Comm.* **17**, 667 (1975); L. Ilver and P.-O. Nilsson, *Sol. St. Comm.* **18**, 677 (1976).
314. L. F. Wagner, Z. Hussain, and C. S. Fadley, *Sol. St. Comm.* **21**, 257 (1977).
315. N. F. Christensen and B. O. Seraphin, *Phys. Rev.* **B4**, 3321 (1972).
316. N. V. Smith, *Phys. Rev.* **B3**, 1862 (1971). Two different choices of spin–orbit parameter were used in this tight-binding scheme for the calculations of Fig. 52.
317. R. J. Baird, L. F. Wagner, and C. S. Fadley, unpublished results.
318. Z. Hussain, N. F. T. Hall, L. F. Wagner, S. P. Kowalczyk, C. S. Fadley, K. A. Thompson, and R. L. Dod, *Sol. St. Commun.* **25**, 907 (1978).
319. R. S. Williams, P. S. Wehner, J. Stöhr, and D. A. Shirley, *Phys. Rev. Lett.* **39**, 302 (1977).